Equivalent Circuit-Based Efficiency Enhancement of On-Chip Antennas for Wideband mm-Wave/THz Radar Systems

Von der Fakultät für Ingenieurwissenschaften,
Abteilung Elektrotechnik und Informationstechnik
der Universität Duisburg-Essen

zur Erlangung des akademischen Grades
Doktor der Ingenieurwissenschaften

genehmigte Dissertation

von

M. Sc. Benedikt Sievert

aus

Krefeld

Erster Gutachter: Prof. Dr. sc. techn. Daniel Erni

Zweiter Gutachter: Prof. Dr.-Ing. Nils Pohl

Tag der mündlichen Prüfung: 25.10.2023

UNIVERSITÄT DUISBURG ESSEN

Offen im Denken

Equivalent Circuit-Based Efficiency Enhancement of On-Chip Antennas for Wideband mm-Wave/THz Radar Systems

Von der Fakultät für Ingenieurwissenschaften,
Abteilung Elektrotechnik und Informationstechnik
der Universität Duisburg-Essen

zur Erlangung des akademischen Grades
Doktor der Ingenieurwissenschaften
genehmigte Dissertation

von
M. Sc. Benedikt Sievert
aus Krefeld

Datum der Einreichung: 03.04.2023
Datum der mündlichen Prüfung: 25.10.2023

Erster Gutachter und Betreuer der Promotion:
Prof. Dr. sc. techn. Daniel Erni
Allgemeine und Theoretische Elektrotechnik, Universität Duisburg-Essen

Zweiter Gutachter der Promotion:
Prof. Dr.-Ing. Nils Pohl
Integrierte Systeme, Ruhr-Universität Bochum

Die vorliegende Dissertation wurde im Rahmen des SFB/TRR 196 MARIE, Projekt C05, erstellt.

Kurzfassung

Bei Radar-Systemen im Millimeterwellen-Bereich stellt die Freiraumdämpfung eine inhärente Begrenzung des Detektionsbereichs dar. In dieser Arbeit werden On-Chip-Antennen für den Betrieb in Frequenzbereichen zwischen 220 GHz und 450 GHz entwickelt, die die Bandbreite der Radar-Systeme abdecken und klein genug sind, um in Antennenarrays eingesetzt zu werden. Die Antennen basieren auf der Mikrostreifenleitungstechnik in Silizium-Germanium (SiGe) Monolithic Microwave Integrated Circuits (MMICs), wobei kapazitive Diskontinuitäten in den Antennenentwurf eingebettet werden, um die Abstrahleffizienz zu erhöhen. Mit einem zugeschnittenen Speise- und Anpassnetzwerk wird die Antennenbandbreite künstlich erhöht, indem mehrere resonante Antennen verschiedener Resonanzfrequenzen kombiniert werden. Um den Wirkungsmechanismus der Antennen zu erklären, die zusätzlichen Strahlungsbeiträge durch die Diskontinuitäten zu beweisen und die physikalische Interpretierbarkeit zu steigern, wird ein vollumfängliches Ersatzschaltbild zur Unterscheidung von Joule'schen Verlusten und Strahlungsbeiträgen entwickelt. Außerdem wird hergeleitet, dass die Strahlung von und die Kopplung zwischen den Diskontinuitäten in Mikrostreifen-basierten Antennen das abgestrahlte Fernfeld vollständig beschreiben. Deshalb können Schaltungs- und Strahlungsparameter wie Eingangsimpedanz, Stromverteilung, Abstrahldiagramm und Abstrahleffizienz mit der Ersatzschaltung beschrieben werden. Das vorgestellte Modell wird durch Ergebnisse aus Vollwellen-Simulationen und Messungen bestätigt, wodurch sowohl die Nutzbarkeit der gezeigten Antennenprototypen für Radar-Anwendungen als auch die Leistungsfähigkeit der Ersatzschaltung gezeigt wird.

Abstract

The free space path loss at millimeter waves inherently limits the reading range of radar systems. In this thesis, on-chip antennas operating in frequency ranges between 220 GHz and 450 GHz are developed, which cover the radar systems' bandwidth and are geometrically small enough for assembly in an antenna array. The antennas are based on microstrip topologies in Silicon Germanium (SiGe) Monolithic Microwave Integrated Circuits (MMICs), where capacitive discontinuities are embedded into the antenna design to increase the radiation efficiency. Using a tailored feeding- and matching network, the overall antenna bandwidth is artificially increased by combining multiple resonant antennas of different operating frequencies. To explain the antenna operation, prove the additional radiation contributions of the discontinuities, and enhance the physical insight, a thorough equivalent circuit model separating dissipation losses and radiation contributions is developed. Furthermore, the radiation and coupling of the discontinuities in the microstrip antenna are shown to describe the antenna far field thoroughly. Thus, the equivalent circuit description can be used to calculate circuit and radiation parameters such as input impedance, current distribution, radiation pattern, and radiation efficiency. The proposed model is confirmed by full-wave and measurement results highlighting both the applicability of the presented antenna prototypes in the radar context and the capabilities of the circuit model.

Contents

1. Introduction

The increasing demand for larger communication data rates or more accurate sensors supported by technological development yields the exploration of higher frequencies in the mm-wave and sub-THz range for existing industrial applications [1], [2] and within fundamental research [3]. This trend is driven by a smaller system integration size resulting from a smaller wavelength and a larger achievable absolute bandwidth obtained when upscaling a constant relative bandwidth to higher frequencies. Consequently, the resulting systems allow for either increased communication data rates or higher resolution for sensing while enabling mobile and small sensors [A4]. In radiating mm-wave applications such as material characterization [5], wireless communication [6], or RAdio Detection And Ranging (Radar) [7], the antenna acts as a transducer between the system and the free space, ultimately enabling the controlled radiation of Electro Magnetic (EM) waves. Since the antenna gain, a fundamental measure of the antenna's ability to radiate into a spatial direction, is incorporated in the second power for the gain budget of a radar system, the antenna performance can dramatically affect the system performance. Beyond conventional distance measurements, antennas operated in an array allow for the spatial selection of the radar imaging area, which enables even real-time back projections of the observed scene [8]. Here, reflections due to mismatch and antenna-to-antenna coupling may decrease system performance significantly and are thus an active field of research [9]. The mentioned antenna-to-antenna coupling and, of course, the size of the antennas determine the suitability for implementation in an array. From this, two essential prerequisites arise for the antenna design within this thesis. First, a suitable antenna must perform as required within the radar bandwidth, typically involving a negligible variation of the radiation pattern versus frequency and a wideband matching. Second, it should preserve the imaging capabilities of the radar system by providing suitable size, sufficient decoupling from other antennas, and only such amplitude- or phase distortions that can be compensated.

Radar systems at mm-waves [10]–[12] prepared for industrial markets or sub-THz demonstrators [A13] are fabricated on-chip since, with increasing frequencies, the attractiveness for on-chip implementation also grows. Because the on-chip environment is not intended as a technology for antenna design, the resulting antenna performance is often suboptimal. Different antenna approaches with fundamental tradeoffs are available in the literature [14], and choosing a suitable approach depends on the application and long-term goals of the system concept. For example, typical backside-radiating

approaches utilize a dielectric lens to mitigate the effect of substrate waves [7], [15], although most lens approaches limit the beamforming capabilities of arrays. On the contrary, frontside-radiating antennas can benefit from an off-chip ground, which requires well-designed backside etched cavities to mitigate substrate waves [16]. Alternatively, antennas with an on-chip ground can be thoroughly fabricated in the chip fabrication run. Consequently, they do not require further assembly asides from the bonding for the mm-wave system [17], [18]. Furthermore, surface waves do practically not impair this antenna concept, as the antenna substrate is electrically very thin. The alternative technologies, i.e., antenna off-chip or antenna in package, suffer from increased transition losses [19] or require higher fabrication effort [20] while the limitations of the on-chip environments are conquered.

To enable efficient on-chip antennas with sufficient bandwidth for mm-wave radar systems, this thesis investigates methods to increase the radiation efficiency of frontside-radiating on-chip antennas while obtaining a moderate antenna bandwidth. In order to achieve frontside-radiation without backside etching, the antennas presented here utilize an on-chip ground plane, and they are derivatives of long-existing microstrip patch antennas [21]. By using capacitive discontinuities, the antenna designer controls another degree of freedom, and additionally, the antenna efficiency can be increased. Last, multiple resonant radiators are combined, increasing the overall operating bandwidth for the final antenna assembly. Additional to the antenna design, the insight into on-chip antenna prototypes operating around 250 GHz, 300 GHz, and 400 GHz is pursued using a simplifying Equivalent Circuit (EC) model. In detail, the model allows for evaluating the most relevant antenna parameters since not only input impedance and current distribution, but even radiation patterns based on far-field superposition can be predicted, as shortly discussed in [A22]. Thorough investigation and separation of radiation and dissipation losses even enable calculating the radiation efficiency of those antennas based on circuit models [A23]. The in-depth analysis of the radiation mechanisms in microstrip discontinuities is of fundamental importance for these models and presented in this thesis. Gaining insights into EM structures with the help of models is both long existing and still actively investigated field of research. For example, the Partial Element Equivalent Circuit (PEEC) [24], which is still used for particular antenna types [25], transforms general geometries of conductors into equivalent circuit models while including losses. Furthermore, very early Method of Moments (MoM) approaches were used to model microstrip antennas, as in [26], [27]. In addition, fundamental investigations and explanations of periodic structures and frequency-selective surfaces utilize circuit representations for physical insight [28]. Last, circuit models of antennas are substantial in modeling the behavior of mm-wave and THz devices, as in [29], [30]. The models presented in this thesis combine both aspects as they increase physical insight on the one hand and, on the other hand, enable investigation of the interplay of antenna and circuits.

This thesis is organized as follows. Chapter 2 introduces mm-wave radar fundamentals and highlights the challenges for the utilized antenna and the integrated on-chip system to motivate the following investigations. The theory for wave propagation in typical

on-chip substrates, including Transmission Line (TL) theory, is presented alongside the commonly used EC representation and derivations for surface waves in Chapter 3. Chapter 4 explains commonly used antenna parameters and investigates radiated fields for fundamental radiators in different media, i.e., in air, with a ground plane, and with a grounded dielectric substrate. In Chapter 5, a generalized design and corresponding circuit model for a suitable on-chip antenna candidate are developed and discussed based on the previous fundamentals. The radiation of different discontinuities within the microstrip technique, on which the antennas are based, is investigated in depth. Chapter 6 presents three antenna prototypes fabricated on-chip, each featuring a linear, circular, or frequency-dependent polarization, respectively. All prototypes offer an increased radiation bandwidth for improved radar resolution, and their applicability in future radar systems is discussed. Finally, Chapter 7 concludes the results of this thesis and gives an outlook on possible future research.

2. mm-Wave FMCW Radar

The localization of so-called targets using electromagnetic radio waves is termed radar. Independent from the specific radar type, the distance between the radar transmitter (Tx), target, and radar receiver (Rx) is evaluated based on the speed of light (c_0 in vacuum) and round trip time, which denotes the time it took a signal from the radar to target and back. This chapter introduces the basic radar principle, discusses system limitations, and presents concepts for a direction of arrival estimation. Furthermore, mm-wave antenna approaches usable for such radar systems are presented, and the challenges associated with integrating these antennas into mm-wave radar systems are discussed.

2.1. Radar Fundamentals

A commonly used classification of radar systems distinguishes between Continuous Wave (CW) and pulse radar. The former either modulates the frequency and phase or operates un-modulated (e.g., for Doppler-based velocity measurements), and the latter involves at least an amplitude modulation to form the pulse. This section describes the fundamental principle of an Frequency Modulated Continuous Wave (FMCW) radar and the basics of range and direction estimation of targets.

2.1.1. FMCW Principle

FMCW radar is a variation of CW radar in which the operating frequency is modulated. Fig. 2.1 shows a simplified FMCW radar system transmitting a frequency-modulated sinusoidal signal towards a target at a distance r_0, which is back reflected towards the receiver. Here, the Tx and Rx antenna are separated to ease the explanation. Besides separate Tx and Rx implementations [31], mm-wave radar systems with a combined Tx/Rx antenna using Wilkinson dividers [18] or hybrids [32] exist. These systems typically implement a Voltage Controlled Oscillator (VCO) and one or more frequency multipliers, usually doublers, on the chip. Besides a receive mixer and optional amplifiers before the frequency doublers, a frequency divider and an external Phase Locked Loop (PLL) are common to generate a stable frequency ramp [33]. The transmit signal s_{tx} undergoes the radio channel, where an antenna transmits it, then it is reflected by the target to be ultimately received by a second antenna and

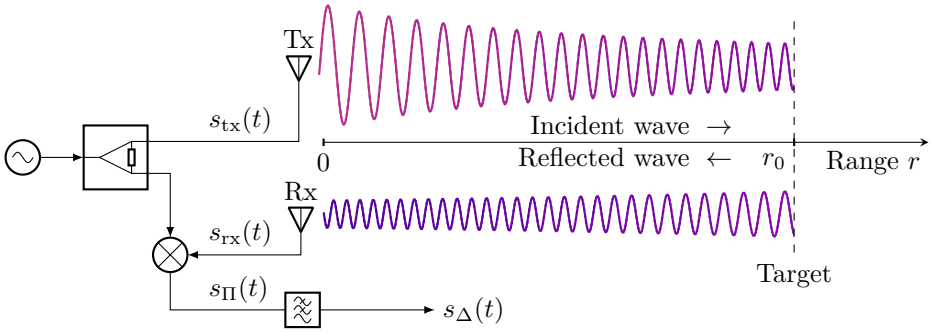

Figure 2.1.: Simplified FMCW radar system with separated Tx and Rx antenna and a single target. The incident and reflected wave are separated graphically to ease understanding, although they are superimposed in a real scenario.

denoted as s_{rx}. Due to the frequency down sweep used as frequency modulation, the received signal $s_{rx}(t)$ will be higher in frequency than $s_{tx}(t)$ since this was transmitted $\Delta t = 2\,r_0/c_0$ ago. The product of both signals $s_\Pi(t)$ is low-pass filtered to yield $s_\Delta(t)$, which contains the information about the round-trip time and, thus, the target distance.

The frequency modulation shown in Fig. 2.2 (a) is represented by a discrete staircase-like ramp since it eases the intuitive explanation of the subsequent signals and renders a good representation of signals generated by a fractional PLL [34, pp. 40]. The period of the chirp signal is referred to as T_c, and the overall bandwidth covered is B. Besides the initially transmitted frequency f_{tx}, the delayed frequency ramp f_{rx} is shown. To simplify the following analysis, only the time frame $t_1 \leq t \leq t_2$ is considered, where both Tx and Rx signals are constant in frequency. It is explicitly noted that the operation of an FMCW radar is not limited to this time frame, but the intuitive explanation is eased. It is assumed that the time frame $t_2 - t_1$ is sufficiently long,

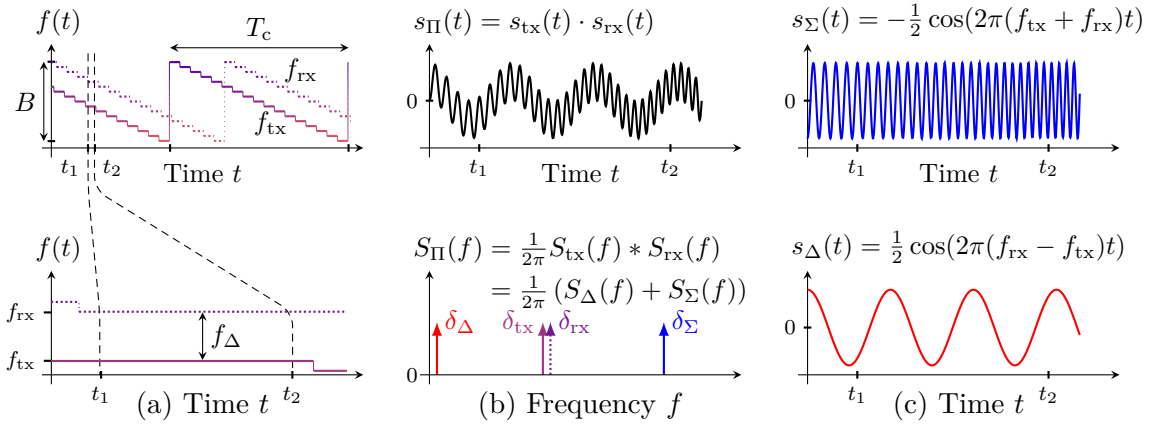

Figure 2.2.: Exemplary diagrams of (a) an FMCW frequency chirp, (b) the corresponding beating signals after the receive mixer, and (c) the separation into sum- and difference frequency.

such that the Radio Frequency (RF) is considered in a steady state and that infinite sinusoidal functions can model it. The product of $\sin(f_{\mathrm{tx}}t)$ and $\sin(f_{\mathrm{rx}}t)$ is depicted in Fig. 2.2 (b) in the time- and frequency domain, where the product in the time domain corresponds to the convolution in the frequency domain. As a result, the product can be represented by a sum of two functions, which contain the difference f_Δ and sum f_Σ of the input frequencies. The low-pass filter in Fig. 2.1 passes only the lower frequency f_Δ, usually called an Intermediate Frequency (IF) signal. This frequency relates the round-trip time to the chirp time and overall radar bandwidth to calculate the target distance. If multiple targets are present, these frequencies will superimpose in dependence on the target distance and their Radar Cross Section (RCS), which measures the effective reflecting area of a radar target. The digitally sampled signal $s_\Delta(t)$ can be investigated concerning the contained frequency components using an efficient Fast Fourier Transform (FFT), where each peak in the IF spectrum refers to a reflection in the radio channel. It should be noted that the difference frequency is not only affected by the distance of the target but also by the Doppler effect if the target moves towards or away from the radar.

2.1.2. Range Estimation and Resolution

As explained above, the IF frequency depends on the round-trip time of the signal and the rate of frequency change of the frequency ramp. Furthermore, the Doppler shift directly affects the received signal frequency since the IF frequency f_Δ relates to the target distance r_0 and velocity v_0 by [35, pp. 27]

$$f_\Delta = \mp \frac{B}{T_\mathrm{c}} \frac{2r_0}{c_0} + \frac{2v_0 f_\mathrm{c}}{c_0}, \tag{2.1}$$

where B is the radar bandwidth, T_c is the frequency chirp time, and f_c is the radar center frequency. To be exact, the Doppler effect varies along the frequency chirp as the transmitted frequency changes, and further discussion on the so-called range-Doppler coupling can be found in [36, pp. 803]. The negative and positive signs correspond to a positive and negative frequency ramp, respectively, indicating the inverse sign of frequency slope. With different frequency ramps for the modulation, the Doppler shift and range can be accessed separately [37]. Furthermore, instead of physically measuring the Doppler shift to evaluate the velocity, successive range measurements can also be compared to evaluate a target's velocity [38]. If multiple bins of range measurements are stored in the memory, the velocity calculation can be implemented as a further FFT along successive range measurements [39]. Estimating ranges from the frequencies f_Δ in a spectrum is straightforward based on the known radar parameters and (2.1). The applied FFT is often combined with a zero-padding of the IF signal, which interpolates the resulting range spectrum. For pulse- and FMCW radar, the achievable resolution is determined by the utilized bandwidth B according to [40,

p. 44]

$$\Delta r = \frac{c_0}{2\,B}, \tag{2.2}$$

where the choice of window function for the FFT might suppress side lobes on the cost of a widened time-domain pulse, resulting in a reduced ability to separate closely spaced targets [40, pp. 44]. An in-depth discussion about radar accuracy is found in [41, pp. 25].

Still, with a limited number of samples, there needs to be a limitation in the maximum readable range. Besides a sufficiently long chirp, which needs to cover the round-trip time of the farthest distant target to avoid ambiguities, the Signal to Noise Ratio (SNR) ultimately determines the maximum reading range. The received signal strength calculates according to the radar transmission equation [38, p. 2.4]

$$P_{\mathrm{rx}} = P_{\mathrm{tx}} \frac{G_{\mathrm{tx}}\, G_{\mathrm{rx}}\, \sigma_{\mathrm{RCS}}\, \lambda_0^2}{(4\pi)^3\, r_0^4}, \tag{2.3}$$

where G_{tx} and G_{rx} describe the gain of the Tx and Rx antenna in the direction of the target, and σ_{RCS} is the RCS of the target. Evaluating the system performance cannot be reduced to simply considering the receiver SNR, which includes noise contributions from the mixer, amplifier, or analog-to-digital converter, since the effect of oscillator phase noise must be included as well. A more in-depth discussion of the radar system's SNR can be found in [40, pp. 25] and [35, pp. 31].

2.1.3. Direction of Arrival Estimation

Triangulation, which involves comparing the ranges of different target-antenna combinations, enables estimating one or multiple target positions using multiple antennas. Classic approaches utilize electronically or mechanically steerable antenna beams, where the observation direction is defined before the radar measurement. This analog beamforming requires phase shifters or vector modulators for transmit and receive paths to define the solid angle to which the radar system is focused. In this configuration, all targets out of this solid angle are missed – or require a further measurement; however, the robustness against interference from other directions is increased. The same applies to mechanically rotating radar dishes since they focus the radar's sensitivity into a particular solid angle and suppress signals from other directions.

With increasing computational power and affordable analog-to-digital converters, beam steering (or advanced algorithms such as MUSIC) can be applied after the radar measurement [39]. Following the analog nomenclature, the postprocessing approach is called digital beamforming, which highlights the idea of defining the antenna pattern in postprocessing. An in-depth overview of digital beamforming and the associated challenges is given in [42, pp. 404]. The digitally sampled signals are weighted with

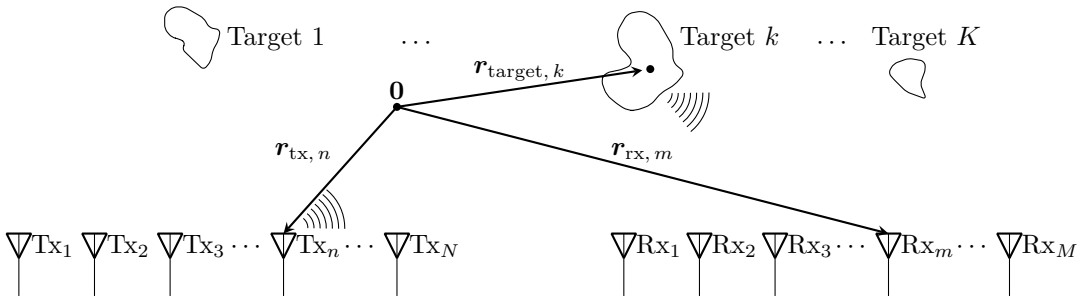

Figure 2.3.: Schematic representation of a Tx-array (left-hand side) with N antennas, an Rx-array (right-hand side) with M antennas, and K exemplary radar targets.

complex weighing factors, which enables the general definition of arbitrary radiation patterns [43, pp. 121]. For equally spaced antennas, the beamforming can be efficiently handled using an FFT [44]. A short overview of different estimation techniques for the direction of arrival in the radar context is given in [9, pp. 23], [45]. These methods are considered subsets of general Multiple Input Multiple Output (MIMO) radar problems, which include all available transmission functions of the different Tx and Rx paths to determine target locations [46, pp. 67]. Fig. 2.3 shows the generally considered geometry used to determine the position of a target. With N Tx and M Rx antennas located at known positions $\boldsymbol{r}_{\mathrm{tx},\,n}$ and $\boldsymbol{r}_{\mathrm{rx},\,m}$, the positions of all targets $\boldsymbol{r}_{\mathrm{target},\,k}$ should be estimated. The estimation techniques usually require obtaining the different radio channels between the n-th Tx and m-th Rx antenna. Either time domain multiplexing, which involves transmitting with only one antenna at a time and receiving on all receive antennas, or other multiplexing techniques can be applied to measure these channels. The subsequent beamforming could either rely on far-field assumptions [9, pp. 18] as they are known from array theory or focus on specific points in the near fields [9, pp. 20] using a pixel-wise back transform [8]. An overview of the processing associated with beamforming for different array topologies and corresponding estimation techniques can be found in [47]. Last, so-called sparse arrays enable larger apertures with moderate antenna count [48].

2.2. mm-Wave Antenna Concepts

Although mm-wave radar is the preferred application considered in this thesis, also in other mm-wave applications such as material characterization [5] or wireless communication [6], the antenna cannot be considered a standalone component of the RF system. For a standalone antenna design, the system needs a transition towards a waveguide technology, as, for example, a rectangular waveguide compatible with a waveguide-conform horn antenna [12]. Consequently, the antenna design process can usually not be separated from the remaining system, which is called antenna- and circuit co-design and discussed in [49]. For antenna-device integration of oscillators [29],

[30], [50] or detectors [A4], [51], the antenna is typically tailored towards the optimum operating point of the device. In radar systems incorporating longer signal paths [12] or Microstrip Line (MSL)-based hybrids and couplers [52], the antenna is designed for a suitable reference impedance. Possible categorizations of mm-wave antennas differ between resonant- and non-resonant approaches, which can be implemented on-chip or off-chip. Further sub-categories are given by different packaging- and fabrication techniques associated with the antenna, e.g., implementing a superstrate, a focusing lens, or dielectric resonators. A very illustrative review of the different techniques is given in [14], and a further overview can be found in [53], [54], and [55]. The following sections present a short discussion of on- and off-chip antennas as well as their characterization.

2.2.1. On-Chip Antennas

An antenna integrated on the same chip as the active devices, such as a mixer, multiplier, detector, oscillator, or a complete system, is called an on-chip antenna. The following paragraphs divide antennas into traveling wave – or non-resonant – and standing wave – or resonant – concepts. Traveling wave antennas can offer a wider bandwidth but often require more space for correct operation. Contrary, standing-wave antennas are often of a size in the order of the wavelength and are thus also limited in their operating bandwidth. Consequently, if operated at a sufficiently high frequency and thus geometrically large compared to a small wavelength, every resonant antenna can behave as a non-resonant antenna and vice versa. A typical example is the bow-tie antenna representing a planar implementation of the bi-conical antenna [56, pp. 500], which is inherently broadband and thus non-resonant. At a sufficiently low frequency, the bow-tie operates highly comparable to a typical resonant dipole [56, pp. 509].

All antenna prototypes presented in this thesis have been designed for SiGe Bipolar – Complementary Metal Oxide Semiconductor (BiCMOS) processes from Infineon Technologies AG. The commercially available SiGe MMICs typically feature roughly 4-5 thin layers and 2-4 thicker metal layers [33], [57]. These are embedded in Silicon Dioxide (SiO_2) of $10\,\mu$m to $15\,\mu$m thickness [58], referred to as the Back End of Line (BEOL). The antennas presented in this thesis are fabricated in Infineon's high-speed BiCMOS processes B11HFC and B12HFC [59], [60]. A perspective view showing the on-chip antenna from Section 6.2 and a generic SiGe layer stack are depicted in Fig. 2.4. Between the layers, a via can be used for inter-layer connections, where the M1-via is used to connect the active devices in the Silicon (Si) Front End of Line (FEOL) with the passive metal layer stack [61, p. 14]. Usually, the Design Rule Check (DRC)-driven filling and cheesing, which means perforating, of the on-chip metal layers inherently limits the antenna performance [62]. When implementing the antenna on-chip, the small distance to the on-chip ground further reduces the antenna bandwidth and efficiency if the on-chip ground is utilized [63]. However, it will be

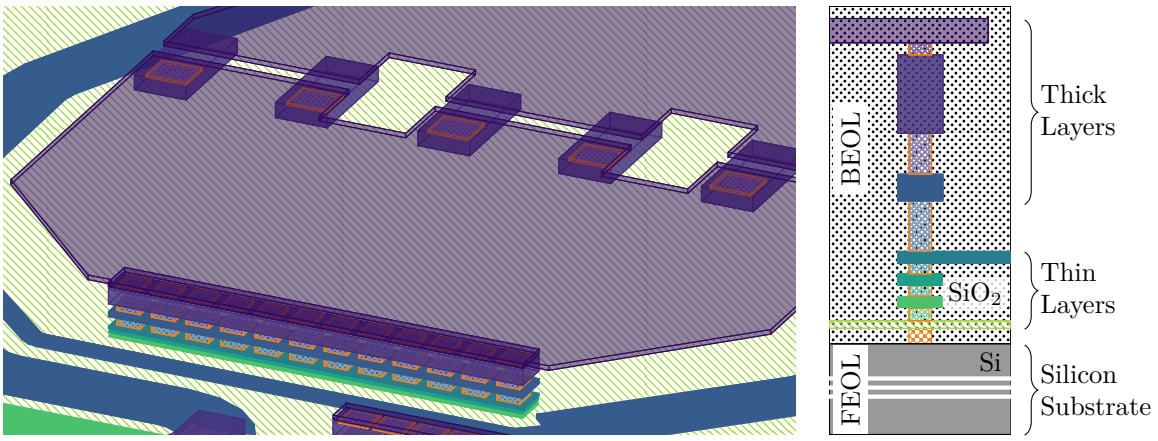

Figure 2.4.: Exemplary perspective view (a) on microstrip lines and an antenna element of the antenna presented in Section 6.2 and (b) exemplary SiGe metal stackup adapted from [33] (not to scale).

shown that such a small distance significantly reduces the disturbing effect of surface waves that occur for electrically thicker substrates. The use of superstrates above the antenna has been investigated theoretically [64]–[66] and implemented on-chip [67]. The concepts of dielectric lenses and dielectric resonators to increase bandwidth and efficiency will be covered separately for traveling- and standing wave antennas in the following paragraphs.

Traveling Wave Concepts

The leaky-wave antenna is a commonly used traveling wave antenna at mm-waves, offering wide bandwidth and beam-steering capabilities. Well-documented design guides and models to estimate the performance of traveling wave antennas can be found in the literature [28], which enables a wide variety of antennas implemented on-chip. An approach based on Substrate Integrated Waveguide (SIW) is presented in [68], where the frequency-dependent beam-steering of the antenna is integrated into the system design. Similarly, the MSL-based leaky-wave antenna presented in [A69] integrates beam-steering into the system concept, which should be integrated with a photonic THz source [A70]. Furthermore, wideband antennas of fractal type contain a considerable fraction of traveling waves; typical examples are spiral- or log-periodic antennas [A71], [A72]. Since using dielectric lenses usually hinders the beam-steering capabilities, a cylindrical lens was utilized in [A69] to increase the aperture in the transversal direction and maintain the beam-steering in the longitudinal direction.

Standing Wave Concepts

Typical representations of resonant on-chip antennas are based on monopole-, dipole- and bow-tie antennas [32], [57] or microstrip-patch antennas for broadside radiation [A13], [73]. Furthermore, radiation in the broadside direction [16] or symmetrized end-fire radiation [74] can be achieved with further processing by removing the silicon wafer under the antenna, referred to as localized backside etching. Typically, broadband solutions usually involve not-using the on-chip ground plane. By omitting this ground, either an off-chip ground (typically using the Printed Circuit Boards (PCB) underneath the chip) or radiation through the FEOL is possible. For the antennas using on-chip ground planes, the achievable radiation efficiency is limited by the minimal distance between the antenna and the ground plane [14]. Although concepts for high impedance surfaces that could relax the limitation of the small distance between ground and antenna and corresponding models have been presented in [A75], [A76], the integration in commercial SiGe stacks still lacks antenna efficiency and frequency bandwidth. The overall performance can be increased significantly with a thicker substrate for the high impedance surface and an additional superstrate. This improved performance is achieved through an increased fabrication effort [77]. Antennas integrated with high-speed devices on III-V semiconductors are typically tailored to the device [29], and usual implementations rely on variants of resonant slot- or dipole-antennas [A78]. Especially with resonant tunneling diodes, considerable array power [79] and extremely high frequencies can be achieved [50], indicating a successful antenna-device co-design. Independent from the technology used for antenna- and device fabrication, dielectric resonators can increase radiation efficiency as they help couple the fields into the free space. However, besides limited bandwidth [A80], the overall positioning of the resonators is crucial and, at best, considered in the design process [81]. Last, using dielectric lenses increases the antenna aperture and thus the system gain, but most often also helps achieve a radiation pattern useable over a wide bandwidth [31]. The approach presented in [32], [82] omits the ground plane, and the antenna radiates through the FEOL. With the dielectric lens, the effect of substrate waves (cf. Section 3.2.3) associated with radiation into the backend is mitigated by sufficiently large antenna gain [15].

2.2.2. Off-Chip and Antenna in Package Solutions

As for on-chip antennas, both standing wave (resonant) and traveling wave (non-resonant) antennas can be implemented off-chip. Sometimes antenna in package solutions [83], [84] are differentiated from other off-chip solutions. However, in the scope of this thesis, they share their key advantages and challenges, which are only shortly mentioned here. As a great advantage, the antenna designer can choose from various substrates such as ceramics [85], glass wafers [86], and support technologies; for instance, etched silicon [87] or high precision milling of metals [88] are available. The

cost and design-rule-driven limitations of antenna size, which apply to on-chip antennas, are often relaxed for off-chip antennas. An essential challenge for off-chip antennas is the connection of active circuitry and antenna, which increases fabrication effort and requires a careful choice of integration technique. Near-field coupling, often applied to antennas in the superstrate [85], is a comparably efficient method to excite the antenna; however, the design of such structures is challenging. The more direct approach using galvanic coupling to ceramic and glass wafers or PCBs requires physical contact established by bumps or bond wires. The RF connection with bond wires is associated with considerable losses even at low mm-wave frequencies [19]. With more effort and a fully differential design approach, the connection with bond wires remains significantly lossy [89] compared to the flip-chip approaches like [20], [84]. The radar system presented in [12] accepts the bond wire losses and feeds into an SIW. This waveguide transitions into a rectangular waveguide, offering significant flexibility using the standardized WR-6.5 waveguide flange. With precise and advanced packaging, direct feeding from an antenna in package into a dielectric rod [90] offers low interconnection losses, high efficiency, and wide bandwidth. Last, the off-chip implementation enables technologies for phase-shifting and beam-steering topologies using, e.g., liquid crystal tuned resonators [A91] or micro-electro-mechanical systems [92].

2.2.3. Antenna Characterization

The characterization of mm-wave antennas is conceptually based on antenna characterization methods utilized at lower frequencies. Challenges arise due to the reduced dynamic range of Vector Network Analyser (VNA) approaches utilizing frequency converters to reach higher frequency bands and the usually tiny antenna- and contact-pad sizes. Two recent overviews of mm-wave antenna measurement systems are found in [93] and [94, p. 2199].

A commonly used antenna characterization technique using on-wafer probes establishes a galvanic contact between the signal source and the antenna. Besides undesired radiation from incompletely contacted probe tips [95], even a probe tip contacting a match radiates [96] and thus influences the measured radiation pattern. A similar effect, namely the radiation of an impedance-matched MSL, is presented and discussed in Section 5.3.3. Classic error models and calibration techniques are transferred onto the chip level to compensate for the error two-port associated with the frequency converters and the on-wafer probe. Although these correction techniques are well-established for lower frequencies, the position accuracy of the probe and a repeatable probe contact is challenging [97], [98]. The strengths and weaknesses between Through-Reflect-Line (TRL) approaches fabricated on the wafer of the device under test and reference calibration substrates from probe manufacturers are discussed in [99]. For n-port measurements, the high cost of the measurement equipment often permits the measurement of all port parameters at one time. Instead, multiple measurements at two ports each are carried out, further limiting the achievable accuracy, where all

other ports are terminated using on-chip resistors [A100], [A101] or other absorbing techniques [61, pp. 137] to apply exact or approximate calibration methods [102].

The gain is measured either in the broadside direction [103] or using robot-based solutions [96], [104], [A105]. For multi-axis robots, a tracking technique is required to obtain the necessary position accuracy for phase-stable measurements [104], whereas inherently spherical systems [A105], [106] are still limited by cable movement [107]. Furthermore, the electrically very large on-wafer probe influences the radiation pattern by shadowing and scattering [108], [109]. With a hybrid approach combining simulation and measurement of far-field data, even the radiation efficiency can be measured for lower mm-wave frequencies [110]. Especially for large aperture antennas, near-field measurements are also applicable [111], [112]. Photonics-enhanced near-field scanning solutions offer fewer metal parts in the antenna proximity in addition to a small probe footprint [113]. Last, measurement methods exist to characterize mm-wave radiation patterns without an on-wafer probe. For example, a high-gain antenna can be terminated with different standards and illuminated in these different conditions, which enables the calculation of the antenna characteristic based on a conventional calibration procedure [114]. Fully operational radar systems can be characterized concerning their radiation pattern using a reference target at different positions [115], [116]. With direct access to off-chip Tx and Rx antenna feeding points, the measurement using a reference target without an operating radar system is also feasible [117].

2.3. Challenges in mm-Wave FMCW Radar Systems

Implementing a mm-wave FMCW radar system on chip is, beyond the previously explained difficulties of implementing corresponding antennas, challenging and, thus, an active field of research in the laboratories of both academia and industry. Besides solutions for general industry [118], [119], mm-wave radar systems on-chip are available from chip manufacturers. These off-the-shelf solutions typically conform to the automotive radar bands; some are evaluated independently [120], and the frequencies covered range from 24 GHz up to 120 GHz [121]. Generally speaking, automotive radar is an important driving force for radar systems, e.g., 77 GHz automotive radar drives a broad range of radar research [122], which results in well-established sensors [123], interference countermeasures [124], and test ranges [125], [126].

The research includes but is not limited to increasing the maximum radar range, the resolution, robustness against other sensors, the scalability for MIMO approaches, and calibrating assembled systems. First, increasing the aperture size of mm-wave radar systems is desirable to compensate for the typically low output power. As the chip area associated with increased aperture size is costly, the presented systems using on-chip antennas typically utilize scalable approaches, which achieve good performance [127]. Here, multiple MMICs are coupled via RF PCBs, where the outstanding MIMO performance is on the cost of the fabrication effort [128]. Alternatively, off-chip arrays

require transitions between MMIC and antenna, increasing the fabrication effort [129]. Although on-chip antennas in SiGe technologies can be realized without additional lenses [17], the technology inherently limits their performance. Although the typically used dielectric lenses naturally limit the beam steering possibilities, they yield excellent gain for both backside [32] and frontside radiating antennas [18]. Antenna coupling is difficult to overcome for dense on-chip arrays, where the antennas must be placed close to one another. Techniques for decoupling antennas off-chip at 60 GHz are discussed in [130], and tailored sparse arrays can effectively reduce the number of required channels [48]. A thorough overview of antenna concepts in the mm-wave radar context is found in [131].

Whereas typical signal processing approaches assume narrowband systems or non-dispersive channels [132, pp. 25], postprocessing the datasets generated by wideband systems requires solutions for dispersion and wideband calibration- and correction methods [A133]. Especially the scalable approaches with multiple MMICs have uncertainties in the antenna position and unknown feeding losses and feeding phases, where the calibration of those systems is necessary to increase accuracy further [45], [134]. Furthermore, even single-antenna systems require radar calibration to reach their highest performance [135]. To additionally improve the phase noise of fully-integrated systems, efforts are made to stabilize VCOs with PLLs [136], and external oscillators are proposed with excellent phase noise [137]. Last, the limited efficiency combined with desired maximized output powers results in significant heating of the radar systems, where large apertures result in an increased density of heat sources. In those cases, careful considerations of the thermal handling and dissipation of heat (possibly via the PCB) need to be considered.

To overcome the antenna's efficiency limitations, a method to increase the achievable radiation efficiency and a thorough analysis of this method are presented in Chapter 5. The following two chapters present and derive the fundamental theory and concepts necessary for this analysis. Furthermore, the antenna prototypes presented in Chapter 6 will be implemented with a feeding network to increase the overall frequency bandwidth of the resonant antenna approaches, which ultimately increases the usually antenna-limited resolution of the radar system.

3. Wave Propagation in On-Chip Substrates

This chapter discusses different wave propagation mechanisms, desired and undesired ones, within typically utilized on-chip substrates. Whenever applicable, the differences between low-permittivity substrates such as SiO_2 with a relative permittivity of $\varepsilon_r = 4.1$ and high-permittivity materials such as Indium Phosphide (InP) or Si, approximated by a relative permittivity of $\varepsilon_r = 12$, will be discussed. The desired propagation along TLs is investigated in the first step since this inherently yields field solutions for the undesired wave propagation mechanisms. If not stated otherwise, the harmonic time dependence is assumed throughout this thesis. Using the phasor notation, vector- and scalar fields as well as circuit quantities are assumed with an implicit time dependence given by $\exp[\mathrm{j}\omega t]$.

A TL guides EM signals in the form of waves along conductor surfaces or material interfaces. In the following, TLs consisting of at least two conductors will be treated.

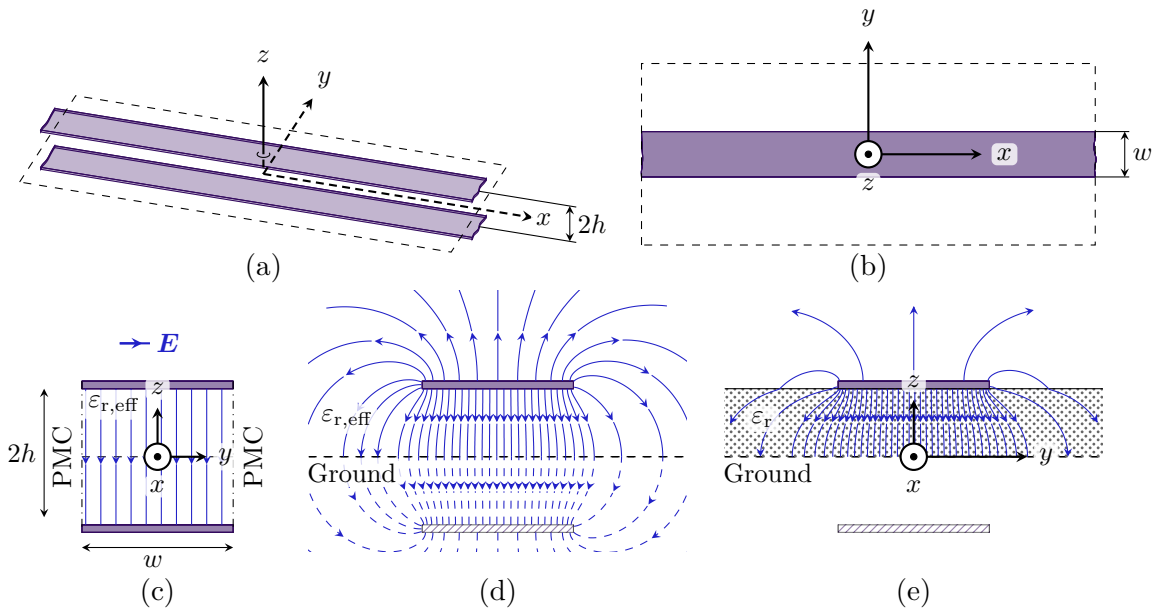

Figure 3.1.: Parallel plate waveguide in (a) perspective, (b) top view, and in the cross section showing (c) the ideal electric field, (d) the actual field with fringing fields, and (e) the substrate effect, as it occurs for the MSL.

Although single-conductor, e.g., rectangular or circular, waveguide setups could be described as a dispersive TL, the explanation below will focus on two or more conductors, especially on the Microstrip Line (MSL). MSLs are a commonly used waveguiding technique for both mm-wave and on-chip design since numerous models and design guidelines exist for the characteristic impedance, bends, miters, stubs, and other discontinuities [138, pp. 183]. At first, an ideal parallel-plate waveguide will be considered here since it has essential commonalities with MSLs but is easier to describe. Figs. 3.1 (a) and (b) depict a perspective and top view on a parallel plate waveguide section of height $2h$ and width w. The cross sections in Figs. 3.1 (c), (d), and (e) show the transition from an idealized parallel plate waveguide laterally terminated by a Perfect Magnetic Conductor (PMC) to a real one with fringing fields and to the MSL solution on a dielectric slab of height h. Although only the static electric fields are depicted here, they render a reliable approximation or the exact solution for the ideal parallel plate waveguide of the commonly used fundamental Transverse Electro Magnetic (TEM) mode. If the MSL is sufficiently wide, most of the field is concentrated below the strip, which can be approximated well by the ideal parallel plate waveguide. For narrow MSL, the approximation by a parallel plate waveguide does not yield quantitatively correct results but qualitative physical insight, which justifies the approximation in this chapter. Thus, the ideal parallel plate waveguide (cf. Fig. 3.1 (c)) will be considered for introducing the core concepts of TLs, as it only depends on the x- and z-direction and can even be reduced to a one-dimensional case depending solely on the propagation in the x-direction. The effect of the substrate-air boundary for the MSL will be considered using a so-called effective relative permittivity as a homogeneous background medium, as shown for comparison in Figs. 3.1 (d) and (e).

3.1. Wave Propagation

Generally speaking, wave propagation is enabled by a time-variant electric and magnetic field, whose cross-product results in a non-zero Poynting vector. A TL of a constant cross section is described by two essential parameters, namely the characteristic impedance Z_C and the complex propagation constant γ. Whereas the characteristic impedance of a lossless line describes the square root of the ratio between magnetic and

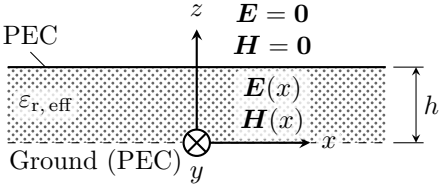

Figure 3.2.: Cross section of the ideal parallel plate waveguide to calculate the fundamental TEM mode.

electric energy per cross section, as the free space impedance η_0 for unguided waves, the frequency-dependent propagation constant γ describes the phase- and group velocity as well as the attenuation of the wave along the propagation direction of the TL. If the propagation constant shows a non-linear frequency dependence, the TL and the propagation constant would be referred to as dispersive, where the dispersion can result from frequency-dependent material properties, loss mechanisms, materials boundaries, and higher-order mode propagation.

Fig. 3.2 shows the longitudinal section of a parallel plate waveguide guiding a wave along the x-direction with an effective relative permittivity $\varepsilon_{\mathrm{r,\,eff}}$. For this initial investigation, the wave propagation is considered in a lossless parallel plate waveguide, which means that the dielectric is lossless and that both conductors, top and bottom, are considered as a Perfect Electric Conductor (PEC). The one-dimensional Helmholz equation needs to be solved to determine the TEM case solution fulfilling

$$\left(\frac{\partial^2}{\partial x^2} + k^2\right) H_y = 0 \tag{3.1}$$

with $k = k_0\sqrt{\varepsilon_{\mathrm{r,\,eff}}}$. The boundary conditions at $z = 0$ and $z = h$ yield the field solution

$$H_y = \left(+H_y^+ \exp\left(-\mathrm{j}\beta x\right) + H_y^- \exp\left(\mathrm{j}\beta x\right)\right), \tag{3.2}$$

$$E_z = \frac{\beta}{\omega\varepsilon_0\,\varepsilon_{\mathrm{r,\,eff}}}\left(-H_y^+ \exp\left(-\mathrm{j}\beta x\right) + H_y^- \exp\left(\mathrm{j}\beta x\right)\right), \tag{3.3}$$

$$\beta = k_0\sqrt{\varepsilon_{\mathrm{r,\,eff}}}, \tag{3.4}$$

$$k_0 = \frac{2\pi\, f}{c_0}, \tag{3.5}$$

with the propagation constant β, which corresponds to the wave number k in the lossless case. All remaining field components are zero by choice of the propagation direction, the fundamental mode, and the boundary conditions. Here, the sign in the exponential functions determines the wave propagation direction, where H_y^+ weights the wave in the $+x$ direction and H_y^- in the $-x$ direction. The following chapters will consider only the wave propagating in the $+x$ direction. By assuming homogeneous fields in the cross section, i.e., no z-dependence, only the solution for the fundamental TEM mode was obtained. Higher-order mode solutions for the parallel plate waveguide could be calculated analytically if $H_y(x, z)$ (Transverse Magnetic (TM) mode) or $E_z(x, z)$ was sought (Transverse Electric (TE) mode). However, the TEM mode is frequently utilized and will be regarded in the following. The solution of the phase constant β indicates a typical definition for the effective permittivity of an arbitrary TL – it compares the propagation constant of the TL to the propagation constant of the same geometry in free space. It can be seen that the waves do not face attenuation ($\beta \in \mathbb{R}$) and will thus propagate unhindered into their respective direction along the waveguide. In the following paragraphs, the dielectric will be considered an arbitrary relative permittivity ε_{r} until the effective permittivity is redefined for the MSL.

3.2. Loss Mechanisms

Losses in TLs can be divided into four classes, which will be explained shortly here and in more depth in the following. The conductor losses, which result from a current density in a conductor of finite conductivity, are also referred to as magnetic losses since the current density in the conductor is directly related to the magnetic field in the TL [139]. Whereas conductor losses can be reduced by increasing the conductor's cross section for low frequencies, the skin effect effectively narrows the utilized conductor cross section and dominates this loss mechanism at high frequencies. Furthermore, the surface roughness of conductors virtually increases the path length and, thus, the corresponding losses. In between the conductors, the substrate losses result from static or alternating electric fields in the dielectric, and they are thus also called electric losses. The last two loss mechanisms only occur at discontinuities of TLs, namely the substrate wave losses, where waves bound to the substrate propagate along the substrate, and radiation or space-wave losses, where the waves diverge from the substrate, which means they are not bound to it. The different effects will be discussed in the following sections.

3.2.1. Conductor- and Substrate Losses

For a conducting half-space, the current distribution in the conductor due to the skin effect can be calculated analytically. The result shows an exponential decay of the current density for increasing distance to the surface. A corresponding penetration depth is described with the so-called skin depth [140]

$$\delta_{\text{skin}} = \sqrt{\frac{2}{\omega\,\mu\,\kappa}}, \tag{3.6}$$

with ω the angular frequency, μ the permeability of the conductor, and κ its conductivity. A simple model for this behavior, which correctly models the power loss due to the field at the surface [141, p. 28], uses the surface resistance [140]

$$R_{\text{surf}} = \sqrt{\frac{\omega\,\mu}{2\,\kappa}}, \tag{3.7}$$

where the surface impedance also describes the inductive behavior of the half-space

$$Z_{\text{surf}} = (1 + \mathrm{j})\,R_{\text{surf}}. \tag{3.8}$$

That means the complex volumetric current distribution and its losses in a conductor can be approximated by a surface current density defined by the tangential electric field and the surface impedance Z_{surf} if the sheet is thick enough (typically several skin depths).

Losses in dielectrics could either result from conductivity, which describes the possibility of moving charges through the dielectric, or polarization losses, which implies heat dissipation due to the vibration or rotation of microscopic dipoles. Whereas the description of the former is closely related to the conductivity σ and the latter to the loss tangent $\tan\delta$, both perspectives are transferable into each other for a monochromatic excitation by [141, p. 11]

$$\varepsilon_0\varepsilon_\mathrm{r}\ \tan\delta = \frac{\sigma}{\omega}. \tag{3.9}$$

The $\tan\delta$ can be included in all calculations using a complex permittivity [141, p. 11]

$$\varepsilon_{\mathrm{r,\ lossy}} = \varepsilon_\mathrm{r}\left(1 - \mathrm{j}\ \tan\delta\right). \tag{3.10}$$

It is noted that a constant $\tan\delta$ can only represent a lossy medium within a limited bandwidth. However, the antenna and the overall radar system investigated in this thesis are sufficiently narrowband to describe the dielectric losses using a constant $\tan\delta$; and the conductor losses will be shown to exceed the dielectric losses in the next section.

3.2.2. Modeling Lossy Transmission Lines

A lossy TL is modeled based on the ideal parallel plate waveguide from above to discuss the conductor and dielectric losses in depth. An exemplary geometry of the problem is depicted in Fig. 3.3, where the solution for the electric and magnetic fields in both domains is sought. In contrast to the case of the ideal parallel plate waveguide, a surface impedance Z_surf at $z = h$ models a top metal layer of finite conductivity according to (3.8). Here, the ground layer is assumed lossless to reduce the complexity of the resulting equations; however, considering losses there as well by using a surface impedance is analog to the derivation below. Besides conductor losses via the surface impedance, dielectric losses are considered in this derivation using a complex permittivity according to (3.10).

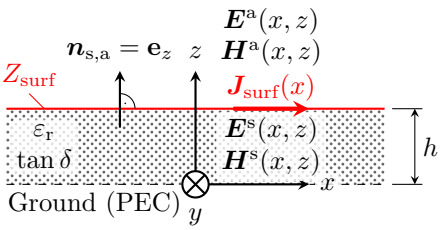

Figure 3.3.: Cross section of the parallel plate waveguide with finite surface conductivity and dielectric losses to model a lossy TL.

In contrast to the above, the field propagates in two different domains, and the unknown coefficients are evaluated by forcing

$$E_x(z=0) = 0, \tag{3.11}$$

$$\boldsymbol{n}_{\mathrm{s,\,a}} \times (\boldsymbol{H}^{\mathrm{a}} - \boldsymbol{H}^{\mathrm{s}})\,|_{z=h} = \boldsymbol{J}_{\mathrm{surf}} = \frac{E_x|_{z=h}}{Z_{\mathrm{surf}}}\mathbf{e}_x, \tag{3.12}$$

$$\boldsymbol{n}_{\mathrm{s,\,a}} \times (\boldsymbol{E}^{\mathrm{a}} - \boldsymbol{E}^{\mathrm{s}})\,|_{z=h} = \mathbf{0}. \tag{3.13}$$

The problem is assumed invariant in y with a magnetic field strength exclusively in the y-direction and wave-propagation in x- (and possibly z-) direction, such that a solution to the Helmholtz equation

$$\left(\frac{\partial^2}{\partial x^2} + \frac{\partial^2}{\partial z^2} + k^2\right) H_y = 0 \tag{3.14}$$

is needed, where k is the wavenumber (k_0 for $z > h$ and $k_{\mathrm{s}} = k_0\sqrt{\varepsilon_{\mathrm{r}}}$ for $z < h$) and H_y the magnetic field strength in the respective medium. The solution to this equation reads

$$H_y^{\mathrm{a}} = H_0 \exp[-\mathrm{j}k_z z] \qquad \exp[-\mathrm{j}\beta x]\,, \tag{3.15}$$

$$H_y^{\mathrm{s}} = (C_1 \exp[-\mathrm{j}p_{\mathrm{s}} z] + C_2 \exp[\mathrm{j}p_{\mathrm{s}} z]) \exp[-\mathrm{j}\beta x]\,, \tag{3.16}$$

if a finite field for large distances z is assumed, and the electric field for the respective regions can be calculated using

$$E_x^{\mathrm{a/s}} = \frac{+\mathrm{j}}{\omega\varepsilon_{\mathrm{a/s}}} \frac{\partial}{\partial z} H_y^{\mathrm{a/s}}, \tag{3.17}$$

$$E_z^{\mathrm{a/s}} = \frac{-\mathrm{j}}{\omega\varepsilon_{\mathrm{a/s}}} \frac{\partial}{\partial x} H_y^{\mathrm{a/s}}. \tag{3.18}$$

In (3.15), the wavenumber k_0 has been rewritten to describe a wave propagating in air

$$k_z^2 + \beta^2 = k_0^2, \tag{3.19}$$

where it should be noted that k_z is only real if $\beta < k_0$, i.e., the wave propagates faster in the TL than in free space. In addition, the wave in air can only exhibit radiation if k_z is real since only then the wave propagates in the z-direction – instead of being exponentially decaying (cf. (3.15)). This condition is well-known for leaky-wave structures, where only a fast wave can radiate from a homogeneous waveguide [28, pp. 262]. At this point, it is evident that a homogeneous TL, either filled with air or with a dielectric, cannot radiate into free space since $\beta \geq k_0$, and the radiation caused by discontinuities will be regarded separately in Section 5.3. Last, the wavenumber in the material (cf. (3.16)) determines β and p_{s} by

$$p_{\mathrm{s}}^2 + \beta^2 = k_{\mathrm{s}}^2. \tag{3.20}$$

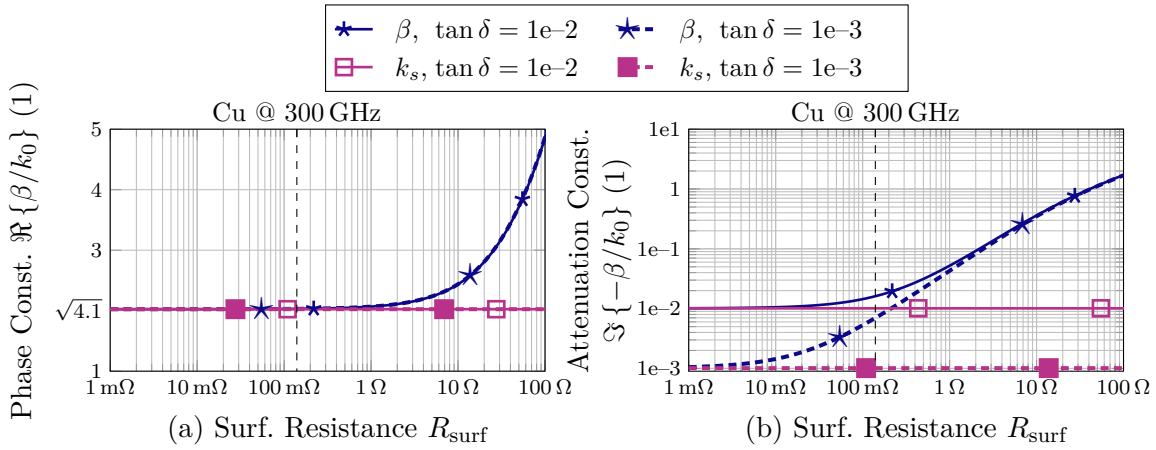

(a) Surf. Resistance R_{surf} (b) Surf. Resistance R_{surf}

Figure 3.4.: Wavenumber β in (a) real and (b) imaginary parts for two different substrate loss tangents and in dependence on the surface resistance of the top metal layer according to (3.21). As expected for moderate dielectric losses, the phase constant β is undistinguishable for both $\tan\delta$.

The solution of (3.15)-(3.18) constraint to (3.11)-(3.13) yields the equation

$$\frac{\omega\varepsilon_0 Z_{\text{surf}}\sqrt{k_0^2-\beta^2}}{\omega\varepsilon_0 Z_{\text{surf}}+\sqrt{k_0^2-\beta^2}} = -\mathrm{j}\frac{\sqrt{k_{\text{s}}^2-\beta^2}}{\varepsilon_{\text{r}}}\tan\left(\sqrt{k_{\text{s}}^2-\beta^2}\,h\right), \tag{3.21}$$

which can be solved numerically for β. At this point, the solution for β could be reinterpreted as $-\mathrm{j}\gamma$, where γ is the complex propagation constant of the modeled TL. Here, the propagation will be modeled by a complex phase constant β to remain consistent with the previous and following sections, and its negative imaginary part can be interpreted as a loss contribution.

For different surface impedances $Z_{\text{surf}} = R_{\text{surf}}(1+\mathrm{j})$ with $1\,\text{m}\Omega \leq R_{\text{surf}} \leq 100\,\Omega$, $f = 300\,\text{GHz}$, and a substrate of height $h = 10\,\mu\text{m}$, relative permittivity $\varepsilon_{\text{r}} = 4.1$, and loss factor $\tan\delta \in \{1\text{e–}3, 1\text{e–}2\}$, the phase constant β has been calculated for the lossy TL. Although (3.21) generally allows for multiple solutions due to the branches of the tangent function, only the solution corresponding to the wave guided by the TL will be considered in this paragraph. Fig. 3.4 shows the normalized phase constant in real and imaginary parts, indicating the wave propagation and attenuation properties, respectively. Whereas the former directly allows reading the square root of the effective permittivity, the latter describes the loss modeled by the propagation constant. As optical guidance, the surface resistance of copper at 300 GHz has also been highlighted, indicating the case for a good conductor. Furthermore, the wavenumber of the substrate k_{s} is given for comparison. Since the lossy conductor results in an electric field in x-direction $|E_x| > 0$, the field inside the conductor is, strictly speaking, dispersive and a fundamental TM mode. In practice, the plot for β indicates that the phase constant is virtually unaffected for good conductors (cf. Fig. 3.4 (a)) and that the loss

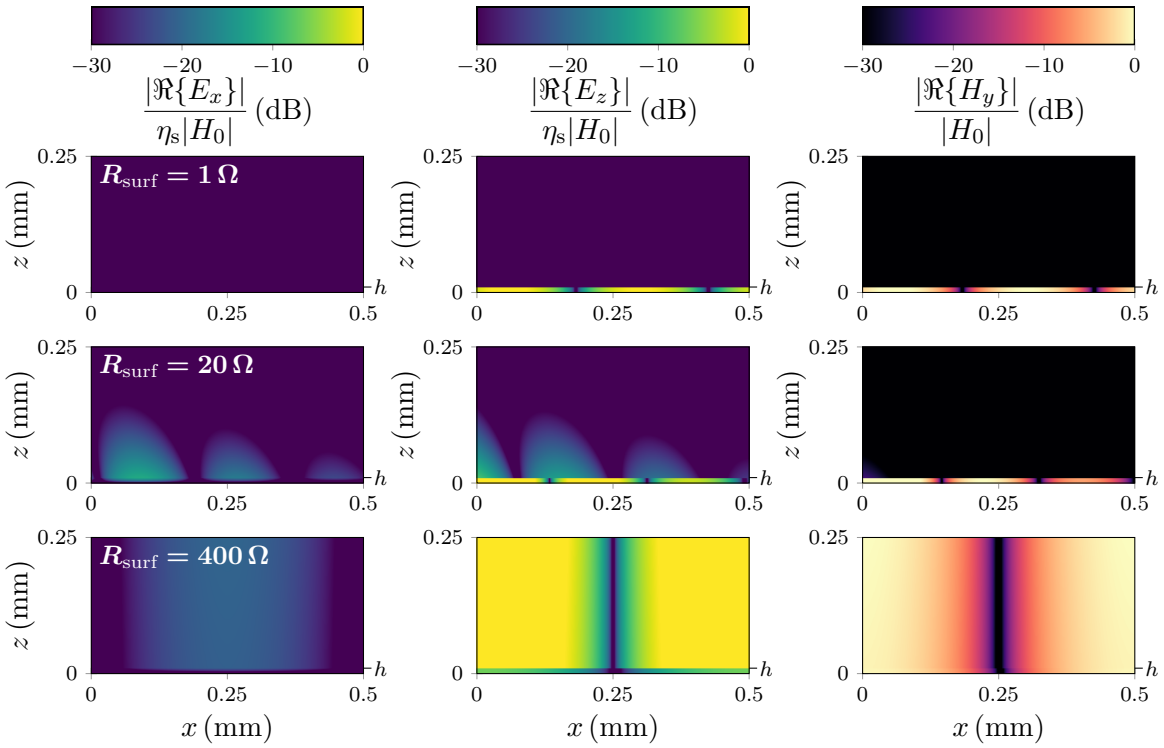

Figure 3.5.: Instantaneous field plot of the parallel-plate waveguide longitudinal cross section for different surface impedances $Z_{surf} = R_{surf}(1 + j)$ and a substrate of permittivity $\varepsilon_r = 4.1$ and height $h = 10\,\mu$m at 300 GHz. At $R_{surf} = 1\,\Omega$ and $20\,\Omega$, the field solution shows the transmissions-line propagation, whereas the solution corresponds to the TM_0 mode of the grounded dielectric slab at $400\,\Omega$, which is covered in the next section.

factor of the propagation constant is still considerably smaller than 1 (cf. Fig. 3.4 (b)), such that the TEM solution for the lossless parallel plate waveguide still renders a good approximation of the phase-constant. It should be noted that the loss factor of k_s depicted in Fig. 3.4 (b) is not precisely the loss factor of the dielectric, which should be $1/2\sqrt{\varepsilon_r}\tan\delta$. Here, it just occurs that the choice of relative permittivity results in $\sqrt{4.1} \approx 2$, which roughly cancels out the 1/2. Last, the losses due to only a lossy top metal layer dominate the loss contributions for the low-loss dielectric ($\tan\delta$ = 1e–3), indicating that the ohmic losses dominate the dielectric losses. For very large surface impedances, the propagation constant's loss tangent approaches 1, meaning the wave is critically damped rather than propagating.

The solution for β can then be used to calculate the unknown coefficients with (3.19)

$$C_1 = C_2 = H_0 \frac{(k_z + \omega\,\varepsilon_0\,Z_{surf})\exp[-jk_z\,h]}{2\omega\,\varepsilon_0\,Z_{surf}\,\cos(k_z\,h)} \tag{3.22}$$

and thus the resulting fields in and above the TL

$$E_x^{\mathrm{a}} = +H_0 \frac{k_z}{\varepsilon_0 \omega} \quad \exp[-\mathrm{j}k_z z] \exp[-\mathrm{j}\beta x] , \tag{3.23}$$

$$E_x^{\mathrm{s}} = -C_1 \frac{\mathrm{j}\, 2p_{\mathrm{s}}}{\varepsilon_0 \varepsilon_{\mathrm{r}} \omega} \quad \sin(p_{\mathrm{s}} z) \exp[-\mathrm{j}\beta x] , \tag{3.24}$$

$$E_z^{\mathrm{a}} = -H_0 \frac{\beta}{\varepsilon_0 \omega} \quad \exp[-\mathrm{j}k_z z] \exp[-\mathrm{j}\beta x] , \tag{3.25}$$

$$E_z^{\mathrm{s}} = -C_1 \frac{2\beta}{\varepsilon_0 \varepsilon_{\mathrm{r}} \omega} \quad \cos(p_{\mathrm{s}} z) \exp[-\mathrm{j}\beta x] . \tag{3.26}$$

Fig. 3.5 shows the field results for different surface resistances. As discussed from the phase constant, a low resistance $R_{\mathrm{surf}} = 1\,\Omega$ results in a quasi-TEM behavior, which means $E_x \approx 0$, and the field is only confined in the TL due to the large conductivity. For an unphysically large surface resistance of $R_{\mathrm{surf}} = 20\,\Omega$, the fields show a strongly attenuated case, but still, the confinement and the dominant field strength indicate a transmission-line mode. Given this significant attenuation, a distinct TM behavior is found due to the non-vanishing longitudinal electric field component resulting from the surface impedance. For the even larger surface impedance $R_{\mathrm{surf}} = 400\,\Omega$, the TL mode would be even more attenuated. However, as stated above, (3.21) describes multiple solutions for β, each referred to as a mode. The $R_{\mathrm{surf}} = 400\,\Omega$-case was solved for the fundamental surface wave mode TM_0, given by the main branch of the tangent function. Here, the wave is weakly attenuated since it barely interacts with the substrate, and the fields extend far into the z-direction. More details on surface waves will be presented in the next section.

This derivation already includes higher-order TM modes of the transmission line, and as shown, the TM surface wave case for large R_{surf} can be calculated. Furthermore, the lossless case from Section 3.1 can be considered using $R_{\mathrm{surf}} = 0$ and $\tan\delta = 0$. Finally, it should be noted that the TL width is not included in the derivation since an infinite extent in the y-direction is assumed. For narrow TLs with a width-to-height ratio $w/h < 1$, the conductor losses typically dominate the dielectric losses even more.

3.2.3. Modeling Substrate Waves

Substrate or surface waves can be excited by discontinuities in waveguiding structures [142]. They need to be considered in mm-wave and on-chip design since they can result in both relevant loss and undesired radiation [143]. The solution for surface waves in a substrate is derived in numerous works [141], [144] very similar to the derivation above, and in fact, $R_{\mathrm{surf}} \to \infty$ in (3.21)-(3.22) gives the same result. The problem will be only solved for the TM case since the fundamental mode is the TM_0 mode, but the evaluation of TE cases is analog.

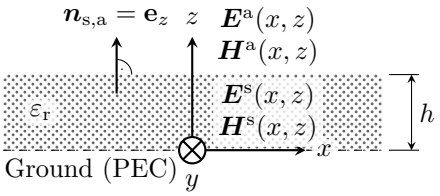

Figure 3.6.: Cross section of the grounded dielectric substrate for the surface-wave calculation.

According to Fig. 3.6, the field is solved in two different domains, and the unknown coefficients are evaluated by the boundary conditions (3.11)-(3.13) for $R_{\mathrm{surf}} \to \infty$. The problem is again assumed invariant in y with a magnetic field strength exclusively in the y-direction and wave-propagation in the x-direction, where the one-dimensional Helmholz equation (3.14) needs to be solved again. As before in (3.15), (3.16), the general solution for the magnetic field reads

$$H_y^{\mathrm{a}} = H_0 \exp[-\mathrm{j}p_{\mathrm{a}}z] \qquad \exp[-\mathrm{j}\beta x]\,, \tag{3.27}$$

$$H_y^{\mathrm{s}} = (C_1 \exp[-\mathrm{j}p_{\mathrm{s}}z] + C_2 \exp[\mathrm{j}p_{\mathrm{s}}z]) \exp[-\mathrm{j}\beta x]\,, \tag{3.28}$$

and the electric field for the respective regions can be calculated using (3.17) and (3.18). Last, with the wavenumber in free space and material

$$p_{\mathrm{a}}^2 + \beta^2 = k_0^2, \tag{3.29}$$

$$p_{\mathrm{s}}^2 + \beta^2 = k_{\mathrm{s}}^2, \tag{3.30}$$

and the boundary conditions at $z = 0$ and $z = h$, the following equation for β is found for the TM case

$$\sqrt{\beta_{\mathrm{TM}}^2 - k_0^2} = \frac{\sqrt{k_{\mathrm{s}}^2 - \beta_{\mathrm{TM}}^2}}{\varepsilon_{\mathrm{r}}} \tan\left(\sqrt{k_{\mathrm{s}}^2 - \beta_{\mathrm{TM}}^2}\, h\right). \tag{3.31}$$

With the correct β, the coefficients can be calculated using

$$C_1 = C_2 = H_0 \frac{\exp[-\mathrm{j}p_{\mathrm{a}}h]}{2\cos(p_{\mathrm{s}}h)}, \tag{3.32}$$

which finally yields the field solution, where the z-dependence in air is described as an exponential decay with the attenuation $\mathrm{j}p_{\mathrm{a}} = \alpha_{\mathrm{a}}$ in

$$H_y^{\mathrm{a}} = +H_0 \qquad \exp[-\alpha_{\mathrm{a}}z]\, \exp[-\mathrm{j}\beta x]\,, \tag{3.33}$$

$$H_y^{\mathrm{s}} = +H_0 \frac{\cos(p_{\mathrm{s}}z)}{\cos(p_{\mathrm{s}}h)} \exp[-\alpha_{\mathrm{a}}h]\, \exp[-\mathrm{j}\beta x]\,, \tag{3.34}$$

$$E_x^{\mathrm{a}} = -H_0 \frac{p_{\mathrm{a}}}{\omega\varepsilon_0} \qquad \exp[-\alpha_{\mathrm{a}}z]\, \exp[-\mathrm{j}\beta x]\,, \tag{3.35}$$

$$E_x^{\mathrm{s}} = -H_0 \frac{p_{\mathrm{s}}}{\omega\varepsilon_0\varepsilon_{\mathrm{r}}} \frac{\sin(p_{\mathrm{s}} z)}{\cos(p_{\mathrm{s}} h)} \exp[-\alpha_{\mathrm{a}} h] \exp[-\mathrm{j}\beta x]\,, \tag{3.36}$$

$$E_z^{\mathrm{a}} = -H_0 \frac{\beta}{\omega\varepsilon_0} \exp[-\alpha_{\mathrm{a}} z] \exp[-\mathrm{j}\beta x]\,, \tag{3.37}$$

$$E_z^{\mathrm{s}} = -H_0 \frac{\beta}{\omega\varepsilon_0\varepsilon_{\mathrm{r}}} \frac{\cos(p_{\mathrm{s}} z)}{\cos(p_{\mathrm{s}} h)} \exp[-\alpha_{\mathrm{a}} h] \exp[-\mathrm{j}\beta x]\,, \tag{3.38}$$

for the TM_n mode, where n is defined by the branch of the tangent function used for solving (3.31), and $n = 0$ represents the main branch.

Analogous, the equation for the TE case can be found by using $E_y(x, z)$, solving the Helmholtz equation, and applying the boundary condition to find

$$\sqrt{k_0^2(\varepsilon_{\mathrm{r}} - 1) - \sqrt{k_{\mathrm{s}}^2 - \beta_{\mathrm{TE}}^2}^2} = -\sqrt{k_{\mathrm{s}}^2 - \beta_{\mathrm{TE}}^2} \cot\left(\sqrt{k_{\mathrm{s}}^2 - \beta_{\mathrm{TE}}^2}\, h\right), \tag{3.39}$$

which can be solved for $p_{\mathrm{s}} = \sqrt{k_{\mathrm{s}}^2 - \beta_{\mathrm{TE}}^2}$ numerically. The propagation constants given by (3.31) and (3.39) have been numerically calculated for different permittivities and substrate heights and are depicted in Fig. 3.7. A normalization of the results to k_0 is carried out to increase interpretability, such that the deviation from the linear k_0 to f behavior is highlighted. Generally speaking, a normalized phase constant β/k_0 close to 1 indicates the wave is mostly unaffected by the substrate. In contrast, a tendency towards $\beta \approx k_{\mathrm{s}}$ can be interpreted as the wave is primarily concentrated in and guided by the dielectric. Furthermore, both a higher frequency and a thicker substrate tend to increase the concentration of the field in the dielectric, which means the electrical thickness could be used as an indication of field confinement. For example, the thin low-permittivity substrate ($\varepsilon_{\mathrm{r}} = 4.1$ and $h = 10\,\mu\mathrm{m}$) shows no distinguishable difference

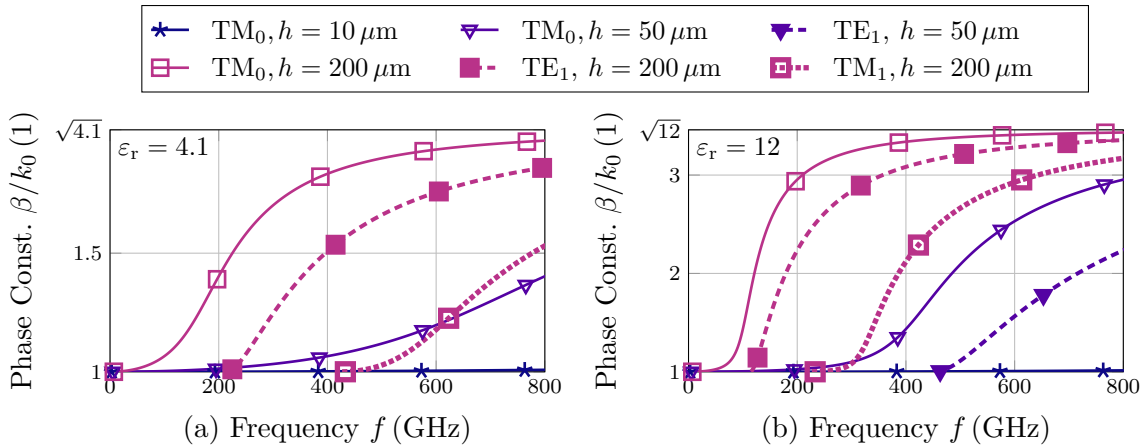

(a) Frequency f (GHz) (b) Frequency f (GHz)

Figure 3.7.: Dispersion diagram of the grounded dielectric slab for (a) $\varepsilon_{\mathrm{r}} = 4.1$ and (b) $\varepsilon_{\mathrm{r}} = 12$ at different frequencies and for different substrates heights h. The phase constants of all modes are normalized to the free space wave number k_0. The higher-order TE_1 and TM_1 modes exist only in a few of the substrates in the considered frequency range.

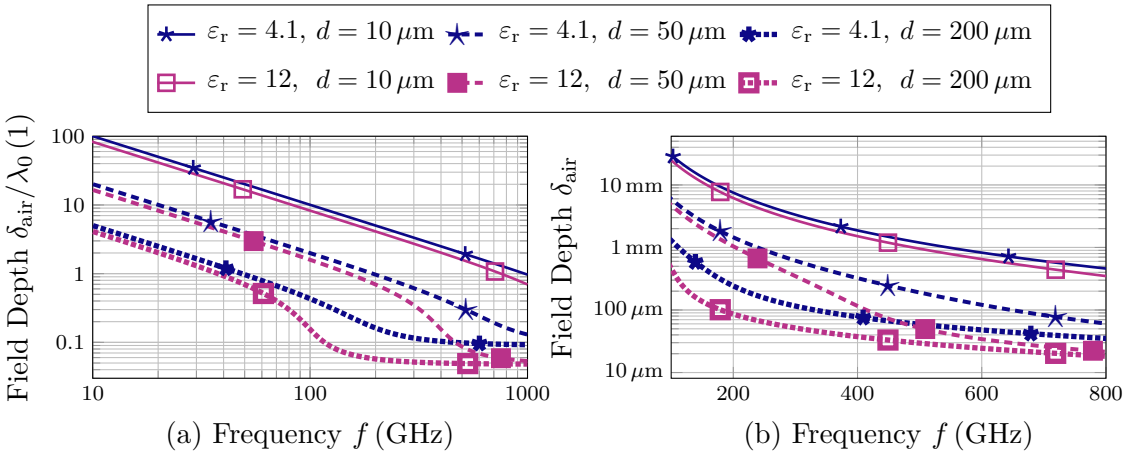

Figure 3.8.: Field penetration depth of the TM_0 mode for $\varepsilon_r = 4.1$ and $\varepsilon_r = 12$ at different frequencies. (a) shows the penetration depth normalized to the free space wavelength λ_0, and (b) depicts the absolute penetration depth.

between β and k_0, such that most energy transport occurs in air. In contrast, the thick high-permittivity substrate ($\varepsilon_r = 12$ and $h = 200\,\mu m$) shows already at 300 GHz a significant normalized phase constant and thus strong confinement of field inside the substrate. Furthermore, the second and third surface waves, TE_1 and TM_1, could also exist in this frequency domain.

From the exponential term in the fields valid for $z > h$, a penetration depth into air could be defined as $\delta_{air} = 1/\alpha_a$. This measure indicates how far the field reaches into the air or, contrary, how much the field is concentrated in the substrate and is depicted for two different materials and three different material heights in Fig. 3.8. For an eased comparability between different frequencies, the depth is normalized to the free space wavelength in Fig. 3.8 (a) and given in absolute height to compare it to the substrate height in Fig. 3.8 (b). Whereas the field depth exceeds the free space wavelength at 300 GHz for the low-height substrate ($h = 10\,\mu m$), it is much smaller than λ_0 for the thick substrate. Comparing the penetration depth to the substrate height (cf. Fig. 3.8 (b)) indicates whether the field is either distributed in air or concentrated in the substrate. For example, the low permittivity substrate with a substrate height of 200 μm exceeds the penetration depth at ≈ 200 GHz. In contrast, the thinner substrate heights $h = 10\,\mu m$ do not exceed the field depth for the investigated frequency range.

Finally, Fig. 3.9 visualizes the non-zero field components of the TM_0 mode at 300 GHz for different substrate heights row-wise and relative permittivities $\varepsilon_r = 4.1$ and 12 in (a) and (b), respectively. The solutions would be TEM waves if it were not for the E_x component depicted in the left column. Whereas the low substrate height shows almost a TEM solution for the low permittivity, all other substrate heights and the solutions for the large permittivity show a non-negligible E_x component. The increasing field confinement in the substrate for increasing substrate heights can be observed for both

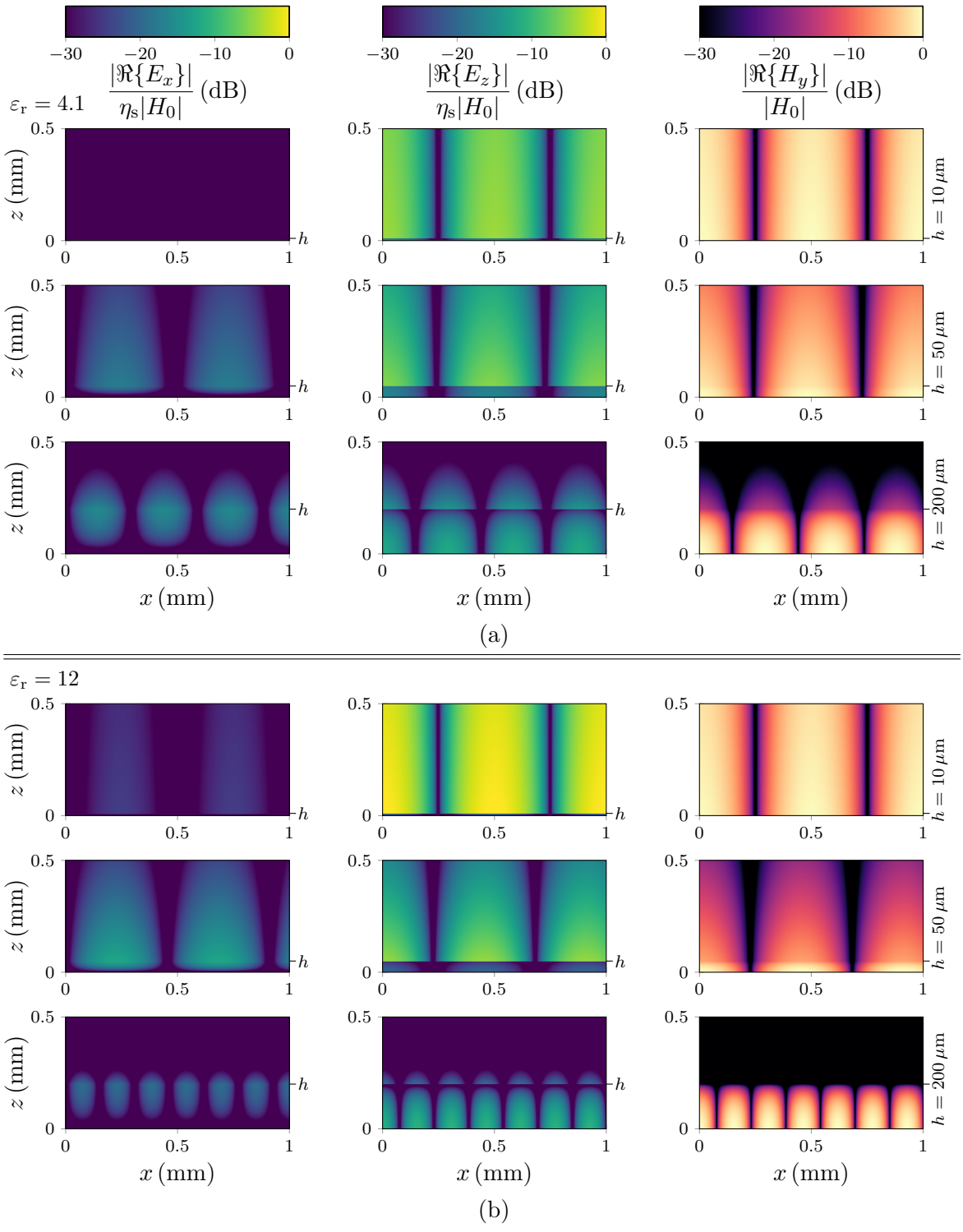

Figure 3.9.: Instantaneous field plot of the grounded dielectric slab in cross section for different substrate permittivities $\varepsilon_r = 4.1$ (a) and $\varepsilon_r = 12$ (b) at 300 GHz. The substrate height changes (from top to bottom) with $h \in \{10\,\mu\text{m}, 50\,\mu\text{m}, 200\,\mu\text{m}\}$.

field components, E_z and H_y. Finally, even the reduced field penetration in air is visible for the large substrate heights. To conclude, the substrates with larger thicknesses or higher permittivities tend to concentrate most of the field inside the dielectric. Vice versa, the electrically thinner substrates have only a minor field contribution inside the dielectric, such that the excitation of surface waves from the dielectric, for example, from circuits based on MSLs, is weaker.

3.3. Field- and Circuit-Based Concepts

This section introduces a general approach to relate EM fields to their description based on circuit models. Using a circuit to simplify complex fields is motivated by the impedance concept, which has been extensively discussed in [145]. The impedance concept essentially allows for calculating the reflection or transmission coefficients of plane waves due to material boundaries. If expanded to guided waves, where the impedance does not only depend on the material properties but also the geometry of the waveguide, the impedance mismatch between two waveguides can still predict both reflection and transmission. Here, the characteristic impedance is, on the one hand, the square root of the ratio between electric and magnetic field energy within the TL; on the other hand, it is the ratio of traveling wave voltage to current for the circuit concept. The direct correspondence between field and circuit quantities allows us to access most scalar measures equivalently in the field- and circuit description, for example, power, reflection coefficients, and losses, if the circuit is chosen well. In the best case, an appropriate circuit will yield results equivalent to the field solution, which coins the term Equivalent Circuit. One of the most commonly used EC representations for a field problem is the TL, which models single-mode wave propagation in any waveguide by a characteristic impedance Z_C representing the ratio of traveling wave voltage and current, a propagation constant γ including the phase- and attenuation constant, and a physical length ℓ of the TL. Besides the inherent modeling of waveguides by TLs, predefined circuit topologies exist for waveguiding structures such as bends, T-sections, gaps, and more [138, pp. 181].

It should be noted that the width of the transmission line was not considered in the previous sections. However, the width-to-height ratio w/h of the cross section of a transmission line affects the characteristic impedance Z_C. Numerical approaches are necessary to determine the physically sound electric current density and field distributions for most waveguiding structures that include material boundaries. The idealized parallel plate waveguide will be investigated as a simple example that can be solved analytically. Fig. 3.10 compares the field- and circuit-based representation of the ideal parallel plate waveguide. Here, the field vectors for the electric and magnetic field strength are depicted at a fixed time instance t_0 (cf. Fig. 3.10 (a)) and compared to the voltage and current along the TL (cf. Fig. 3.10 (c)). To show the wave propagation direction, voltage and current along the TL are represented for a second time

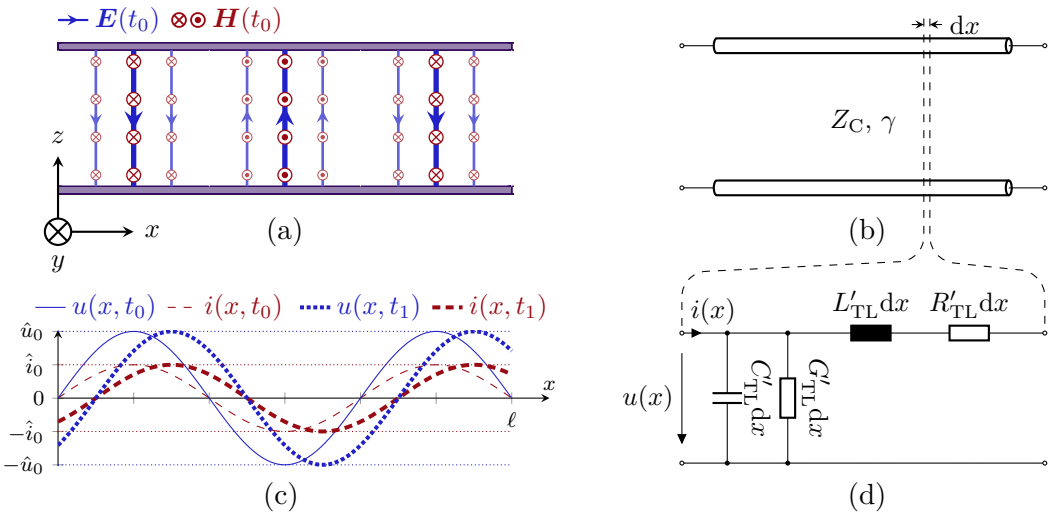

Figure 3.10.: Cross section of the parallel plate waveguide with (a) instantaneous traveling wave electric and magnetic fields, (b) its EC representation, (c) corresponding voltages u and currents i, and (d) EC model for an infinitesimal short length $\mathrm{d}x$.

$t_1 > t_0$. The equivalent circuit symbol and the lumped component representation for an infinitesimally short section of length $\mathrm{d}x$ are depicted in Figs. 3.10 (b) and (d).

The lumped elements of the TL dominating the phase (L'_{TL}, C'_{TL}) are calculated by comparing the stored magnetic or electric energy per unit length averaged over a cycle ($T = 1/f$ with f the operating frequency) to the TL current and voltage for the series and shunt elements, respectively [141, pp. 52]. An ideal parallel plate waveguide of width w, height h, and relative permittivity ε_{r} yields

$$L'_{\mathrm{TL}} = \mu_0 \frac{h}{w}, \tag{3.40}$$

$$C'_{\mathrm{TL}} = \varepsilon_0 \varepsilon_{\mathrm{r}} \frac{w}{h}. \tag{3.41}$$

Analogous, the circuit elements dominating the losses (R'_{TL}, G'_{TL}) compare the dissipated power per unit length during one cycle to voltage and current, as above, which yields

$$R'_{\mathrm{TL}} = 2\frac{R_{\mathrm{surf}}}{w}, \tag{3.42}$$

$$G'_{\mathrm{TL}} = \varepsilon_0 \varepsilon_{\mathrm{r}} \tan\delta \frac{w}{h}. \tag{3.43}$$

Here, the conductor losses account for the top and bottom plate losses using the sheet model introduced in Section 3.2 with the surface resistance according to (3.7). The additional internal inductance given by the reactance of the sheet model is usually small compared to L'_{TL} and is thus not included here. A more detailed discussion on

the skin and proximity effect convering the internal inductance and ohmic losses is given in the next section in the context of the incremental inductance rule [140]. With these quantities, the TL theory yields a characteristic impedance and propagation constant [145]

$$Z_\mathrm{C} = \sqrt{\frac{R'_\mathrm{TL} + \mathrm{j}\omega\, L'_\mathrm{TL}}{G'_\mathrm{TL} + \mathrm{j}\omega\, C'_\mathrm{TL}}}, \tag{3.44}$$

$$\gamma = \sqrt{(R'_\mathrm{TL} + \mathrm{j}\omega\, L'_\mathrm{TL})\,(G'_\mathrm{TL} + \mathrm{j}\omega\, C'_\mathrm{TL})}. \tag{3.45}$$

The complex propagation constant derived here is identical to the modeling of the lossy transmission line in Section 3.2 if the fields above the line are neglected. Consequently, the field distribution above the TL is not included in the circuit. However, this is of no practical relevance since most TLs utilize good conductors, and hence the fields vanish strongly in air. Whereas the circuit describes only the quasi-TEM solution of the TL, the fundamental TM_0 mode of the grounded dielectric slab is exclusively included in the field solution. Again, this difference is not a drawback per se, as one of the simplifications of using ECs results from excluding needless modes. Here, the tradeoff between excluding needless features and including sufficient circuit elements for the desired accuracy is essential for the usability and physical interpretability of ECs. Last, the voltage reflection coefficient of a TL connected to an arbitrary load impedance Z_L is given by

$$\Gamma = \frac{Z_\mathrm{L} - Z_\mathrm{C}}{Z_\mathrm{L} + Z_\mathrm{C}}. \tag{3.46}$$

This coefficient applies at any transmission line connected to an impedance Z_L, which might be a circuit, antenna, or another transmission line, and generally $|\Gamma| \leq 1$ holds. With the complete set of parameters to describe an arbitrary transmission line, the following section presents a thorough EC model for MSLs.

3.4. Microstrip Line Circuit Model

With the intense use of microstrip-based structures in microwave systems, numerous models for MSLs and similar structures (such as a parallel-plate waveguide on a dielectric slab) have been developed. In perspective and top view, an exemplary MSL section is depicted in Fig. 3.11, where the grounded dielectric with the relative permittivity ε_r and height h is covered with a strip of width w. Models in the literature aim to define an effective permittivity, which models the effect of the dielectric slab with sufficient accuracy and enables the relation of the TL parameters for the free space case $\varepsilon_\mathrm{r} = 1$ to the dielectric case $\varepsilon_\mathrm{r} > 1$. In chronological order, the model for the parallel plate TL [146] has been simplified, reformulated for the MSL [147], and improved in accuracy, yielding similar outcomes of different approaches published in

close succession [148], [149]. Finally, even the attenuation due to metal losses has been described in [139] using the so-called incremental inductance rule [140]. Here, the commonly used result for the characteristic impedance from Wheeler will be given with short remarks, and the full explanation can be found in [139]. Once the characteristic impedance is known, the effective permittivity $\varepsilon_{\mathrm{r,\,eff}}$, the propagation constant γ, and finally, conductor and dielectric losses can be accessed. According to [139], the characteristic impedance calculates to

$$Z_{\mathrm{C}} = \frac{42.2\,\Omega \ln\left[1 + \frac{4h}{w_{\mathrm{eff}}}\left[\frac{14 + 8/\varepsilon_{\mathrm{r}}}{11}\frac{4h}{w_{\mathrm{eff}}} + \sqrt{\left(\frac{14 + 8/\varepsilon_{\mathrm{r}}}{11}\frac{4h}{w_{\mathrm{eff}}}\right)^2 + \frac{1 + 1/\varepsilon_{\mathrm{r}}}{2}\pi^2}\right]\right]}{\sqrt{\varepsilon_{\mathrm{r}} + 1}}, \tag{3.47}$$

where the effective width w_{eff} includes the effect of the MSL thickness t averaged from capacitive and inductive influence

$$w_{\mathrm{eff}} = w + \frac{\varepsilon_{\mathrm{r}} + 1}{2\varepsilon_{\mathrm{r}}}\frac{1}{\pi}\ln\left[\frac{4\exp[1]}{\sqrt{\left(\frac{t}{h}\right)^2 + \left(\frac{1/\pi}{w/t + 1.1}\right)^2}}\right]. \tag{3.48}$$

Although the $\tan\delta$ could be included as a complex permittivity ε_{r}, this is not recommended here since a more sophisticated approach will be presented later in this section. The effective permittivity relates the characteristic impedance considering the dielectric to the characteristic impedance for the air case, and thus the phase constant can be evaluated straight away with

$$\varepsilon_{\mathrm{r,\,eff}} = \left(\frac{Z_{\mathrm{C}}|_{\varepsilon_{\mathrm{r}} = \varepsilon_{\mathrm{r,\,substrate}}}}{Z_{\mathrm{C}}|_{\varepsilon_{\mathrm{r}} = 1}}\right)^2, \tag{3.49}$$

$$\beta = \Im\{\gamma\} = \frac{2\pi f\sqrt{\varepsilon_{\mathrm{r,\,eff}}}}{c_0}. \tag{3.50}$$

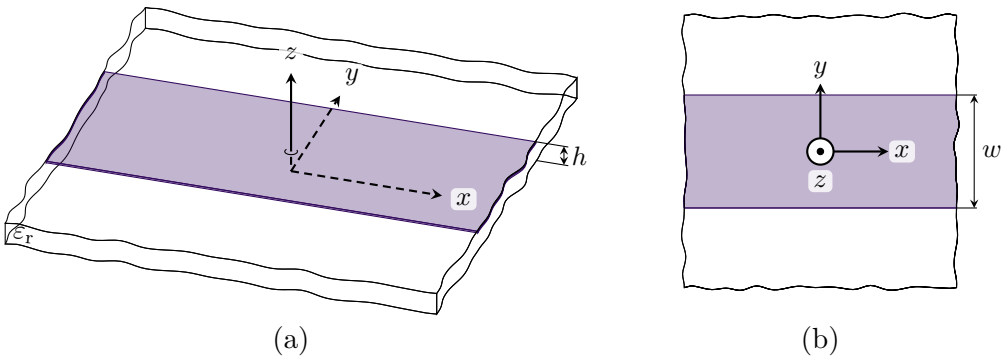

(a) (b)

Figure 3.11.: Geometry of the MSL in (a) perspective and (b) top view.

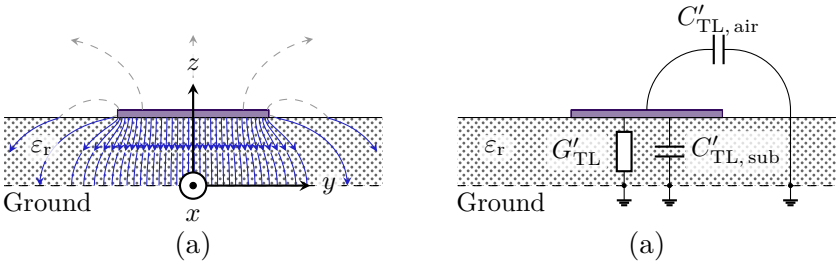

Figure 3.12.: Cross section of (a) the MSL with fringing fields and (b) circuit representation for the fields in air in and in the substrate.

To fully describe the TL with losses based on (3.47)-(3.50), the inductance, capacitance, conductance, and resistance per unit length will be defined based on the given parameters. The dominant inductance and capacitance per unit length are directly accessible from (3.44) and (3.45) if low losses ($R'_{TL} \ll \omega L'_{TL}$ and $G'_{TL} \ll \omega C'_{TL}$) are assumed:

$$L'_{TL} = \frac{Z_C \beta}{\omega} \tag{3.51}$$

$$C'_{TL} = \frac{\beta}{\omega Z_C} \tag{3.52}$$

To discuss the electric losses, Fig. 3.12 (a) shows the electric field lines at an exemplary MSL. The fractions of the field, which result in no dielectric losses, are plotted using dashed lines as a visual aid. A dielectric filling factor (or fraction) is commonly derived [146], [147] and used for loss calculations [150] to describe the substrate losses. It describes the ratio of the capacitances per unit length $C'_{TL,sub}$ caused by the dielectric to the total capacitance per unit length C'_{TL} of the TL. The difference between C'_{TL} and $C'_{TL,sub}$ is the capacitance $C'_{TL,air}$ modeling the field lines through the air and dielectric (cf. Fig. 3.12 (b)). To access the substrate losses, they are assumed to only occur at the capacitance $C'_{TL,sub}$, highlighted by the conductance $G'_{TL} = \omega C'_{TL,sub} \tan\delta$. Relating the capacitances for both cases yields

$$C'_{TL,sub} = C'_{TL} \frac{\varepsilon_r}{\varepsilon_{r,eff}} \frac{\varepsilon_{r,eff} - 1}{\varepsilon_r - 1} \tag{3.53}$$

and, thus, for the conductance

$$G'_{TL} = \omega \tan\delta \frac{\varepsilon_r}{\varepsilon_{r,eff}} \frac{\varepsilon_{r,eff} - 1}{\varepsilon_r - 1} C'_{TL}. \tag{3.54}$$

It should be noted that the field lines accounted for by $C'_{TL,air}$ will eventually penetrate the substrate, terminate on the ground plane, and thus also introduce losses, which are not accessible by this method and thus neglected here. To determine the error

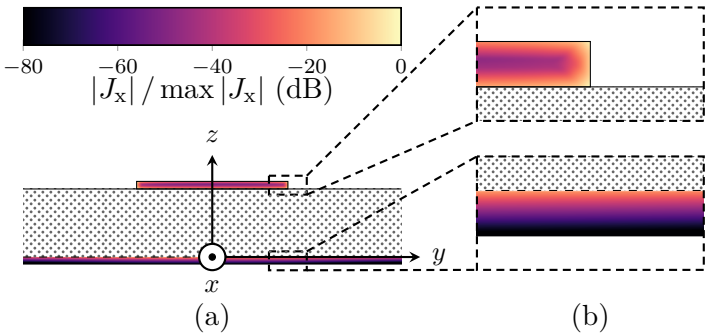

Figure 3.13.: Cross section of the MSL showing (a) the magnitude of the current density in both conductors and (b) magnified insets of the current density at the MSL edge.

margin, the upper bound for the dielectric losses would assume the whole material lossy according to

$$G'_{\mathrm{TL}} \leq \omega \tan\delta \, C'_{\mathrm{TL}}. \tag{3.55}$$

The magnetic loss is discussed in the following. Fig. 3.13 (a) shows the current density calculated using a full-wave Finite Element Method (FEM) solver in the cross section and a detailed view of the conductor edges in (b). The skin effect, which effectively decreases the conductor cross section, can be seen clearly. To access the resulting conductor losses, the incremental inductance rule from [140] will be shortly presented. Here, Wheeler states that the internal inductance and resistance, modeling the magnetic field storage and the losses, respectively, increase in the same manner for increasing penetration depth, i.e., are proportional to each other. This property holds for a sufficiently thick conductor, where the thickness should be at least twice the skin depth (or fourfold if the conductor has a current density on the top and bottom surface). Furthermore, it holds only for a sufficiently large curvature of the conductor, implying the surface roughness needs to be negligible. From the statement, it follows that the resistance of a conductor can be directly calculated from its internal impedance [140]

$$R_{\mathrm{skin}} = \omega L_{\mathrm{internal}}. \tag{3.56}$$

From this circuit perspective, one can show that the surface impedance of a conducting sheet is

$$Z_{\mathrm{surf}} = (1 + \mathrm{j})\sqrt{\pi f \mu \kappa}, \tag{3.57}$$

which is in full accordance with the result from field calculations and highlights the potential of circuit-based concepts once more [140]. The internal inductance measures the field energy stored in the conductor and is accessed by calculating the change in

total inductance due to recessing all metal surfaces by half a skin depth. With the change of total inductance ΔL, the resistance of the conductor is given by

$$R = \omega \Delta L. \tag{3.58}$$

This rule is also applicable for inductances and resistances per unit length and will be applied to the MSL. Given the geometry of the line, namely its height h, top conductor thickness t, and width w, the inductance per unit length L'_{TL} is calculated based on (3.51). As a follow-up, the geometry of the line will be changed to recess all metal surfaces by $\delta_{\mathrm{skin}}/2$, such that

$$\widetilde{h} = h + \delta_{\mathrm{skin}}, \qquad \widetilde{t} = t - \delta_{\mathrm{skin}}, \qquad \text{and} \qquad \widetilde{w} = w - \delta_{\mathrm{skin}} \tag{3.59}$$

hold, and the new inductance per unit length $\widetilde{L}'_{\mathrm{TL}}$ is calculated. The resistance per unit length due to conductor losses is then

$$R'_{\mathrm{TL}} = \omega \left(\widetilde{L}'_{\mathrm{TL}} - L'_{\mathrm{TL}} \right). \tag{3.60}$$

As a significant outcome of the incremental inductance rule, the resistance per unit length can be calculated from the inductance. The approximation only requires sufficiently small surface roughness, which is not considered here, and accepts errors due to edges with curvature smaller than the skin depth δ_{skin} [140]. With the existing MSL model including a description of the inductance, calculating the resistance considering the skin effect is straightforward.

To summarize this chapter, the interaction between surface waves and dielectric substrates is shown to depend dominantly on the electrical thickness of the substrate. Furthermore, all elements per unit length to describe an undisturbed MSL can be calculated using (3.51)-(3.52), (3.54), and (3.60). The next chapter covers essential antenna parameters and fundamental radiators, which will be used to model MSL discontinuities.

4. Antenna Fundamentals and Radiation Principles

An antenna is the transducer between an RF system and radiated EM-fields and, thus, an essential component in any radiating system, may it provide wireless communication or perform radar. This chapter presents the most commonly utilized parameters for antenna characterization and calculates radiated far fields as well as derivatives of these fields for fundamental radiators.

4.1. Antenna Parameters

The performance of an antenna is usually evaluated by its ability to radiate or receive provided power in a specified frequency range, with a particular radiation direction, and the desired polarization. With only linear material properties and Maxwell's set of linear equations for electrodynamics, antennas are reciprocal [56, p. 147]. Reciprocity is a well-known property of passive linear two-port networks, and extending this to a set of transmitting and receiving antennae is straightforward [151, p. 94]. Therefore, linear antennas can be investigated only in transmit or receive mode, and the radiation pattern or input impedance is identical in both operating conditions.

4.1.1. Impedance, Feeding, and Matching

The antenna impedance is the fundamental measure to describe and analyze the antenna mismatch [43, p. 35]. Here, the reflection coefficient of a TL loaded with the antenna impedance given by (3.46) describes the ratio of the reflected voltage wave to the incident voltage wave and is thus a direct measure of the reflected power. In order to maximize the antenna efficiency, minimizing the reflected power and, thus, the reflection coefficient can be achieved by targeting a conjugate complex impedance match between the antenna and feeding waveguide. The feeding waveguide can be any waveguiding topology, including both single- and multi-conductor topologies, where coaxial cables, rectangular and circular waveguides, and planar structures as a Coplanar Waveguide (CPW), MSL, or SIW are only an excerpt of the commonly used structures. Whereas the waveguides are typically only slightly dispersive and thus of relatively constant impedance, the feed point impedance of resonant antennas is significantly

frequency-dependent. Thus, the fractional bandwidth of these antennas is typically limited by antenna mismatch, referred to as matching bandwidth [56, p. 70]. For visualization, the input parameters of the antenna are usually presented by real and imaginary parts or as a locus in the Smith chart [152]. For single port antennas, the input reflection coefficient Γ is identical to the input scattering parameter S_{11}. Consequently, for multi-port antenna arrangements, as they occur in arrays, both the input matching $S_{\ell\ell}$ and mutual coupling between antennas $S_{\ell m}$ with $\ell \neq m$ must be considered [151, p. 176].

4.1.2. Radiation

It will be shown in Sections 4.2 and 4.3 that radiation is a fundamental property of alternating currents, which means any oscillating current generates radiation. The radiation of an antenna is usually classified using the directivity $D(\theta, \varphi)$, gain $G(\theta, \varphi)$, and realized gain $G^{\text{real}}(\theta, \varphi)$ functions. If one of these quantities is given without spatial information, the maximum in θ and φ is usually evaluated. The directivity can be calculated using the radiated electric far field $\boldsymbol{E}^{\text{far}}$ of an antenna using [56, pp. 41]

$$D(\theta, \varphi) = \frac{4\pi\, r^2 \, \left\| \boldsymbol{E}^{\text{far}}(r, \theta, \varphi) \right\|^2}{2\eta_0 P^{\text{rad}}}, \tag{4.1}$$

$$P^{\text{rad}} = \frac{1}{2\eta_0} \oiint_{\Omega} \left\| \boldsymbol{E}^{\text{far}}(r, \theta, \varphi) \right\|^2 \, r^2 \, \mathrm{d}\Omega, \tag{4.2}$$

where $\mathrm{d}\Omega = \sin\theta \, \mathrm{d}\theta \, \mathrm{d}\varphi$ is the solid angle chosen for the parametrization of a unit sphere, the distance r needs to be chosen sufficiently large to be considered in the far field, and η_0 is the free space wave impedance. As a function of elevation and azimuth, the directivity represents the spatial distribution of radiated power. If the normalization is carried out to the accepted power P^{acc}, namely the power which enters the antenna terminal, the gain is found

$$G(\theta, \varphi) = \frac{P^{\text{rad}}}{P^{\text{acc}}} D(\theta, \varphi) = \eta_{\text{rad}} D(\theta, \varphi), \tag{4.3}$$

with $\eta_{\text{rad}} \leq 1$ the antenna's radiation efficiency. Finally, by considering the impedance mismatch of the antenna, the realized gain is [153, p. 478]

$$G^{\text{real}}(\theta, \varphi) = \frac{P^{\text{rad}}}{P^{\text{inc}}} D(\theta, \varphi) = \eta_{\text{mis}} \, \eta_{\text{rad}} D(\theta, \varphi), \tag{4.4}$$

with $\eta_{\text{mis}} = 1 - |\Gamma|^2$ the mismatch loss due to the reflection coefficient Γ at the antenna terminal, which results in a reduced accepted power compared to the incident power, $P^{\text{acc}} \leq P^{\text{inc}}$. As the realized gain includes the radiation pattern, the radiation efficiency, and the impedance mismatch, it is a valuable measure of the characterization and comparison of antenna prototypes. Thus, the antenna bandwidth is limited by both

the impedance bandwidth, indicating the ability to feed the power into the antenna, and the pattern bandwidth, measuring the ability to radiate power in a desired manner given a current in the antenna.

The ability to radiate power can be modeled by a radiation resistance or conductance, which quantifies the radiated power for an input current or voltage, respectively. Although no information about the radiation pattern is contained in the radiation resistance, it enables describing the antenna efficiency η_{rad} in combination with a dissipation resistance or conductance, which models the dissipation losses [154]. It will be defined in the following sections, where different fundamental radiators are investigated, if applicable.

4.2. Vertical Dipole Radiation

This chapter discusses the radiation of an electrically short current filament, the so-called Hertzian Dipole, and the effect of boundary conditions from the on-chip environment on this dipole. The term vertical refers to the x-y-plane, which will be used as a reference plane for applying different boundary conditions, for example, a PEC. The results exclusively valid for this dipole orientation are labeled with a $\perp$ symbol. A convenient description of free space radiation given a current density is obtained using the magnetic vector potential, which calculates according to [155, p.288]

$$\boldsymbol{A}(\boldsymbol{r}) = \frac{\mu_0}{4\pi} \iiint\limits_{V'} \boldsymbol{J}(\boldsymbol{r'}) \frac{\exp[-\mathrm{j}k_0|\boldsymbol{r}-\boldsymbol{r'}|]}{|\boldsymbol{r}-\boldsymbol{r'}|}\,\mathrm{d}V', \tag{4.5}$$

where the distances are calculated according to

$$\boldsymbol{r'} = x'\mathbf{e}_x + y'\mathbf{e}_y + z'\mathbf{e}_z, \tag{4.6}$$

$$\boldsymbol{r} = x\,\mathbf{e}_x + y\,\mathbf{e}_y + z\,\mathbf{e}_z. \tag{4.7}$$

The vector potential is calculated in the point $(x|y|z)$ for sources defined at $(x'|y'|z')$. This description assumes a homogeneous background medium of permeability μ_0 and permittivity ε_0, which results in the free space wavenumber $k_0 = 2\pi f\sqrt{\mu_0\varepsilon_0}$. The quantities derived in the following sections will be utilized to model the radiation of microstrip antennas.

4.2.1. Vertical Dipole in Homogeneous Background Medium

If the current density can be approximated by a surface current density $\boldsymbol{J}_{\mathrm{surf}}$, the integral in (4.5) reduces to a surface integral according to

$$\boldsymbol{A} = \frac{\mu_0}{4\pi} \iint\limits_{S'} \boldsymbol{J}_{\mathrm{surf}} \frac{\exp[-\mathrm{j}k_0|\boldsymbol{r}-\boldsymbol{r'}|]}{|\boldsymbol{r}-\boldsymbol{r'}|}\,\mathrm{d}S', \tag{4.8}$$

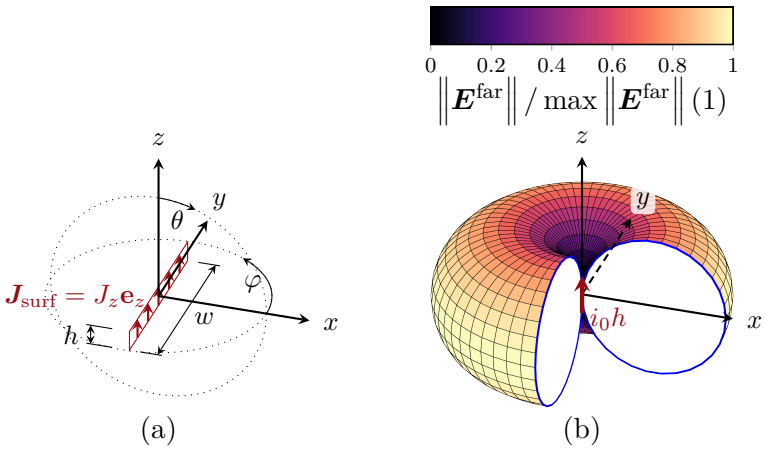

Figure 4.1.: Geometry of (a) the z-directed surface current density and (b) the corresponding radiation pattern of the vertical dipole in air. The radiation pattern is normalized to the maximum value and given using a linear scale. The x-z and y-z cuts are introduced to ease the interpretation of the radiation pattern.

which can be simplified for large distances [151, p. 39]

$$\boldsymbol{A} \approx \frac{\mu_0}{4\pi|\boldsymbol{r}|} \exp[-\mathrm{j}k_0|\boldsymbol{r}|] \iint_{S'} \boldsymbol{J}_{\text{surf}} \exp[\mathrm{j}k_0 \boldsymbol{r'} \cdot \mathbf{e}_r] \, \mathrm{d}S', \tag{4.9}$$

where $\mathbf{e}_r$ is the unit vector in the $\boldsymbol{r}$ direction. With the far-field approximation for the vector potential $\boldsymbol{A}$ already in use, the electric far field can be calculated accordingly with

$$\boldsymbol{E} \approx -\mathrm{j}\omega \left(A_\theta \mathbf{e}_\theta + A_\phi \mathbf{e}_\phi\right). \tag{4.10}$$

The θ and φ components are calculated from cartesian components with [141, p. 713]

$$\mathbf{e}_\theta = +\mathbf{e}_x \cos\theta\cos\varphi + \mathbf{e}_y \cos\theta\sin\varphi - \mathbf{e}_z \sin\theta, \tag{4.11}$$

$$\mathbf{e}_\varphi = -\mathbf{e}_x \sin\varphi \qquad + \mathbf{e}_y \cos\varphi. \tag{4.12}$$

For the z-directed current density depicted in Fig. 4.1 (a), the vector potential is obtained using (4.9)

$$\boldsymbol{A} = -\frac{J_z \mu_0 \, wh}{4\pi \, |\boldsymbol{r}|} \exp[-\mathrm{j}k_0|\boldsymbol{r}|] \operatorname{sinc}\left(k_0 \frac{w}{2} \sin\varphi \sin\theta\right) \operatorname{sinc}\left(k_0 \frac{h}{2} \cos\theta\right) \sin\theta \, \mathbf{e}_\theta. \tag{4.13}$$

In [156], it is shown that for $\max(w, h) < 0.5\lambda_0$ the vector potential can be approximated well using $\operatorname{sinc} x \approx 1$, and with (4.10)

$$E_{\theta,\,\text{air}\perp} \approx \mathrm{j}\omega \frac{J_z \mu_0 \, wh}{4\pi|\boldsymbol{r}|} \exp[-\mathrm{j}k_0|\boldsymbol{r}|] \sin\theta, \qquad E_{\varphi,\,\text{air}\perp} = 0 \tag{4.14}$$

holds, which directly corresponds to the far-field solution for an electric dipole (also referred to as Hertzian dipole) of length h with current $i_0 = J_z w$ [56, p. 153]:

$$E_{\theta,\,\mathrm{air}\perp} \approx \mathrm{j}\frac{\omega i_0 \mu_0\, h}{4\pi|\boldsymbol{r}|}\exp[-\mathrm{j}k_0|\boldsymbol{r}|]\sin\theta, \qquad E_{\varphi,\,\mathrm{air}\perp} = 0. \tag{4.15}$$

A visualization of the radiation pattern according to (4.15) is depicted in Fig. 4.1 (b). The radiated power can be accessed using (4.2)

$$P_{\mathrm{air}}^{\mathrm{rad}} = i_0^2\,\frac{\pi}{3}\eta_0\sqrt{\varepsilon_{\mathrm{r}}}\left(\frac{h}{\lambda_0}\right)^2. \tag{4.16}$$

Finally, an equivalent radiation resistance can be calculated with

$$R_{\mathrm{air}}^{\mathrm{rad}} = \frac{2P_{\mathrm{rad,\,air}}}{|i_0|^2} = \frac{2\pi}{3}\,\eta_0\,\sqrt{\varepsilon_{\mathrm{r}}}\left(\frac{h}{\lambda_0}\right)^2. \tag{4.17}$$

Given a small electrical height $h \ll \lambda_0$, the radiation resistance is expected to be very small compared to the free space impedance $\eta_0 \approx 377\,\Omega$ and the typical characteristic impedance $Z_{\mathrm{C}} = 50\,\Omega$. The conceivably significant impedance mismatch shall not be considered here [56, p. 156] since the antennas presented in this thesis will consist of more than just a short current filament. However, the radiation resistance $R_{\mathrm{air}}^{\mathrm{rad}}$ will be compared to the radiation resistance resulting from different boundaries in the proximity of the current filament. In the following sections, all dipoles will be considered of fixed strength $i_0\,h$ since this section has shown that electrically small current density apertures are modeled well using the uniform dipole.

4.2.2. Vertical Dipole with Ground Plane

If the current filament is affected by a ground plane, the effect of the ground can be modeled using an image current, as depicted in Fig. 4.2 (a). The original and image current are shifted by a distance of $h/2$ in opposing directions along the z-axis. The resulting far field can then be expressed as

$$E_{\theta,\,\mathrm{pec}\perp} = E_{\theta,\,\mathrm{air}\perp}\left(\exp[\mathrm{j}k_0 h/2\cos(\theta)] + \exp[-\mathrm{j}k_0 h/2\cos(\theta)]\right). \tag{4.18}$$

For electrically small distances $k_0 h/2$, the radiated electric field is approximately doubled, and the radiated power is accessed by integrating $E_{\theta,\,\mathrm{pec}\perp}$ over the upper hemisphere (with $E_{\varphi,\,\mathrm{pec}\perp} = 0$)

$$P_{\mathrm{hemi}}^{\mathrm{rad}} = \frac{1}{2}\int_0^{2\pi}\int_0^{\pi/2}\frac{|E_\theta|^2 + |E_\varphi|^2}{\eta_0} r^2 \sin\theta\,\mathrm{d}\theta\,\mathrm{d}\varphi, \tag{4.19}$$

$$P_{\mathrm{pec}\perp}^{\mathrm{rad}} = i_0^2\,\frac{2\pi}{3}\eta_0\sqrt{\varepsilon_{\mathrm{r}}}\left(\frac{h}{\lambda_0}\right)^2. \tag{4.20}$$

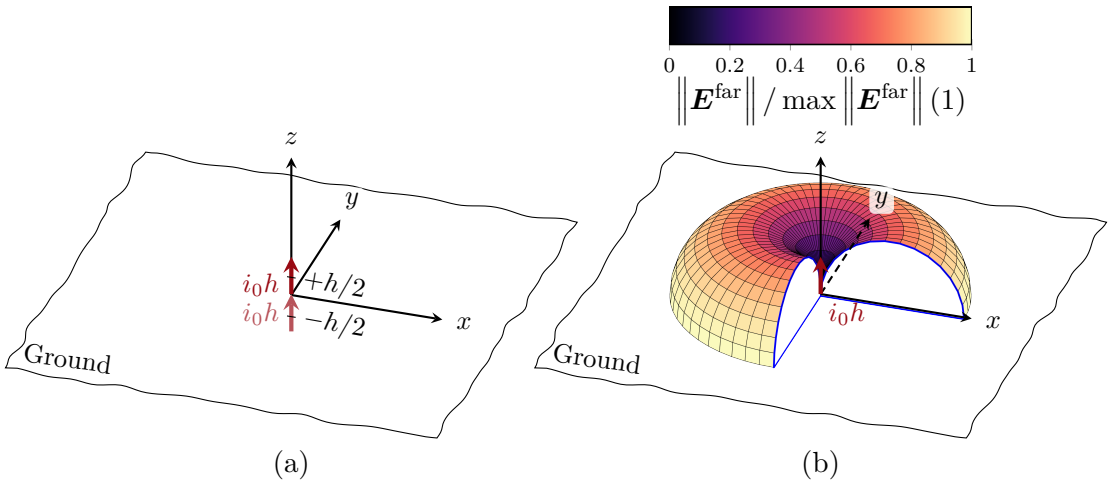

Figure 4.2.: Geometry of (a) the vertical dipole over the ground plane and (b) the corresponding radiation pattern. The radiation pattern is normalized to the maximum value and given using a linear scale. The x-z and y-z cuts are introduced to ease the interpretation of the radiation pattern.

Finally, an equivalent radiation resistance can be accessed

$$R_{\text{pec}\perp}^{\text{rad}} = \frac{2P_{\text{pec}\perp}^{\text{rad}}}{|i_0|^2} = \frac{4\pi}{3}\,\eta_0\,\sqrt{\varepsilon_{\text{r}}}\left(\frac{h}{\lambda_0}\right)^2 = 2R_{\text{air}}^{\text{rad}}, \tag{4.21}$$

which is twice the radiation resistance of the free space case, only limited by the approximation of an electrically small distance h to the ground. The normalized radiation pattern of the electric far field is depicted in Fig. 4.2 (b), and it is identical to the free space case for $\theta \leq \pi/2$ and zero for $\theta > \pi/2$.

4.2.3. Vertical Dipole in Grounded Dielectric Slab

If a dielectric slab is located between the dipole and ground plane (cf. Fig. 4.3), the field solution is typically based on a suitable Green's function, which includes the dielectric effect on the source field [157, pp. 264]. For thorough explanations of the Green's function concept and ways to derive it, it is referred to Sommerfeld [158], and further explanations with additional diagrams can be found in [157, pp. 264]. The shortened derivation in the following assumes an electric dipole in a grounded dielectric slab. A z-directed current between the ground and the substrate surface is modeled using the height h and position $z' = h/2$ for the infinitesimal dipole according to Fig. 4.3 (a). The extensive derivation of the field solution is given in [159]. This chapter will outline the fundamental approach and discuss substantial interim results. As above for the free space case, [159] assumes a vector potential in each domain, namely A_z^1 for $h < z$ and A_z^2 for $0 \leq z \leq h$ in cylindrical coordinates, where the vector potential $\boldsymbol{A}$ has only a z-component

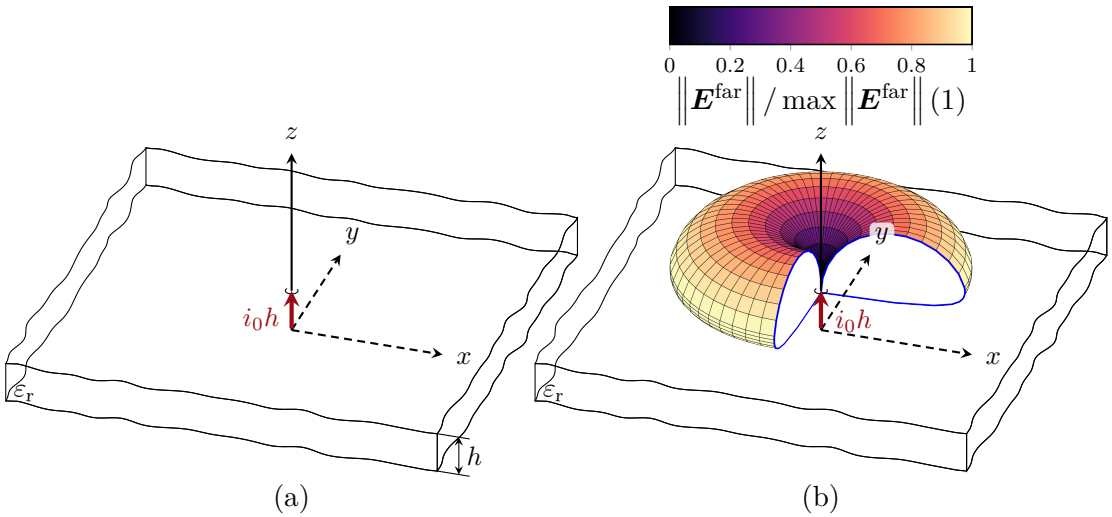

Figure 4.3.: Geometry of (a) the vertical dipole in a grounded dielectric substrate and (b) the corresponding radiation pattern. The radiation pattern is normalized to the maximum value and given using a linear scale. The x-z and y-z cuts are introduced to ease the interpretation of the radiation pattern.

$$A_z^1(\rho, z) = -2\mathrm{j}\omega\mu\varepsilon \int_0^\infty \frac{\cosh(mz')\exp[-\ell(z-d)]}{M(k_0, \beta, \varepsilon_\mathrm{r}, d)} \beta J_0(\beta\rho)\,\mathrm{d}\beta, \tag{4.22}$$

$$\begin{aligned} A_z^2(\rho, z) = \mathrm{j}\omega\mu\varepsilon \frac{p(z')}{4\pi\varepsilon_\mathrm{r}\varepsilon_0} \Bigg[& \frac{\exp[-\mathrm{j}k_\mathrm{s}R']}{R'} + \frac{\exp\left[-\mathrm{j}k_\mathrm{s}R^V\right]}{R^V} \\ & -2\int_0^\infty \frac{(\ell - m/\varepsilon_\mathrm{r})\cosh(mz')\cosh(mz)\exp[-md]}{mM(k_0, \beta, \varepsilon_\mathrm{r}, d)} \beta J_0(\beta\rho)\,\mathrm{d}\beta \Bigg], \end{aligned} \tag{4.23}$$

using

$$\begin{aligned} \ell^2 &= \beta^2 - k_0^2, \\ m^2 &= \beta^2 - k_\mathrm{s}^2, \\ M &= \ell\cosh(md) + \frac{m}{\varepsilon_\mathrm{r}}\sinh(md), \\ R' &= \sqrt{\rho^2 + (z-z')^2}, \\ R^V &= \sqrt{\rho^2 + (z+z')^2}, \\ p(z') &= \frac{i_0\, h}{\omega}. \end{aligned}$$

The results have been rewritten to a vector potential $\boldsymbol{A}$ [155, p. 306] since the original derivation is carried out for a Hertzian potential $\boldsymbol{\Pi}_\mathrm{E}$ [159]. To evaluate the boundary conditions at $z = h$, the application of a Fourier-Bessel transform [160, p. 371] yields

a description of the boundary conditions and vector potentials in the β (instead of ρ) domain, and the general solution in β domain is given in dependence on unknown coefficients $A(\beta)$, which can be solved using the boundary conditions. The integral of the back-transform can be evaluated asymptotically for the far field [159, pp. 43].

Here, it is observed that the denominator M can be rearranged using $m = -\mathrm{j}\sqrt{k_\mathrm{s}^2 - \beta^2}$ and $\ell = \sqrt{\beta^2 - k_0^2}$ to

$$M = \sqrt{\beta^2 - k_0^2} - \frac{\sqrt{k_\mathrm{s}^2 - \beta^2}}{\varepsilon_\mathrm{r}} \tan\left(\sqrt{k_\mathrm{s}^2 - \beta^2}\right) \tag{4.24}$$

and the poles of the integrals in (4.22)-(4.23), which result from $M = 0$, give the equation for the TM surface wave (3.31). By substituting m and ℓ, it has been assumed that m would be a negative imaginary and ℓ a positive real number since this describes the characteristic of surface waves according to Section 3.2. Thus, the zeros of $M(k_0, \beta, \varepsilon_\mathrm{r}, d)$ determine the surface wave solution, which is the Eigensolution of the corresponding structure.

In [159, p. 35], it is rigorously shown that the power contributions of guided and radiated, or surface wave and space wave, can be separated. Thus, the total power of the dipole can be accessed by [159]

$$\begin{aligned} P_{\mathrm{diel}\perp}^{\mathrm{tot}} = \frac{|p|^2 \omega \sqrt{\varepsilon_\mathrm{r}} k_0^3}{4\pi\varepsilon_0} \Bigg[& \frac{1}{3} - \frac{\cos(2k_\mathrm{s} z')}{4k_\mathrm{s}^2 z'^2} + \frac{\sin(2k_\mathrm{s} z')}{8k_\mathrm{s}^3 z'^3} \\ & - \Im\left\{ \int_0^\infty I(\beta) \left(\frac{\ell}{m} - \frac{1}{\varepsilon_\mathrm{r}} \right) \frac{\exp[-mh]\cosh^2(mz')}{\sqrt{\varepsilon_\mathrm{r}}^3 \cosh(mh)} \mathrm{d}\beta \right\} \Bigg] \end{aligned} \tag{4.25}$$

with

$$I(\beta) = \frac{\beta^3 k_0^{-3}}{\ell + \dfrac{m}{\varepsilon_\mathrm{r}} \tanh(md)}, \tag{4.26}$$

where the pole defined by the denominator of I determines the surface wave power [142]. The asymptotic evaluation of the integral is carried out in [159]. It separates the surface wave contributions (the last term with the sum over n) from space waves

according to

$$
\begin{aligned}
&-\Im\left\{\int_0^\infty I(\beta)\left(\frac{\ell}{m}-\frac{1}{\varepsilon_\mathrm{r}}\right)\frac{\exp[-mh]\cosh^2(mz')}{\sqrt{\varepsilon_\mathrm{r}}^3\cosh(mh)}\mathrm{d}\beta\right\}=-\frac{\sqrt{\varepsilon_\mathrm{r}-1}}{3\sqrt{\varepsilon_\mathrm{r}}}\\
&-\frac{\sin\left(2\,z'k_0\sqrt{\varepsilon_\mathrm{r}-1}\right)}{4k_0z'\sqrt{\varepsilon_\mathrm{r}}^3}-\frac{\sqrt{\varepsilon_\mathrm{r}-1}}{6\sqrt{\varepsilon_\mathrm{r}}^3}+\sqrt{\varepsilon_\mathrm{r}-1}\frac{\cos\left(2z'k_0\sqrt{\varepsilon_\mathrm{r}-1}\right)}{4\sqrt{\varepsilon_\mathrm{r}}^3\,k_0^2\,z'^2}-\frac{\sin\left(2z'k_0\sqrt{\varepsilon_\mathrm{r}-1}\right)}{8k_0^3\,z'^3\sqrt{\varepsilon_\mathrm{r}}^3}\\
&+\frac{1}{\sqrt{\varepsilon_\mathrm{r}}^3}\int_0^1\frac{x^3\left[\dfrac{\sqrt{1-x^2}}{\sqrt{\varepsilon_\mathrm{r}-x^2}}-\dfrac{1}{\varepsilon_\mathrm{r}}\right]\cos^2\left(zk_\Delta\right)\left[\dfrac{1}{\varepsilon_\mathrm{r}}\sqrt{\varepsilon_\mathrm{r}-x^2}\,\tan^2\left(dk_\Delta\right)-\sqrt{1-x^2}\right]}{\dfrac{1}{\varepsilon_\mathrm{r}^2}(\varepsilon_\mathrm{r}-x^2)\tan^2\left(dk_\Delta\right)+1-x^2}\,\mathrm{d}x\\
&+\frac{\pi}{\sqrt{\varepsilon_\mathrm{r}}^5k_0^3}\sum_{n=1}^{N}\frac{\beta_n^2\cos\left(z'\sqrt{\varepsilon_\mathrm{r}k_0^2-\beta_n^2}\right)\widetilde{Q}(\beta_n,k_0,\varepsilon_\mathrm{r},d)}{\cos\left(d\sqrt{\varepsilon_\mathrm{r}k_0^2-\beta_n^2}\right)}
\end{aligned}
\tag{4.27}
$$

with the abbreviation $k_\Delta = k_0\sqrt{\varepsilon_\mathrm{r}-x}$ and β_n the propagation constant of the n-th surface wave solution and

$$
\widetilde{Q}(\beta_n,k_0,\varepsilon_\mathrm{r},d)=\frac{\sqrt{\beta_n^2-k_0^2}\,(\varepsilon_\mathrm{r}k_0^2-\beta_n^2)}{k_0^2\,(\varepsilon_\mathrm{r}-1)+d\sqrt{\beta_n^2k_0^2}\left[\varepsilon_\mathrm{r}\,(\beta_n^2-k_0^2)+\left(k_0^2-\dfrac{\beta_n^2}{\varepsilon_\mathrm{r}}\right)\right]}. \tag{4.28}
$$

Using (4.25)–(4.27), the power and, thus, the radiation resistance of a current filament in a grounded dielectric slab can be evaluated numerically. It should be noted that the power consists of radiated (space wave) and surface wave power and that the separation of both contributions is physical [159, p. 35].

Since the derived vector potential solutions are exact, the absence of a dielectric ($\varepsilon_\mathrm{r}=1$) yields a vanishing integral according to (4.27), and the radiated power simplifies to

$$
P_{\mathrm{diel}\perp}^{\mathrm{tot}}\Big|_{\varepsilon_\mathrm{r}=1}=i_0^2\,\pi\eta_0\left(\frac{h}{\lambda_0}\right)^2\left[\frac{1}{3}-\frac{\cos\left(2k_\mathrm{s}z'\right)}{4k_\mathrm{s}^2z'^2}+\frac{\sin\left(2k_\mathrm{s}z'\right)}{8k_\mathrm{s}^3z'^3}\right]\approx i_0^2\,\frac{2\pi}{3}\eta_0\left(\frac{h}{\lambda_0}\right)^2, \tag{4.29}
$$

which converges to the solution for the current filament over the ground plane for small electric heights z'. In this case, the radiation resistance equals the solution for the vertical dipole over the ground plane given by (4.21).

The power representing radiation or surface wave excitation for the current filaments presented so far are compared for different frequencies in Fig. 4.4 (a) and permittivities in Fig. 4.4 (b). Here, the dielectric height (if existent) is $h = 2\,z' = 10\,\mu\mathrm{m}$, $i_0 = 1\,\mathrm{A}$, and $\varepsilon_\mathrm{r} = 4.1$. By choice of $i_0 = 1\,\mathrm{A}$, the radiation resistance is directly related to the radiated power by a factor of $2\,\mathrm{A}^{-2}$. As the results above have shown, the introduction of the ground plane doubles the vertical dipole's radiation resistance. The

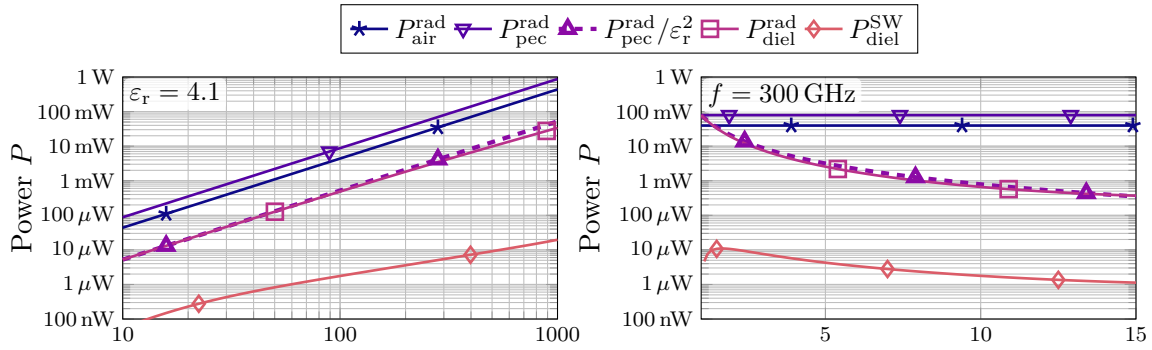

(a) Frequency f (GHz) (b) Rel. Permittivity ε_{r} (1)

Figure 4.4.: Radiated power of a vertical dipole in free space, above a ground plane, and on a grounded dielectric as a function of (a) frequency and (b) relative permittivity of the dielectric. For comparison, the ground plane case is divided by $\varepsilon_{\mathrm{r}}^2$ since this represents the radiated power of the dielectric case well. The height of the dipole and the substrate is $h = 10\,\mu$m, and the dipole is located $z' = h/2$ above ground.

dielectric slab, however, drastically reduces the radiation resistance and, consequently, the radiated power. It is found that the radiated power of the dipole over the ground plane divided by $\varepsilon_{\mathrm{r}}^2$ gives a good approximation of the grounded dielectric case, which will be explained in the next paragraph. Finally, the surface wave power excited by this dipole is orders of magnitude smaller than the radiated power, which renders this contribution negligible given the small electric height of the substrate. Consequently, the surface wave contributions are negligible for the small dielectric thicknesses dealt with in this thesis. Thus, a further simplified expression for the electric far field can be obtained based on the results from [159, pp. 20], yielding

$$E_{\theta,\,\mathrm{diel}\perp} = E_{\theta,\,\mathrm{air}\perp} \frac{2\,\cos\theta}{\varepsilon_{\mathrm{r}}\cos\theta - \mathrm{j}\sqrt{\varepsilon_{\mathrm{r}} - \sin^2\theta}\,\tan\left(k_0 h\sqrt{\varepsilon_{\mathrm{r}} - \sin^2\theta}\right)} \cdot \frac{\cos\left(k_0 z'\sqrt{\varepsilon_{\mathrm{r}} - \sin^2\theta}\right)}{\cos\left(k_0 h\sqrt{\varepsilon_{\mathrm{r}} - \sin^2\theta}\right)}\,\exp[\mathrm{j}\,k_0 z'\cos\theta]\,, \tag{4.30}$$

where all terms $\propto r^{-1/2}$ have been neglected, as these cylindrical waves describe solutions guided by the grounded substrate, specifically surface waves. The radiation pattern obtained from (4.30) is depicted in Fig. 4.3 (b). Except for the grazing direction, the pattern is highly comparable to the radiation of the vertical dipole over the ground plane, which is further elaborated in [56, pp. 837]. If the electric height of the substrate is small compared to the wavelength, further approximations using $\tan(x) \approx x$ and $\cos(x) \approx 1$ yield

$$E_{\theta,\,\mathrm{diel}\perp} \approx E_{\theta,\,\mathrm{air}\perp} \frac{2}{\varepsilon_\mathrm{r} - \mathrm{j}\dfrac{\varepsilon_\mathrm{r} - \sin^2\theta}{\cos\theta} k_0 h}, \tag{4.31}$$

which can be further simplified if the dominant radiation is within $0 \leq \theta < \pi/2$ and $k_0 h \ll 1$ holds yielding

$$E_{\theta,\,\mathrm{diel}\perp} \approx E_{\theta,\,\mathrm{air}\perp} \frac{2}{\varepsilon_\mathrm{r}} \approx E_{\theta,\,\mathrm{pec}\perp} \frac{1}{\varepsilon_\mathrm{r}}. \tag{4.32}$$

Thus, the radiated power can be approximated as well by

$$P^\mathrm{rad}_{\mathrm{diel}\perp} \approx i_0^2 \, \frac{2\pi}{3\,\varepsilon_\mathrm{r}^2} \eta_0 \left(\frac{h}{\lambda_0}\right)^2 = \frac{P^\mathrm{rad}_{\mathrm{pec}\perp}}{\varepsilon_\mathrm{r}^2}, \tag{4.33}$$

which explains the good fit between the approximation $P^\mathrm{rad}_{\mathrm{pec}\perp}/\varepsilon_\mathrm{r}^2$ and the exact result in Fig. 4.4. Finally, an equivalent radiation resistance can be accessed

$$R^\mathrm{rad}_{\mathrm{diel}\perp} = \frac{2P^\mathrm{rad}_{\mathrm{diel}\perp}}{|i_0|^2} \approx \frac{4\pi}{3\,\varepsilon_\mathrm{r}^2}\,\eta_0 \left(\frac{h}{\lambda_0}\right)^2 = \frac{2}{\varepsilon_\mathrm{r}^2} R^\mathrm{rad}_\mathrm{air}. \tag{4.34}$$

4.3. Horizontal Dipole Radiation

This section discusses the radiation of a dipole $i_0\,\ell$ oriented parallel to the x-axis. For comparability, the applied boundary conditions are electrically and geometrically equivalent to the previous chapter. Consequently, the horizontal dipole in a homogeneous background medium emits the same but rotated electromagnetic far field as the vertical dipole. The distinction between horizontal and vertical dipole becomes necessary when applying the boundary conditions in the x-y-plane in Sections 4.3.2 and 4.3.3. All solutions exclusively valid for the parallel dipole are labeled with a $\parallel$ symbol.

4.3.1. Horizontal Dipole in Homogeneous Background Medium

The short dipole horizontal to the x-y-plane is depicted in Fig. 4.5 (a). As for the vertical dipole, the vector potential is calculated, but here A_x exists, and so both φ and θ components are non-zero.

$$\boldsymbol{A}_{\mathrm{air}\parallel} = \frac{\mu_0 i_0 \ell}{4\pi} \frac{\exp[-\mathrm{j}\beta R]}{R} \mathbf{e}_x \tag{4.35}$$

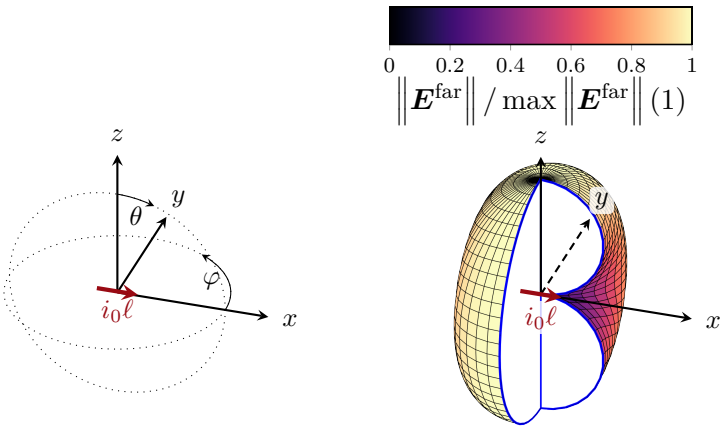

(a) (b)

Figure 4.5.: Geometry of (a) the horizontal dipole and (b) the radiation pattern of the horizontal dipole in air. The radiation pattern is normalized to the maximum value and given using a linear scale. The x-z and y-z cuts are introduced to ease the interpretation of the radiation pattern.

In the far field, the electric field is then given by

$$E_{\theta,\,\text{air}\parallel} = -\text{j}\frac{\omega\mu_0 i_0 \ell}{4\pi}\frac{\exp[-\text{j}\beta R]}{R}\cos\theta\cos\phi, \tag{4.36}$$

$$E_{\varphi,\,\text{air}\parallel} = +\text{j}\frac{\omega\mu_0 i_0 \ell}{4\pi}\frac{\exp[-\text{j}\beta R]}{R} \qquad \sin\phi, \tag{4.37}$$

$$\tag{4.38}$$

which results in the same radiated power as the vertical dipole in a homogeneous medium for $h = \ell$

$$P_{\text{air}}^{\text{rad}} = i_0^2\,\frac{\pi}{3}\eta_0\sqrt{\varepsilon_\text{r}}\left(\frac{h}{\lambda_0}\right)^2, \tag{4.39}$$

resulting in an equal radiation resistance (cf. (4.17))

$$R_{\text{air}}^{\text{rad}} = \frac{2P_{\text{air}}^{\text{rad}}}{|i_0|^2} = \frac{2\pi}{3}\,\eta_0\,\sqrt{\varepsilon_\text{r}}\left(\frac{h}{\lambda_0}\right)^2. \tag{4.40}$$

4.3.2. Horizontal Dipole with Ground Plane

As before, the method of images is used to consider the effect of a conducting ground plane. The image dipole modeling the ground is of opposing sign, as depicted in Fig. 4.6 (a), which enforces $\boldsymbol{E}_{\tan} = \boldsymbol{0}$ at the ground yielding

$$E_{\theta,\,\text{pec}\parallel} = E_{\theta,\,\text{air}\parallel}\left(\exp[\text{j}k_0 h\cos(\theta)] - \exp[-\text{j}k_0 h\cos(\theta)]\right), \tag{4.41}$$

$$E_{\varphi,\,\text{pec}\parallel} = E_{\varphi,\,\text{air}\parallel}\left(\exp[\text{j}k_0 h\cos(\theta)] - \exp[-\text{j}k_0 h\cos(\theta)]\right). \tag{4.42}$$

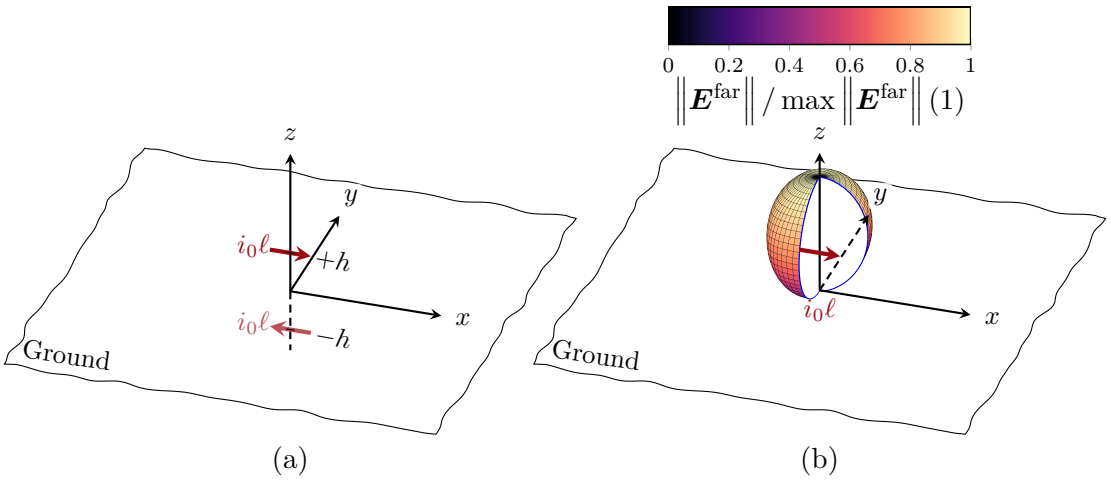

Figure 4.6.: Geometry of (a) the horizontal dipole over the ground plane and (b) the corresponding radiation pattern. The radiation pattern is normalized to the maximum value and given using a linear scale. The x-z and y-z cuts are introduced to ease the interpretation of the radiation pattern.

Hence the electric far field is proportional to $2\mathrm{j}\sin(k_0 h\cos\theta)$. Again, this can be simplified for electrically small substrate thicknesses using $\sin(x) \approx x$, and the integration according to (4.19) over φ and θ uses standard integrals and yields

$$P_{\text{pec}\parallel}^{\text{rad}} = i_0^2 \frac{16}{15}\pi^3 \eta_0 \left(\frac{h}{\lambda_0}\right)^2 \left(\frac{\ell}{\lambda_0}\right)^2 . \tag{4.43}$$

The complete solution for arbitrarily (large) distances to the ground is given in [56, p. 197]. Finally, an equivalent radiation resistance can be accessed

$$R_{\text{pec}\parallel}^{\text{rad}} = \frac{2P_{\text{pec}\parallel}^{\text{rad}}}{|i_0|^2} = \frac{32}{15}\pi^3 \eta_0 \left(\frac{h}{\lambda_0}\right)^2 \left(\frac{\ell}{\lambda_0}\right)^2 . \tag{4.44}$$

Here, a typical property of antennas with grounded substrates of low thickness can be recognized – the radiated power is proportional to h^2/λ_0^2, which implies that shorter ground distance also reduces the radiated power. Antennas on low-thickness grounded substrates are thus anticipated of limited radiation efficiency. The electric far-field pattern depicted in Fig. 4.6 (b) shows a slight asymmetry in the x-y-plane, where the pattern is broader in the y-direction.

4.3.3. Horizontal Dipole on Grounded Dielectric Slab

A drawing of the horizontal dipole on the grounded dielectric slab is depicted in Fig. 4.7 (a), and the dipole is of strength $i_0\ell$ and on a substrate of height h. Whereas the vertical dipole in the grounded dielectric slab could be described in a cylindrical coordinate system, the horizontal dipole results in both x- and z-component of the

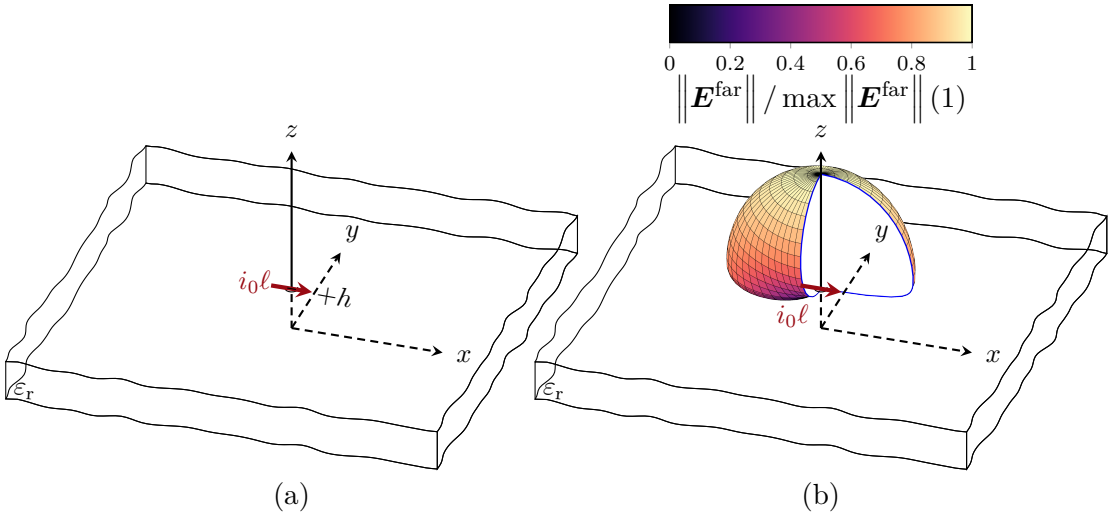

Figure 4.7.: Geometry of (a) the horizontal dipole over a grounded dielectric and (b) the corresponding radiation pattern. The radiation pattern is normalized to the maximum value and given using a linear scale. The x-z and y-z cuts are introduced to ease the interpretation of the radiation pattern.

vector potential [161]. The solution provided in [161] again uses two Hertzian potential functions for the air and dielectric region, respectively, and their solution is obtained by integrating along the k_x and k_y space. Based on Green's functions for a grounded dielectric slab, [162] presents the electric field strength for a horizontal dipole on the substrate's surface. In both cases, the involved integrals are not integrable; however, they can be approximated for the far-field solution using the saddle-point method (also known as the pass method or method of steepest descent [158, p. 99]) and expanding the terms asymptotically. Compared to [159], the residuum caused by the pole(s), which again describes the dielectric slab's eigensolutions corresponding to substrate waves, is neglected.

Since [163] and [159] have shown that the surface wave and space-wave contributions are orthogonal and can thus be treated separately, the surface wave power can be calculated independently from the radiated power [161]. The solutions from [161] contradict the later results in [162]; however, [164] already pointed out that the eigensolutions in [161] fail to fulfill their expectation, namely the fundamental TM and TE modes of the grounded dielectric slab. The resulting radiated field for a horizontal dipole on the surface of the dielectric ($z' = h$) is thus given based on [162]

$$E_{\theta,\,\text{diel}\parallel} = E_{\theta,\,\text{air}\parallel}\,\frac{2\sqrt{\varepsilon_\text{r} - \sin^2\theta}}{\sqrt{\varepsilon_\text{r} - \sin^2\theta} - \text{j}\varepsilon_\text{r}\,\cos\theta\,\cot\left(\sqrt{\varepsilon_\text{r} - \sin^2\theta}\,k_0 h\right)}, \tag{4.45}$$

$$E_{\varphi,\,\text{diel}\parallel} = E_{\varphi,\,\text{air}\parallel}\,\frac{2\,\cos\theta}{\cos\theta - \text{j}\sqrt{\varepsilon_\text{r} - \sin^2\theta}\cot\left(\sqrt{\varepsilon_\text{r} - \sin^2\theta}\,k_0 h\right)}, \tag{4.46}$$

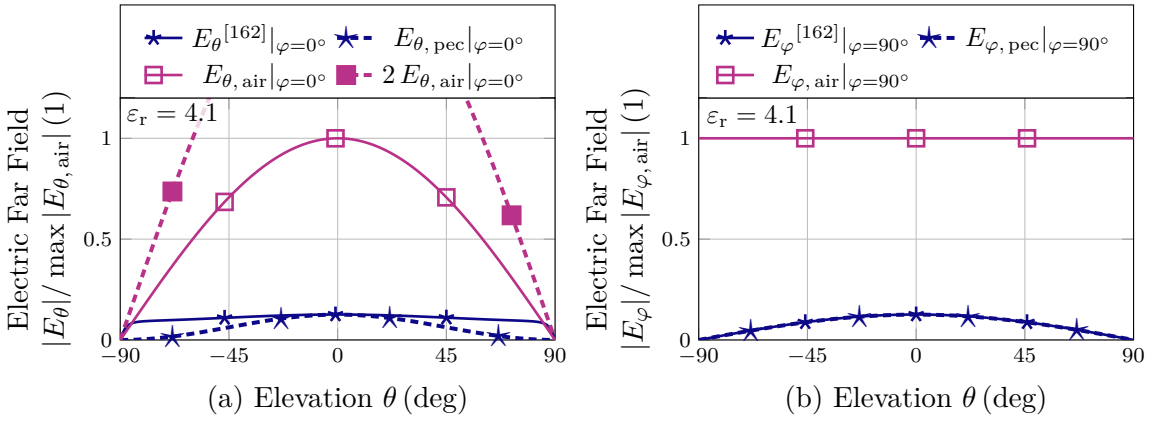

Figure 4.8.: Electric far field for the horizontal dipole in air for (a) the $\varphi = 0°$ cut plane and (b) the $\varphi = 90°$ cut plane with a ground plane and on a grounded dielectric slab at 300 GHz. The ground plane distance equals the dielectric height of $h = 10\,\mu$m, and the relative permittivity of the dielectric is assumed $\varepsilon_\mathrm{r} = 4.1$.

where (4.46) has been corrected by a factor j in the denominator. The approximation gets less accurate for values far off broadside, thus for large angles θ, but by substituting $\varepsilon_\mathrm{r} = 1$, the result exactly represents the horizontal dipole over the ground plane (cf. Section 4.2.2).

Although only approximate, the solution provided allows for a simplified treatment of the dielectric – it practically multiplies correction factors to the φ and θ components, as shown for the ground plane in (4.41) and (4.42). The resulting radiation patterns in both the x-z- and the y-z-plane are compared for the different cases, namely dipole in air, with a ground plane, and with a grounded dielectric substrate, and are depicted in Fig. 4.8. At first, the existence of the ground plane with or without dielectric and the resulting opposed image dipole decreases the radiated far field compared to the free space case. As expected from theory [56, p. 837], the ground plane behaves very similarly to the grounded dielectric slab for the broadside direction ($\theta = 0$), and the difference between the grounded dielectric slab and ground plane increases for the θ-polarization for angles near grazing. Here, the electric far field converges to the two-fold value of $E_{\theta,\,\mathrm{air}}$, which is also depicted in the diagram. The φ-polarization of the dielectric case is practically indistinguishable from the grounded case for small dielectric heights.

Since the resulting electric far field with the additional factors accounting for the dielectric are not integrable, the integration is carried out numerically for the grounded dielectric slab. Alternatively, for small electric heights of the substrate $k_0 h$, (4.45) and (4.46) can be approximated using $k_0 h \ll 1$, $\sin(x) \approx x$, and $\cos(x) \approx 1$ for sufficiently

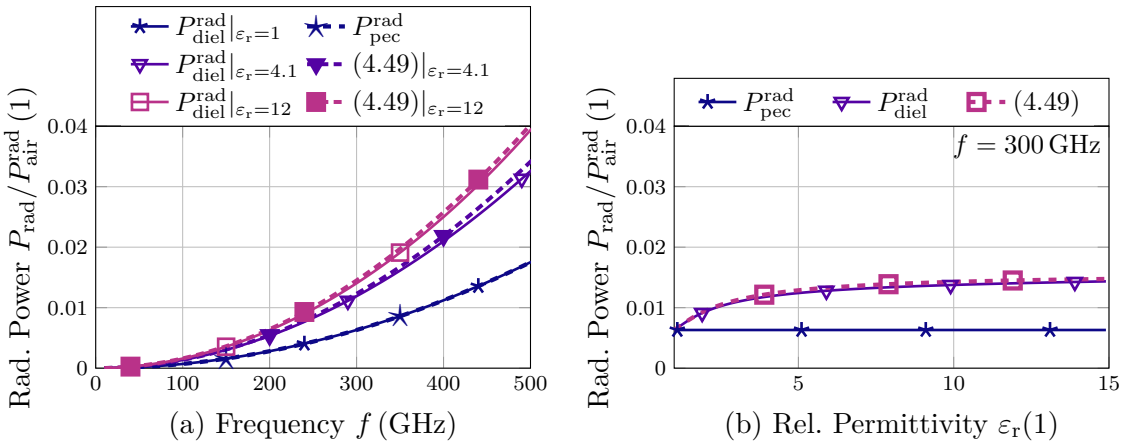

Figure 4.9.: Radiated power of a horizontal dipole above a ground plane and on a grounded dielectric as a function of (a) frequency and (b) relative permittivity. The height of the dipole above ground and the dielectric thickness is $h = 10\,\mu\mathrm{m}$.

small arguments, yielding

$$E_{\theta,\,\mathrm{diel}\parallel} \approx E_{\theta,\,\mathrm{air}\parallel}\, 2\mathrm{j}\, k_0 h\, \frac{\varepsilon_\mathrm{r} - \sin^2\theta}{\varepsilon_\mathrm{r}\,\cos\theta}, \tag{4.47}$$

$$E_{\varphi,\,\mathrm{diel}\parallel} \approx E_{\varphi,\,\mathrm{air}\parallel}\, 2\mathrm{j}\, k_0 h\, \cos\theta. \tag{4.48}$$

This result resembles the relatively flat E_θ in the $\varphi = 0°$ cut and approaches the E_φ solution with only the ground plane in the $\varphi = 90°$ cut. Again, the integration of (4.47) and (4.48) over the upper hemisphere, according to (4.19), is covered by standard integrals yielding

$$P^{\mathrm{rad}}_{\mathrm{diel}\parallel} \approx i_0^2\, \frac{8}{15}\pi^3\, \eta_0 \left(\frac{h}{\lambda_0}\right)^2 \left(\frac{\ell}{\lambda_0}\right)^2 \frac{5\,\varepsilon_\mathrm{r}(\varepsilon_\mathrm{r}-1)+2}{\varepsilon_\mathrm{r}^2}, \tag{4.49}$$

which directly allows for the calculation of an approximate radiation resistance

$$R^{\mathrm{rad}}_{\mathrm{diel}\parallel} = \frac{2\,P^{\mathrm{rad}}_{\mathrm{diel}\parallel}}{|i_0|^2} \approx \frac{16}{15}\pi^3\, \eta_0 \left(\frac{h}{\lambda_0}\right)^2 \left(\frac{\ell}{\lambda_0}\right)^2 \frac{5\,\varepsilon_\mathrm{r}(\varepsilon_\mathrm{r}-1)+2}{\varepsilon_\mathrm{r}^2}. \tag{4.50}$$

To show the accuracy of the approximation, Fig 4.9 depicts the radiated power obtained by integrating (4.45) and (4.46) over a hemisphere according to (4.19). The numerical integration is straightforward since the integrand does not show any poles, so this result is considered the reference solution. The limitation of this assumption is given by the neglected surface-wave terms and not by the accuracy of the numerical integration. Additionally, the reference solution for the horizontal dipole over the ground plane and the approximation according to (4.49) are depicted. Whereas the

frequency behavior is dominated by f^2, due to the electric height of the substrate $k_0 h$, the substrate effect seems to converge to ≈ 2 for sufficiently large permittivities. This behavior is a strong argument against the typically used $P^{\mathrm{rad}} \propto \sqrt{\varepsilon_{\mathrm{r}}}$ behavior, which results from assuming a homogeneous dielectric background medium with $\eta = \eta_0 \sqrt{\varepsilon_{\mathrm{r}}}$ [156], and it highlights the necessity for a careful treatment of the dielectric slab. The approximation presented in (4.49) seems to diverge for higher frequencies caused by $k_0 h \ll 1$ becoming a weaker approximation. Besides this minor limitation, the approximation resembles the frequency- and permittivity dependence well.

The next chapter introduces an on-chip antenna approach utilizing discontinuities to increase the antenna's radiation efficiency. The results presented in this chapter provide the underlying basis for estimating the radiated power of these microstrip-based discontinuities. For example, the vertical current filament represents an essential part of a short-circuited MSL.

5. Capacitively Enhanced Antennas

This chapter presents antennas enhanced by capacitive discontinuities to compensate for the efficiency limitations of on-chip microstrip patch antennas. Based on a conventional microstrip patch, an EC model is presented and shortly discussed. The EC linked to the antenna geometry will enable insight into the operating bandwidth and radiation efficiency for the capacitively enhanced antenna. Finally, the radiation contributions from different MSL discontinuities are presented to be used in the given ECs.

5.1. Patch Antenna Concept

Fig. 5.1 shows a conventional microstrip patch antenna of length ℓ and width w on a grounded dielectric substrate of height h. For the fundamental operation, the length ℓ is approximately determined by the half-wavelength $\lambda_{\text{eff}}/2$ utilizing the effective permittivity $\lambda_{\text{eff}} = \lambda_0/\sqrt{\varepsilon_{\text{r,eff}}}$, and the width is usually chosen $w > \ell$. Typical for microstrip antennas, a wide bandwidth can only be achieved using an electrically thick substrate, as in [165]. The equivalent circuit model for the microstrip antenna depicted in Fig. 5.2 (b) is mapped to the geometry. Here, the operation of an edge-fed patch is determined by one conductance and one capacitance modeling the radiating edges of the patch, and a transmission line modeling the longitudinal edge, thus the wave propagation along the microstrip structure [21], [166]. The radiation of the patch

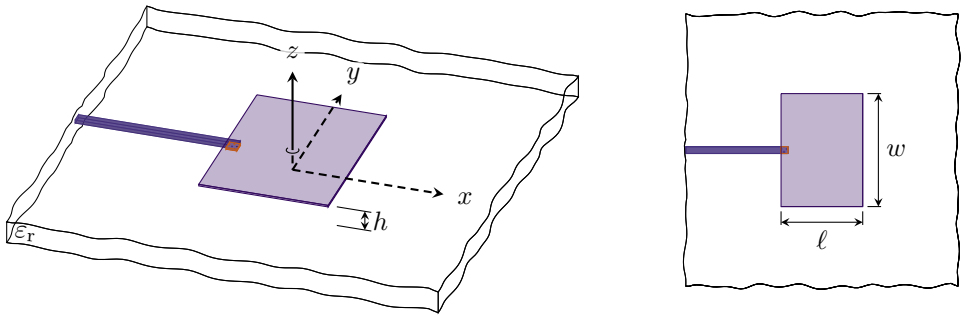

(a) (b)

Figure 5.1.: Geometry of the microstrip patch antenna of length ℓ and width w in (a) perspective view and (b) top view. The rectangular orange-colored via connects the feed line to the microstrip patch antenna.

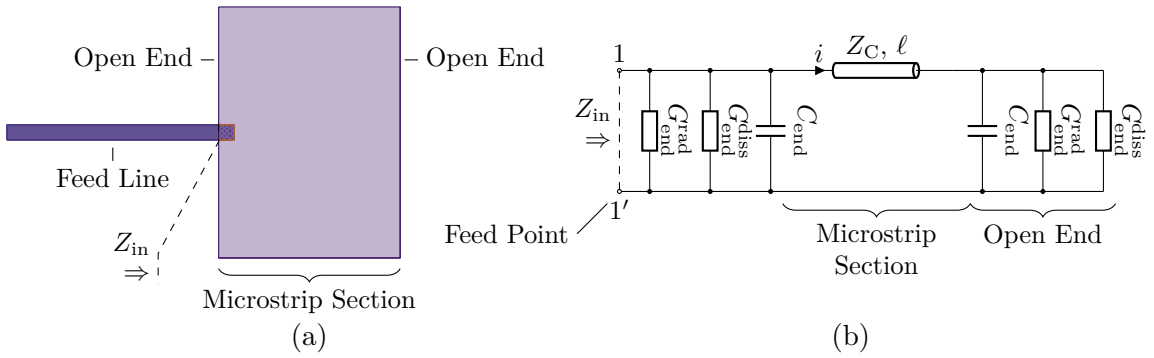

Figure 5.2.: Top view on (a) the patch antenna (cf. Fig. 5.1) with the essential domains labeled and (b) corresponding EC to describe the fundamental operation, where the EC is based on [21], [166].

antenna has been attributed to the fringing fields at the edges of the patch by models [21], [166] and measurements [167], and all the different models presented [56, pp. 811] share the concept of the radiating slot. Estimations for the radiation conductance $G_{\text{end}}^{\text{rad}}$ are given in [21] with an estimate of the impedance bandwidth based on the EC description. Such and similar models already hint at the usefulness of well-chosen ECs, and the impedance bandwidth is found to be linearly dependent on the substrate height [21]. Later, the radiated electric field based on a magnetic current density representing the electric field in the slot is given in [166]. The accuracy of the presented models will be discussed in more detail in Section 5.3.1. With the understanding of the fundamental radiator, even the mutual coupling between radiators of one antenna or between different antennas can be investigated [167]. It will be shown that the mutual coupling between the open-circuited terminations of the patch antenna is negligible compared to the radiation for an antenna length of $\approx \lambda_0/2$ (cf. Section 5.3.5). A fundamental numerical investigation of patch antennas based on the MoM is presented in [27]. Moreover, a general model for the fundamental operation, radiation pattern, and an equivalent circuit are given in [56, pp. 811].

The EC representation of the microstrip line, including the determination of the propagation constant γ and the characteristic impedance Z_{C}, have been discussed in Section 3.4. Equivalent capacitances representing the open end are given in the literature based on the numerical evaluation of an electrostatic MoM [168], [169] and expressed as empirical formulas [170], [171]. An extension length $\Delta\ell$ relates the length of a TL with a real open circuit to an equivalent TL with an ideal open circuit without fringing fields in the longitudinal direction. If this idea is applied to the capacitance per unit length of the TL, the additional capacitance representing the fringing field of the open end is found [166]

$$C_{\text{end}} = C'_{\text{TL}} \Delta\ell. \tag{5.1}$$

The corresponding dissipation conductance can be estimated by the upper limit

$$G_{\text{end}}^{\text{diss}} < \omega \tan\delta \, C_{\text{end}}, \tag{5.2}$$

where the dielectric losses are assumed in the whole domain. Following the transmission line EC, a dielectric filling factor (cf. (3.54)) could be used for a more accurate description. For the end capacitances described in this thesis, the radiation will exceed the dielectric dissipation, so a detailed treatment of the end capacitance losses is omitted. Furthermore, a current distribution deviating from the current distribution in the MSL is neglected, although it would increase $G_{\text{end}}^{\text{diss}}$ by ohmic losses in the strip. The thorough treatment of the transversal currents is discussed shortly in [142] and ultimately requires numerical full-wave simulations. Finally, the radiation mechanism modeled by the radiation conductance $G_{\text{end}}^{\text{rad}}$ will be explained and derived in Section 5.3.1.

5.2. Capacitive Discontinuities

It has been shown in [21] that microstrip antennas based on electrically thin substrates suffer from limited radiation efficiency and bandwidth. To increase the radiation efficiency of microstrip-based antennas, capacitive discontinuities have been introduced in [A172]. The term capacitive discontinuity describes two galvanically isolated microstrip lines, which are coupled dominantly by a capacitance and will be referred to as a gap shortly. The geometry of a general capacitively enhanced antenna is depicted in Fig. 5.3 (a) with the corresponding EC in Fig. 5.3 (b), where each of the N capacitive discontinuities is represented by a dominating gap capacitance C_{gap}, a radiation conductance $G_{\text{gap}}^{\text{rad}}$, and a dissipation conductance $G_{\text{gap}}^{\text{diss}}$. As for the patch, the mutual coupling between the radiators is not considered for the initial investigation; a detailed discussion of the mutual coupling effects is presented in Section 5.3.4. Each unit cell consists of two transmission line sections with an overall length of ℓ and one capacitive discontinuity. The circuit elements associated with the unit cell will be subscripted using UC. Separating the antenna into periodic sections forming unit cells is not mandatory since the antenna approach does not require periodicity. However, with periodicity, the analysis methods from periodic structures can be used conveniently [28, p. 84].

Compared to a conventional patch antenna, whose geometrical length is determined by substrate selection and operating frequency, this concept features extra degrees of freedom. The gap capacitance can be adjusted by the design of the discontinuity, and each capacitance reduces the phase shift per unit cell. In contrast, the length of the transmission line ℓ increases this phase shift. Thus, the number of unit cells N and the total antenna length $N \cdot \ell > \lambda_{\text{eff}}/2$ can be chosen freely by a suitable choice of the capacitance C_{gap}. The following tradeoff should be considered when optimizing radiation efficiency. An overall longer antenna allows for more capacitances, which should increase the radiated power; however, longer microstrip sections will dissipate more power due to dielectric and ohmic losses. In contrast to the metamaterial transmission lines [28, p. 83], there is no limitation to each unit cell's length. For the fundamental

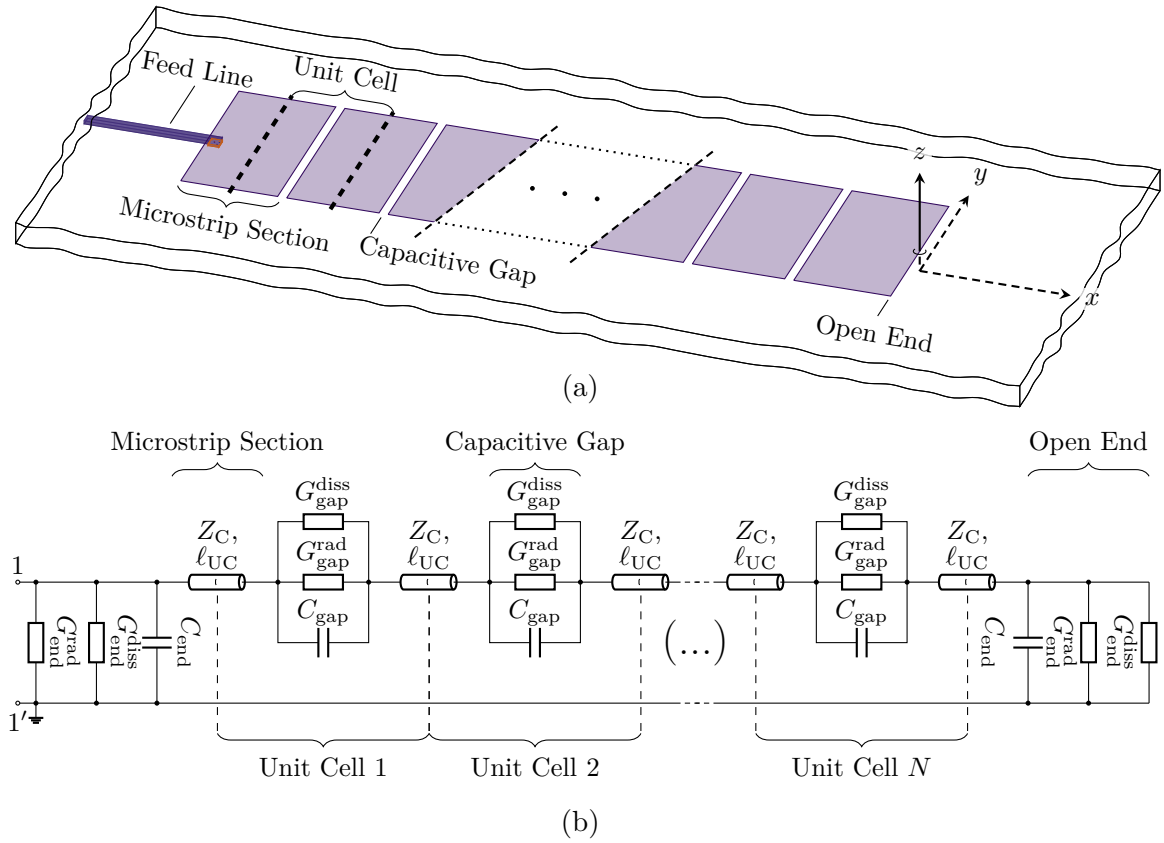

Figure 5.3.: Geometry of (a) a general capacitively enhanced microstrip antenna and (b) EC consisting of N UCs with a capacitive gap and two terminating open circuits.

operation similar to the $\lambda_{\text{eff}}/2$ resonance of a patch, the phase shift of all unit cells should add up to π, which indicates the phase shift per unit cell $\phi_{\text{UC}} \approx \pi/N$, where the influence of the end capacitance has been neglected. Naturally, the electrical length of the unit cell could be increased by an even multiple $2n\pi$, $n \in \mathbb{N}$, which would ultimately increase the losses in the transmission line and thus decrease the overall radiation efficiency.

5.2.1. Dispersion Diagram

As stated above, the antenna concept does not require a periodicity for correct operation. However, a periodic antenna can be fundamentally described by its unit cell. The following dispersion diagram analysis requires the *ABCD* matrix description of the unit cell and is based on [141, pp. 382]. Fig. 5.4 shows the simplified equivalent circuit used within this section. Besides neglecting all loss contributions, an ideal, meaning undisturbed, periodicity is assumed, which means the unit cells extend in both direc-

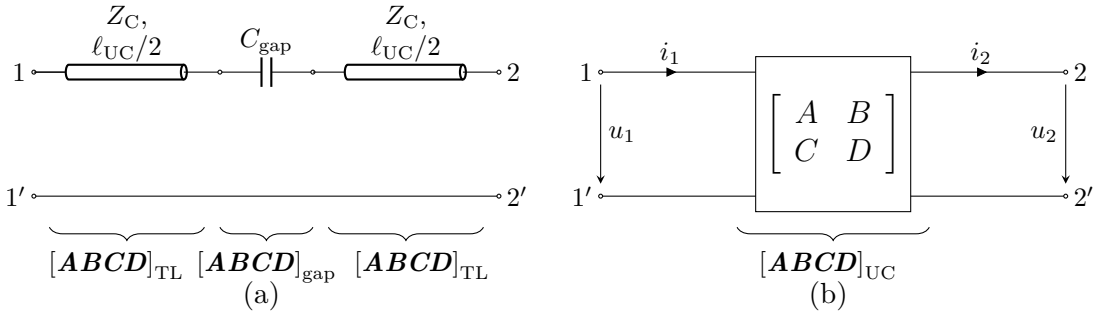

Figure 5.4.: Equivalent circuit representation of (a) a lossless unit cell for the dispersion analysis and (b) its formal representation by an $ABCD$ matrix.

tions infinitely. Although the later realized antennas will only use a small number of unit cells, the fundamental understanding developed here will also be of importance for these prototypes. Generally speaking, the dispersion of the unit cell is described by its propagation constant $\gamma_{UC}(f)$ as a function of frequency, which describes both the attenuation α_{UC} and phase shift β_{UC} along the length ℓ_{UC}. By relating the input and output voltage and current of two succeeding unit cells [141, p. 383]

$$u_{n+1} = u_n \exp[-\gamma_{UC}\,\ell_{UC}]\,, \qquad i_{n+1} = i_n \exp[-\gamma_{UC}\,\ell_{UC}] \tag{5.3}$$

and inserting u_n and i_n into the $ABCD$ equation graphically represented in Fig. 5.4 (b)

$$\begin{bmatrix} u_n \\ i_n \end{bmatrix} = \begin{bmatrix} A & B \\ C & D \end{bmatrix} \cdot \begin{bmatrix} u_{n+1} \\ i_{n+1} \end{bmatrix} \tag{5.4}$$

gives

$$\mathbf{0} = \begin{bmatrix} A - \exp[\gamma_{UC}\,\ell_{UC}] & B \\ C & D - \exp[\gamma_{UC}\,\ell_{UC}] \end{bmatrix} \cdot \begin{bmatrix} u_{n+1} \\ i_{n+1} \end{bmatrix}. \tag{5.5}$$

All non-trivial solutions (representing arbitrarily scaled voltages and currents at the two-port) are obtained by a vanishing determinant of the matrix in (5.5) with $AD - BC = 1$ for a reciprocal network [141, p. 191], which yields

$$\cosh(\gamma_{UC}\,\ell_{UC}) = \frac{A + D}{2}. \tag{5.6}$$

This equation can be solved for $\gamma_{UC}\,\ell_{UC}$ with a phase-ambiguity of $2\pi n$, $n \in \mathbb{N}^0$, representing an inherent part of (5.3). If the unit cells are electrically sufficiently short, such that

$$\phi_{UC} = \Im\{\gamma_{UC}\}\,\ell_{UC} < \pi \tag{5.7}$$

holds, the ambiguity is resolved by $n = 0$. Alternatively, the phase has to be unwrapped starting at a frequency where (5.7) is fulfilled. The $ABCD$ matrix is calculated based on

the $ABCD$ matrix of a lossless TL with characteristic impedance Z_C and propagation constant β_TL and the $ABCD$ matrix of the capacitive gap

$$[\boldsymbol{ABCD}]_\mathrm{TL} = \begin{pmatrix} \cos(\beta_\mathrm{TL}\,\ell_\mathrm{UC}/2) & \mathrm{j}Z_\mathrm{C}\,\sin(\beta_\mathrm{TL}\,\ell_\mathrm{UC}/2) \\ \dfrac{\mathrm{j}}{Z_\mathrm{C}}\sin(\beta_\mathrm{TL}\,\ell_\mathrm{UC}/2) & \cos(\beta_\mathrm{TL}\,\ell_\mathrm{UC}/2) \end{pmatrix}, \tag{5.8}$$

$$[\boldsymbol{ABCD}]_\mathrm{gap} = \begin{pmatrix} 1 & \dfrac{1}{\mathrm{j}\,\omega C_\mathrm{gap}} \\ 0 & 1 \end{pmatrix}, \tag{5.9}$$

$$[\boldsymbol{ABCD}]_\mathrm{UC} = [\boldsymbol{ABCD}]_\mathrm{TL}\;[\boldsymbol{ABCD}]_\mathrm{gap}\;[\boldsymbol{ABCD}]_\mathrm{TL}\,. \tag{5.10}$$

Thus, the characteristic equation for the propagation constant reads

$$\cosh(\gamma_\mathrm{UC}\,\ell_\mathrm{UC}) = \frac{\sin(\beta_\mathrm{TL}\,\ell_\mathrm{UC}) + 2\omega C_\mathrm{gap}\,Z_\mathrm{C}\,\cos(\beta_\mathrm{TL}\,\ell_\mathrm{UC})}{2\omega C_\mathrm{gap}\,Z_\mathrm{C}}, \tag{5.11}$$

where β_TL needs to be considered a function of frequency for the dispersion diagram calculation. Equation (5.11) is evaluated numerically for $Z_\mathrm{C} = 20\,\Omega$, $\varepsilon_{\mathrm{r,\,eff}} = 4$ with different gap capacitances C_gap or unit cell lengths ℓ_UC. The resulting phase shift $\phi_\mathrm{UC} = \beta_\mathrm{UC}\,\ell_\mathrm{UC}$ of the unit cell is calculated using the phase constant $\beta_\mathrm{UC} = \Im\{\gamma_\mathrm{UC}\}$ and given in Fig. 5.5. These values are chosen similarly to the properties of the prototypes in Section 6.1. Additionally to the electrical length $\phi_\mathrm{UC} = \beta_\mathrm{UC}\,\ell_\mathrm{UC}$ of the unit cell, the so-called lightline is added by dotted lines. This line represents a non-dispersive TEM wave propagation in a medium of effective permittivity $\varepsilon_{\mathrm{r,\,eff}}$, which also approximates the conventional patch antenna. The discontinuity decreases for increasing C_gap (cf. Fig. 5.5 (a)); thus, the dispersion diagram converges towards the lightline solution. In the case of different unit cell lengths, several lightline solutions exist. Furthermore, the longer unit cell lengths also allow for a second branch in the dispersion diagram, corresponding to the solution for $\phi_\mathrm{UC} > \pi$. The $\lambda/2$ operating frequency of $2 \leq N \leq 5$ unit cells is highlighted by their respective electrical length $\phi_\mathrm{UC} = \pi/N$ with the corresponding projection onto the frequency axis using dashed lines for one exemplary case ($C_\mathrm{gap} = 20\,\mathrm{fF}$ and $\ell_\mathrm{UC} = 150\,\mu\mathrm{m}$) in Fig. 5.5 (a) and (b), respectively. According to [A172], the dispersion diagram calculated with the EC model agrees well with full-wave driven- and eigenmode solutions.

Despite the phase shift per unit cell, the dispersion diagram reveals another fundamental property of the capacitively enhanced antenna. Since a low-frequency cutoff exists at $\beta_\mathrm{UC}\,\ell_\mathrm{UC} = 0$, the dispersion curve will always exist above the lightline and converge towards it for larger $\beta_\mathrm{UC}\,\ell_\mathrm{UC}$. Consequently, the dispersion curve shows a smaller slope than the lightline, meaning a smaller frequency shift achieves the same phase shift (compared to the lightline), which indicates a narrower frequency bandwidth. As the lightline approximates the dispersion diagram of a patch antenna, this means that the capacitively enhanced microstrip antenna is intrinsically more narrowband compared to the conventional microstrip patch approach [A172].

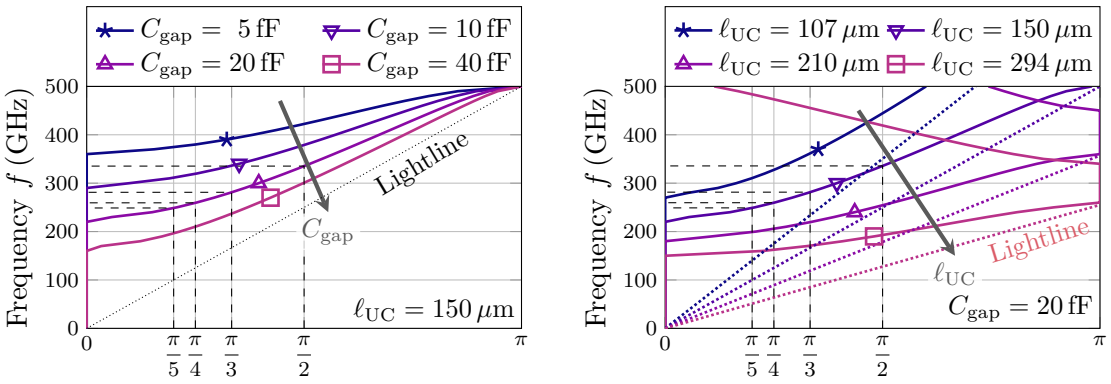

(a) Phase Shift per UC ϕ_{UC} (rad)

(b) Phase Shift per UC ϕ_{UC} (rad)

Figure 5.5.: Dispersion diagram for an exemplary antenna with $Z_{\mathrm{C}} = 20\,\Omega$, $\varepsilon_{\mathrm{r,eff}} = 4$ for (a) different gap capacitances C_{gap} and (b) different unit cell lengths ℓ_{UC}. The highlighted electrical lengths correspond to $\phi_{\mathrm{UC}} = \pi/N$ for the desired $\lambda/2$ operation.

5.2.2. Radiation Efficiency

Through thorough analysis of different loss mechanisms within the unit cell, the analytical estimation of the radiation efficiency at resonance has been presented in [A23] and is shortly recapitulated here. The EC for the lossy unit cell is depicted with different simplification steps in Fig. 5.6. It is assumed that the resonance frequency is ω_0 and that the resonance condition is given by the propagation constant of the unit cell

$$\ell_{\mathrm{tot}} = \frac{\pi}{|\Im\{\gamma_{\mathrm{UC}}\}|} = \frac{\pi}{\beta_{\mathrm{UC}}}, \tag{5.12}$$

with $\ell_{\mathrm{tot}} = N\ell_{\mathrm{UC}}$ the total length of the antenna. It will be shown that the result becomes less accurate for long transmission line sections and fewer unit cells since the homogenization involved in the derivation becomes imprecise. Contrary, the mutual coupling between the radiators, which is neglected in this derivation, increases for smaller unit cells and thus reduces the accuracy as well (cf. Section 5.3.4). Despite these limitations, this homogenized model is helpful for an order of magnitude estimation and initial physical insight. Fig. 5.6 (a) shows the symmetrical unit cell of the capacitively enhanced antenna utilized above. In the following, an asymmetric representation with a transmission line on the left-hand side will be used, as shown in Fig. 5.6 (b). The shunt elements of the series gaps can be converted to series elements denoted by a tilde (cf. Fig. 5.6 (c)). For a homogenized model, it is assumed that N series elements are distributed homogeneously along the total length of the antenna ℓ_{tot}, which yields

$$\widetilde{C}'_{\mathrm{gap}} = \frac{\ell_{\mathrm{tot}}}{N} \frac{\left(G^{\mathrm{rad}}_{\mathrm{gap}} + G^{\mathrm{diss}}_{\mathrm{gap}}\right)^2 + (\omega_0 C_{\mathrm{gap}})^2}{\omega_0^2 C_{\mathrm{gap}}}, \tag{5.13}$$

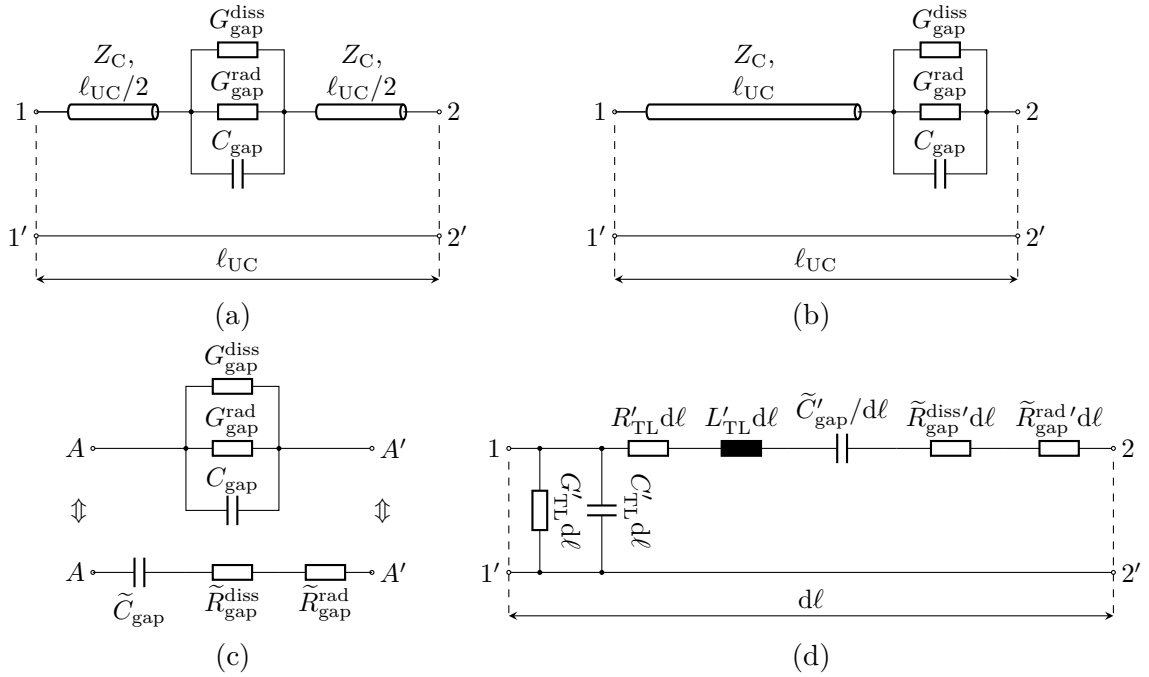

Figure 5.6.: Simplification of the EC unit cell from (a) a symmetric representation to (b) an asymmetric one. The shunt-to-series transformation of the gap (c) is used to define the final homogenized EC model (d) based on [A23].

$$\widetilde{R}_{\mathrm{gap}}^{\mathrm{diss}\prime} = \frac{N}{\ell_{\mathrm{tot}}} \frac{G_{\mathrm{gap}}^{\mathrm{diss}}}{\left(G_{\mathrm{gap}}^{\mathrm{rad}} + G_{\mathrm{gap}}^{\mathrm{diss}}\right)^2 + (\omega_0 C_{\mathrm{gap}})^2}, \tag{5.14}$$

$$\widetilde{R}_{\mathrm{gap}}^{\mathrm{rad}\prime} = \frac{N}{\ell_{\mathrm{tot}}} \frac{G_{\mathrm{gap}}^{\mathrm{rad}}}{\left(G_{\mathrm{gap}}^{\mathrm{rad}} + G_{\mathrm{gap}}^{\mathrm{diss}}\right)^2 + (\omega_0 C_{\mathrm{gap}})^2}, \tag{5.15}$$

where the reciprocal term in (5.13) results from $\widetilde{C}'_{\mathrm{gap}}$ being inversely proportional to its impedance. These elements describe an infinitesimally short transmission line section according to Fig. 5.6 (d).

For this homogeneous model, the series impedance and shunt admittance per unit length [28, p. 61] can be determined

$$Z' = R'_{\mathrm{TL}} + \widetilde{R}_{\mathrm{gap}}^{\mathrm{diss}\prime} + \widetilde{R}_{\mathrm{gap}}^{\mathrm{rad}\prime} + \mathrm{j}\omega \left(L'_{\mathrm{TL}} - \frac{1}{\omega^2 \widetilde{C}'_{\mathrm{gap}}} \right), \tag{5.16}$$

$$Y' = G'_{\mathrm{TL}} + \mathrm{j}\omega C'_{\mathrm{TL}}, \tag{5.17}$$

to calculate

$$\gamma_{\mathrm{UC,\,hom}} = \sqrt{Z'\,Y'}, \qquad Z_{\mathrm{UC,\,hom}} = \sqrt{\frac{Z'}{Y'}}. \tag{5.18}$$

The homogenized transmission-line representation of the unit cell is thus determined by its characteristic impedance $Z_{\mathrm{UC,\,hom}}$ and its propagation constant $\gamma_{\mathrm{UC,\,hom}}$. With the following simplification, which holds for dominantly capacitive gaps that fulfill $\omega C_{\mathrm{gap}} \gg \max(G'^{\mathrm{rad}}_{\mathrm{gap}}, G'^{\mathrm{diss}}_{\mathrm{gap}})$, the complexity is reduced using

$$\widetilde{C}'_{\mathrm{gap}} \approx \frac{N}{\ell_{\mathrm{tot}}}\, C_{\mathrm{gap}}, \qquad \widetilde{R}'^{\mathrm{diss}}_{\mathrm{gap}} \approx \frac{\ell_{\mathrm{tot}}}{N}\, \frac{G'^{\mathrm{diss}}_{\mathrm{gap}}}{(\omega\, C_{\mathrm{gap}})^2}, \qquad \widetilde{R}'^{\mathrm{rad}}_{\mathrm{gap}} \approx \frac{\ell_{\mathrm{tot}}}{N}\, \frac{G'^{\mathrm{rad}}_{\mathrm{gap}}}{(\omega\, C_{\mathrm{gap}})^2}. \tag{5.19}$$

With the assumption of a lossless unit cell, the phase constant at the resonance frequency ω_0 can be calculated by

$$\Im\{\gamma_{\mathrm{UC}}\} = \beta_{\mathrm{UC}} \approx \omega_0 \sqrt{C'_{\mathrm{TL}} \left(L'_{\mathrm{TL}} - \frac{N}{\omega_0^2\, C_{\mathrm{gap}}\, \ell_{\mathrm{tot}}} \right)}, \tag{5.20}$$

which gives, with the resonance condition (5.12), a quadratic equation concerning ℓ_{tot}. Solving this to only positive lengths gives [A23]

$$\ell_{\mathrm{tot}} = \frac{N}{2\omega_0^2\, C_{\mathrm{gap}}\, L'_{\mathrm{TL}}} + \frac{1}{\omega_0} \sqrt{\frac{N^2}{4\omega_0^2\, C_{\mathrm{gap}}^2\, L'^2_{\mathrm{TL}}} + \frac{\pi^2}{C'_{\mathrm{TL}}\, L'_{\mathrm{TL}}}}. \tag{5.21}$$

This equation can be used as an initial guess for the resonant length of a capacitively enhanced microstrip antenna, where only the gap capacitance C_{gap}, the number of gaps N, and the reactive parameters of the utilized microstrip line L'_{TL} and C'_{TL} need to be known.

Furthermore, the homogeneous model includes the power dissipation in each circuit element. The current and voltage distributions are assumed to represent an ideal open-ended $\lambda/2$ resonator with a sine-shaped current and a corresponding cosine-shaped voltage distribution [141, pp. 60]. Given the input voltage wave amplitude u_0^+, the power dissipation for shunt and series elements along the homogenized transmission line calculates by

$$P_{\mathrm{series}} = \int_0^{\ell_{\mathrm{tot}}} \frac{R'_{\mathrm{series}}\, 2|u_0^+|^2}{|Z_{\mathrm{UC,\,hom}}|^2} \sin^2(\beta_{\mathrm{UC}}\, \ell)\, \mathrm{d}\ell = \frac{R'_{\mathrm{series}}}{|Z_{\mathrm{UC,\,hom}}|^2} \frac{2|u_0^+|^2}{\beta_{\mathrm{UC}}} \int_0^{\pi} \sin^2(\varphi)\, \mathrm{d}\varphi, \tag{5.22}$$

$$P_{\mathrm{shunt}} = \int_0^{\ell_{\mathrm{tot}}} G'_{\mathrm{shunt}}\, 2|u_0^+|^2 \cos^2(\beta_{\mathrm{UC}}\, \ell)\, \mathrm{d}\ell = G'_{\mathrm{shunt}} \frac{2|u_0^+|^2}{\beta_{\mathrm{UC}}} \int_0^{\pi} \cos^2(\varphi)\, \mathrm{d}\varphi, \tag{5.23}$$

where the resonance condition (5.12) has been used to substitute $\varphi = \beta_{\mathrm{UC}}\ell$. By relating the power of the radiation conductance $G'^{\mathrm{rad}}_{\mathrm{gap}}$ or its representative $\widetilde{R}'^{\mathrm{rad}}_{\mathrm{gap}}$ to the total power dissipated in all elements in Fig. 5.6 (d), the radiation efficiency is found [A23]

$$\eta_{\mathrm{rad}} \approx \frac{\dfrac{\widetilde{R}'^{\mathrm{rad}}_{\mathrm{gap}}}{|Z_{\mathrm{UC,\,hom}}|^2}}{\dfrac{\widetilde{R}'^{\mathrm{rad}}_{\mathrm{gap}}}{|Z_{\mathrm{UC,\,hom}}|^2} + \dfrac{\widetilde{R}'^{\mathrm{diss}}_{\mathrm{gap}}}{|Z_{\mathrm{UC,\,hom}}|^2} + \dfrac{R'_{\mathrm{TL}}}{|Z_{\mathrm{UC,\,hom}}|^2} + G'_{\mathrm{TL}}}, \tag{5.24}$$

where the approximations of (5.19) can be inserted to give

$$\eta_{\mathrm{rad}} \approx \frac{\dfrac{N}{\ell_{\mathrm{tot}}} \dfrac{G_{\mathrm{gap}}^{\mathrm{rad}}}{(\omega\, C_{\mathrm{gap}})^2}}{\dfrac{N}{\ell_{\mathrm{tot}}} \dfrac{G_{\mathrm{gap}}^{\mathrm{rad}} + G_{\mathrm{gap}}^{\mathrm{diss}}}{(\omega\, C_{\mathrm{gap}})^2} + R'_{\mathrm{TL}} + |Z_{\mathrm{UC,\,hom}}|^2\, G'_{\mathrm{TL}}}. \tag{5.25}$$

The approximations within these derivations assumed at first a dominantly capacitive gap, which can be verified by confirming $\omega C_{\mathrm{gap}} \gg \max(G_{\mathrm{gap}}^{\mathrm{rad}}, G_{\mathrm{gap}}^{\mathrm{diss}})$, and second a resonant sinusoidal current distribution along the antenna, which would imply that the discontinuities do not alter the current distribution. The evaluation of the current distribution in the following Chapter 6 will show that the typically used number of gaps N is too small for this assumption to be fulfilled, which means the current distribution is not sinusoidal. Furthermore, the radiation contributions from the radiating open ends of the microstrip antenna are neglected. Since the standing wave voltage is known according to [141, pp. 60], the radiation contribution from radiation conductances representing the end capacitance could be added to the radiated power. Given the approximations above, the radiation efficiency calculated by (5.25) can increase physical insight, balance different loss contributions, and roughly estimate the radiation efficiency of an antenna candidate at resonance. For a more precise evaluation of the radiation efficiency, the equivalent circuit model (cf. Fig. 5.3 (b)) could be evaluated using a conventional circuit simulator, which will consider both the precise current distribution along the microstrip sections, the radiation by the open ends, as well as the coupling between the radiators (cf. Section 5.4.2).

In either case, the circuit-based estimation of the radiation efficiency requires the loss description of the transmission line given in Section 3.4, as well as the dissipation and radiation contributions of the gap and the open end. For a well-designed capacitive gap, the radiated power should significantly exceed the dissipated power to maximize the radiation efficiency. The radiated power and radiation conductance for different microstrip discontinuities, including the gap and the open case, are calculated and discussed in the next section.

5.3. Microstrip Radiation

The equivalent radiation resistances or conductances used in the previous sections will be derived based on general discontinuities in microstrip lines. The general method presented in [173], [174] approximates microstrip lines by line currents to introduce models of different microstrip discontinuities and has been extended to microstrip resonators in [175]. Usually, tailored numerical approaches [176] to evaluate microstrip and other structures embedded in the substrate implement solvers based on the MoM utilizing Green's functions for the specific substrate [66], [177]. These methods also facilitate

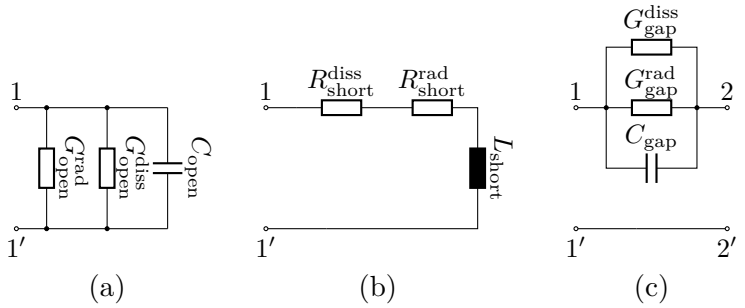

Figure 5.7.: EC models for (a) the open circuit, (b) the short circuit, and (c) the capacitive gap separating dissipation and radiation losses.

the separation of surface-wave (also referred to as substrate wave) and radiated (also referred to as space-wave) power [178]. Since it has been shown in Section 4.2.3 that the surface wave contributions are orders of magnitude smaller than the space wave contributions, if the substrate is electrically thin, the surface-wave power is neglected in this EC representation. Fig. 5.7 shows the ECs for the microstrip discontinuities discussed in the following sections, the open circuit, the short circuit, and the gap. A series topology of capacitance, loss-, and radiation resistance could achieve a frequency-independent EC model for the open circuit case [179]. However, the chosen topology eases the physical insight, as the radiated power can be directly related to the open-end voltage yielding the corresponding radiation conductance. Accordingly, the current is identified as a dissipation and radiation driving force in the short circuit EC. The use of a voltage-driven shunt EC for the gap will be justified in Section 5.3.5.

5.3.1. Open-Circuited Microstrip Line

The commonly used open circuit terminates a microstrip by truncating the conducting strip and is shortly referred to as an open end. In the analysis below, the substrate and ground plane are still assumed to be of infinite size, and losses are not considered for simplicity. A key motivation of modeling with equivalent circuits is separating different physical effects, such as radiation, dissipation, or field energy storage, and their attribution to different sections of the device to be modeled. Consequently, this analysis only investigates the radiation by an open-circuited MSL. The dominant capacitive effect of such lines has been investigated in a broad range numerically [168], [169] and translated into models [170], [171]. The loss description of the MSL using an EC has been covered in Section 3.4.

Fig. 5.8 (a) shows a microstrip open circuit and (b) its equivalent representation by line currents. A few things need to be considered when describing the MSL using line currents. First, line currents would result in an infinite characteristic impedance of the transmission line. Whenever needed, the characteristic impedance of the actual MSL will be assumed to model it correctly. Accordingly, whenever the propagation constant

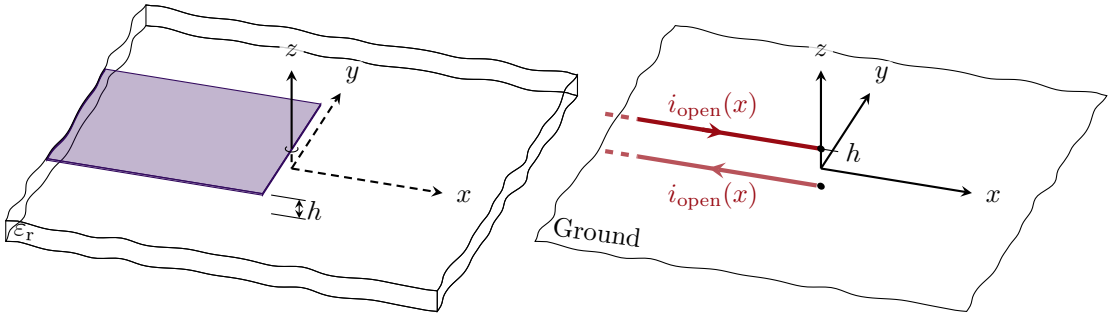

Figure 5.8.: Geometry of (a) the MSL open circuit and (b) its representation by a line current $i_{\text{open}}(x)$ above the ground plane.

or phase constant is of interest, the corresponding value for the MSL to be modeled will be used. Furthermore, the investigations above have shown that considering the dielectric generally yields terms that cannot be integrated fundamentally, such that initially, only a line above ground without substrate is investigated. A current $i_{\text{open}}(x)$ and its reversed image below the ground plane are assumed to be determined by an incident wave with the propagation constant β_{TL} and an out-of-phase current reflection due to the open circuit. The radiation contribution is assumed negligible small, such that $\Gamma = 1$ holds [173] in

$$i_{\text{open}}(x) = i^{+}_{\text{open}} \left(\exp[-\mathrm{j}\beta_{\text{TL}} x] - \Gamma \exp[+\mathrm{j}\beta_{\text{TL}} x]\right). \tag{5.26}$$

The magnetic vector potential is found by integrating along the extent of the top line-current $+i_{\text{open}}(x)$ according to (4.8), which yields the typical far-field approximation (cf. [43, p. 31])

$$A_{x,\,\text{top},\,\text{open}} = A_0(r) \int_{-L}^{0} \Big(\exp[-\mathrm{j}x'(\beta_{\text{TL}} - k_0 \cos\varphi \sin\theta)] - \exp[\mathrm{j}x'(\beta_{\text{TL}} + k_0 \cos\varphi \sin\theta)] \Big)\, \mathrm{d}x', \tag{5.27}$$

$$A_{x,\,\text{top},\,\text{open}} = A_0(r) \left[\frac{\exp[-\mathrm{j}x'(\beta_{\text{TL}} - k_0 \cos\varphi \sin\theta)]}{-\mathrm{j}(\beta_{\text{TL}} - k_0 \cos\varphi \sin\theta)} - \frac{\exp[\mathrm{j}x'(\beta_{\text{TL}} + k_0 \cos\varphi \sin\theta)]}{\mathrm{j}(\beta_{\text{TL}} + k_0 \cos\varphi \sin\theta)} \right]_{-L}^{0}, \tag{5.28}$$

with

$$A_0(r) = \frac{\mu_0\, i^{+}_{\text{open}}}{4\pi} \frac{\exp[-\mathrm{j}k_0 r]}{r}. \tag{5.29}$$

Here, the extent of the line current was assumed in the range of $-L \leq x' \leq 0$; however, the choice of L naturally affects the result. The limit of $L \to \infty$ could be physically interpreted – the line would extend from infinity up to the discontinuity at $x = 0$, but this interpretation yields problems summarized below. In [173], the effect and interpretation of the lower integration bound are discussed and presented here shortly. First, for any finite extent of L, two radiation contributions arise, namely at $x = -L$ and $x = 0$. The interplay of both contributions depends on their electrical distance affecting their coupling, and the radiation originating from both discontinuities is generally speaking physically sound. Unfortunately, the investigation of $L \to \infty$ does not converge. Furthermore, if losses of the MSL are assumed, then the exponential decay along the line enforces an infinite current at $x = -L$ in the limit of L. Although at an infinite distance, this current would radiate spherical waves with a typical r^{-2}-decay. Since the radiated waves with r^{-2} will always exceed the guided waves with $\exp[-\alpha r]$ for sufficiently large distances r, the radiation from $x = -L$ will exceed the radiation from $x = 0$ in the limit. In [173], it is suggested not to evaluate the lower bound and to investigate only one discontinuity at $x = 0$. Especially in the light of a full EC, where each discontinuity will be modeled by its distinct sub-circuit, this method fits the purpose of investigating an isolated discontinuity. On the far end of the EC, the second terminating discontinuity, which might be the one at $x = -L$, will be modeled by its own circuit.

Thus, the resulting vector potential for the top current $+i_{\text{open}}(x)$ reads

$$A_{x,\,\text{top},\,\text{open}} = A_0(r)\,\text{j}\left(\frac{1}{\beta_{\text{TL}} - k_0\,\cos\varphi\,\sin\theta} + \frac{1}{\beta_{\text{TL}} + k_0\,\cos\varphi\,\sin\theta}\right). \tag{5.30}$$

Both fractions are simplified toward a common denominator. The superposition with the inverse image current below the ground plane yields a factor $2\text{j}\,\sin\left(k_0 h\cos\theta\right)$ (cf. Section 4.3.2), which can, for electrically small heights $k_0 d$, be approximated with $\sin(x) \approx x$

$$A_{x,\,\text{pec},\,\text{open}} = -2\,k_0 h A_0(r)\left(\frac{2\beta_{\text{TL}}}{\beta_{\text{TL}}^2 - k_0^2\,\cos^2\varphi\,\sin^2\theta}\right)\cos\theta. \tag{5.31}$$

The resulting electric far field reads then according to (4.10)

$$E_{\theta,\,\text{pec},\,\text{open}} = \quad \text{j}\omega\,2\,k_0 h A_0(r)\left(\frac{2\beta_{\text{TL}}}{\beta_{\text{TL}}^2 - k_0^2\,\cos^2\varphi\,\sin^2\theta}\right)\cos^2\theta\,\cos\varphi, \tag{5.32}$$

$$E_{\varphi,\,\text{pec},\,\text{open}} = -\text{j}\omega\,2\,k_0 h A_0(r)\left(\frac{2\beta_{\text{TL}}}{\beta_{\text{TL}}^2 - k_0^2\,\cos^2\varphi\,\sin^2\theta}\right)\cos\theta\,\sin\varphi. \tag{5.33}$$

Inserting $A_0(r)$ and simplifying yields

$$E_{\theta,\,\text{pec},\,\text{open}} = \quad \text{j}\omega\,k_0 h\frac{\mu_0\,i_{\text{open}}^{+}}{\pi}\,\frac{\exp[-\text{j}k_0 r]}{r}\left(\frac{\beta_{\text{TL}}\,\cos^2\theta\,\cos\varphi}{\beta_{\text{TL}}^2 - k_0^2\,\cos^2\varphi\,\sin^2\theta}\right), \tag{5.34}$$

$$E_{\varphi,\,\text{pec},\,\text{open}} = -\text{j}\omega\,k_0 h\frac{\mu_0\,i_{\text{open}}^{+}}{\pi}\,\frac{\exp[-\text{j}k_0 r]}{r}\left(\frac{\beta_{\text{TL}}\,\cos\theta\,\sin\varphi}{\beta_{\text{TL}}^2 - k_0^2\,\cos^2\varphi\,\sin^2\theta}\right). \tag{5.35}$$

At first, it is noted that the radiation pattern based on (5.34)-(5.35), depicted in Fig 5.9, is highly similar to the radiation pattern of the horizontal dipole over a ground plane. In this figure, the permittivity only affects the propagation velocity along the line, but not the radiated field by polarization. The similarity of both radiation patterns will be used to include the dielectric by considering the factor of the horizontal dipole derived before, which is ≈ 2 (cf. Section 4.3.3).

The integration to determine the radiated power is shown in Appendix A, which yields

$$P^{\mathrm{rad}}_{\mathrm{pec,\,open}} = \pi\eta_0\,|i^{+}_{\mathrm{open}}|^2 \left(\frac{h}{\lambda_0}\right)^2 \left(\frac{\beta_{\mathrm{TL}}}{k_0}\right)^2 \left[3 - \left(\frac{k_0}{\beta_{\mathrm{TL}}}\right)^2 + \frac{k_0^4 + 2\beta_{\mathrm{TL}}^2\,k_0^2 - 3\beta_{\mathrm{TL}}^4}{2\beta_{\mathrm{TL}}^3 k_0}\,\ln\left|\frac{\beta_{\mathrm{TL}} + k_0}{\beta_{\mathrm{TL}} - k_0}\right|\right], \quad (5.36)$$

where h is the dielectric height, and β_{TL} is the propagation constant along the transmission line, which could be rewritten as $k_0\sqrt{\varepsilon_{\mathrm{r,\,eff}}}$. The radiation should now be related to the open circuit voltage to define the radiation conductance of the open end. Given the characteristic impedance Z_{C} and the incident current i^{+}_{open}, the open circuit voltage is expected to be $u_{\mathrm{open}} = 2i^{+}_{\mathrm{open}}Z_{\mathrm{C}}$. Thus the radiation conductance is given by

$$G^{\mathrm{rad}}_{\mathrm{pec,\,open}} = \frac{2P^{\mathrm{rad}}_{\mathrm{pec,\,open}}}{|2i^{+}_{\mathrm{open}}Z_{\mathrm{C}}|^2} \quad (5.37)$$

$$= \frac{\pi\,\eta_0}{2Z_{\mathrm{C}}^2}\left(\frac{h}{\lambda_0}\right)^2 \left(\frac{\beta_{\mathrm{TL}}}{k_0}\right)^2 \left[3 - \left(\frac{k_0}{\beta_{\mathrm{TL}}}\right)^2 + \frac{k_0^4 + 2\beta_{\mathrm{TL}}^2\,k_0^2 - 3\beta_{\mathrm{TL}}^4}{2\beta_{\mathrm{TL}}^3 k_0}\,\ln\left|\frac{\beta_{\mathrm{TL}} + k_0}{\beta_{\mathrm{TL}} - k_0}\right|\right]. \quad (5.38)$$

Although this radiation conductance incorporates the information about the dielectric within the characteristic impedance Z_{C} and the propagation constant β_{TL}, the effect of the dielectric on the radiated fields is not yet considered. With the results from the horizontal dipole on the grounded dielectric slab (cf. (4.45)-(4.46)), the electric far field of the open circuit with a substrate is represented by

$$E_{\theta,\,\mathrm{diel,\,open}} = \frac{E_{\theta,\,\mathrm{pec,\,open}}}{\mathrm{j}2k_0h\cos\theta}\,\frac{2\sqrt{\varepsilon_{\mathrm{r}} - \sin^2\theta}}{\sqrt{\varepsilon_{\mathrm{r}} - \sin^2\theta} - \mathrm{j}\varepsilon_{\mathrm{r}}\,\cos\theta\,\cot\left(\sqrt{\varepsilon_{\mathrm{r}} - \sin^2\theta}\,k_0h\right)}, \quad (5.39)$$

$$E_{\varphi,\,\mathrm{diel,\,open}} = \frac{E_{\varphi,\,\mathrm{pec,\,open}}}{\mathrm{j}2k_0h\cos\theta}\,\frac{2\,\cos\theta}{\cos\theta - \mathrm{j}\sqrt{\varepsilon_{\mathrm{r}} - \sin^2\theta}\cot\left(\sqrt{\varepsilon_{\mathrm{r}} - \sin^2\theta}\,k_0h\right)}. \quad (5.40)$$

Instead of integrating these terms to access the radiated power, the similarity between the radiation pattern of the horizontal dipole above the ground plane (cf. Fig. 4.6 (b))

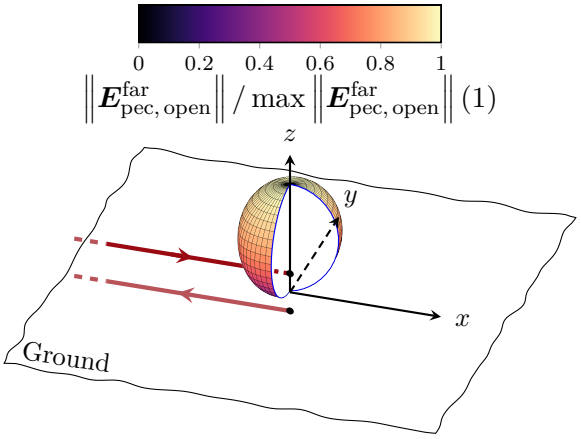

Figure 5.9.: Radiation pattern of the open-circuited MSL with $h = 10\,\mu\mathrm{m}$, $\varepsilon_\mathrm{r} = 4.1$, and $\beta_\mathrm{TL} = k_0\sqrt{\varepsilon_\mathrm{r}}$ at 300 GHz. The radiation pattern is normalized to the maximum value and given in a linear scale. The x-z and y-z cuts are introduced to ease the interpretation of the radiation pattern.

and the open-circuited MSL (cf. Fig. 5.9) is used. If both radiated far fields were identical, the impact of the dielectric correction factors on the radiated power would be identical. Here, the patterns are very similar, and thus the impact of the dielectric is considered approximately by comparing the radiated power $P^{\mathrm{rad}}_{\mathrm{pec}\|}$ with $P^{\mathrm{rad}}_{\mathrm{diel}\|}$. The relation is graphically depicted in Fig. 4.9 (b) and is calculated by relating (4.49) to (4.43)

$$P_{\mathrm{diel,\,open}} \approx P_{\mathrm{pec,\,open}} \frac{5\,\varepsilon_\mathrm{r}(\varepsilon_\mathrm{r}-1)+2}{2\varepsilon_\mathrm{r}^2}. \tag{5.41}$$

This method is approximative for two reasons. First, the dielectric effect was considered only approximately in (4.49), and second, the electric far fields of horizontal dipole and open-circuited MSL differ slightly. It will be shown that the radiated power and radiation conductance obtained by this method is in excellent agreement with the outcome of full-wave simulations (cf. Section 6.1.2). The estimation for the radiated power reads

$$\begin{aligned} P^{\mathrm{rad}}_{\mathrm{diel,\,open}} = {} & \pi\eta_0 \left|i^{+}_{\mathrm{open}}\right|^2 \left(\frac{h}{\lambda_0}\right)^2 \left(\frac{\beta_\mathrm{TL}}{k_0}\right)^2 \frac{5\,\varepsilon_\mathrm{r}(\varepsilon_\mathrm{r}-1)+2}{2\varepsilon_\mathrm{r}^2} \\ & \cdot \left[3 - \left(\frac{k_0}{\beta_\mathrm{TL}}\right)^2 + \frac{k_0^4 + 2\beta_\mathrm{TL}^2 k_0^2 - 3\beta_\mathrm{TL}^4}{2\beta_\mathrm{TL}^3 k_0} \ln\left|\frac{\beta_\mathrm{TL}+k_0}{\beta_\mathrm{TL}-k_0}\right|\right], \end{aligned} \tag{5.42}$$

which results in

$$\begin{aligned} G^{\mathrm{rad}}_{\mathrm{diel,\,open}} = {} & \frac{\pi\,\eta_0}{2Z_\mathrm{C}^2} \left(\frac{h}{\lambda_0}\right)^2 \left(\frac{\beta_\mathrm{TL}}{k_0}\right)^2 \frac{5\,\varepsilon_\mathrm{r}(\varepsilon_\mathrm{r}-1)+2}{2\varepsilon_\mathrm{r}^2} \\ & \cdot \left[3 - \left(\frac{k_0}{\beta_\mathrm{TL}}\right)^2 + \frac{k_0^4 + 2\beta_\mathrm{TL}^2 k_0^2 - 3\beta_\mathrm{TL}^4}{2\beta_\mathrm{TL}^3 k_0} \ln\left|\frac{\beta_\mathrm{TL}+k_0}{\beta_\mathrm{TL}-k_0}\right|\right]. \end{aligned} \tag{5.43}$$

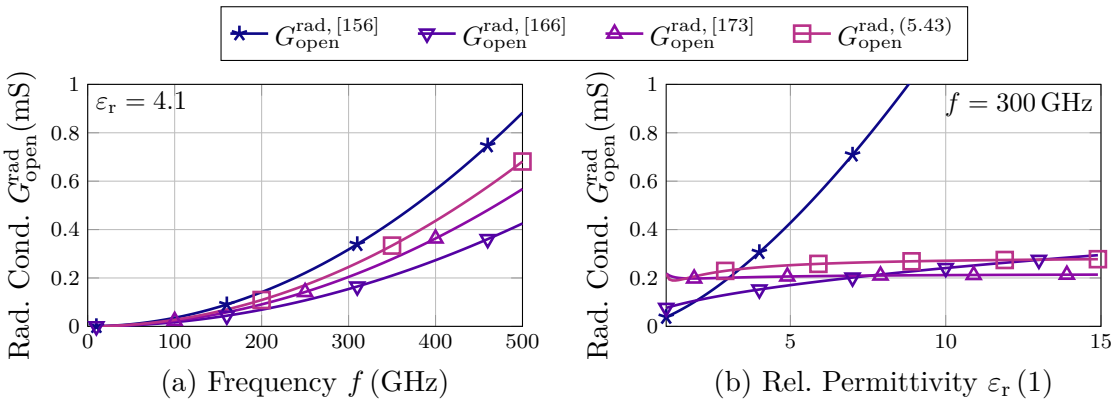

Figure 5.10.: Analytically calculated radiation conductance of an open-circuited MSL of width $w = 83\,\mu\text{m}$, height $h = 10\,\mu\text{m}$, and characteristic impedance of $Z_{\text{C}} = 23\Omega/\sqrt{\varepsilon_{\text{r}}}$ for (a) $\varepsilon_{\text{r}} = 4.1$ and (b) $f = 300\,\text{GHz}$. The conductances presented in [156], [166], and [173] are also given for comparison.

This solution will, for brevity, be referred to as $G_{\text{open}}^{\text{rad}}$ since most practical MSL implementations utilize a dielectric, which needs to be considered. Fig. 5.10 shows the radiation conductance calculated by (5.43) compared to other results from the literature. The derivation in [156] considers the electric field at the open end as the fundamental radiation mechanism for the open-circuited MSL. However, this derivation assumes a homogeneous background medium of relative permittivity $\varepsilon_{\text{r, eff}}$ instead of specifically including the dielectric slab, presumably resulting in a more significant error for larger permittivities. Similarly, the open circuit is treated as a slot in free space in [21] and [166], where the dielectric permittivity is ignored in the former and treated by including the background impedance η_{eff} in the latter. As a comparison, the radiation conductance given by (7) in [166] is evaluated numerically and depicted as well. In contrast to these approaches, the solution presented in [173] calculates the radiated power based on a discontinuous microstrip current similar to the method of this section; however, the dielectric effect is approximated by a polarization current density. The radiated power is, as above, used to calculate the radiation conductance according to (5.37).

5.3.2. Short-Circuited Microstrip Line

A short-circuited MSL and the corresponding model based on line currents are depicted in Fig. 5.11. The short circuit results in a vertical current filament $2\,i_{\text{short}}^{+}h$, which superposes with the semi-infinite line currents $i_{\text{short}}(x)$ of the MSL. Since [159] has already presented a solution for the electric far field of the vertical current filament in a grounded substrate (cf. Section 4.2.3), the radiation caused by the horizontal MSL currents will be derived in the same coordinate system. Both contributions are

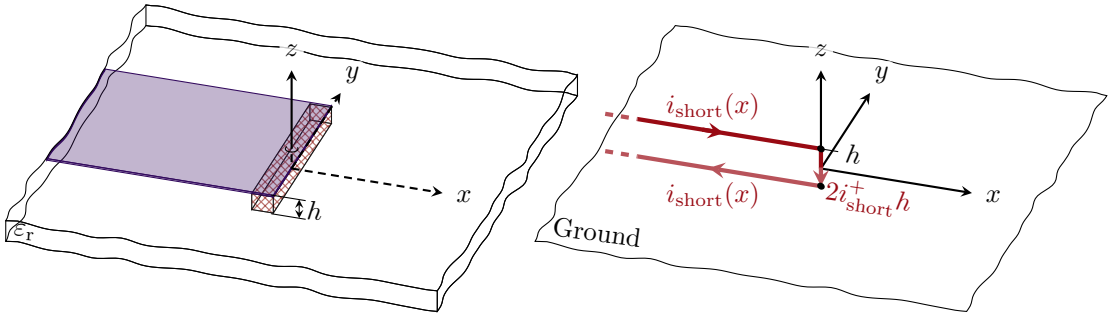

(a) (b)

Figure 5.11.: Geometry of (a) the MSL short circuit and (b) its representation by the line current $i_{short}(x)$, as well as a vertical dipole $2i^+_{short}h$ above the ground plane.

differentiated using the $\perp$ symbol to highlight the field and radiation caused by the vertical current and the $\parallel$ symbol for contributions from the horizontal current in the strip. The procedure is similar to the open case above; only the sign of the reflection coefficient is reversed, resulting in

$$i_{short}(x) = i^+_{short}\left(\exp[-j\beta_{TL}x] - \Gamma\exp[+j\beta_{TL}x]\right) \tag{5.44}$$

with $\Gamma = -1$, which gives

$$A_{x,\,pec,\,short_\parallel} = jA_0\left(\frac{1}{\beta_{TL} + k_0\cos\varphi\,\sin\theta} - \frac{1}{\beta_{TL} - k_0\cos\varphi\,\sin\theta}\right)2j\sin(k_0h\cos\theta) \tag{5.45}$$

using the superposition with the current below the ground plane, where the dielectric is not considered yet, as above. The effect of the ground can again be approximated for small dielectric heights, and the corresponding electric field is directly accessed, yielding

$$E_{\theta,\,pec,\,short_\parallel} = \frac{j\omega\mu_0 i^+_{short}}{2\pi}\frac{\exp[-j\,k_0\,r]}{r}\left(\frac{-2\cos\varphi\,\sin\theta}{(\beta_{TL}/k_0)^2 - \cos^2\varphi\,\sin^2\theta}\right)h\cos\theta\cos\theta\cos\varphi, \tag{5.46}$$

$$E_{\varphi,\,pec,\,short_\parallel} = \frac{j\omega\mu_0 i^+_{short}}{2\pi}\frac{\exp[-j\,k_0\,r]}{r}\left(\frac{-2\cos\varphi\,\sin\theta}{(\beta_{TL}/k_0)^2 - \cos^2\varphi\,\sin^2\theta}\right)h\cos\theta(-\sin\varphi). \tag{5.47}$$

Here, the effect of the dielectric can again be considered using the results of the horizontal dipole, i.e. (4.45)-(4.46)

$$E_{\theta,\,diel,\,short_\parallel} = \frac{E_{\theta,\,pec,\,short_\parallel}}{j2k_0h\cos\theta}\frac{2\sqrt{\varepsilon_r - \sin^2\theta}}{\sqrt{\varepsilon_r - \sin^2\theta} - j\varepsilon_r\,\cos\theta\,\cot\left(\sqrt{\varepsilon_r - \sin^2\theta}\,k_0h\right)}, \tag{5.48}$$

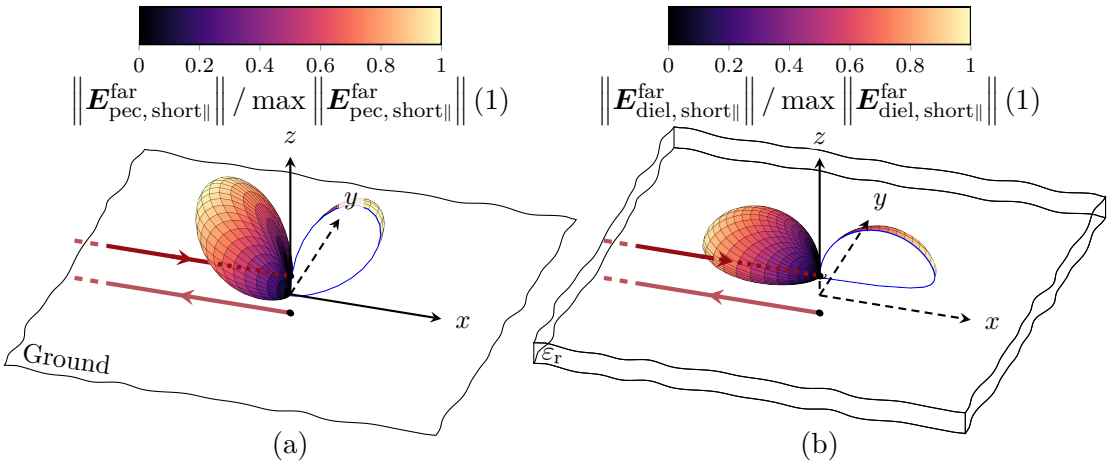

Figure 5.12.: Radiation pattern of the short-circuited MSL resulting from the line current (a) without and (b) with the substrate effect applied to the radiated fields. The substrate is considered by the parameters $h = 10\,\mu\text{m}$, $\varepsilon_{\text{r}} = 4.1$, and $\beta_{\text{TL}} = k_0\sqrt{\varepsilon_{\text{r}}}$. The radiation pattern is normalized to the maximum value and given in a linear scale. The x-z cut is introduced to ease the interpretation of the radiation pattern, and the radiation pattern vanishes in the y-z-cut.

$$E_{\varphi,\,\text{diel, short}\parallel} = \frac{E_{\varphi,\,\text{pec, short}\parallel}}{\text{j}2k_0h\cos\theta}\,\frac{2\,\cos\theta}{\cos\theta - \text{j}\sqrt{\varepsilon_{\text{r}} - \sin^2\theta}\,\cot\left(\sqrt{\varepsilon_{\text{r}} - \sin^2\theta}\,k_0h\right)}, \tag{5.49}$$

and the resulting radiation pattern for the ground and the grounded dielectric is depicted in Fig. 5.12 (a) and (b), respectively.

Finally, the electric field θ-component of the strip current $i_{\text{short}}(x) = 2\,i^{+}_{\text{short}}\,\cos(\beta_{\text{TL}}x)$ is superimposed with the field solution of the vertical current filament (cf. Section 4.2.3) modeling the via to the ground plane. Here, the dipole is now assumed of strength $-2i^{+}_{\text{short}}\,h$, according to the current at the end of the MSL, and the reversed dipole direction compared to Section 4.2.3, which gives

$$\begin{aligned} E_{\theta,\,\text{diel, short}\perp} = -\frac{\text{j}\omega\mu_0\,(2i^{+}_{\text{short}})h}{4\pi}\,\frac{\exp[-\text{j}\,k_0\,r]}{r}\,\sin\theta\,\frac{\cos\left(k_0z'\sqrt{\varepsilon_{\text{r}} - \sin^2\theta}\right)}{\cos\left(k_0h\sqrt{\varepsilon_{\text{r}} - \sin^2\theta}\right)} \\ \cdot\,\frac{2\,\cos\theta}{\varepsilon_{\text{r}}\cos\theta - \text{j}\sqrt{\varepsilon_{\text{r}} - \sin^2\theta}\,\tan\left(k_0h\sqrt{\varepsilon_{\text{r}} - \sin^2\theta}\right)}. \end{aligned} \tag{5.50}$$

Superimposing the vertical via and horizontal MSL current contributions, the total electric far field of the short-circuited MSL is given as

$$E_{\theta,\,\text{diel, short}} = E_{\theta,\,\text{diel, short}\parallel} + E_{\theta,\,\text{diel, short}\perp} \tag{5.51}$$

$$E_{\varphi,\,\text{diel, short}} = E_{\varphi,\,\text{diel, short}\parallel} \tag{5.52}$$

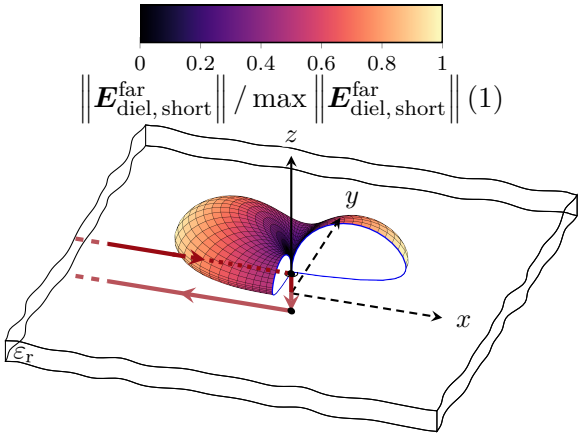

Figure 5.13.: Radiation pattern of the short-circuited MSL resulting from the line current with $h = 10\,\mu\mathrm{m}$, $\varepsilon_\mathrm{r} = 4.1$, and $\beta_\mathrm{TL} = k_0\sqrt{\varepsilon_\mathrm{r}}$ with the influence of the substrate. The radiation pattern is normalized to the maximum value and given in a linear scale. The x-z and y-z cuts are introduced to ease the interpretation of the radiation pattern.

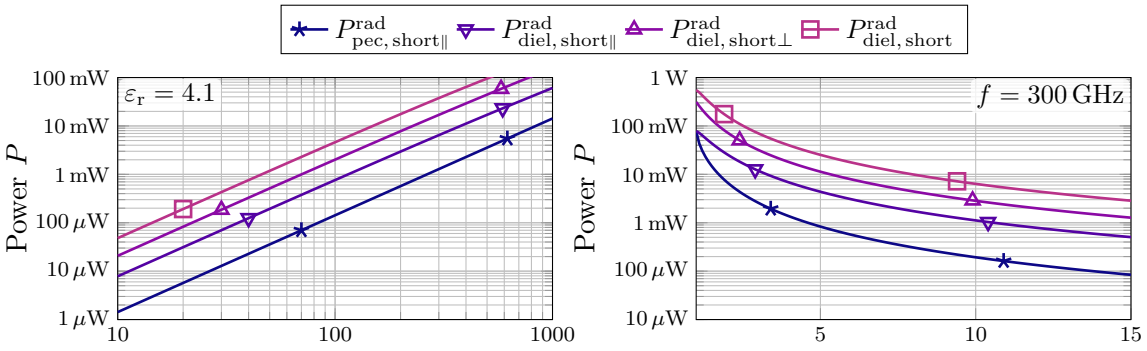

(a) Frequency f (GHz) (b) Rel. Permittivity ε_r (1)

Figure 5.14.: Radiated power of (a) the short-circuited MSL as a function of frequency and (b) relative permittivity of the dielectric. The height of the MSL and the substrate is $h = 10\,\mu\mathrm{m}$.

and depicted in Fig. 5.13. The radiated power $P^{\mathrm{rad}}_{\mathrm{diel,\,short}}$ can be obtained by numerically integrating the electric fields (5.51) and (5.52) according to (4.19). The radiation resistance of the short can be accessed by relating $P^{\mathrm{rad}}_{\mathrm{diel,\,short}}$ to the current in the short circuit, namely $2i^{+}_{\mathrm{short}}$, yielding

$$R^{\mathrm{rad}}_{\mathrm{short}} = \frac{2P^{\mathrm{rad}}_{\mathrm{diel,\,short}}}{4\left|i^{+}_{\mathrm{short}}\right|^2}. \tag{5.53}$$

The resulting radiated power for a unit current $i^{+}_{\mathrm{short}} = 1\,\mathrm{A}$ is depicted in Fig. 5.14 in dependence on frequency and permittivity. From the electric field solutions, it can be

seen that these radiation contributions are not orthogonal. Thus only the total radiated power $P^{\mathrm{rad}}_{\mathrm{diel,\,short}}$, resulting from fields of the horizontal strip currents and the vertical post currents, is assumed to be a valid representation of the short-circuited MSL. The other powers only quantify the radiated power per single element, considering either only the current elements parallel or vertical to the substrate surface. The line currents parallel to the substrate play, together with the open-circuit solution, a fundamental role describing an arbitrarily terminated MSL presented in the next section.

5.3.3. Terminated Microstrip Line

As the more general case compared to open- or short-circuited MSL, it is assumed that an arbitrary termination yields a reflection factor Γ for a given piece of MSL. The termination might be another MSL or a capacitive discontinuity in the chip context. More generally, any change in the waveguiding structure in the lateral direction will yield such reflection. For the cases where the termination includes an MSL on the right-hand side, the influence of the transmitted current (and also the possible reflection from a current originating from the right-hand side) will be considered later (cf. Section 5.3.5). In the considered geometry, thus, only the left-hand side ($x < 0$) of the geometry is assumed to carry a current, and the equivalent circuit representation uses an arbitrary load impedance Z_{L}, as depicted in Fig. 5.15.

The assumed current reads, as for open- and short circuits above, in dependence on the reflection factor Γ

$$i_{\mathrm{term}}(x) = i^{+}_{\mathrm{term}} \left(\exp[-\mathrm{j}\beta_{\mathrm{TL}} x] - \Gamma \exp[+\mathrm{j}\beta_{\mathrm{TL}} x]\right). \tag{5.54}$$

As in the above, the vector potential of the current above the ground plane (without

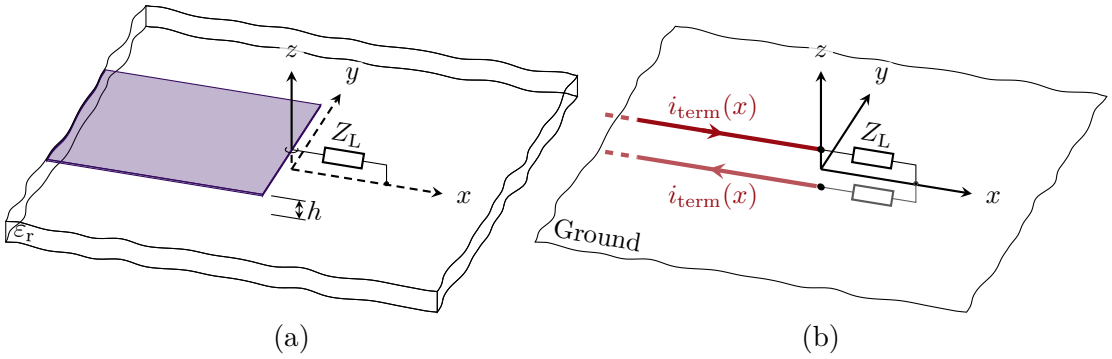

(a) (b)

Figure 5.15.: Geometry of (a) the MSL terminated by Z_{L} and (b) its representation by a line current $i_{\mathrm{term}}(x)$ above the ground plane.

the dielectric effect) can be given directly

$$A_{x,\,\mathrm{pec,\,term}} = \mathrm{j}A_0 \left(\frac{1}{\beta_{\mathrm{TL}} + k_0 \cos\varphi\, \sin\theta} + \Gamma \frac{1}{\beta_{\mathrm{TL}} - k_0 \cos\varphi\, \sin\theta} \right) 2\mathrm{j} \sin(k_0 h \cos\theta), \tag{5.55}$$

with $A_0 \propto i^{+}_{\mathrm{term}}$, and the corresponding electric fields could be calculated as above. It is straightforward to show that the resulting vector potential for the current $i_{\mathrm{term}}(x)$ can be given as a superposition of open- and short-circuit solutions. The vector potential of the open circuit and short circuit are referred to as $A_{\mathrm{x,\,open}}$ and $A_{\mathrm{x,\,short}}$, respectively. The here used solution for the short circuit considers only the contributions parallel to the MSL marked with the $\parallel$ symbol since the vertical current has no physical counterpart in the considered discontinuity. It should be noted that these quantities have not been calculated in the chapter above, as the dielectric effect was only considered for the far-field approximation of the electric field strength. If the vector potential is calculated, it yields

$$A_{\mathrm{x,\,term}} = A_{\mathrm{x,\,open}} \frac{1+\Gamma}{2} + A_{\mathrm{x,\,short}} \frac{1-\Gamma}{2}. \tag{5.56}$$

As a remarkable outcome, not only the trivial open- and short circuit ($\Gamma = \pm 1$) are covered with this result, but also the matched case $\Gamma = 0$ yields radiation, which has been claimed in [173]. With knowledge of the vector potentials $A_{\mathrm{x,\,short}}$ and $A_{\mathrm{x,\,open}}$, the corresponding electric far fields using spherical coordinates $\boldsymbol{E}_{\mathrm{short}}$ and $\boldsymbol{E}_{\mathrm{open}}$ could be integrated to access the radiated power of the terminated case

$$\begin{aligned} |\boldsymbol{E}_{\mathrm{term}}|^2 = \quad & \left| E_{\theta,\,\mathrm{open}} \frac{1+\Gamma}{2} \right|^2 + \left| E_{\theta,\,\mathrm{short}} \frac{1-\Gamma}{2} \right|^2 \\ & + \left| E_{\theta,\,\mathrm{short}} E_{\theta,\,\mathrm{open}} \frac{(1-\Gamma)(1+\Gamma)}{4} \right| \\ & + \left| E_{\varphi,\,\mathrm{open}} \frac{1+\Gamma}{2} \right|^2 + \left| E_{\varphi,\,\mathrm{short}} \frac{1-\Gamma}{2} \right|^2 \\ & + \left| E_{\varphi,\,\mathrm{short}} E_{\varphi,\,\mathrm{open}} \frac{(1-\Gamma)(1+\Gamma)}{4} \right|, \end{aligned} \tag{5.57}$$

which yields using (4.19) the radiated power

$$\begin{aligned} P^{\mathrm{rad}}_{\mathrm{term}} = & \frac{1}{2} \frac{|(1-\Gamma)(1+\Gamma)|}{4} \int_0^{2\pi} \int_0^{\pi/2} \frac{|E_{\theta,\,\mathrm{short}} E_{\theta,\,\mathrm{open}}| + |E_{\varphi,\,\mathrm{short}} E_{\varphi,\,\mathrm{open}}|}{\eta_0} |\boldsymbol{r}|^2 \sin\theta \,\mathrm{d}\theta \,\mathrm{d}\varphi \\ & + P^{\mathrm{rad}}_{\mathrm{open}} \left| \frac{1+\Gamma}{2} \right|^2 + P^{\mathrm{rad}}_{\mathrm{short}} \left| \frac{1-\Gamma}{2} \right|^2. \end{aligned} \tag{5.58}$$

The integral describes the shared radiation potion of open and short circuits, which would be zero for orthogonal far fields and $\sqrt{P^{\mathrm{rad}}_{\mathrm{open}}\, P^{\mathrm{rad}}_{\mathrm{short}}}$ for proportional far fields.

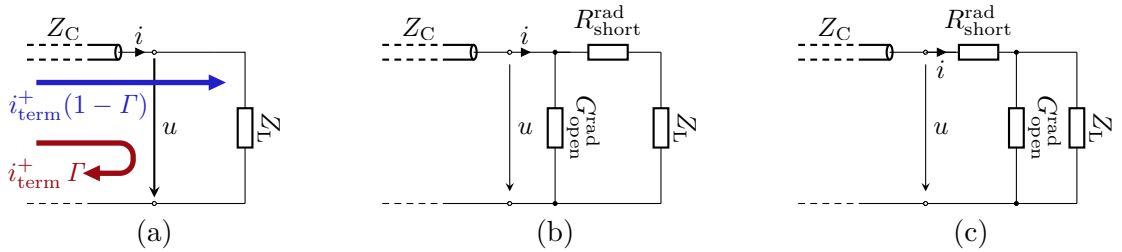

Figure 5.16.: MSL terminated by (a) an arbitrary load impedance Z_L and (b, c) two possible EC models intended to weight the radiated power in G^{rad}_{open} with $|u|^2$ and the power in R^{rad}_{short} with $|i|^2$.

This expression will be used in Section 5.3.4 to describe the coupling between two different sources, and it will be shown that this is zero for open- and short circuit. The handling of such coupling, if it can or shall not be neglected, is also described there. The remaining two summands proportional to P^{rad}_{open} and P^{rad}_{short} will be related to the voltage and current to calculate the EC parameters. Fig. 5.16 (a) shows the current waves and the associated voltage and current at the end of the terminated transmission line. The arbitrary load impedance and the corresponding reflection coefficient Γ determine u and i according to

$$u = Z_C\, i^+_{term}\,(1+\Gamma), \tag{5.59}$$

$$i = \quad i^+_{term}\,(1-\Gamma). \tag{5.60}$$

Including these expressions to replace $|1 \pm \Gamma|$ in (5.58) and the vanishing coupling integral (cf. Section 5.3.4) yields

$$P^{rad}_{term} = P^{rad}_{open}\left|\frac{u}{2Z_C i^+_{term}}\right|^2 + P^{rad}_{short}\left|\frac{i}{2i^+_{term}}\right|^2. \tag{5.61}$$

If the remaining parts are compared to the definition of open circuit radiation conductance (5.38) and short circuit radiation resistance (5.53), a handy expression is obtained reading

$$P^{rad}_{term} = G^{rad}_{open}\frac{|u|^2}{2} + R^{rad}_{short}\frac{|i|^2}{2}. \tag{5.62}$$

Thus, the radiation of an arbitrarily terminated transmission line is conveniently modeled using the radiation conductance of the open circuit in shunt and the radiation resistance of the short circuit in series, and two possible realizations are depicted in Figs. 5.16 (b) and (c). Whereas the first circuit (cf. Fig. 5.16 (b)) models the open circuit precisely, i.e., the radiated power is equal to the power derived from the MSL currents for $Z_L \to \infty$, the short circuit with $Z_L = 0$ will show a small radiation contribution from the open, since the voltage drop of the short $u = R^{rad}_{short} i$ results in

a radiation contribution proportional to $G_{\mathrm{open}}^{\mathrm{rad}}$. Vice versa, the second approach (cf. Fig. 5.16 (c)) models the short circuit exactly and is only approximate for the open circuit. The occurring error is usually negligible in both cases. The voltage over the short radiation resistance is diminishingly small compared to the open circuit voltage, and the current through the open radiation conductance is usually tiny compared to the short circuit current. This problem – choosing an appropriate topology – is known from T, Γ, or Π circuit models used for discrete models of TLs. Since most terminations dealt with in this thesis are more similar to the open circuit than to the short circuit, i.e. $-\pi/2 \leq \angle\Gamma \leq \pi/2$, the circuit topology in Fig. 5.16 (b) will be used from now on.

The radiation of the vertical via has been excluded in this section since all MSL discontinuities covered in this thesis, except for the short circuit, do not contain the vertical current contribution. If necessary, this contribution could be treated by adding its far field to the corresponding far field of the short. The coupling between different discontinuities is covered in the next section.

5.3.4. Coupling Between Microstrip Discontinuities

An arbitrary arrangement of short- and open circuit radiators is considered, as depicted in Fig. 5.17 (a). Each radiator is excited by a corresponding current i_m or voltage u_n for short and open, respectively, resulting in an electric far field $\boldsymbol{E}_{\mathrm{short},\,m}$ or $\boldsymbol{E}_{\mathrm{open},\,n}$ proportional to its excitation. This section evaluates the effect of coupling between those fundamental sources on the radiated power and aims to define a multiport to access the radiated power from the excitation voltages and currents, as depicted in Fig. 5.17 (b). Based on this result, coupling between arbitrary discontinuities in the MSL can be accessed using the results for the fundamental open- and short-circuited MSLs and the herein-developed circuit model. For the two different source types, namely open and short circuit, which generate the far fields $\boldsymbol{E}_{\mathrm{open,\,n}}(u_n)$ and $\boldsymbol{E}_{\mathrm{short,\,m}}(i_m)$, respectively, the total radiated power shall be determined. It is assumed that each of the N sources representing an open circuit depends on an excitation voltage u_n, as each of the M sources representing a short circuit accordingly depends on a current i_m. The total radiated power is accessed by integrating the superimposed electric far field according to

$$P = \frac{1}{2\eta_0} \oiint_S \left(\sum_{n=1}^{N} \left(\boldsymbol{E}_{\mathrm{open},\,n}(u_n)\right) + \sum_{m=1}^{M} \left(\boldsymbol{E}_{\mathrm{short},\,m}(i_m)\right) \right) \cdot \left(\sum_{\nu=1}^{N} \left(\boldsymbol{E}_{\mathrm{open},\,\nu}(u_\nu)\right) + \sum_{\mu=1}^{M} \left(\boldsymbol{E}_{\mathrm{short},\,\mu}(i_\mu)\right) \right)^{*} \mathrm{d}S. \tag{5.63}$$

This integration is separated into four different power terms, which cover the open circuit self- and mutual radiation, the open- to short circuit mutual radiation, the

short- to open circuit mutual radiation, and the short circuit self- and mutual radiation according to

$$\begin{aligned} P =& \frac{1}{2\eta_0} \oiint_S \left(\sum_{n=1}^{N} \sum_{\nu=1}^{N} \left(\boldsymbol{E}_{\text{open},\,n}(u_n) \ \cdot \boldsymbol{E}^*_{\text{open},\,\nu}(u_\nu) \right) \right) \mathrm{d}S \\ &+ \frac{1}{2\eta_0} \oiint_S \left(\sum_{n=1}^{N} \sum_{\mu=1}^{M} \left(\boldsymbol{E}_{\text{open},\,n}(u_n) \ \cdot \boldsymbol{E}^*_{\text{short},\,\mu}(i_\mu) \right) \right) \mathrm{d}S \\ &+ \frac{1}{2\eta_0} \oiint_S \left(\sum_{m=1}^{M} \sum_{\nu=1}^{N} \left(\boldsymbol{E}_{\text{short},\,m}(i_m) \cdot \boldsymbol{E}^*_{\text{open},\,\nu}(u_\nu) \right) \right) \mathrm{d}S \\ &+ \frac{1}{2\eta_0} \oiint_S \left(\sum_{m=1}^{M} \sum_{\mu=1}^{M} \left(\boldsymbol{E}_{\text{short},\,m}(i_m) \cdot \boldsymbol{E}^*_{\text{short},\,\mu}(i_\mu) \right) \right) \mathrm{d}S. \end{aligned} \tag{5.64}$$

Each of the summands is now considered a single power contribution. To distinguish these power terms, the superscripts O and S will indicate coupling between open and short. These terms are compared to a circuit representation of the respective power contributions, using either a conductance G, a complex coupling factor K or $\tilde{K}$, or a resistance R, yielding

$$P^{\mathrm{O,O}}_{n,\,\nu} = \Re\left\{ \frac{1}{2\eta_0} \oiint_S \left(\boldsymbol{E}_{\text{open},\,n}(u_n) \cdot \boldsymbol{E}^*_{\text{open},\,\nu}(u_\nu) \right) \mathrm{d}S \right\} = \frac{G_{n,\,\nu}}{2} \Re\left\{ u_n \, u^*_\nu \right\}, \tag{5.65}$$

$$P^{\mathrm{O,S}}_{n,\,\mu} = \Re\left\{ \frac{1}{2\eta_0} \oiint_S \left(\boldsymbol{E}_{\text{open},\,n}(u_n) \cdot \boldsymbol{E}^*_{\text{short},\,\mu}(i_\mu) \right) \mathrm{d}S \right\} = \Re\left\{ \frac{K_{n,\,\mu}}{2} u_n \, i^*_\mu \right\}, \tag{5.66}$$

$$P^{\mathrm{S,O}}_{m,\,\nu} = \Re\left\{ \frac{1}{2\eta_0} \oiint_S \left(\boldsymbol{E}_{\text{short},\,m}(i_m) \cdot \boldsymbol{E}^*_{\text{open},\,\nu}(u_\nu) \right) \mathrm{d}S \right\} = \Re\left\{ \frac{\tilde{K}_{m,\,\nu}}{2} i_m \, u^*_\nu \right\}, \tag{5.67}$$

$$P^{\mathrm{S,S}}_{m,\,\mu} = \Re\left\{ \frac{1}{2\eta_0} \oiint_S \left(\boldsymbol{E}_{\text{short},\,m}(i_m) \cdot \boldsymbol{E}^*_{\text{short},\,\mu}(i_\mu) \right) \mathrm{d}S \right\} = \frac{R_{m,\,\mu}}{2} \Re\left\{ i_m \, i^*_\mu \right\}. \tag{5.68}$$

The total radiated power is thus accessible by multiplying the voltage- and current-vectors $\boldsymbol{u}$, $\boldsymbol{i}$ with coupling matrices $[\boldsymbol{G}] \in \mathbb{R}^{N\times N}$, $[\boldsymbol{K}] \in \mathbb{C}^{N\times M}$, $[\tilde{\mathbf{K}}] \in \mathbb{C}^{M\times N}$, and $[\boldsymbol{R}] \in \mathbb{R}^{M\times M}$ with

$$P_{\text{rad}} = \frac{1}{2} \Re\Big\{ \boldsymbol{u}^{\mathsf{T}} \cdot ([\boldsymbol{G}] \cdot \boldsymbol{u}^*) + \boldsymbol{u}^{\mathsf{T}} \cdot ([\boldsymbol{K}] \cdot \boldsymbol{i}^*) + \boldsymbol{i}^{\mathsf{T}} \cdot \left([\tilde{\mathbf{K}}] \cdot \boldsymbol{u}^* \right) + \boldsymbol{i}^{\mathsf{T}} \cdot ([\boldsymbol{R}] \cdot \boldsymbol{i}^*) \Big\}, \tag{5.69}$$

where $\boldsymbol{i}^*$ indicates the complex conjugate of $\boldsymbol{i}$ and $\boldsymbol{u}^{\mathsf{T}}$ is the transposed vector $\boldsymbol{u}$ without complex conjugation. Comparing each radiated power with the exciting voltages or currents in (5.65)-(5.68) yields the definition of each coupling element $G_{n,\,m}$, $K_{n,\,m}$,

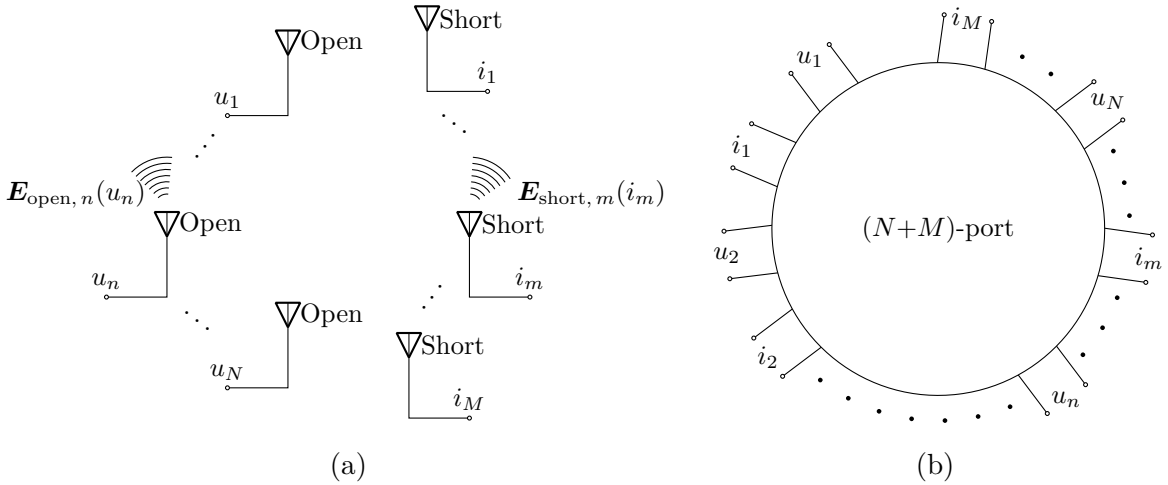

Figure 5.17.: Coupling between N open and M short radiators (a) fed by sources of strength u_n and i_m, respectively, and (b) corresponding $(N{+}M)$-port network model.

$\tilde{K}_{n,\,m}$, and $R_{n,\,m}$, which are presented below in (5.74)-(5.78). The matrices $[\boldsymbol{G}]$, $[\boldsymbol{K}]$, $[\tilde{\boldsymbol{K}}]$, and $[\boldsymbol{R}]$ are constructed by calculating these coupling elements. Since the electric far fields for open- and short circuits have been defined above, the integration can be carried out numerically. The resulting matrix equation defines a linear network, which accesses the radiated power. It can be realized by circuit elements using controlled sources, for example, current-controlled current sources for the coupling from short to open circuits or voltage-controlled current sources for open-to-open coupling. The mutual conductance is in full accordance with the result from [167], which has been used to describe the coupling of open-circuited MSLs. The coupling conductance, coupling factor, or coupling resistance depends on the type of source, which can be open and short circuit, the distance between the sources, namely offset in the x- and y-directions, and the orientation of sources, typically involving a rotation around the z-axis by 0 or π. These factors will be normalized [151, pp. 179] using the self-conductance $G_{n,\,n}$ or resistance $R_{n,\,n}$ of the utilized source type to ease the interpretation. The normalized coupling coefficients $g_{n,\,m}$, $k_{n,\,m}$, $\tilde{k}_{n,\,m}$, and $r_{n,\,m}$ are denoted using lowercase letters, yielding

$$G_{n,\,m} = g_{n,\,m}\sqrt{G_{n,\,n}\,G_{m,\,m}}, \tag{5.70}$$

$$K_{n,\,m} = k_{n,\,m}\sqrt{R_{n,\,n}\,G_{m,\,m}}, \tag{5.71}$$

$$\tilde{K}_{n,\,m} = \tilde{k}_{n,\,m}\sqrt{G_{n,\,n}\,R_{m,\,m}}, \tag{5.72}$$

$$R_{n,\,m} = r_{n,\,m}\sqrt{R_{n,\,n}\,R_{m,\,m}}. \tag{5.73}$$

These normalized coupling coefficients are evaluated for different offsets Δx along the longitudinal direction of the MSL and $\Delta y = 0$ and are depicted in Fig. 5.18. Here,

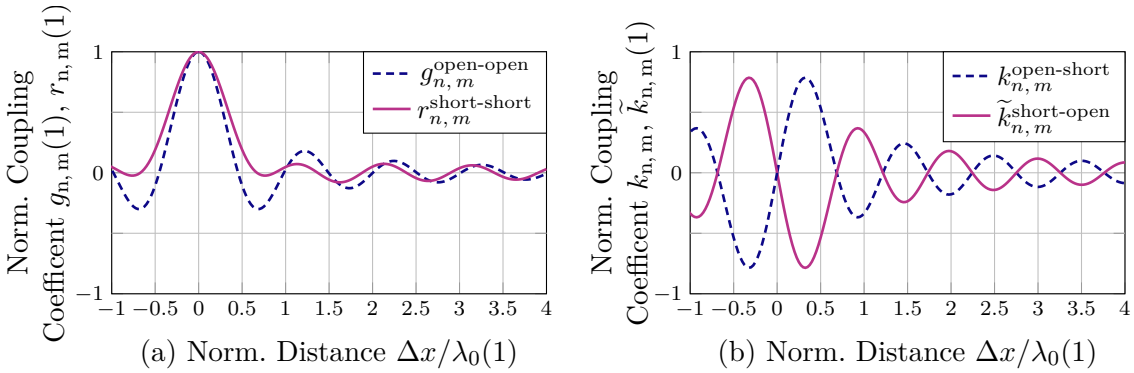

(a) Norm. Distance $\Delta x/\lambda_0(1)$ (b) Norm. Distance $\Delta x/\lambda_0(1)$

Figure 5.18.: Normalized mutual coupling coefficients (a) between two open or short circuits at normalized distance d/λ_0 and (b) between short- and open circuits and vice versa. A substrate of $h = 10\,\mu$m height, relative permittivity $\varepsilon_r = 4.1$, and a frequency of 300 GHz are assumed in all cases.

a relative permittivity $\varepsilon_r = 4.1$, a frequency of 300 GHz, and a dielectric height of $h = 10\,\mu$m are assumed. Whereas, as expected, the envelope of the coupling coefficients decreases for increasing source distance, the zeros and local maxima of the coupling coefficients show interference effects, which result from in- and out-of-phase coupling. It is evident from Fig. 5.18 (b) that open and short circuits are inherently decoupled if colocated, meaning that their far fields are orthogonal since the coupling factors $k_{n,m}$ and $\tilde{k}_{n,m}$ are zero for $\Delta x = 0$. This orthogonality also explains the vanishing integral in (5.58), which correlated the open- and short circuits' far fields. Furthermore, $k_{n,m}(x) = -k_{m,n}(-x)$ and $\tilde{k}_{n,m}(x) = -\tilde{k}_{m,n}(-x)$ follow from the odd symmetry of the short circuit's radiation pattern. For other source fields, for example, when considering the vertical current caused by the via of the short circuit, $k_{n,m}$ and $\tilde{k}_{n,m}$ might be complex-valued, and the simple $k_{n,m}(x) = -\tilde{k}_{m,n}(x)$ symmetry seen in Fig. 5.18 (b) might not hold.

Coupling between two terminated MSLs

To illustrate the previous derivation, the coupling between two terminated MSLs will be discussed with a corresponding circuit model. The geometry of two MSLs with the relative offsets Δx and Δy in the x- and y-direction is depicted in Figs. 5.19 (a) and (b). As arbitrary loads, two termination impedances $Z_{L,1/2}$ are used here; however, any other termination or connection of the MSLs can also be modeled in the circuit. The characteristic impedances of the MSLs are denoted by $Z_{C,1/2}$. Fig. 5.19 (c) shows the corresponding EC model with the self-radiation conductance $G_{i,i}$ and resistance $R_{i,i}$ of the open and short circuit, as defined in Sections 5.3.1 and 5.3.2. The mutual coupling conductance $G_{i,j}$, resistance $R_{i,j}$, and factors $K_{i,j}$ and $\tilde{K}_{i,j}$ with $i \neq j$ will be calculated in the following.

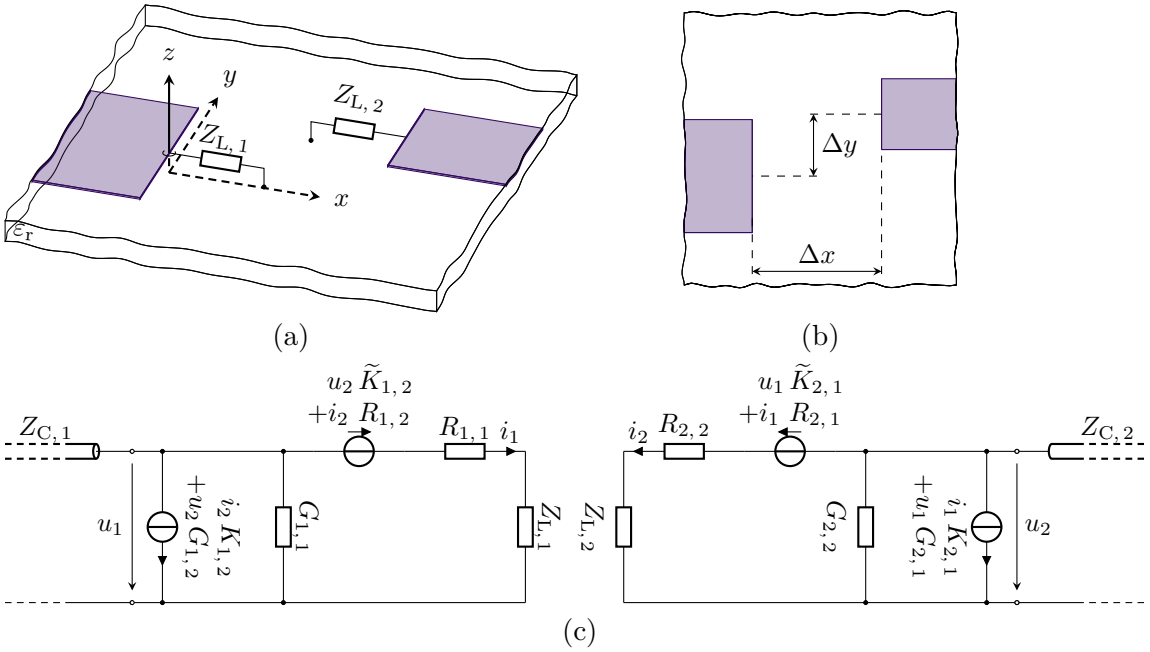

Figure 5.19.: Geometry of two terminated MSLs with the termination impedances $Z_{\mathrm{L},\,i}$ and an offset in x- and y-direction in (a) perspective view and (b) top view. The corresponding equivalent circuit model is given in (c).

It is assumed that the electric far fields of the open and short circuit are accessible, i.e., $\boldsymbol{E}_{\mathrm{open}}(r,\theta,\varphi)$ and $\boldsymbol{E}_{\mathrm{short}}(r,\theta,\varphi)$ are known for excitation strengths u_0 and i_0, and that the radiation conductances $G_{1,\,1} = G^{\mathrm{rad}}_{\mathrm{open}}|_{Z_{\mathrm{C},\,1}}$ and $G_{2,\,2} = G^{\mathrm{rad}}_{\mathrm{open}}|_{Z_{\mathrm{C},\,2}}$ or resistances $R_{1,\,1} = R^{\mathrm{rad}}_{\mathrm{short}}|_{Z_{\mathrm{C},\,1}}$ and $R_{2,\,2} = R^{\mathrm{rad}}_{\mathrm{short}}|_{Z_{\mathrm{C},\,2}}$ for the standalone radiation sources have been determined. Here, the first source is considered the left-hand side MSL located at the origin, and the second source is displaced and rotated by π, resulting in an inverted electric field strength. The mutual conductance is then calculated based on (5.65) by

$$G_{1,\,2} = \frac{\int_0^{2\pi}\int_0^{\pi/2} \boldsymbol{E}_{\mathrm{open}}(r,\theta,\varphi)\cdot\left(-\boldsymbol{E}_{\mathrm{open}}(r,\theta,\varphi)\,t(\theta,\varphi,\Delta x,\Delta y)\right)^*\, r^2\sin\theta\,\mathrm{d}\theta\,\mathrm{d}\varphi}{\eta_0|u_0|^2} \tag{5.74}$$

with a source translation in the far field described by

$$t(\theta,\varphi,\Delta x,\Delta y) = \exp[\mathrm{j}k_0\left(\Delta x\cos\varphi\,\sin\theta + \Delta y\sin\varphi\,\sin\theta\right)]\,, \tag{5.75}$$

using a large radius r or even the limit $r\to\infty$. Accordingly, the mutual coupling

factors and mutual resistance can be calculated using (5.66)-(5.68)

$$K_{1,2} = \frac{\int_0^{2\pi}\int_0^{\pi/2} \boldsymbol{E}_{\text{open}}(r,\theta,\varphi)\cdot\left(-\boldsymbol{E}_{\text{short}}(r,\theta,\varphi)\,t(\theta,\varphi,\Delta x,\Delta y)\right)^{*} r^2\sin\theta\,\mathrm{d}\theta\,\mathrm{d}\varphi}{\eta_0\,u_0\,i_0^{*}}, \quad (5.76)$$

$$\tilde{K}_{1,2} = \frac{\int_0^{2\pi}\int_0^{\pi/2} \boldsymbol{E}_{\text{short}}(r,\theta,\varphi)\cdot\left(-\boldsymbol{E}_{\text{open}}(r,\theta,\varphi)\,t(\theta,\varphi,\Delta x,\Delta y)\right)^{*} r^2\sin\theta\,\mathrm{d}\theta\,\mathrm{d}\varphi}{\eta_0\,u_0\,i_0^{*}}, \quad (5.77)$$

$$R_{1,2} = \frac{\int_0^{2\pi}\int_0^{\pi/2} \boldsymbol{E}_{\text{short}}(r,\theta,\varphi)\cdot\left(-\boldsymbol{E}_{\text{short}}(r,\theta,\varphi)\,t(\theta,\varphi,\Delta x,\Delta y)\right)^{*} r^2\sin\theta\,\mathrm{d}\theta\,\mathrm{d}\varphi}{\eta_0|i_0|^2}. \quad (5.78)$$

By the reciprocity of linear radiators in linear media [151, pp. 94], $G_{m,n} = G_{n,m}$ and $R_{m,n} = R_{n,m}$ hold. Since the open- and short radiation show an even- and odd radiation pattern, $k_{n,m}(x) = -k_{n,m}(-x) = -\tilde{k}_{n,m}(x)$ holds (cf. Fig. 5.18). Last, since all normalized coefficients fulfill $|g_{n,m}| \leq 1$, $|r_{n,m}| \leq 1$, $|k_{n,m}| \leq 1$, and $|\tilde{k}_{n,m}| \leq 1$, the radiated power can naturally not fall below zero. The radiation is included in the circuit simulation using the derived elements, as depicted in Fig. 5.19 (c), and the total radiated power of these coupled lines is calculated by evaluating (5.69). If more radiators are included, calculating more coupling elements and expanding the circuit representation is straightforward.

5.3.5. Microstrip Gap Discontinuity

The radiation properties of a microstrip gap are thoroughly defined by the previous Section 5.3.4, which covers arbitrarily coupled discontinuities in MSLs. However, as the gap is one of the key enhancements used to increase the radiation efficiency of on-chip antennas, a few typically usable simplifications will be discussed shortly, as they might ease the physical insight.

The specific gap geometry, e.g., interdigital or Metal Insulator Metal (MIM) structures, will be considered by the equivalent electrostatic capacitance C_{gap}. Various geometries could implement this capacitance (cf. Chapter. 6), and it will be shown that the radiation of the gap can be modeled independently from the geometry used. For a simple edge-coupled MSL, MoM-based numerical solutions exist [169], [180] besides empirically fitted formulations [170], [181]. To obtain physical insight into the radiation mechanism, this section presents two complementary approaches to describe the microstrip gap, starting with a very intuitive model using a series EC. As a second approach, the coupling model from the previous section will be simplified to ease the insight while maintaining high accuracy.

Series EC Model

A straightforward model for the gap radiation relates the voltage along the gap to the radiated power using a series conductance, as presented in [A182]. This model assumes an infinite length of the transmission line at the left- and right-hand side of the gap and thus neglects both the TL-based coupling to the remaining antenna as well as the field-coupling to the other radiators. Consequently, it is only a first-order approximation. Although a model with frequency-independent circuit elements is conceivably possible [179], the circuit elements will be determined with an explicit frequency dependence to ease the physical understanding. An even-odd analysis will demonstrate that only the odd excitation of the gap yields radiation, and this radiation is accessible from the results of the open-circuited MSL in Section 5.3.1. An exemplary current density and electric-field strength along the microstrip gap are depicted in Fig. 5.20 (a) and (b) for the even and odd mode excitation, respectively. The phase of the input currents i_1 and i_2 at the two-port of the gap is observed to determine the terms even and odd. Here, an in-phase excitation with $i_1 = i_2$ indicates the even case, and the opposing $i_1 = -i_2$ renders the odd excitation. Considering the even mode, the discontinuity is barely recognizable since the currents and voltages naturally extend, practically unhindered, along the gap. No radiation contribution is expected in this case, as the discontinuity is practically invisible in the current and voltage distribution. This behavior is consistent with the proposed series EC model since a voltage $|u_{\mathrm{gap}}| \approx 0$ along the gap dissipates no power in a series radiation conductance. In contrast, for the odd mode, the electric field changes rapidly along the gap, yielding a large voltage $|u_{\mathrm{gap}}|$ and thus radiation modeled by the radiation conductance in series.

To investigate the odd excitation, a PEC symmetry plane is assumed in the center of the gap, and the excitation from the left-hand side will be found as an image-current on the right-hand side, as shown in Fig. 5.21. Here, the incident feed current i^{+}_{open} separates

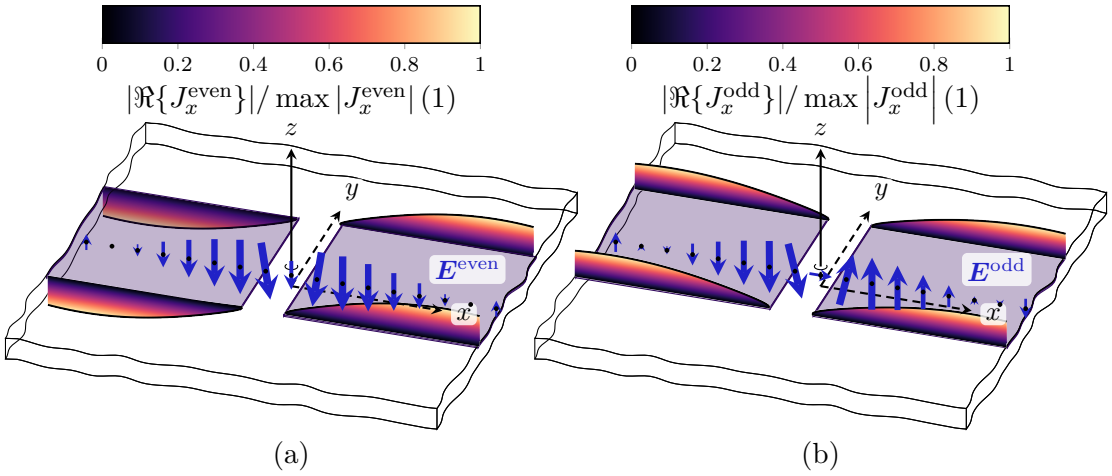

Figure 5.20.: Electric field vector $\boldsymbol{E}$ and current density x-component J_x on the MSL gap for (a) the even excitation and (b) the odd excitation.

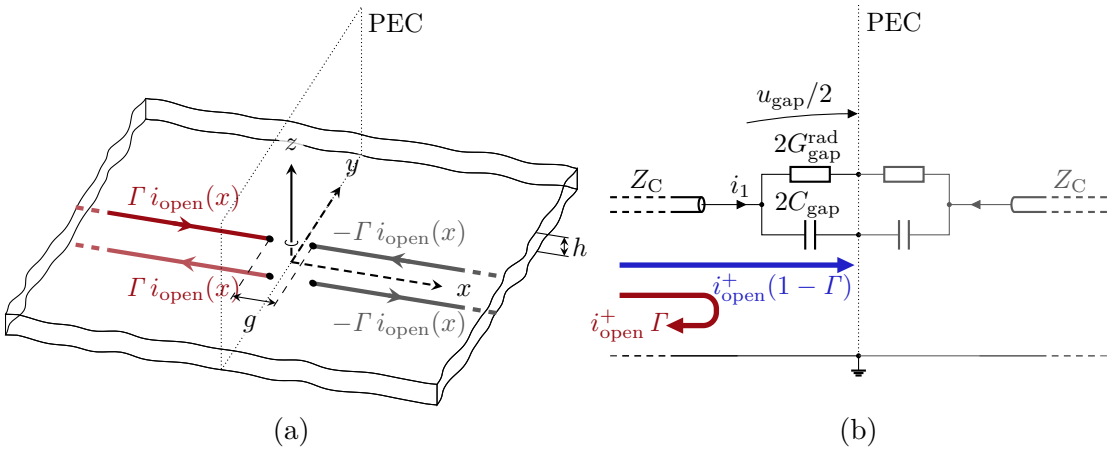

Figure 5.21.: Line currents for the odd excitation (a) in perspective view and (b) as EC representation of a generic capacitive gap in an MSL. The symmetry plane is replaced by a PEC to model the odd excitation.

into a reflected current $\Gamma\, i^+_{\mathrm{open}}$ and a current through the gap $i_1 = (1-\Gamma)\, i^+_{\mathrm{open}}$, where the voltage reflection factor

$$\Gamma = \frac{Z_{\mathrm{in}} - Z_{\mathrm{C}}}{Z_{\mathrm{in}} + Z_{\mathrm{C}}} = \frac{Z_{\mathrm{gap}}/2 - Z_{\mathrm{C}}}{Z_{\mathrm{gap}}/2 + Z_{\mathrm{C}}} \tag{5.79}$$

with $Z_{\mathrm{gap}} = (G_{\mathrm{rad}} + \mathrm{j}\omega C_{\mathrm{gap}})^{-1}$ is used. As discussed in [173], the current through the discontinuity does not radiate for the same reason an undisturbed MSL does not radiate. However, the reflected current $\Gamma\, i^+_{\mathrm{open}}$ yields the radiation of the open-circuited MSL weighted with the factor Γ^2. The total radiated power can be accessed by integrating the far field of the open circuit $E_{\theta,\,\mathrm{open}}$ weighted with its image from the PEC by $2\cos(\cos\varphi\, \sin\theta\, k_0 g/2)$ yielding

$$P^{\mathrm{rad}}_{\mathrm{gap}} = \frac{1}{2\eta_0} \int_{\pi/2}^{3\pi/2} \int_{0}^{\pi/2} |\Gamma|^2 \left| E_{\theta,\,\mathrm{open}}\, 2\cos\left(\cos\varphi\, \sin\theta\, k_0 \frac{g}{2}\right)\right|^2 |\boldsymbol{r}|^2 \sin\theta\, \mathrm{d}\theta\, \mathrm{d}\varphi. \tag{5.80}$$

For small gaps, the field approaches $2E_{\theta,\,\mathrm{open}}$, the integration domain along θ is halved due to the PEC, and the radiated power can be related to the radiated power of the open by

$$P^{\mathrm{rad}}_{\mathrm{gap}} = 2|\Gamma|^2\, P^{\mathrm{rad}}_{\mathrm{open}}, \tag{5.81}$$

where $P^{\mathrm{open}}_{\mathrm{rad}}$ is given for the dielectric case by (5.42). The radiated power can be related

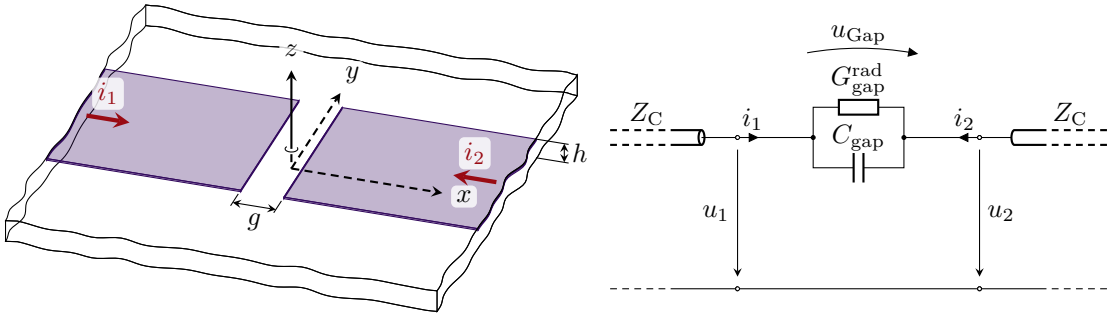

(a) (b)

Figure 5.22.: Geometry of (a) the gap in perspective view and (b) the series EC model of a generic capacitive gap in an MSL.

to the voltage across the gap $u_{\mathrm{gap}} = (1-\Gamma)\, i^{+}_{\mathrm{open}}\, Z_{\mathrm{gap}}$ defining

$$\begin{aligned} 2G^{\mathrm{rad}}_{\mathrm{gap}} = \frac{2\,P^{\mathrm{rad}}_{\mathrm{gap}}}{|u_{\mathrm{gap}}/2|^2} &= \frac{2\,(2|\Gamma|^2\,P^{\mathrm{rad}}_{\mathrm{open}})}{|(1-\Gamma)\,i^{+}_{\mathrm{open}}\,Z_{\mathrm{gap}}/2|^2}\,\frac{|2\,Z_{\mathrm{C}}|^2}{|2\,Z_{\mathrm{C}}|^2} \\ &= \frac{2\;P^{\mathrm{rad}}_{\mathrm{open}}}{|2\,^{+}_{\mathrm{open}}\,Z_{\mathrm{C}}|^2}\,\frac{2|\Gamma|^2\,|2Z_{\mathrm{C}}|^2}{|Z_{\mathrm{gap}}/2|^2\,|1-\Gamma|^2} \\ &= G^{\mathrm{rad}}_{\mathrm{open}}\,\frac{2|\Gamma|^2\,|2Z_{\mathrm{C}}|^2}{|Z_{\mathrm{gap}}/2|^2\,|1-\Gamma|^2} \\ &= G^{\mathrm{rad}}_{\mathrm{open}}\,\frac{2|Z_{\mathrm{gap}}/2 - Z_{\mathrm{C}}|^2}{|Z_{\mathrm{gap}}/2|^2}. \end{aligned} \tag{5.82}$$

If the capacitance C_{gap} dominates the radiation conductance, the radiation conductance can be approximated by inserting $Z_{\mathrm{gap}} = (\mathrm{j}\omega\, C_{\mathrm{gap}})^{-1}$, resulting in

$$G^{\mathrm{rad}}_{\mathrm{gap}} \approx G^{\mathrm{rad}}_{\mathrm{open}}\,\left(1 + (2\omega C_{\mathrm{gap}}\,Z_{\mathrm{C}})^2\right), \tag{5.83}$$

which is also depicted in an equivalent circuit representation in Fig. 5.22. It needs to be highlighted that several assumptions yielded this circuit. First, the gap is terminated by an infinite TL of characteristic impedance Z_{C}, which neglects the influence of any other neighboring elements on the current distribution of the antenna. This termination directly influences the gap voltage u_{gap}, which has been used to relate the radiated power to the radiation conductance. Second, field coupling to other gaps via substrate or air is not considered, which means the error increases for more and closer collocated gaps. The general result, however, is in full accordance with the approximation given in [A182], which has been derived for large discontinuities, implying small gap capacitances, yielding

$$G^{\mathrm{rad}}_{\mathrm{gap}} \approx G^{\mathrm{rad}}_{\mathrm{open}} \quad \text{for } (\omega C_{\mathrm{gap}})^{-1} \gg Z_{\mathrm{C}}.$$

This result is remarkable since the discontinuity of the current introduced by the gap yields the radiation. In this first-order approximation, the radiation depends only on the voltage and the feeding MSL; it is independent of the gap topology and the resulting gap capacitance.

Reduced Coupling Model

Whereas the previous model only considered the coupling between the directly neighboring open circuits constructing the gap, a more general model would include the coupling between all radiating elements into the circuit representation, as discussed in Section 5.3.4. The typically used capacitive discontinuities represent a large impedance compared to the characteristic impedance of the MSL, i.e. $(\omega C_{\mathrm{gap}})^{-1} \gg Z_{\mathrm{C}}$. Thus, the voltage-driven radiation contribution of the conductance associated with the open-circuit radiation substantially exceeds the current-driven radiation contribution of the short circuit, represented by the radiation resistance. Furthermore, since the current is continuous in the gap, the radiation contributions from the left- and right-hand side short will cancel out. This effect is entirely included in the coupling model of Section 5.3.4, where the mutual radiation resistances would cancel the self-radiation resistances. Since the effect cancels out either way, there is no benefit in including it in the circuit, as it generally increases complexity for both interpreting the circuit and solving it using a circuit simulator. When leaving out all radiation resistances associated with short circuit radiation, the coupling with these elements can also be left

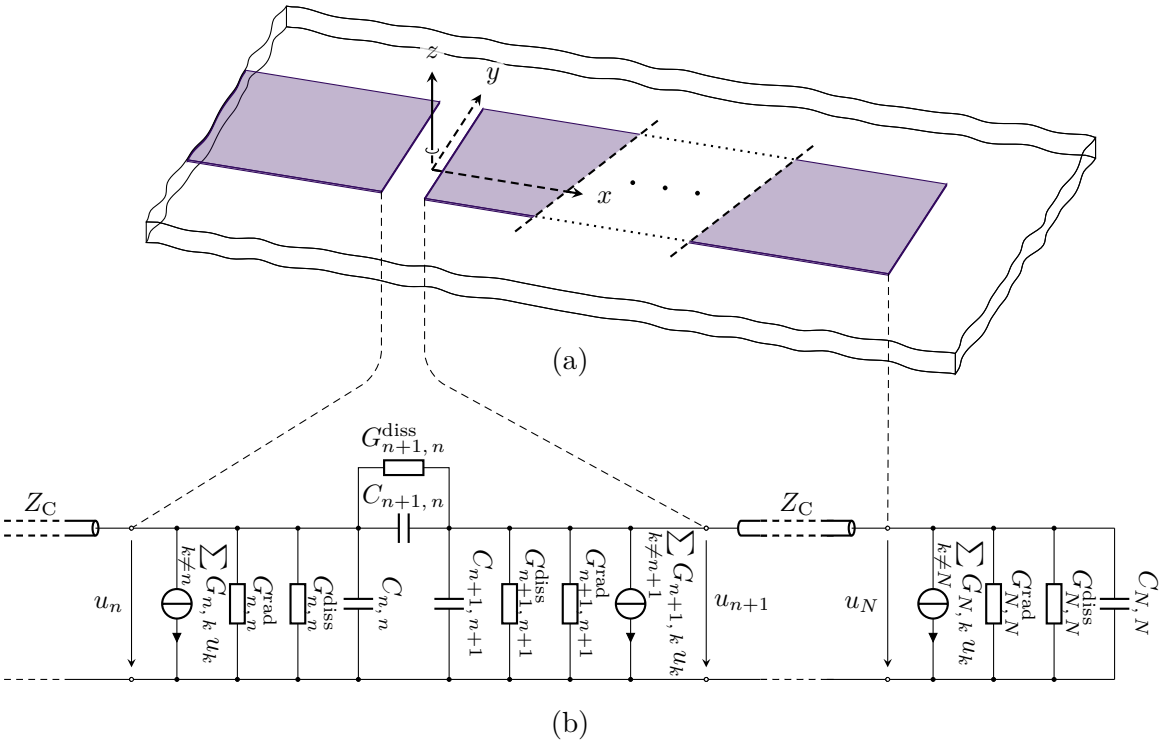

Figure 5.23.: Antenna geometry (a) with gap and end radiation and (b) reduced coupling model of the gap considering the mutual coupling between different radiators utilizing the mutual conductances $G_{m,\,n}$.

out, and the radiated power is evaluated after simplifying (5.69)

$$P_{\mathrm{tot}} = \frac{1}{2}\Re\left\{\sum_{n=1}^{N} u_n i_n^*\right\} = \frac{1}{2}\Re\left\{\boldsymbol{u}^{\mathsf{T}} \cdot ([\boldsymbol{G}] \cdot \boldsymbol{u}^*)\right\}. \tag{5.84}$$

The n-th current due to mutual coupling considers the coupling between multiple discontinuities using the matrix elements according to (5.65). It is included by

$$i_{n,\,\mathrm{mut}} = \sum_{k \neq n} G_{n,\,k}\, u_k, \tag{5.85}$$

which can be directly included in an EC representation using voltage-controlled current sources, as shown in Fig. 5.23. Here, an exemplary gap and an open circuit are explicitly shown – all other gaps are included in the circuit accordingly. The reactive and dissipative elements characterizing the gap and open end are also included. In the sum over $k \neq n$ for the n-th radiator, the mutual current contributions from all other radiators are conveniently considered. This means the element's coupling is considered as a current fed into the circuit and as an additive or subtractive radiation contribution.

5.3.6. Microstrip Step Discontinuity

As for the microstrip gap discussed above, the discontinuity resulting from a change in microstrip width will be discussed here shortly. Again, the general model for arbitrarily terminated MSLs also holds here, but it can be simplified without losing accuracy. Figs. 5.24 (a) and (b) show an abrupt change in microstrip width from w_1 to w_2. A continuous tapered line is well approximated by cascading sufficiently small steps, incrementally in- or decreasing the overall MSL width [141, pp. 261]. The general EC model considering the radiation contributions of open- and short-circuited lines (cf. Section 5.3.4) is depicted in Fig. 5.24 (c). Here, only a single discontinuity is considered due to a change in MSL width. If more discontinuities occur within the structure, their effect must be included in the controlled voltage- and current sources, as shown above for the capacitive gaps. As the width change naturally occurs at the same location, the corresponding coupling conductances, resistances, and factors are evaluated for a normalized distance $\Delta x = 0$ (cf. Fig. 5.18). The radiation resistances associated with the short circuit are independent of the MSL width and thus identical for the left- and right-hand side ($R_{1,\,1} = R_{2,\,2}$, $R_{1,\,2} = R_{2,\,1}$). The anti-phase currents $i_1 = -i_2$ thus cancel the short circuit radiation contributions. Furthermore, the coupling factors are $K_{1,\,2} = K_{2,\,1} = \tilde{K}_{1,\,2} = \tilde{K}_{2,\,1} = 0$ for $\Delta x = 0$, which results from the orthogonality of open- and short-circuit radiation. Thus the change in MSL width can be modeled using only the (mutual) radiation conductances of the open circuits, as depicted in Fig. 5.24 (d). The coupling to more width steps or gap discontinuities in the MSL is straightforward and has been explained for gaps in the previous section.

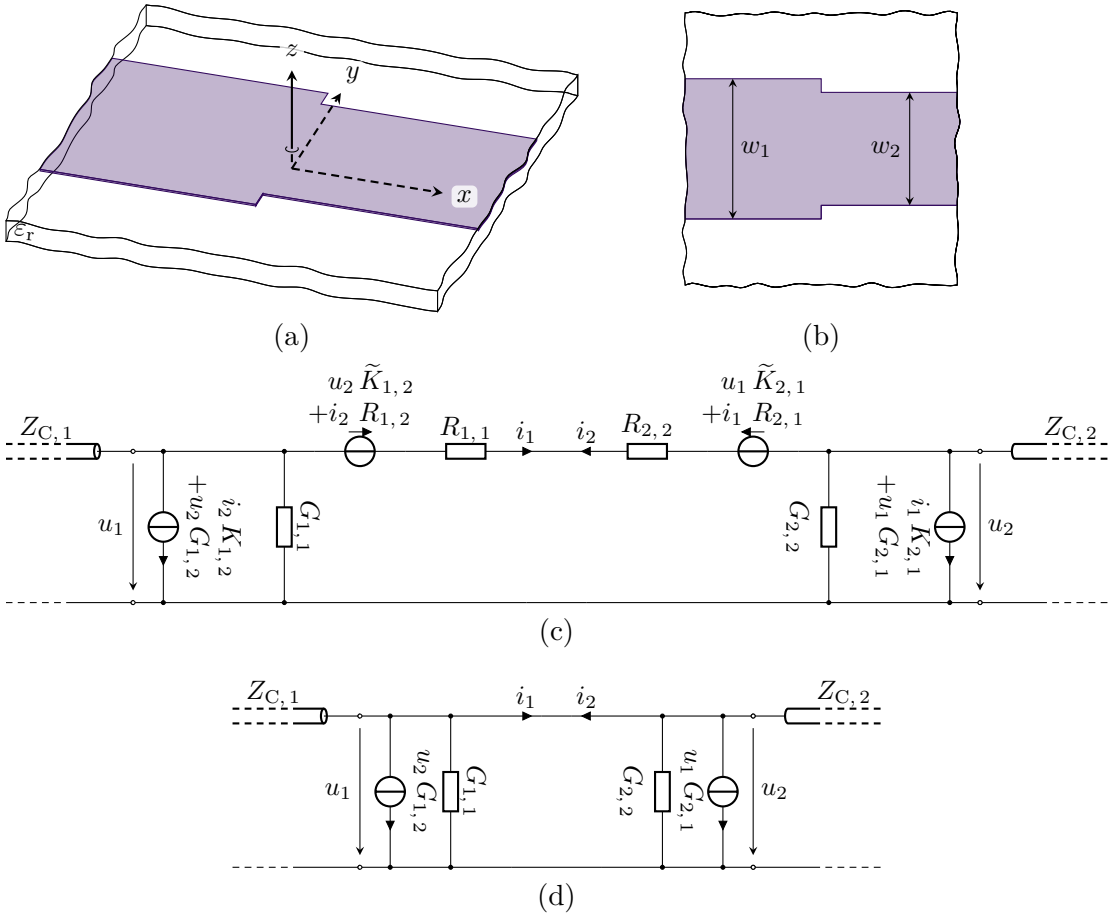

Figure 5.24.: Geometry of the MSL step discontinuity in (a) perspective and (b) top view, (c) its full EC model utilizing the results from the arbitrarily terminated MSLs, and (d) the simplified model.

5.4. Circuit Simulation

Different circuit-simulation approaches will be discussed to investigate the antenna parameters based on the above EC models. Whereas the most general description of the circuit using a netlist will work for any circuit, tailored solution approaches for different circuit layouts might reduce computation time. The results of the different models are later compared to full-wave Finite Difference Time Domain (FDTD) results in Chapter 6.

5.4.1. Cascade Matrix Method

The series EC presented in Section 5.3.5 essentially consists of cascaded two-ports, which are conveniently described using *ABCD* matrices, as given by (5.8)-(5.10), and

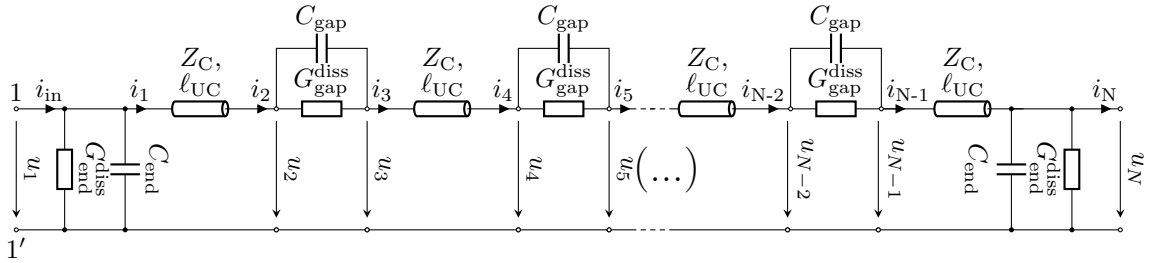

Figure 5.25.: Series EC for the cascade matrix method. The voltages and currents used for calculating the power are marked. A corresponding antenna geometry is depicted in Fig. 5.3 (a).

for other typical two-ports impedances in [141, p. 190]. The *ABCD* matrices enable a simple calculation of the input impedance, which can be directly accessed using

$$Z_{\mathrm{in}} = \frac{A_{\mathrm{tot}}}{C_{\mathrm{tot}}} \tag{5.86}$$

with

$$\begin{aligned}[\boldsymbol{ABCD}]_{\mathrm{tot}} &= \begin{bmatrix} A_{\mathrm{tot}} & B_{\mathrm{tot}} \\ C_{\mathrm{tot}} & D_{\mathrm{tot}} \end{bmatrix} \\ &= [\boldsymbol{ABCD}]_{\mathrm{end}} \cdot [\boldsymbol{ABCD}]_{\mathrm{TL}} \cdot [\boldsymbol{ABCD}]_{\mathrm{gap}} \cdot \cdots\cdots \cdot [\boldsymbol{ABCD}]_{\mathrm{end}}\,,\end{aligned} \tag{5.87}$$

where the total *ABCD* matrix of the antenna is calculated by cascading the corresponding two-ports in the order of the geometrical arrangement in the antenna. An EC representation utilizing the series conductance model of the gap is given in Fig. 5.25. For accessing the radiated or dissipated power, the input vector of the last *ABCD* element is defined according to the antenna termination as $(u_{\mathrm{term}}, u_{\mathrm{term}}/Z_{\mathrm{term}})^{\mathsf{T}}$, where u_{term} is an arbitrary voltage. The resulting vector would read $(u_{\mathrm{term}}, 0)$ for the typical open circuit, and the output vector of the last *ABCD* element becomes the input vector of the second last *ABCD* matrix. By continuing this process up to the first *ABCD* matrix, the input voltage and current, which can be used to calculate the accepted power and the current- and voltage-vector at each *ABCD* matrix, are known. Since the fundamental *ABCD* matrices are simple networks, assigning dissipated and radiated powers to the elements within the *ABCD* subcell with the given input and output voltage and current is straightforward. By comparing radiated to accepted power, the radiation efficiency can be calculated. Since this method does not require any matrix inversions but evaluates each circuit section after another, the complexity is $\in \mathcal{O}(n_{\mathrm{f}} \cdot n_{\mathrm{mat}})$, and the evaluation of $n_{\mathrm{f}} = 1000$ frequency points of a typical antenna described by $n_{\mathrm{mat}} = 11$ *ABCD* matrices considered in this thesis (cf. Section 6.1) takes $\approx 3\,\mathrm{s}$ or $3\,\mathrm{ms}$ per frequency point. The simplicity of the network limits the accuracy of the resulting radiation efficiency estimation since the mutual coupling between the discontinuities is not considered.

5.4.2. Netlist Evaluation with SPICE

To include the mutual coupling for open- and short circuits, the EC models including the mutual coupling are converted into a Simulation Program with Integrated Circuit Emphasis (SPICE)-compatible netlist. SPICE and its derivatives became quasi-standard in integrated circuit analysis after its initial development in the 1970s [183]. Although the netlist for the antenna consists of only linear circuit elements, the capabilities of SPICE and its successors allow even for the connection to a non-linear frontend. The transmission lines are modeled by T-equivalent circuits representing each a $10\,\mu$m section, and the netlists are written for a single frequency to allow for the arbitrary frequency dependence, which occurs when handling the mutual conductances of the fundamental radiators. By monitoring the current through each resistance and assigning it to radiation or dissipation, the total radiated and dissipated power can be accessed and related to give the radiation efficiency. The complete EC model, including mutual conductances, coupling factors, and resistances, is expected to be the most accurate of the circuit-based antenna calculations. It represents the complete EC-based antenna model presented in this chapter and is thus considered the benchmark solution for accuracy. The evaluation of 100 frequency points of a typical antenna (cf. Section 6.1) takes $\approx 240\,$s or $2.4\,$s per frequency point, mainly caused by the increased effort due to the controlled voltage and current sources modeling the coupling between the fundamental radiators; and by the discretized TL model resulting in a large number of nodes.

5.4.3. Radiation Postprocessing

To overcome the drawbacks of both previous methods, where the series EC can be fastly evaluated on the cost of accuracy, and the full model in SPICE is very accurate but comparably slow, a hybrid method is presented in the following. For all the antennas covered in this thesis, the radiative elements have a negligible influence on the current distribution of the antenna, which is dominated by the reactive elements. Thus, the current- and voltage distribution is calculated along the antenna without considering the mutual coupling between the radiators. This calculation can be carried out based on the efficient forward solution using the $ABCD$ matrices. Whereas the dissipation contributions are calculated in this step, the radiation contributions are calculated in postprocessing. From the currents i_n and voltages u_n at the discontinuities and the conductance, coupling, and resistance matrix, the radiated power P_{rad} according to (5.69) can be calculated. Evaluating the matrix products to consider the coupling is a tremendously reduced computational effort compared to using SPICE to solve, i.e., invert, the linear system representing the circuit. It needs to be highlighted that the currents in the shunt path calculated by $[\boldsymbol{G}] \cdot \boldsymbol{u}^* + [\boldsymbol{K}] \cdot \boldsymbol{i}^*$ and the voltages in the series path by $[\tilde{\mathbf{K}}] \cdot \boldsymbol{u}^* + [\boldsymbol{R}] \cdot \boldsymbol{i}^*$ are not fed back into the circuit, which is the essential difference to the full circuit evaluation using SPICE. In the end, the radiated and total,

i.e., the sum of radiated and dissipated, powers can be compared to give the radiation efficiency.

With the presented EC model of the antenna in general and the method to describe the coupling between the discontinuities, the thorough description of the antenna prototypes using an EC model is enabled. A comparison of the different circuit evaluation methods is given in the following chapter. Furthermore, the circuit simulation results will be compared to full-wave simulation and mm-wave measurement results.

6. Antenna Prototypes

This chapter presents three antenna prototypes developed for mm-wave radar systems and compares full-wave and EC simulation results with measurements. All antennas are designed for and manufactured in the SiGe processes offered by Infineon Technologies AG and operate around 250 GHz, 300 GHz, and 400 GHz. By using an on-chip ground plane, the prototypes show frontside radiation without additional fabrication steps. The effectively utilized substrate has a thickness of approximately 10 μm and is electrically very thin, which means surface waves are neither dominantly excited from nor concentrated within the substrate.

6.1. Linear Polarized Antenna

The antenna presented in this section has been discussed in [A23] along with its series EC representation. It consists of two resonant antenna element pairs with resonance frequencies f_A and f_B chosen to enable a widened operating bandwidth compared to single resonators. The antenna elements are aligned in parallel to achieve a linear polarization and fed by a feeding network enabling the frequency selectivity in favor of the antenna element closest to its resonance. Although this antenna was intended to operate at 250 GHz, the gap capacitance was overestimated in the original design, resulting in an operation at 300 GHz. The following sections consider an improved capacitance estimation resulting in the correct modeling of the manufactured prototype, and the initial overestimation will be discussed in Section 6.4.2.

6.1.1. Design Concept

A schematic of the general feeding concept is depicted in Fig. 6.1. Here, a common feeding point divides into two pairs of branches, one connecting antenna A via a $\mathrm{TL_A}$ and one connecting antenna B correspondingly via $\mathrm{TL_B}$. A shunt resonance characterizes antennas A and B at their respective operating frequencies $f_\mathrm{A} = 290\,\mathrm{GHz}$ and $f_\mathrm{B} = 310\,\mathrm{GHz}$, corresponding to a maximized input impedance. Here, the shunt resonance results from a $\lambda/2$ standing wave current distribution along the antenna length, comparable to a microstrip patch antenna. Both $\mathrm{TL_A}$ and $\mathrm{TL_B}$ operate roughly as $\lambda/4$ transformers at the frequencies $f_\mathrm{A/B}$, which means the maximized input impedance at resonance $Z_\mathrm{A/B}$ is transformed into a minimum input impedance $\widetilde{Z}_\mathrm{A/B}$. The TLs

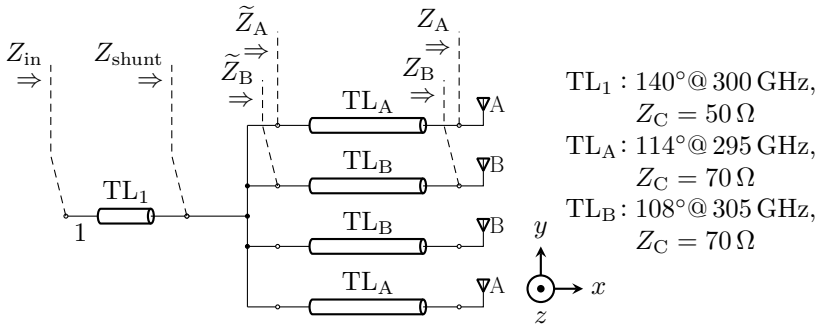

Figure 6.1.: Exemplary antenna feeding network for frequency selectivity between antennas A and B adapted from [A23]. The characteristic impedances of the TLs and their corresponding electrical lengths are also given.

are slightly too long to operate as conventional $\lambda/4$ transformers due to the shifted operating frequency, resulting in a suboptimal operation. Finally, the shunt connection of all feeding TLs will deliver most of the power into the minimal impedance, which means the antenna at resonance is favored.

6.1.2. Geometry and EC

The antenna elements A and B are geometrically highly comparable, so their general EC representation is identical. An exemplary element's geometry and its EC representation using series conductances for the radiating gaps are depicted in Fig. 6.2. Although this EC representation is the least accurate from the ones presented in Section 5.3.5, it serves as an intuitive and fast visualization of the antenna concept. Along the total antenna length of $\approx 600\,\mu$m, the current distribution at resonance approximates a sinusoidal $\lambda/2$ standing wave, which means both open-circuited terminations on the left- and right-hand side will feature a large voltage and almost zero current. The antenna consists of 5 MSL sections connected via four capacitive gaps. Strictly speaking, the MSL sections at both ends of the resonator are changed in length compared to the central MSL sections of length ℓ_0, which means this antenna is not periodic in the sense of the depicted unit cell. The slight deviation from a strict periodicity does not affect the general working principle [28, S. 79] and can be considered in the EC using the length ℓ_1. Last, the antenna depicted here is operated with a single-ended feed line; however, a differential feeding from both antenna sides is conceivably possible. A detailed drawing of the utilized capacitive gap, which uses a floating (galvanically not connected) metal layer to build up the capacitance, is depicted in Fig. 6.3. The uppermost metal layer in Infineon's B11HFC technology is aluminum, and the remaining copper layers are submerged in a SiO_2/Silicon Nitride (Si_3N_4) mixture approximated by a relative permittivity of $\varepsilon_{\text{r}} = 4.1$. The height between the top metal and the floating copper layer is referred to as h_{Float} and is not shown in the graphic for clarity. Last, the substrate height h refers to the distance between the lowermost (M1) and

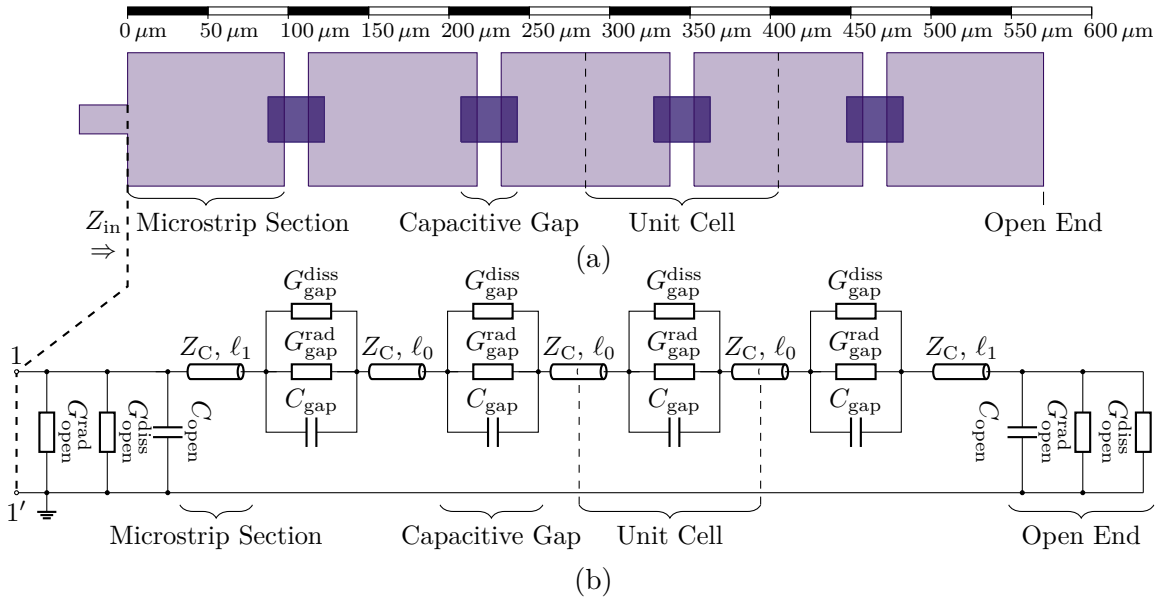

Figure 6.2.: Geometry in (a) top view and (b) corresponding EC representation of a linear polarized antenna element. The different antenna parts are marked in geometry and circuit representation for comparison.

uppermost metal layer (Alu). Furthermore, although not shown in the drawing, the top layer is submerged in the SiO_2/Si_3N_4 mixture, which means the effective permittivity of the actual structure increases compared to (3.49). All dimensions are given in Table 6.1.

In [A23], the EC parameters of Fig. 6.2 (b), including reactive, dissipative, and radiative elements, have been extracted from full-wave simulations. The procedure will be shortly summarized here, and the results will be compared to the expressions for the MSL from Section 3.4 and to the series path radiation conductances of Section 5.3. A multiport simulation is carried out to obtain EC elements from full-wave simulations, where S, Y, or Z parameters describing the coupling between the ports are extracted. The dominant, mostly reactive elements can be directly accessed from these parameters if, for example, Y-parameters combined with a shunt representation (cf. Fig. 5.7 (c)) are used and if the reference plane is shifted according to the requirements of the EC representation. When extracting the typically smaller dissipating and radiating elements, in fact, minor phase errors in $Y_{2,1}$ yield significantly inaccurate results for $G_{2,1}$. A field-based extraction has been carried out to counteract this mechanism in [A23]. Here, the dissipation within a closed volume and the radiation through its surface are evaluated numerically. Evaluating Poynting's theorem [184, pp. 10] and using the incident, reflected, and transmitted power along the feeding MSL from the full-wave simulation, the radiated and dissipated power can be accessed and related to a voltage or current, which yields the equivalent radiation conductance or resistance. The resulting EC elements for the MSL extracted from full-wave simulations in [A23]

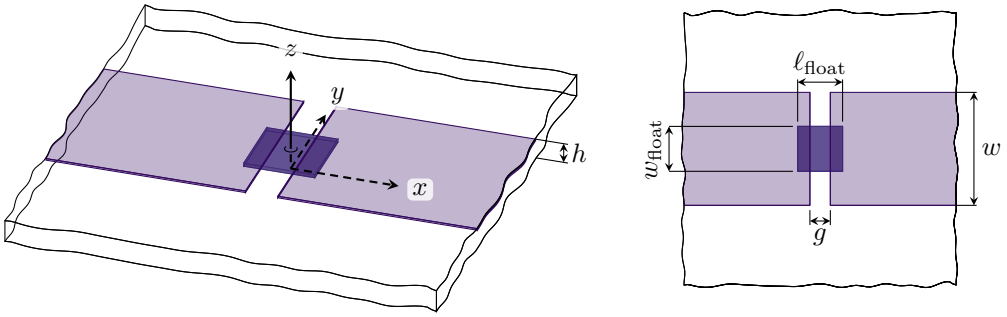

(a) (b)

Figure 6.3.: Gap geometry of the linear polarized antenna in (a) perspective and (b) top view.

Label	Antenna Type A	Antenna Type B	Description
ℓ_0	120 μm	120 μm	Center MSL length
ℓ_1	112.5 μm	105 μm	End MSL length
w	83 μm	83 μm	MSL width
ℓ_{Float}	34.6 μm	34.6 μm	Floating patch length
w_{Float}	33 μm	27.75 μm	Floating patch width
g	15 μm	15 μm	Gap width
h	9.5 μm	9.5 μm	Substrate height
h_{Float}	0.45 μm	0.45 μm	Floating patch insulator height

Table 6.1.: Dimensions of the linear polarized antenna elements A and B.

are compared to (3.51)-(3.52) for L'_{TL} and C'_{TL}, respectively, and to (3.54), (3.60) for G'_{TL} and R'_{TL} in Fig. 6.4. The series elements are in excellent agreement, whereas both shunt elements show a slight deviation. Here, the relative permittivity utilized in (3.52) and (3.54) was increased to $\varepsilon_{\text{r}} = 4.8$ for modeling the upper layer submerged in the SiO_2/Si_3N_4 mixture, yielding $\varepsilon_{\text{r,eff}} \approx 4.1$. Furthermore, the EC elements for the series representation of the gap are compared to the analytical solution in Fig. 6.5 (a). Both corresponding gap capacitances and dissipation conductance from full-wave simulations are given in Fig. 6.5 (b). The excellent agreement between FDTD extracted values and the analytical gap model confirms the extraction method from [A23] and the derivation in Section 5.3.1.

Given the outstanding agreement between the analytical expressions presented above and the FDTD extracted results from [A23], the analytical models will be used to describe the MSL and the radiation contributions in the EC model. If not mentioned otherwise, the EC model refers to the *ABCD* matrix method combined with radiation postprocessing (cf. Section 5.4.3). As the gap capacitance strongly depends on the specific geometry chosen, the capacitance calculated by the FDTD method at 300 GHz will be used as C^{gap}, in this case, $C_{\text{A}}^{\text{gap}} = 23.3\,\text{fF}$ and $C_{\text{B}}^{\text{gap}} = 20.0\,\text{fF}$. The corresponding

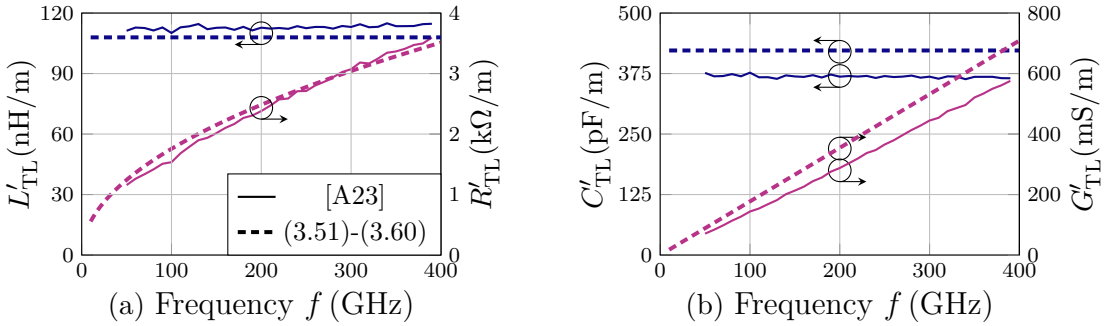

Figure 6.4.: Circuit elements per unit length of the TL for (a) the series path and (b) the shunt path comparing the analytical expressions from Section 3.4 to the extracted values from [A23].

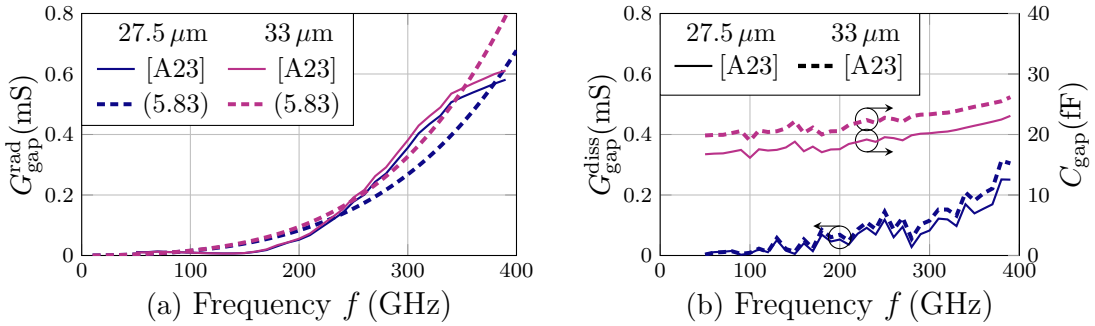

Figure 6.5.: Circuit elements of the capacitive gap for the series EC comparing the analytical expressions from Section 5.3.1 to values extracted similar to [A23]. (a) shows the radiation conductance versus frequency, whereas (b) depicts the dissipation conductance and the gap capacitance for two widths w_{Float}. The values differ slightly from [A23] due to the consideration of the Si_3N_4 inclusion in the SiO_2.

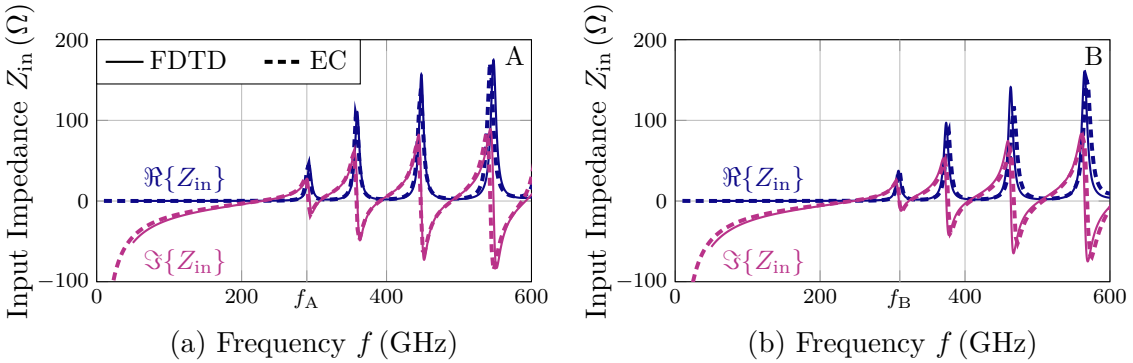

Figure 6.6.: Comparison of the input impedance for the antenna elements A and B calculated by the EC and an FDTD solver.

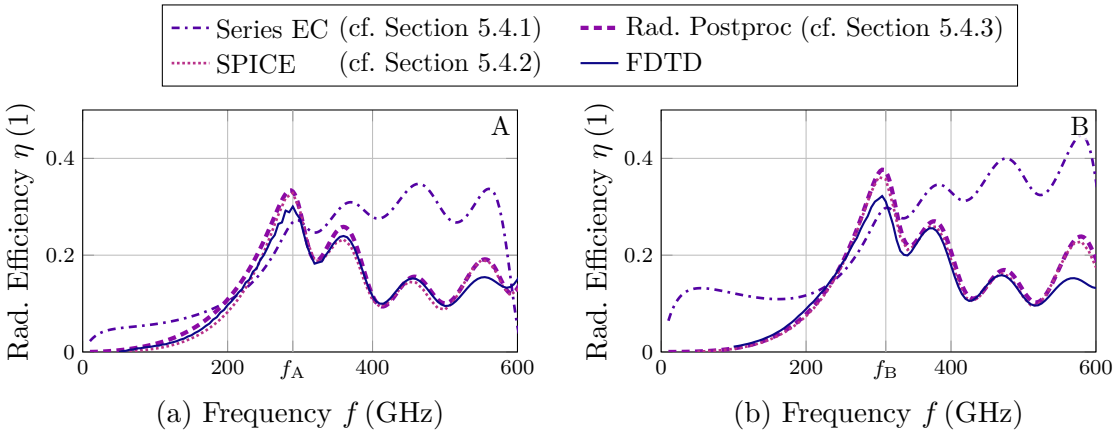

Figure 6.7.: Comparison of the radiation efficiency for the antenna elements A and B calculated by the different circuit-based approaches and an FDTD solver.

dielectric losses are estimated using the $\tan\delta$ of the utilized substrate.

For each antenna A and B, the input impedance is calculated using the EC model and compared to full-wave FDTD simulations of the corresponding antenna. The calculated input impedances are depicted in Fig. 6.6 and show an excellent agreement between both simulations. Compared to [A172], where only the resonance frequencies without considering losses were calculated, even the real part of the input impedance can be calculated using the full EC model. Fig. 6.7 compares the different methods to estimate the radiation efficiency using the *ABCD*-based circuit simulation, namely the least precise series EC model, the more precise radiation postprocessing, and the most accurate and computationally expensive SPICE simulation, to the full-wave result. Here, all methods estimate a similar radiation efficiency at the fundamental resonance of both antennas, marked with f_A and f_B. The series EC neglects any coupling between the radiators, which also means that the destructive interference associated with higher-order standing waves on the resonator is not included. As an effect, the series EC overestimates the radiation efficiency at $\approx 380\,\text{GHz}$, $\approx 450\,\text{GHz}$, and $\approx 580\,\text{GHz}$. As expected, the radiation postprocessing achieves a better agreement and includes the interference effect for the higher-order modes. The remaining minor difference to the SPICE solution is feeding the coupling back into the circuit – which is only considered in the SPICE model evaluating the full model from Fig. 5.23. All EC models tend to overestimate the efficiency, which could be caused by an oversimplified loss model for the capacitive gap, considering only dielectric but no ohmic losses.

Given the accurate input impedance and radiation efficiency estimation, only the antenna's directivity must be obtained to access the antenna's realized gain. With the radiation model of the open circuit from Section 5.3.1, calculating the directivity can be directly carried out by superimposing the radiation contributions of each open circuit weighted with the corresponding voltage. The obtained radiation pattern can be normalized to the total radiated power to give the directivity, which is given in the broad-

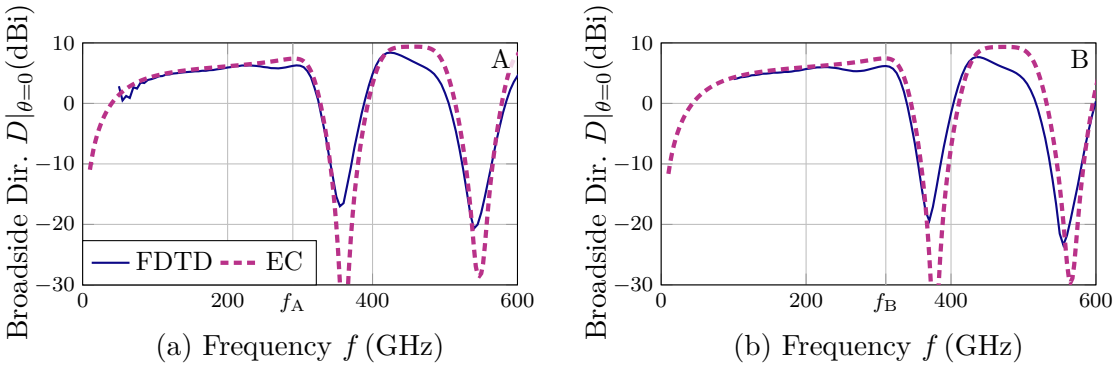

Figure 6.8.: Comparison of the broadside directivity ($\theta = 0$) of both antenna elements A and B calculated by the radiation postprocessing of the EC solution and an FDTD solver.

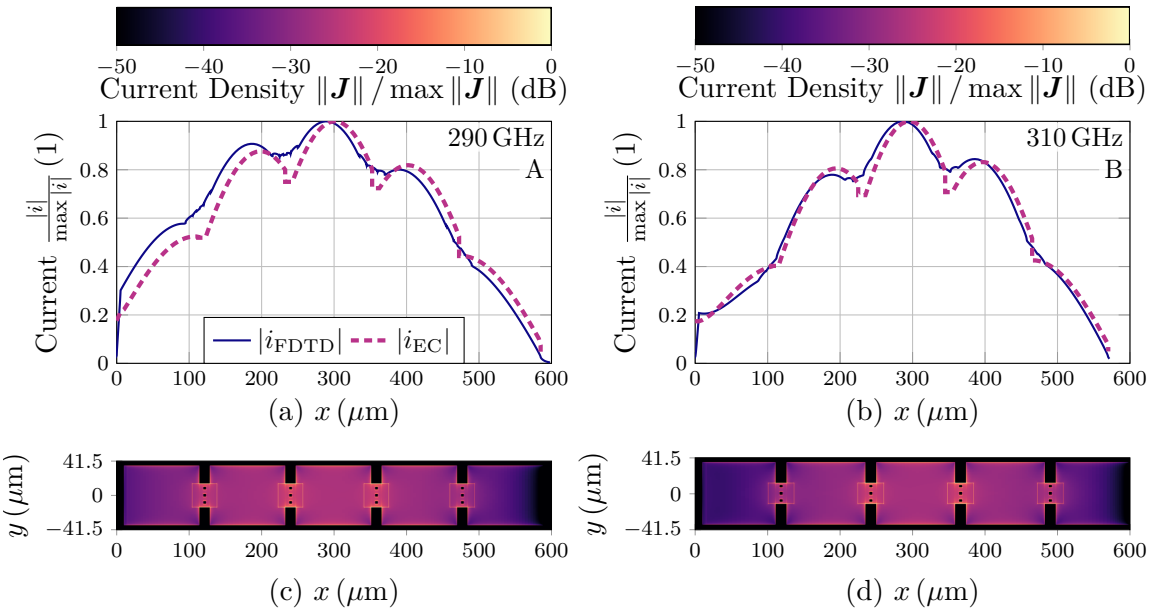

Figure 6.9.: Current distribution (a, b) along the antenna length and (c, d) the projection of the current density into the x-y-plane calculated using an FDTD method for both antennas A and B.

side direction ($\theta = 0$) in Fig. 6.8. Whereas the far field superimposed using the EC model assumes an infinite ground plane and substrate, the structure simulated in the FDTD solver utilized a finite substrate- and ground area of $1500\,\mu\mathrm{m} \times 1400\,\mu\mathrm{m}$. Nevertheless, the agreement to the circuit result is exceptional. Especially the broadside-nulls, which occur at the even mode numbers of the antenna, are included, as in [A23]. Although not a key antenna parameter, the current distribution along the antenna can be observed to increase the physical insight. The current density in the two upper metal layers is projected into one cross section and depicted in Figs. 6.9 (c) and (d).

To compare it to the circuit result, which only considers a concentrated line current i in the transversal direction, the current density in the conductor is integrated along the y-z-plane yielding the current depicted in Fig. 6.9 (a) and (b), which compares excellently to the circuit-based current.

6.1.3. Antenna Assembly

The main principle of the antenna assembly, namely distributing the power into the antenna pair closer to resonance, has been explained in Section 6.1.1. The resulting antenna geometry with the feeding network is depicted in Fig. 6.10 (a). Here, characteristic points along the feeding network are highlighted for a detailed investigation, namely the feeding point at the left-hand side, the shunt point, where the element's feeding lines are separated, and the individual feed points of the antenna elements A and B. Using the EC for the single antennas and standard transmission line equations, the input impedance and admittance at different points in the feeding network

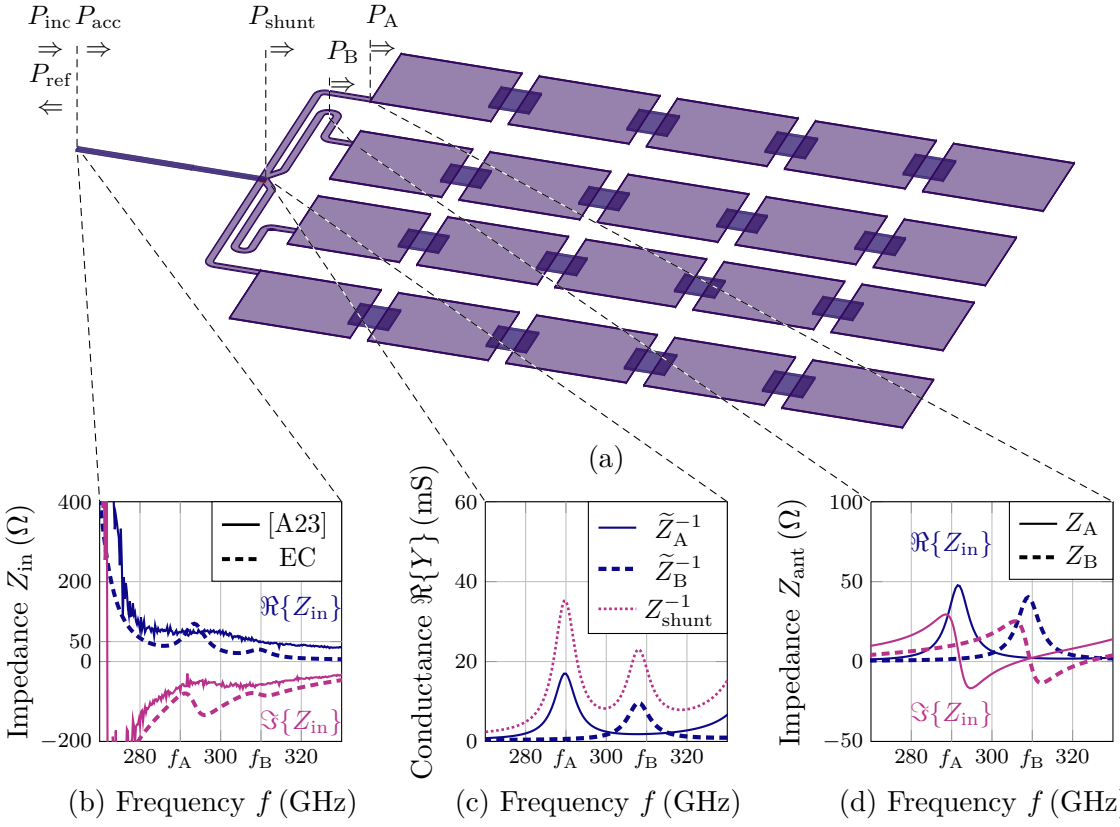

Figure 6.10.: Geometry of (a) the antenna assembly without substrate and ground plane for clarity and (b, c, d) input impedance or admittance at different positions within the feeding network, including the measured input impedance from [A23].

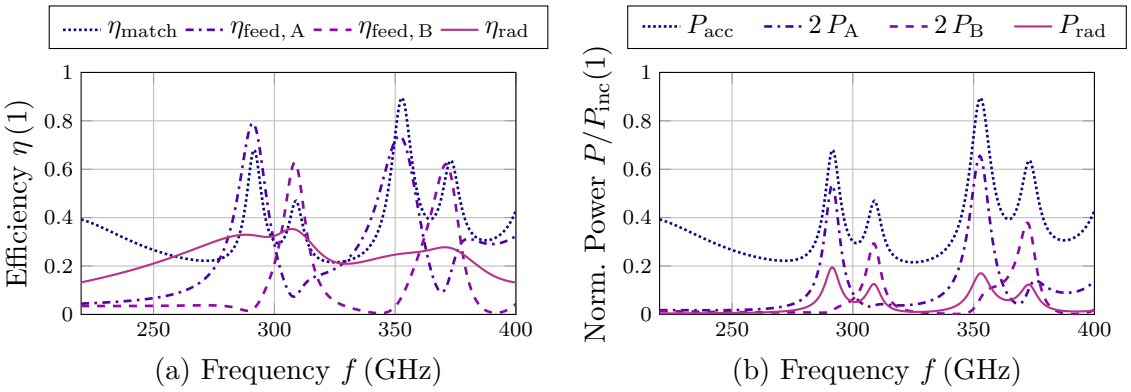

Figure 6.11.: Efficiencies for (a) different loss mechanisms in the feeding network and (b) corresponding power levels due to these efficiencies.

can be calculated. They are depicted in Figs. 6.10 (b), (c), and (d) and schematically highlighted in Fig. 6.2. In their fundamental operating mode, the antennas can be represented by shunt resonators characterized by a peaking input impedance at resonance. This peaking input impedance does not allow for the direct shunt connections of antennas with different resonance frequencies, as the shunt connection favors the smaller impedance. To overcome this, the individual feed lines of the antennas are approximately 90° in electrical length and thus act as a $\lambda/4$ transformer. Each feed line transforms the peaking input impedances (cf. Fig. 6.10 (d)) into peaking input admittances (cf. Fig. 6.10 (c)), which are more convenient for discussing shunt connections. The total admittance at the shunt point adds the admittances of two antenna element pairs, A or B, to finally obtain the resonances of both antenna elements. This admittance is transformed into the input impedance Z_{in} depicted in Fig. 6.10 (b) and compared to the measurement result from [A23]. It should be noted that the measurement result includes the effect of the Ground Signal Ground (GSG) pad used for probing on-chip antennas, which is not included in the circuit model. As explained in [A23], the precise calculation of the gap capacitance initially failed for this prototype, yielding an underestimated capacitance value. Consequently, the desired operating frequency was shifted from 250 GHz to 300 GHz, and thus the antenna is not ideally matched at the input pads. Despite this mismatch, the overall antenna performance is still acceptable. An in-depth discussion of the design difficulties of these antenna types and their interplay with the on-chip environment is presented in Section 6.4. The EC model presented here is based on capacitance values extracted with a more detailed model of the on-chip layers, which was set up to understand the shifted operating frequency.

Furthermore, the power losses in the different sections can be obtained using the EC representation of the feeding network. Fig. 6.11 (a) shows different efficiency measures

defined according to

$$\eta_{\text{match}} = \frac{P_{\text{acc}}}{P_{\text{inc}}}, \qquad \eta_{\text{feed, A/B}} = \frac{P_{\text{A/B}}}{P_{\text{acc}}}, \qquad \eta_{\text{rad}} = \frac{P_{\text{A}}^{\text{rad}} + P_{\text{A}}^{\text{rad}}}{P_{\text{A}} + P_{\text{B}}}. \tag{6.1}$$

Whereas η_{match} accounts for the mismatch between antenna and generator, $\eta_{\text{feed, A/B}}$ accounts for the losses along the feeding network up to antennas A and B. All mismatch losses inside the feeding network caused by mismatched antennas outside their operating frequency are included here. Last, the radiation efficiency η_{rad} combines the radiation efficiencies of the single antennas considering the input power delivered by the feeding network. It should be noted that the resulting radiation efficiency is not the most accurate estimate, as the radiation postprocessing was used here instead of the more accurate SPICE model. The power levels resulting from these efficiencies are depicted in Fig. 6.11 (b), which shows the drastic effect of the antenna mismatch, the comparatively minor losses along the feeding network, and, finally, the reduced radiated power compared to the incident power.

6.1.4. Antenna Measurement

The characterization of the antenna is carried out using the spherical wafer antenna measurement system presented in [A105]. It utilizes a VNA and frequency extenders, which up- and down-convert coaxially fed RF signals in the cm-wave regime to mm-waves traveling in rectangular waveguides. The mm-waves are fed into either a reference antenna or an antenna under test in the center of the measurement system. A measurement receiver is moved around the center with a constant radius, i.e., in a spherical coordinate system. More details on the measurement system and an in-depth investigation of the systematic limitations, resolution, and internal reflections are given in [A105]. Fig. 6.13 (a) shows a Computer Aided Design (CAD) model of the measurement system, and a photograph of the system realization is depicted in Fig. 6.13 (b). Besides the two motorized axes used for positioning the receiver in elevation and azimuth, the polarization of the receiver can be rotated to measure E_θ and E_φ.

A micrograph of the antenna fabricated in Infineon's B11HFC technology is depicted in Fig. 6.13 (a). The top aluminum metallization in green and the floating metal patches to increase the gap capacitance in orange are clearly distinguishable. A photograph of the measurement system with the receiver at an exemplifying measurement point in the E-plane with the on-wafer probe contacting the on-chip antenna is given in Fig. 6.13 (b). As the probe is electrically huge compared to the on-chip antenna, several measures are implemented to reduce its effect on the measurement as far as possible. First, the probe body results in a severely shadowed area, where a far-field measurement cannot obtain the antenna pattern [108]. Consequently, the radiated power, directivity, and efficiency cannot be calculated. If measurement and simulation obtain a good agreement, a hybrid approach, which stitches simulated and measured

patterns [109], could obtain the antenna parameters mentioned above. Second, even for a well-matched on-chip contact, the on-wafer probe itself will cause a radiation contribution [185]. Even though this contribution is weak [186], it might be in the order of magnitude of electrically small on-chip antennas or the cross-polarization of larger antennas. Last, even if the shadowed region can be accepted and the probe's radiation is negligible, the fields radiated from the antenna will be scattered at the metalized probe body, resulting in an interference-disturbed measurement [108], [187]. As shown in Figs. 6.13 (c) and (d), most of the metal parts of the probe facing towards the antenna are covered with absorbing material to suppress the effect; nevertheless, slight undulations can be observed in the measured pattern.

To calculate the far field for the EC model, the radiated far fields of the EC's fundamental radiators are superimposed, and the directivity is obtained by normalization. Here, the far fields of the fundamental radiators are again weighted with the corresponding voltage, which includes the feeding network frequency selectivity and interference effects. By including the radiation and mismatch losses, the realized gain is obtained and depicted in Figs. 6.14 (a) over frequency and in (b) as a radiation pattern. It is evident in Fig. 6.14 (a) that the realized gain of the measurement is in good agreement with the gain of the EC, which does not include the mismatch loss. However, the realized gain of measurement and EC show a significant offset. The EC, which does not include the GSG pad, seems to overestimate the mismatch. Also, both EC and measurement show two resonances in the realized gain, each at $\approx 290\,\mathrm{GHz}$ and $\approx 310\,\mathrm{GHz}$, highlighting the desired multi-resonant operating principle. In the measurement, the second resonance at 310 GHz is weaker than the EC simulation, resulting in a worse agreement overall. At 290 GHz, where the agreement of the realized gain between measurement from [A23] and EC model is best, the E- and the H-plane are compared in Fig. 6.14 (b). Besides the part of the E-plane, which cannot be measured due to probe shadowing [108], [109], the agreement is excellent, especially considering the difficulties associated with mm-wave antenna measurements [96] and the simplicity

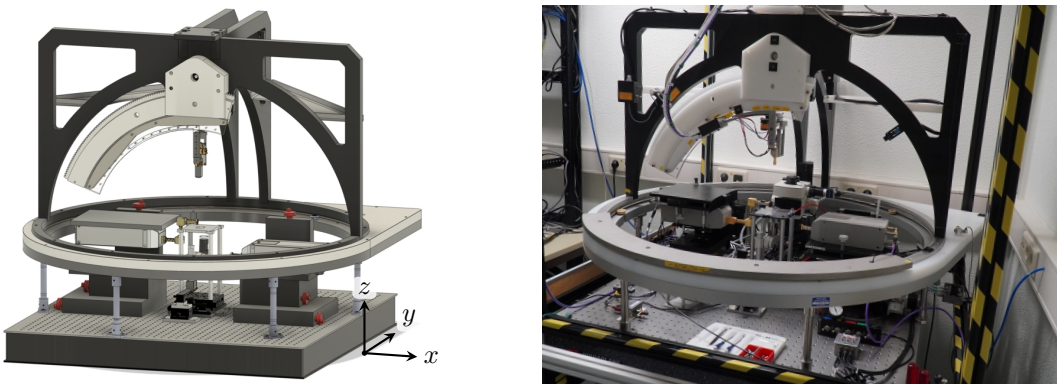

(a) (b)

Figure 6.12.: CAD perspective view (a) and photograph (b) of the spherical wafer antenna measurement system (cf. [A105]).

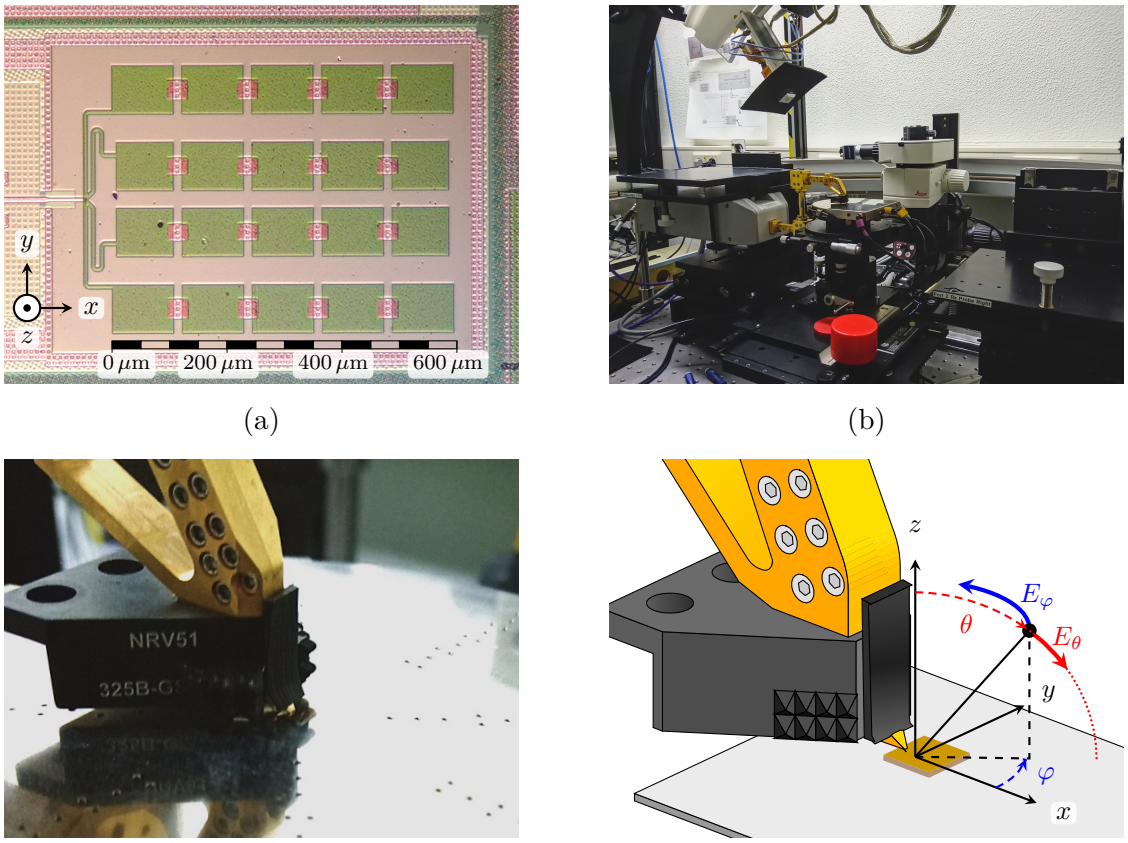

(a) (b)

(c) (d)

Figure 6.13.: Micrograph of (a) the linear polarized on-chip antenna, photograph of (b) the characterization of the antenna radiation pattern E-plane in the spherical wafer antenna measurement system (cf. [A105]), (c) the wafer probe contacting the linear polarized chip antenna, and (d) schematic drawing of the probe with measurement coordinate system.

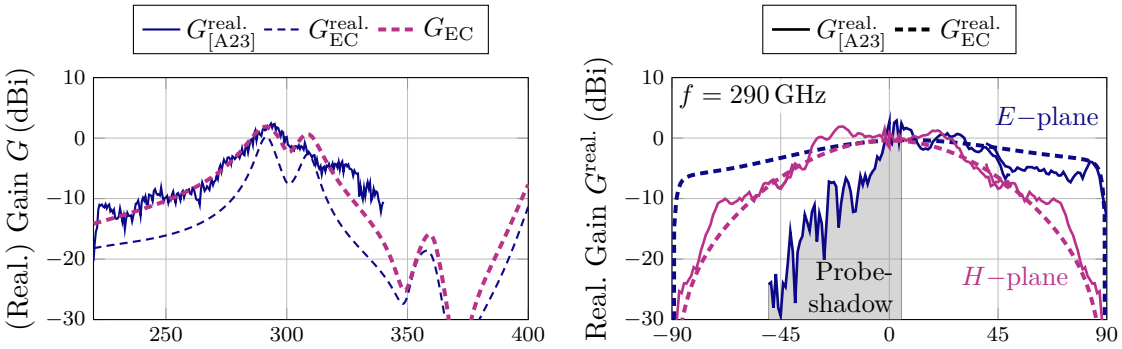

(a) Frequency f (GHz) (b) Elevation θ (deg)

Figure 6.14.: Realized gain for the antenna assembly (a) over frequency, as well as (b) in E- and H-plane comparing measurements from [A23] and the EC results.

of the EC model.

6.1.5. Near-field Measurement

The antenna operation can be investigated more in-depth with the coaxial cable based near-field probes presented in [A188]. Whereas the far-field measurement presented above only indicates the correct operation by the desired gain over frequency behavior, the near-field measurement can provide insight into the dominant current densities on the chip. Fig. 6.15 shows the utilized coaxial cable based field probe and the actual near-field measurement. The coaxial cable is lowered to hover slightly over the chip surface to capture the magnetic near field close to the actual current densities in the on-chip metal layers. For acquiring the data, the coaxial cable is moved on a cartesian x-y grid with a step size of 12.5 μm, while a commercial GSG probe feeds the on-chip antenna. As explained in [A188], the coaxial cable is sufficiently flexible such that both collisions with the on-wafer probe or the chip only result in a reversible elastic deformation of the cable. Thus these collisions do not result in damaging the on-chip prototype or the GSG probe.

Fig. 6.16 depicts the measured y-component of the magnetic field strength H_y and compares it to the x-component of the simulated current density J_x. The measured near field is depicted with the original pixel spacing of 12.5 μm without interpolation. Although the obtained near fields are blurred by the aperture of the field probe and the distance to the current density, the similarity and, thus, the indication for the desired operation can be seen in the direct comparison. Note that the displayed dynamic range has been reduced for the measured data to account for the blurred nature of the measured field. Here, the outer antenna pair A is more dominant at the lower

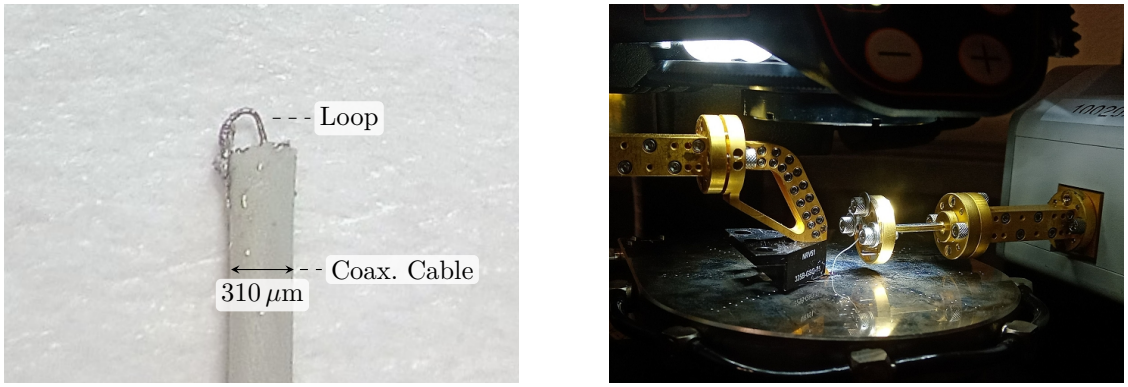

(a) (b)

Figure 6.15.: Photograph of (a) the coaxial cable based H-field probe utilizing a wire loop and (b) the magnetic field measurement above the chip surface (cf. [A188]).

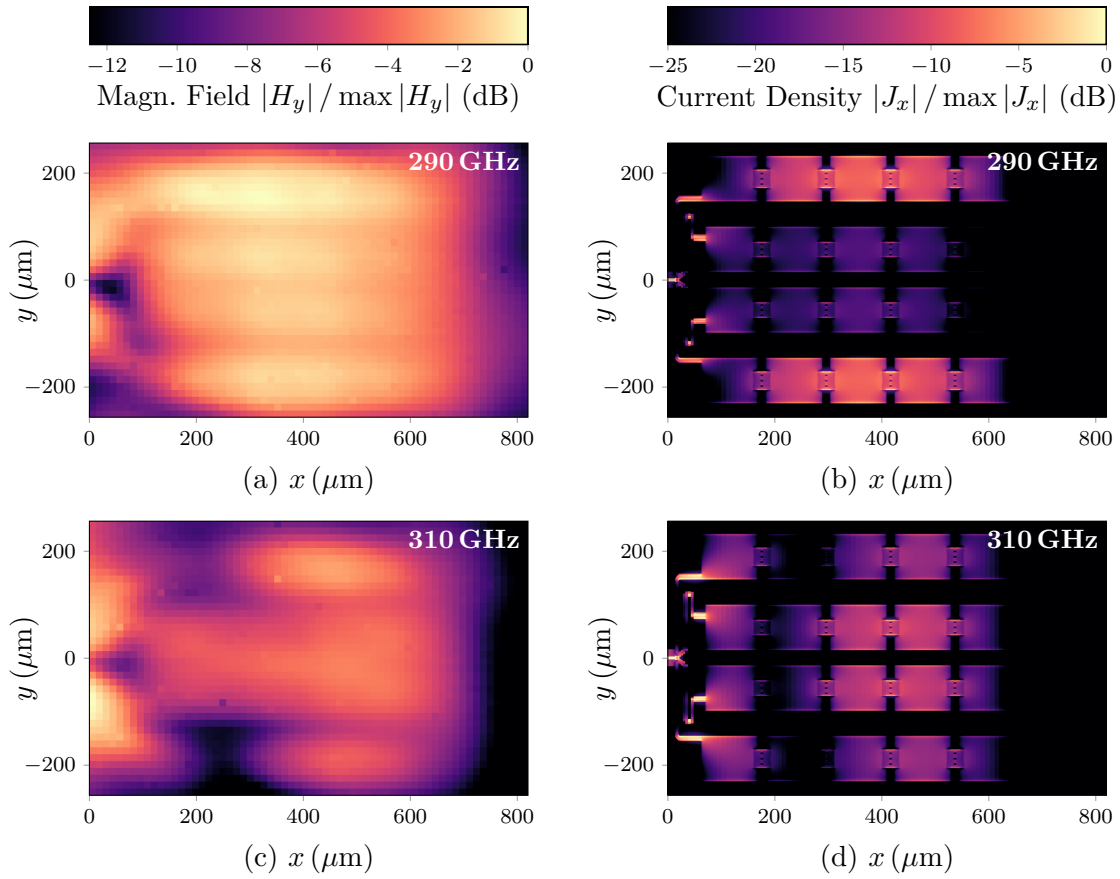

Figure 6.16.: Top view on (a, c) the measured magnetic field strength y-component H_y above the chip and (b, d) the simulated current density x-component J_x at 290 GHz and 310 GHz, respectively. The dynamic range of the measured field is reduced to ease the comparison.

frequency, whereas the central antenna pair B dominates the fields at the higher frequency. Furthermore, it can be seen that the strong coupling of the colocated antenna pairs prevents a more distinct separation of the different operating modes. A method to decrease the coupling and, thus, improve the frequency selectivity of the antenna approach will be presented with the following two prototypes. Last, it is shown in [A188] that a conventional Near Field to Far Field (NF2FF) transform can be utilized to calculate the radiated far fields of the antenna from measured E- and H-fields on the chip surface. The evident benefit of this method is the reduced effect of the on-wafer probe on the calculated far-field patterns since shadowing and scattering at the probes are mitigated by performing the near-field measurement close to the chip surface. Fig. 6.17 shows the measured and NF2FF-transformed directivity radiation pattern for the upper half-space ($\theta \leq \pi/2$) in excellent agreement with the FDTD result. An in-depth discussion and further cut planes comparing the results from the NF2FF to the full-wave FDTD result can be found in [A188]. The next section presents an advanced and improved prototype based on the core concept of this antenna.

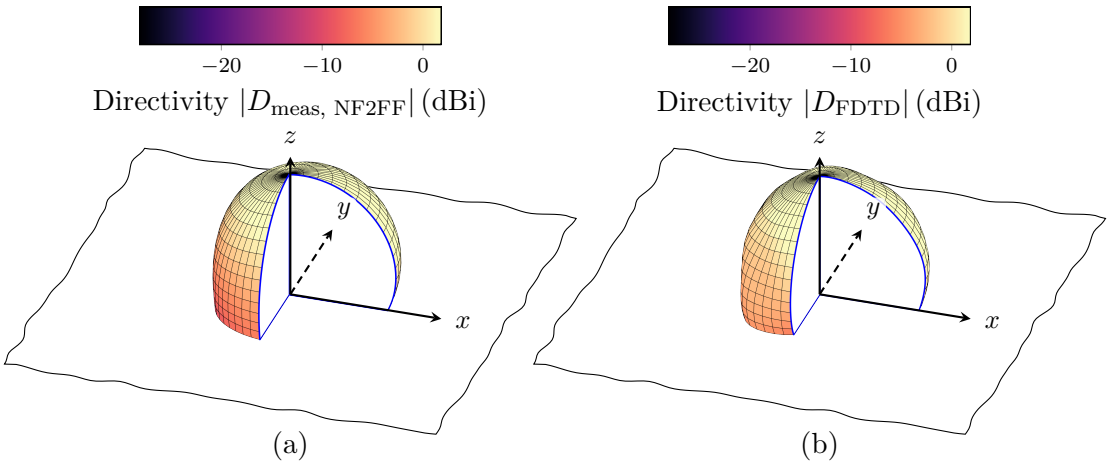

Figure 6.17.: Far field for the linear polarized antenna at 305 GHz calculated (a) from the measured near fields with an NF2FF and (b) by the FDTD method. The x-z and y-z cuts are introduced to ease the interpretation of the radiation pattern.

6.2. Circular Polarized Antenna

This section presents an on-chip antenna concept to radiate Circular Polarization (CP) over an increased bandwidth. To obtain the Right Hand Circular Polarized (RHCP) radiation, a combined feeding and matching network enables, on the one hand, a frequency selectivity in favor of the most suitable of two antenna groups. On the other hand, the feeding phase within each antenna group corresponds to the radiator's geometrical position, such that a CP is radiated. The ideal polarization purity would be achieved for a vanishing Left Hand Circular Polarized (LHCP) radiation, which is usually only possible within a limited bandwidth.

6.2.1. Design Concept

A circuit representation of the antenna feeding network is given in Fig. 6.18. The designed TL lengths are given at the respective design frequency of the network, which is $f = 250\,\text{GHz}$. At both poles 1 and 1′, a differential feed is required. It can be seen that each antenna arm, A or B, is paired with an arm at the respective opposing direction fed out-of-phase, such that two paired antenna arms build up a dipole. Two dipoles of the set are geometrically orthogonal and fed with a phase difference of $\pi/2$, such that a CP is obtained. To increase the overall bandwidth, the antennas of type A are designed for an operating frequency of $f_\text{A} = 230\,\text{GHz}$, whereas the antennas of type B are designed for the feeding network center frequency $f_\text{B} = 250\,\text{GHz}$. It should be noted that only a suboptimal operation is possible outside the center frequency of the network since standard MSLs are used to obtain the necessary phase shifts. As for the linear polarized antenna in the previous section, the frequency selectivity

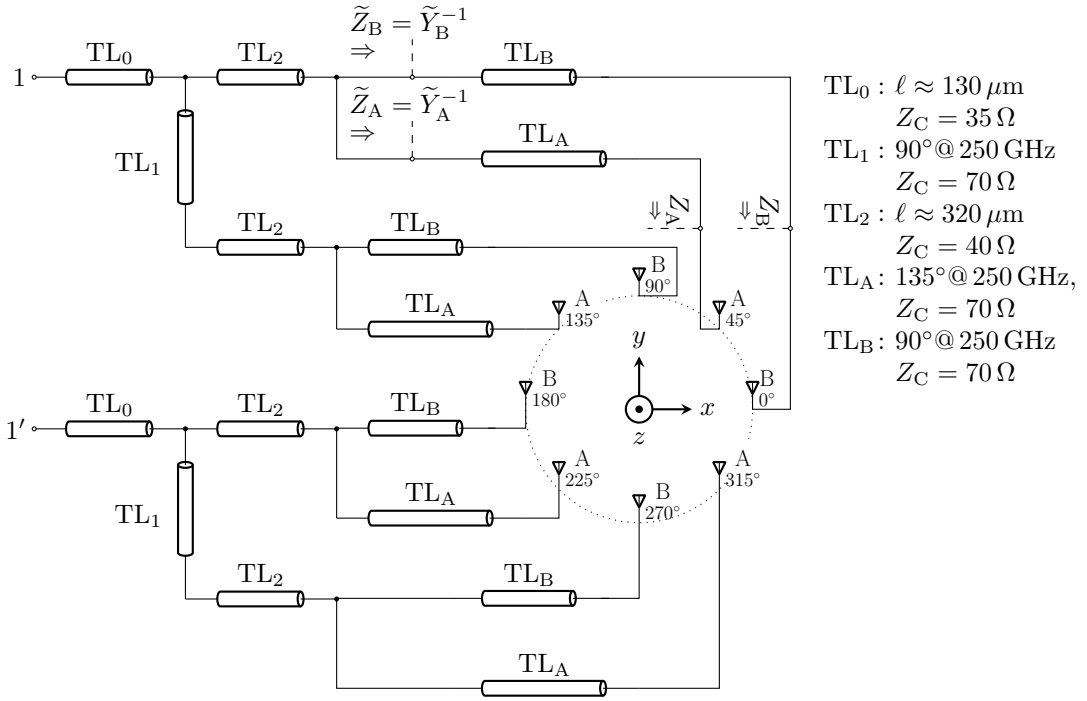

Figure 6.18.: Exemplary antenna feeding network to obtain the CP and broadband matching of the on-chip antenna, adapted from [A189].

towards either antenna A or B is achieved using $\approx \lambda/4$ impedance transformers, which are here built using $\mathrm{TL_A}$ and $\mathrm{TL_B}$. Last, the geometrical feeding point orientation for each antenna is also highlighted in the drawing since it corresponds to the ideal feeding phase of the network. The following sections will discuss the performance of the single antenna arm, two antenna arms building a dipole, and the overall antenna assembly consisting of 8 antenna arms (or 4 dipoles). More details on the antenna design can be found in [A189].

6.2.2. Geometry and EC

Both antenna arms A and B utilize the same concept; however, their geometry differs slightly to obtain different resonance frequencies and utilize most of the available chip area. The antenna arms are short-circuited and operate thus as $\lambda/4$ resonators [190], utilizing a series capacitance to increase the radiation efficiency. The top view on both antenna arms and the corresponding EC model is given in Fig. 6.19. Since the MSL width varies along the antenna, the characteristic impedance to describe the line in the EC depends on the position. To use the circuit simulation techniques mentioned in Section 5.4, the tapered lines are segmented into small sections of constant width. Here, for each segment of constant width, the circuit elements are easily calculated based on the MSL description of Section 3.4. The line is segmented into lines of $2\,\mu$m length, which is even at mm-waves considered small compared to the wavelength. As

for the series EC model of the linear polarized antenna, a radiation conductance $G_{\text{open}}^{\text{rad}}$ is assigned to the capacitive gap and a radiation resistance $R_{\text{short}}^{\text{rad}}$ to the short at the end of the MSL. A further radiation contribution is expected from the change in MSL width, and it is included in the radiation postprocessing (cf. Section 5.4.3) with the step discontinuity model from Section 5.3.6. The overall radiation is thus a result of the coupling between the open- and short MSL end, the capacitive gap, and the change in line width. A detailed drawing of the utilized capacitive gap is depicted in Fig. 6.20. The gap concept is similar for both antenna arms, where a via has been inserted at one end of the gap to connect the floating metal layer to the left- or right-hand side electrode. Thus, the overall capacitance obtained with this floating layer is approximately doubled compared to the case without the via. The remaining geometry, which includes the castellation of the top layer, is chosen to fulfill the DRC and enable a minimized gap width, which reduces the length of the overlapping metal pads and thus reduces the ohmic losses. An excerpt of the dimensions is given in Table 6.2.

The parameters of the circuit elements are partly calculated using full-wave solvers and partly calculated using analytical- or empirical formulas. In detail, the elements per unit length of the MSL are calculated using (3.51)-(3.60), and the self- and mutual

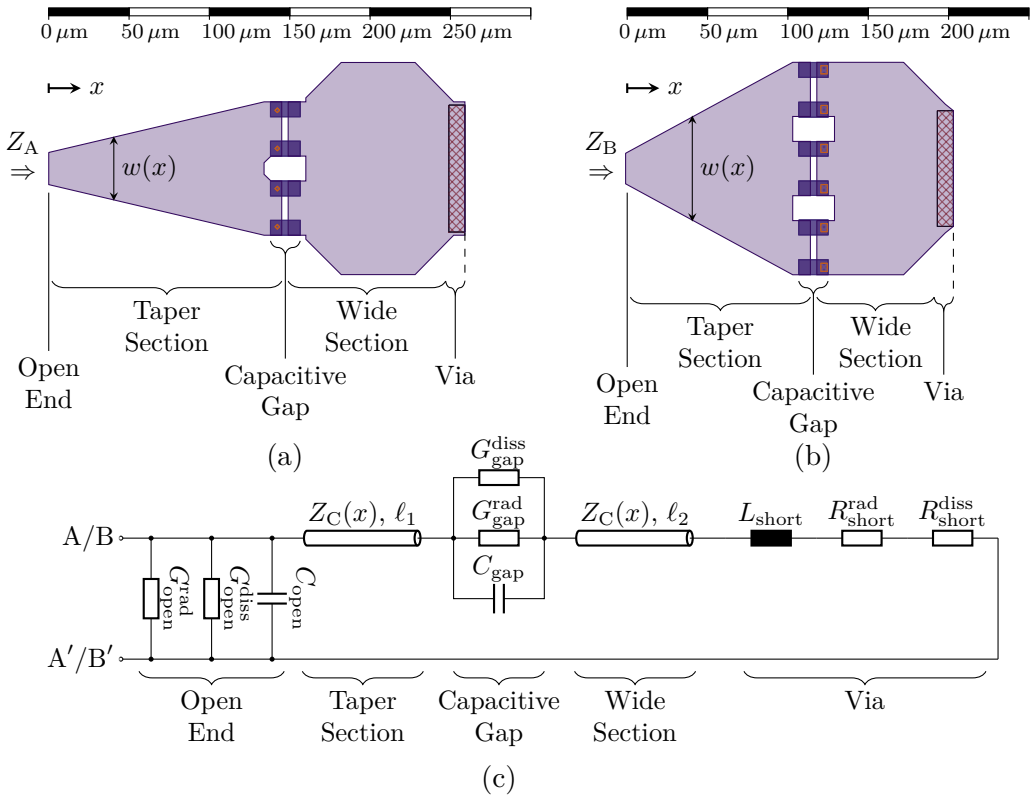

Figure 6.19.: Geometry in (a, b) top view for antenna arms A and B, respectively, and (c) corresponding EC representation, adapted from [A189]. Selected antenna parts are highlighted in geometry and circuit representation.

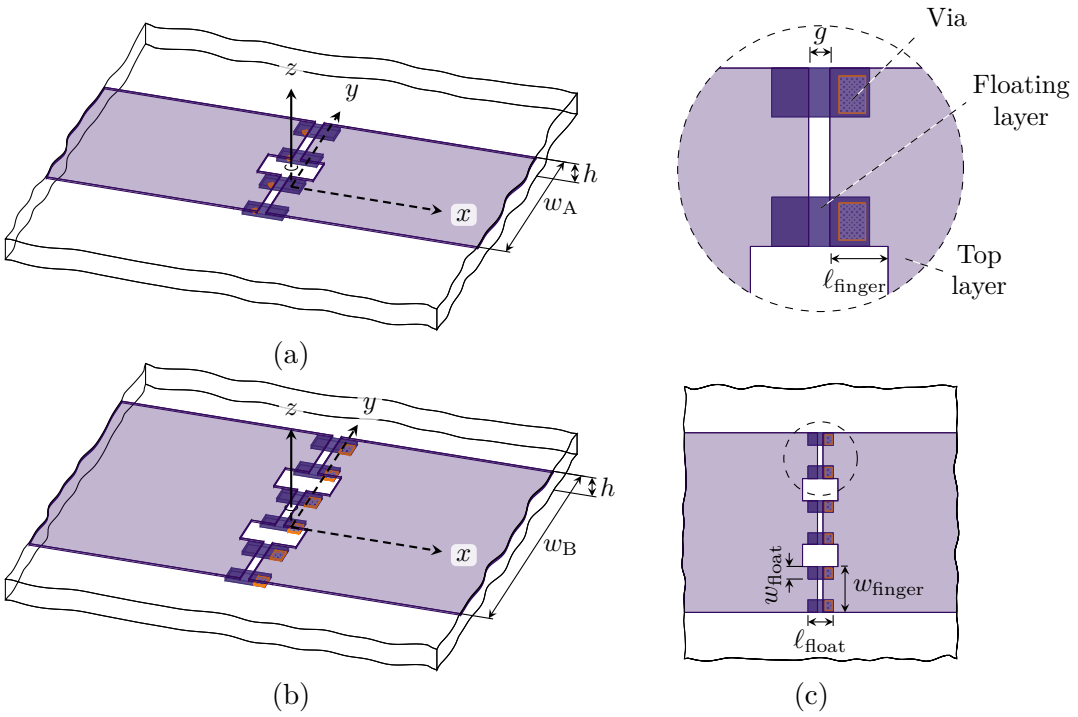

Figure 6.20.: Gap geometry (a, b) of the antenna arms A and B, as well as a top and detailed view of the gap of B (c).

Label	Antenna Type A	Antenna Type B	Description
$\min(w(x))$	$20\,\mu$m	$20\,\mu$m	Narrowest antenna width
$\max(w(x))$	$132\,\mu$m	$132\,\mu$m	Widest antenna width
ℓ_1	$153\,\mu$m	$118\,\mu$m	Length of taper section
ℓ_2	$102\,\mu$m	$83\,\mu$m	Length of wide section
$w_{finger} \times \ell_{finger}$	$34\,\mu$m $\times$ $11\,\mu$m	$34\,\mu$m $\times$ $11\,\mu$m	Area of a finger
$w_{float} \times \ell_{float}$	$8.5\,\mu$m $\times$ $18.5\,\mu$m	$9.3\,\mu$m $\times$ $18.5\,\mu$m	Area of a floating patch
g	$4\,\mu$m	$4\,\mu$m	MSL gap width

Table 6.2.: Dimensions of the antenna arms A and B of the RHCP antenna.

radiation conductances, resistances, and coupling factors are accessed using the results of open- and short-circuited MSL in (5.74)-(5.78). Furthermore, the capacitance of the gap is accessible using an electrostatic or full-wave electrodynamic solver, which both give similar results, as expected for the electrically small extent of the gap. Only the inductance and dissipation resistance of the short are calculated using a full-wave simulation, as the via grids connecting the metal layers on-chip result in very complicated and electrically tiny structures. The input impedance of each antenna arm is calculated using the EC model and a circuit simulation, e.g., the method based on *ABCD* matrices (cf. Section 5.4.1). Fig. 6.21 shows the input impedance calculated by

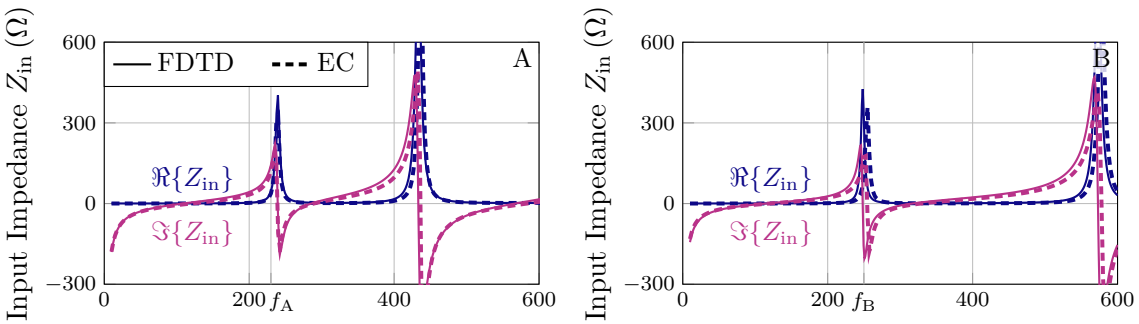

Figure 6.21.: Comparison of the input impedance for both antenna arms A and B calculated by the EC and an FDTD solver.

the EC model and compares it to full-wave FDTD results. Additionally, the desired operating frequencies of both antennas are marked here. The slight frequency shift between the actual resonance frequency of antenna A and f_{A} will be compensated by the feeding TL (cf. Fig. 6.18). As for the linear polarized antenna, the agreement between the circuit- and full-wave simulation is excellent.

Furthermore, the current along the antenna length is compared to results from a full-wave FDTD solution. As for the linear polarized antenna, the current density is integrated over the transversal cross sections of the antenna to give the overall current. Figs. 6.22 (a) and (b) depict the current normalized to its maximum value for both antenna candidates. Although it cannot be compared to an EC result, the norm of the electric current density calculated by the FDTD solver is given in Figs. 6.22 (c) and (d). The currents of all different layers have been projected into one plane to highlight the large vertical current densities in the short circuit. In either of these figures, the desired $\lambda/4$ resonance can be clearly recognized.

A dipole consisting of two antenna arms each is fed differentially to investigate the radiation efficiency and the broadside directivity, as depicted in Fig. 6.23. The existing circuit analysis can be extended to consider the shape of the dipoles by calculating the coupling conductances, resistances, and factors within and between the antenna radiators. The respective radiator positions of the second antenna arm are mirrored around the center line of the dipole, and the current- and voltage directions need to be reversed compared to the first antenna arm. Although the size of the coupling matrices doubles for each dimension, the calculation of the radiated power (and thus the radiation efficiency) using (5.69) and the radiation postprocessing from Section 5.4.3 is computationally very efficient. Due to the multitude of radiators resulting from the spatially very fine resolution used to model the tapered MSLs, the circuit simulation using SPICE becomes less feasible. Since it has been shown that the difference between the radiation postprocessing and the SPICE model is negligibly small (cf. Fig. 6.7), only the former is carried out here. The calculated radiation efficiency is depicted in Fig. 6.24. Here, the agreement is good over a broad bandwidth. It should be noted

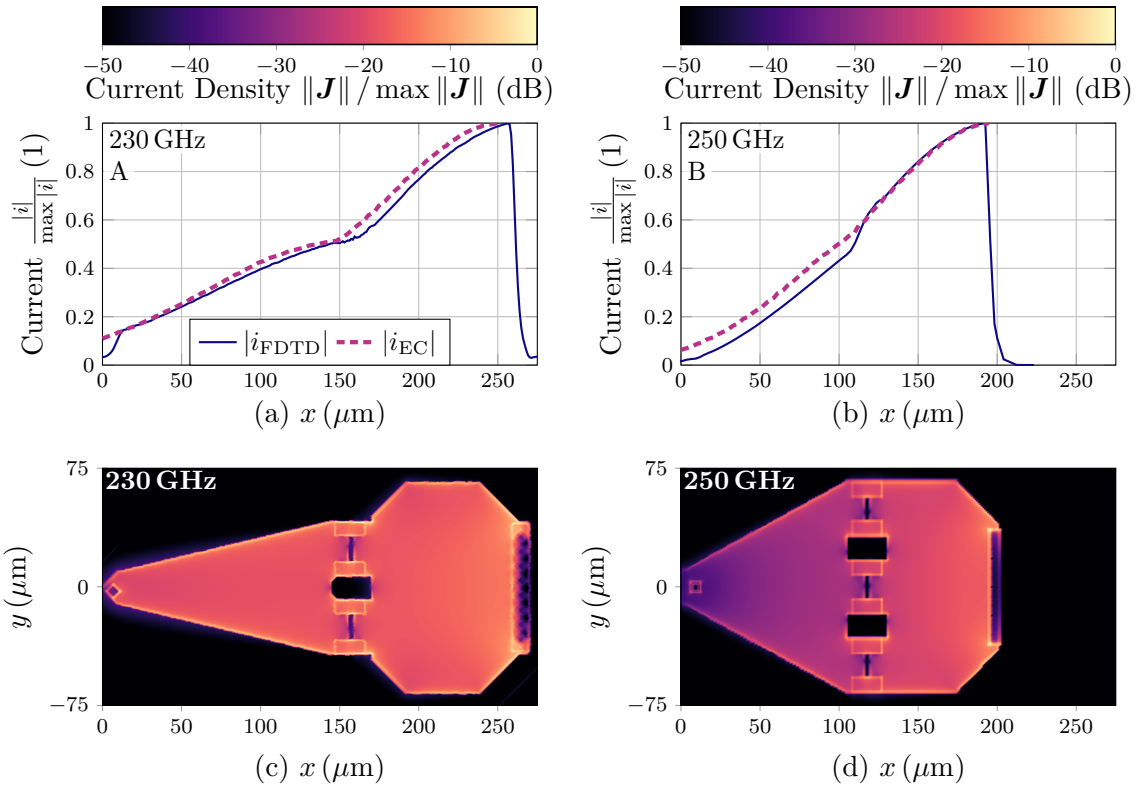

Figure 6.22.: Current distribution along the antenna arm length (a, b) and the projection of the current density into the x-y-plane calculated using an FDTD method (c, d) for both antenna arms A and B.

that the EC model still approximates the radiation with a severe simplification. In all coupling models discussed above, the current responsible for the radiation is considered only in the longitudinal direction, meaning current along the antenna length. As can be seen in Figs. 6.22 (c) and (d), the tapered sections of the MSL carry currents in transversal directions. These y-directed current densities are not considered in the radiation efficiency calculation. A more thorough investigation could model the antenna using line currents, which follow the contour of the metalized antenna, and the

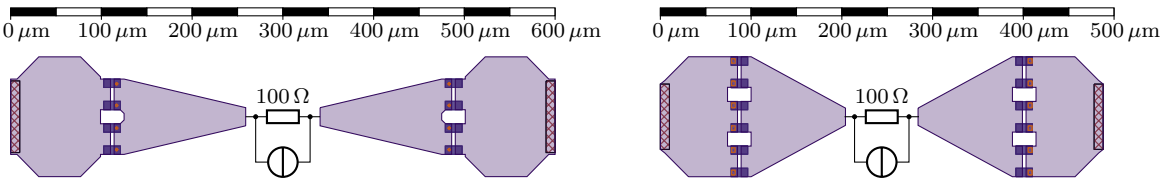

Figure 6.23.: Two antenna arms connected with a common source to assemble a dipole for Antenna A and B.

Green's function for currents on a grounded dielectric slab (cf. Section 4.3.3). In the final consequence, this leads to a tailored MoM approach well-suited for microstrip antennas [27], [142]. Besides the computational effort associated with the numerical evaluation of an infinite two-dimensional integral in $\boldsymbol{k}$-space [142], using the MoM undermines the EC approach of this thesis and, thus, the intuitive insight into the antenna operation.

As the radiation pattern associated with open- and short circuits are known (cf. Sections 5.3.1 and 5.3.2), these can be superimposed using the corresponding source strengths (voltage or current) from the circuit simulation at the respective radiator positions in the antenna. The superimposed far fields can be normalized to express directivity and are depicted for the broadside direction ($\theta = 0$) in Fig. 6.25. For very low frequencies, the directivity of the full-wave solution decreases monotonically. This is supposed to result from the finite ground size used in the FDTD simulation.

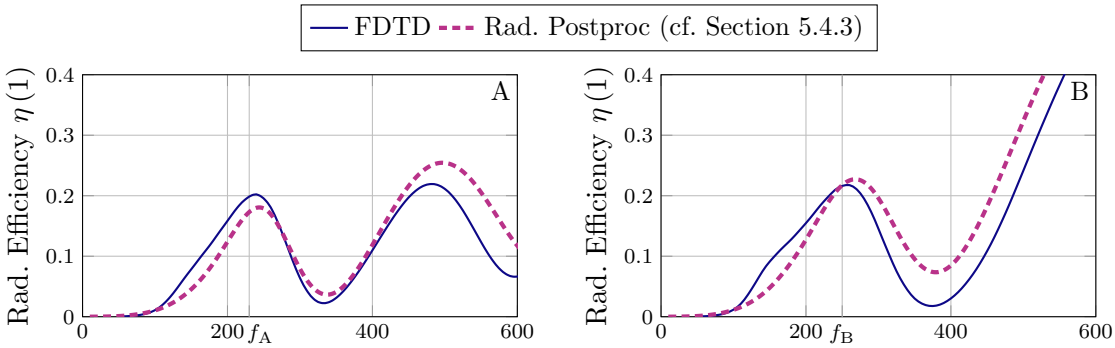

(a) Frequency f (GHz) (b) Frequency f (GHz)

Figure 6.24.: Comparison of the radiation efficiency for antenna arms A and B calculated by the EC model and an FDTD solver.

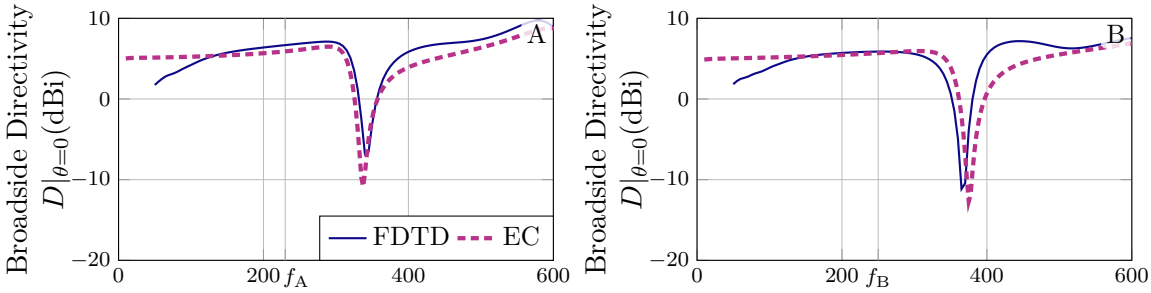

(a) Frequency f (GHz) (b) Frequency f (GHz)

Figure 6.25.: Comparison of the broadside directivity ($\theta = 0$) for both antenna dipoles A and B calculated by the radiation postprocessing of the EC solution and an FDTD solver.

Furthermore, the more significant deviations between the circuit and full-wave result at around 400 GHz could presumably be mitigated by including the physical current density vector field instead of considering only longitudinal currents, which would, as discussed above, lead to an MoM approach and, thus, a full-wave solution. Most importantly, an excellent agreement between the circuit- and the full-wave solution is seen around the operating frequencies.

6.2.3. Antenna Assembly

The final on-chip antenna design is assembled from two type A and B dipole pairs. To obtain the feeding phases discussed in Section 6.2.1, an MSL network, as depicted in Fig. 6.26 (a), is designed. This feeding network utilizes a lower metal layer within the on-chip stackup, which on the one hand, decreases coupling to the antenna elements and eases design, but on the other hand, increases losses within the network. Furthermore, it can be seen that the specific antenna geometries of the antenna arms A and B conformally map to maximize the utilized chip area. A rat-race balun for a center frequency of 250 GHz generates a differential feed signal from a single-ended on-wafer probe. Figs. 6.26 (b)-(c) show the input impedance at different locations in the feeding network to give insight into the matching mechanism. As for the linear polarized antenna, the $\lambda/4$ TLs at the antenna feed points transform the maximized input impedance (cf. Fig. 6.26 (b)) into a maximized admittance, which yields the distribution of the incident power into the antenna being closer to its resonance frequency. As a result, the input impedance at the antenna feed is relatively close to $50\,\Omega$ over a moderate bandwidth (cf. Fig. 6.26 (c)). With this feeding network, the mismatch loss of the antenna is acceptable ($|S_{11}| < -8\,\mathrm{dB}$) over a wide bandwidth of $\approx 40\,\mathrm{GHz}$. Given the resonances still visible in the input impedance, the antenna cannot be considered well-matched over a large bandwidth. The measurement and EC simulation of the realized RHCP gain over frequency will show a similar bandwidth, which shows that the feeding and matching network is a well-designed compromise between matching performance and polarization purity, i.e., the axial ratio of the CP. With a full-wave FDTD solver, the instantaneous current density on the chip antenna prototype is calculated and depicted in Figs. 6.26 (d) and (e). Here, two instants in time separated by a phase lag of $\pi/2$ are depicted to highlight the delayed excitation of the different dipoles. For an ideal CP, the orthogonal antenna elements would be excited with orthogonal feed currents, i.e., the maximum excitation current in one dipole coincides with a zero excitation current in the other dipole. Furthermore, the feeding network should excite the vertical and horizontal dipoles B at 250 GHz and the tilted dipoles A at 230 GHz. As intended, the vertical and horizontal dipole arms show a dominant current density at 250 GHz and an almost orthogonal feed. For the lower frequency, the tilted dipole elements intended to operate at 230 GHz show the same desired orthogonal feed, with only slight leakage to the vertical antenna arms.

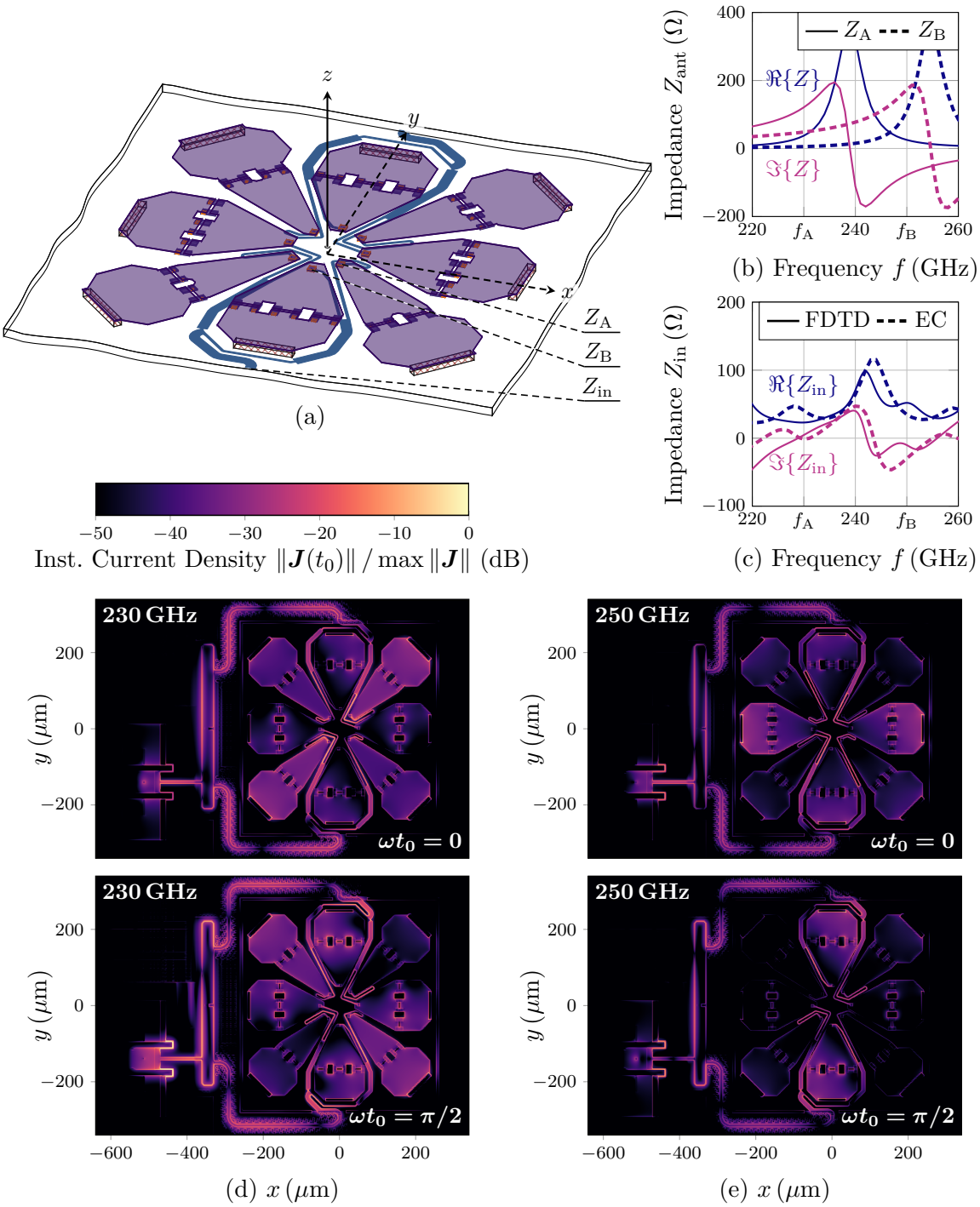

Figure 6.26.: Geometry (a) in perspective view, (b-c) input impedance, and (d-e) current density of the RHCP antenna assembly. (b) shows the input impedance at the antenna arm feed points and (c) the impedance at the assembly feed point. The instantaneous current density calculated with the FDTD method is shown in (d) at 230 GHz and (e) at 250 GHz.

6.2.4. Antenna Measurement

The measurement setup from [A105] (cf. Sec. 6.1.4) has been utilized to characterize the radiation pattern of the RHCP on-chip antenna fabricated in Infineon's B11HFC process. As before, the on-wafer probe is covered using absorbing material, and a micrograph of the contacted antenna and a photograph of the probe are given in Fig. 6.27. On the lefthand-side edge of the micrograph in Fig. 6.27 (a), the edge of the resonant graphite absorber covering the probe can be seen as well. Although the measurement setup has been shown to enable relatively phase-stable measurements [A105], excellent phase stability is required to calculate right- and left-handed CP from orthogonal components at mm-waves. A few different approaches to characterizing CP at mm-waves are presented in [A189] and discussed here exemplarily. Most straightforward, a measurement antenna with inherent RHCP could be used; however, the presented approaches are usually band-limited [191]. Amplitude-only measurements in a sufficient number can be carried out to virtually trace the envelope of the elliptical- or circular polarization [192], [193] without requiring phase information. Since even minimal movements of the measurement receivers can result in recognizable phase errors [194], a consistent receiver position must be ensured for CP measurement methods relying on the phase information. This consistency could be achieved by sufficiently accurately fabricated rotary joints, as shown for the WR10-band in [195] or a phase-stable polarizer [196]. The polarizer method was further simplified in [A189], where two rectangular waveguides are rotated around their transversal axis by ±45°. This misalignment enables the measurement of two orthogonal polarizations, here E_φ and E_θ, with highly repeatable amplitude- and phase measurements. A 3D-printed collet was used to ensure the correct alignment of the flanges and to rotate the receiving antenna, essentially constructing a sleeve bearing with the static waveguide flange. A photograph and CAD drawings of the receiver with a polarization switchable receive

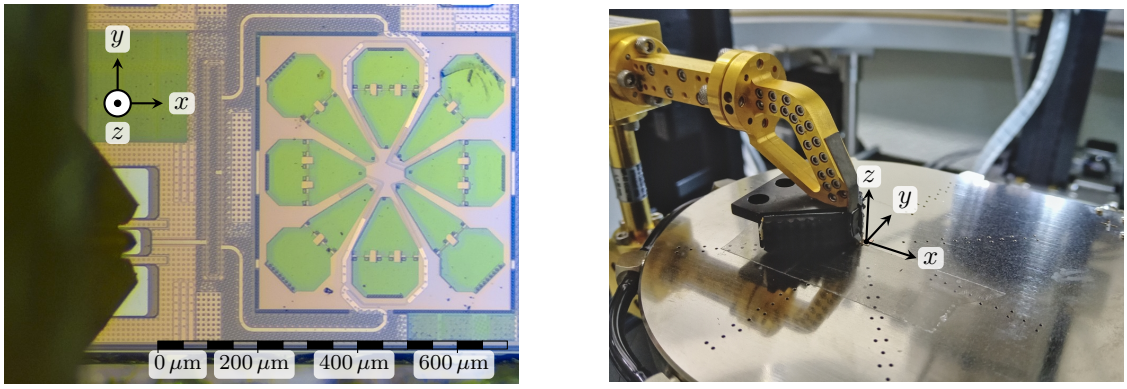

(a) (b)

Figure 6.27.: Measurement of the RHCP on-chip antenna (a) as a micrograph and (b) photograph with the absorber-covered on-wafer probe contacting the GSG pads.

antenna are shown in Fig. 6.28. To enable the rotation of the waveguides, the typically used alignment pins are removed, and the radial clearance of the collet-flange bearing determines the alignment accuracy. By measuring well-known polarized radiators like waveguide-based horn antennas, the repeatability of insertion loss and phase shift of this transition can be verified [A189].

The E_φ and E_θ components of the radiated far fields are measured in direct succession for each measurement point to reduce the phase error resulting from the movements of RF cables on measurement robots [197] and temperature drift of the measurement system. That approach increases the wear of the waveguide flanges; however, no change in the transmission properties of the polarization changer was observed after the antenna measurement. A superposition of the electric far fields E_φ and E_θ is performed according to

$$E_{\mathrm{RHCP}} = \frac{E_\theta - \mathrm{j}E_\varphi}{\sqrt{2}}, \qquad E_{\mathrm{LHCP}} = \frac{E_\theta + \mathrm{j}E_\varphi}{\sqrt{2}} \tag{6.2}$$

to obtain the measured RHCP and LHCP gain. The measured far fields are normalized using a well-known standard gain horn antenna and are depicted in broadside direction over frequency in Fig. 6.29 (a). For comparison, the far fields superimposed from the

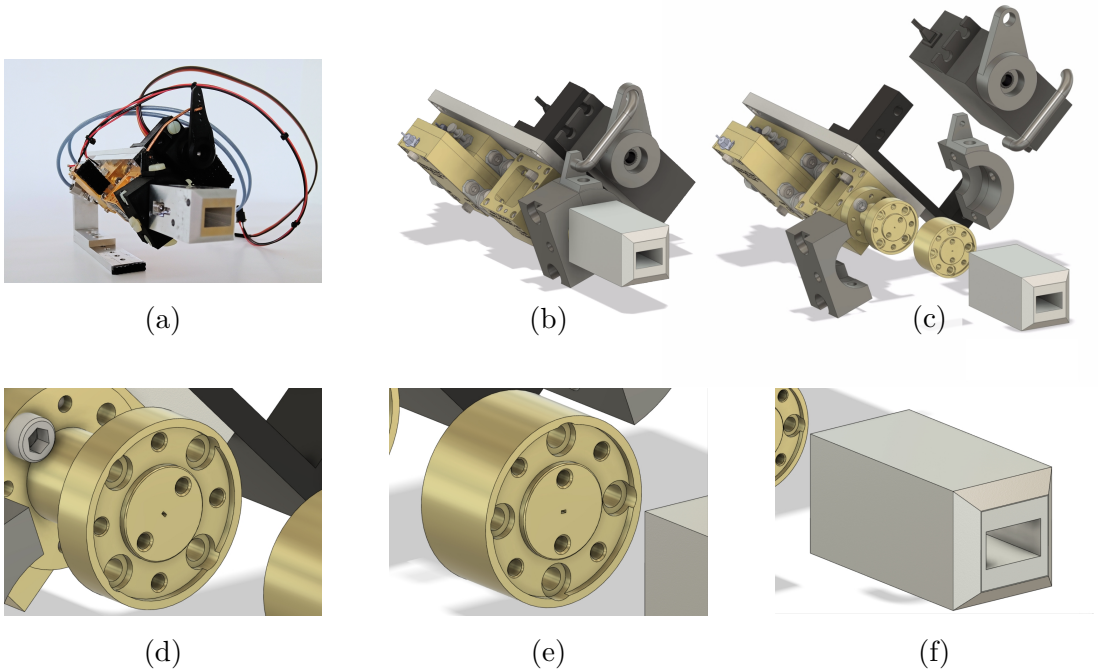

Figure 6.28.: Phase-stable polarization changer in E_φ-orientation as (a) a photograph, (b) CAD model assembled, and (c) CAD model in exploded view. The details of (d) the static waveguide flange, (e) the rotated flange, and (f) the attached rotated horn antenna are depicted to highlight the waveguide orientation.

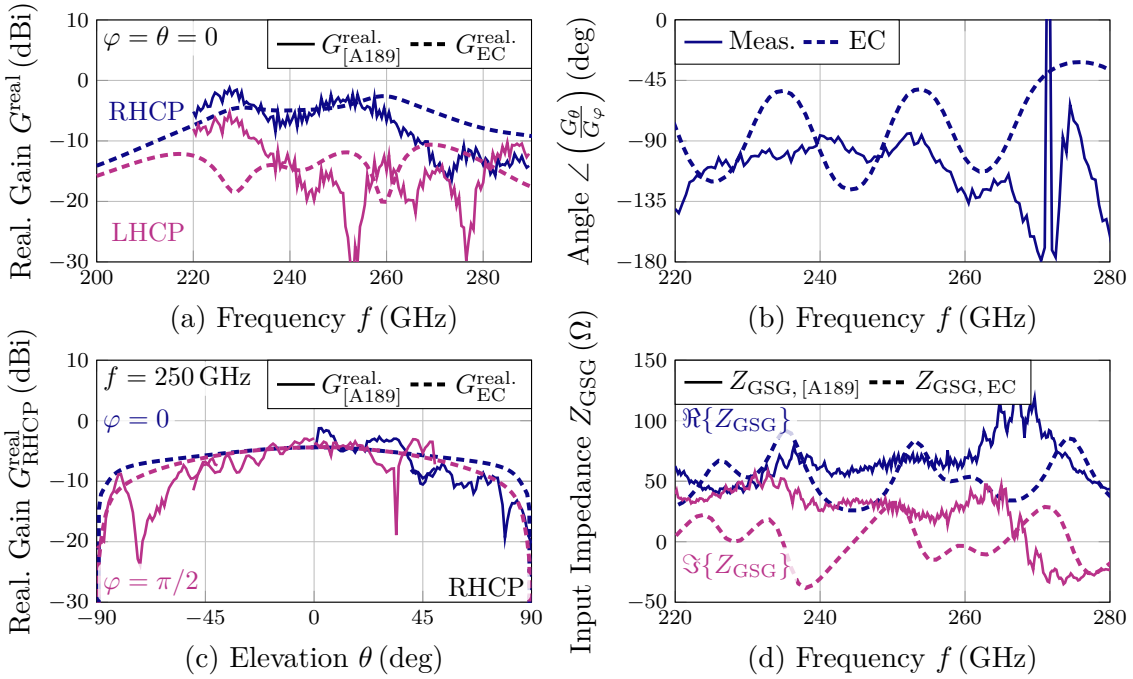

Figure 6.29.: Realized gain of (a) the RHCP antenna assembly over frequency in broadside direction ($\varphi = \theta = 0$), (b) phase difference between φ and θ polarization, (c) $\varphi = 0$ and $\varphi = \pi/2$ cut plane, and (d) input impedance comparing measurements from [A189] and the EC results.

EC representation are given as well. Here, the feeding network determines the feeding phase and amplitude of the single antenna arms. Since the radiation of each antenna arm is modeled using a current- or voltage-weighted superposition of the fundamental radiator contributions within the antenna arm, the overall far-field superposition is straightforward. When comparing the measurement with the EC result, the measured antenna exceeds the antenna gain predicted by the EC. Furthermore, a frequency shift between both solutions and a worse agreement for cross-polarisation (LHCP) is observed. First, the losses within the TL feeding network are calculated for the center frequency $f = 250\,\text{GHz}$, yielding an overestimation of the losses for lower and an underestimation of the losses for higher frequencies. Second, the bends and tee sections of the feeding network are not included in the EC model. Instead, only the geometrical length and effective permittivity of the TLs were considered to preserve the model's simplicity. Last, the measurement of the LHCP faces the same difficulties as the measurement of any other cross-polarization. It is discussed in [A189] that even small contributions of the RHCP radiated by the antenna and reflected at the probe yield an LHCP contribution. This issue is also seen in the disagreement for the LHCP predicted by measurement and simulation. To further evaluate the feeding network, the obtained phase relation between E_θ and E_φ is given in Fig. 6.29 (b). The phase approaches the desired $-90°$ in a wide bandwidth, although the EC simulation shows much larger undulations than the measurement. Again, the EC uses a simplified

model for the feeding network, which neglects dispersion, frequency-dependent losses, and coupling between the lines. Although the framework to describe coupled lines has been described for a long time [198, pp. 9], the effort to evaluate complex TL geometries using this framework is not comparable to convenient full-wave simulation tools, which allow for arbitrarily complex geometries. Thus, including coupled lines in the EC model is not pursued. Fig. 6.29 (c) shows the co-polarization in exemplary cut planes at 250 GHz; more cut planes and cross-polarization can be found in [A189]. Last, the input impedance seen through the balun and GSG pads is compared for measurement and EC model. Here, the resonant GSG pads are not modeled in the EC model, as they are designed to obtain a well-matched situation around 250 GHz. Furthermore, the measurement indicates a more inductive and less resonant behavior of the input impedance. The overall agreement between the on-wafer measurement and the EC model is still satisfactory. A more detailed investigation of the measured far fields and a comparison with FDTD results yielding outstanding agreement are shown in [A189].

6.2.5. Antenna Group Delay

Up to this point, the antenna prototypes have been discussed using well-established characteristics, such as gain, impedance, or efficiency. This chapter discusses the effect of group delay of the radar MMIC on the imaging capabilities of the radar system. For a transmission channel with no multipath contributions, the group delay calculates from the transmission coefficient T according to

$$\tau_{\mathrm{g}} = -\frac{\partial \angle(T)}{\partial \omega}. \tag{6.3}$$

It represents the physical delay of energy density per frequency slot through a system. In the context of ultra-wideband antennas, group delay is used to measure the transmission channel's quality including the antenna characteristic [199, pp. 83]. Here, the ideal group delay would be constant over the operating bandwidth, indicating a linear phase behavior and, thus, no phase distortion. A pulse transmitted via this system would maintain its shape, i.e., its general appearance and its pulse width. The actual group delay of any frequency-selective system represents a distortion of the channel, which will broaden the pulse due to the different run times of the different frequency components. Since Maxwell's equations require any frequency $f > 0$ to enable propagating waves, every antenna shows at least a high-pass behavior and, thus, a distortion of the transmission phase. Both antenna prototypes presented in this chapter are assemblies of resonant antennas. Although their performance was described as wideband or increased bandwidth, they are essentially multi-resonant. If not appropriately compensated, the resulting frequency-dependent group delay affects their performance in a radar system. Generally speaking, the straightforward radar theory presented in Sections 2.1.1 and 2.1.2 assumes a non-dispersive channel, implying that all frequency components of the utilized radar bandwidth face the same delay in the

radar channel. As the delay is used to estimate the target distance, any disturbance directly affects the radar imaging ability. In [A133], the effect of the multi-resonant CP antenna utilized in a fictive 1×16 Single Input Multiple Output (SIMO) system is investigated. It is shown that the distortion of the phase-fronts has a severe impact on the image quality of the radar system and that a partial compensation using a type of radar calibration [18], [200] is possible. Before the group delay of an antenna can be considered in the radar system, it needs to be determined. Only the RHCP is considered here, as the antenna dominantly radiates this component. An approach using a full-wave FDTD solver and the general measurement setup is described in [A133] and repeated here shortly. In both cases, the transfer function between the antenna and an arbitrary point in the far field must be accessed over a broad bandwidth. Furthermore, the frequency resolution should be sufficiently fine to calculate the derivative from (6.3) numerically. In an FDTD solver, the time-domain response of the system under test is explored, such that the broadband evaluation of the radiated far fields in specific points is straightforward and involves only an FFT. Last, any multipath contributions within the simulation and measurement setup must be suppressed for a precise group delay measurement.

Fig. 6.30 (a) shows the schematic measurement setup and methods to control multipath contributions and (b) the corresponding measurement photo. The transmission coefficient S_{21} evaluates the received signal strength compared to the transmitted signal strength, and its group delay is evaluated using (6.3). Any multipath reception within the measurement yields interference at the receiver, ultimately hindering the calculation of a reasonable antenna group delay. For example, the scatterer within the free space wave propagation in Fig. 6.30 (a) will scatter waves transmitted from the antenna into the receiving horn antenna. The utilized microscope, horn-antenna, and mm-wave chuck are covered with pyramidal absorber material to reduce these free space scattering effects. Furthermore, reflections within the waveguides due to mis-

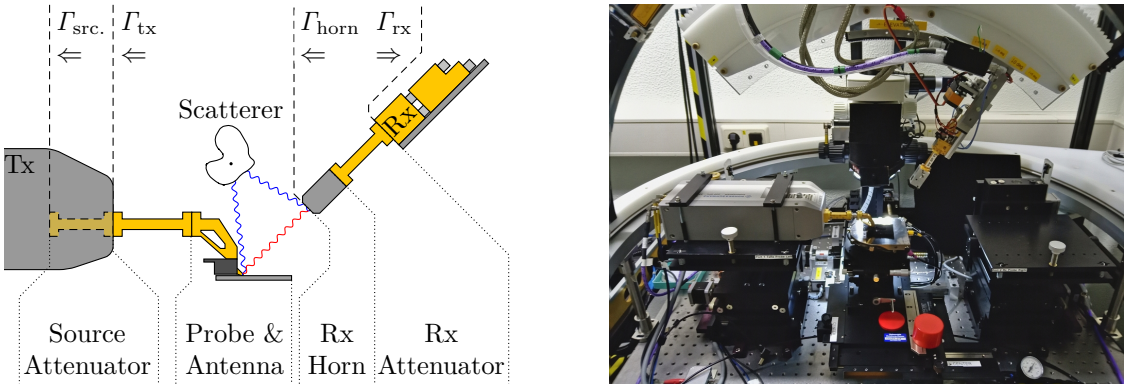

(a) (b)

Figure 6.30.: Group delay characterization for the CP on-chip antenna in the spherical wafer antenna measurement setup (a) as schematic drawing and (b) photograph of the measurement (cf. [A105]).

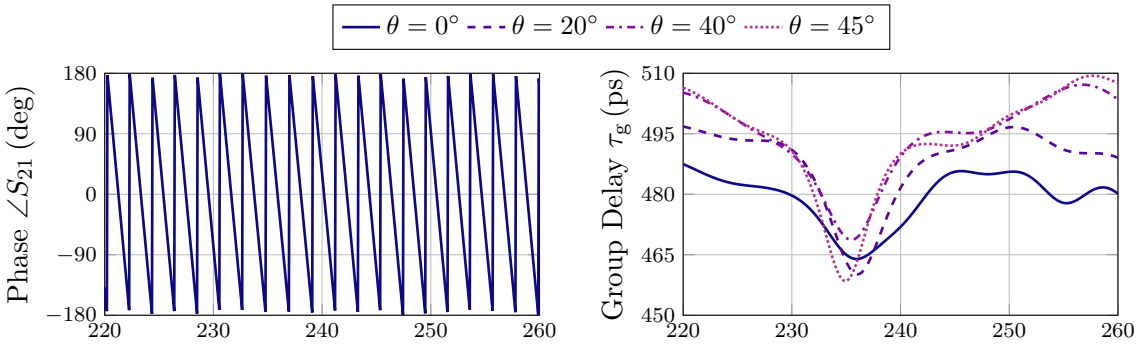

(a) Frequency f (GHz) (b) Frequency f (GHz)

Figure 6.31.: Measured phase (a) of the transmission coefficient S_{21} between CP on-chip antenna and measurement horn antenna for the broadside direction ($\varphi = \theta = 0°$) and (b) resulting group delay for different elevation angles θ at $\varphi = 0°$ (cf. [A133]).

match can yield multipath effects, as discussed in the following. Practically, even a well-matched on-chip antenna will cause reflections at the tips of the on-wafer probe, which yields a wave traveling back into the Tx. Suppose this signal faces a mismatch Γ_{tx} at the transmitter reference plane caused by, e.g., a source mismatch $\Gamma_{\mathrm{src.}}$. In that case, it will be reflected into the antenna, partially radiated into space, and then received by the Rx, yielding a second contribution with an additional delay proportional to twice the feeding waveguide length. The variable source attenuator is set to $\approx 15\,\mathrm{dB}$ to reduce this contribution, which on the one hand, reduces the system's dynamic range by $\approx 15\,\mathrm{dB}$, but on the other hand, the reflection coefficient due to source mismatch could be reduced up to $\approx 30\,\mathrm{dB}$, if the waveguides were in perfect alignment. Furthermore, it was found that the receiver mismatch Γ_{rx} is significant for the delicate group delay measurement, such that the here reflected signal is fed back into the Rx horn. Here, the reflection of the horn antenna Γ_{horn} resulted in a second wave traveling into the receiver, again with a round-trip time proportional to the horn- and Rx-waveguide length. Again, this round-trip contribution is sufficiently suppressed using a fixed 15 dB waveguide attenuator. Last, a system error correction, or VNA calibration, was performed using waveguide calibration standards, and the S-matrix of the on-wafer probe was measured separately and compensated as well. The use of the attenuators and other effects for measurement of antenna group delay can be found in [201].

The measured received phase $\angle S_{21}$ and group delay τ_{g} are depicted in Fig. 6.31 for a time-gating window of 288 ps length. An exemplary $\varphi = 0$ plane is shown for different angles θ to discuss the change in group delay along the elevation axis. As a result of the time-gating, both group delay and especially phase are exceptionally smooth for a mm-wave on-wafer measurement, such that the efforts made to reduce any multipath and the related interference effects appear successful. In [A133], a simulation with three targets at different positions in front of a SIMO radar is carried out, as

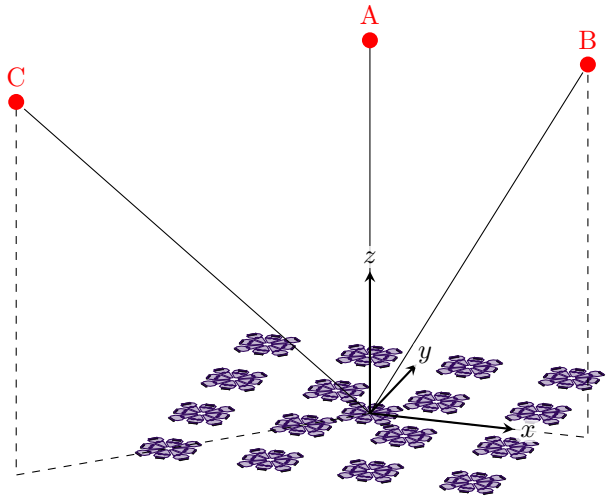

Figure 6.32.: Drawing of the 1 × 16 SIMO array with three radar targets A, B, and C. The locations of the targets related to the Tx antenna center are also given. For clarity, neither the antenna-to-antenna spacing within the array nor the distance to the targets is to scale.

depicted in Fig. 6.32. For each target, the corresponding position relative to the central Tx antenna is also given. The considered array utilizes 1 Tx and 16 Rx antennas, and the measured group delay associated with the target positions is applied to the simulated received signal. Based on different compensation methods, the group delay is compensated using the antennas' broadside-group delay ($\varphi = \theta = 0$). Fig. 6.33 (a) shows the simulated range along the z-axis ($\theta = 0$) with an SNR of 20 dB and the applied group delay. Although all three targets can be identified, the detailed view in Fig. 6.33 (b) reveals the effect of group delay. The solid curve without group delay indicates the narrowest pulse for target A and two broader pulses for targets B and C, which are off-broadside directions. With the applied group delay and no compensation, the broadside pulse in particular, and all other target pulses in general, are widened significantly, effectively reducing the radar resolution. Using any of the suggested compensation methods (cf. [A133]), the group delay is equalized successfully, finally achieving a narrow pulse again. A more detailed discussion of the off-broadside targets and different imaging cut planes are given in [A133]. Finally, it should be noted that the group delay compensation was applied to the IF signals before any radar processing. On the one hand, this simplifies postprocessing since data acquisition, group delay compensation, and radar imaging can be carried out independently. On the other hand, this compensation is suboptimal for targets far off broadside, as the antenna group delay for these directions differs from the broadside group delay (cf. Fig. 6.31 (b)). The group delay processing could conceivably be also implemented into digital beamforming algorithms, for example, by applying the optimal group delay compensation to each pixel or voxel; however, the computational effort rises with this method, and convenient simplifications (such as FFT-beamformers [44]) cannot

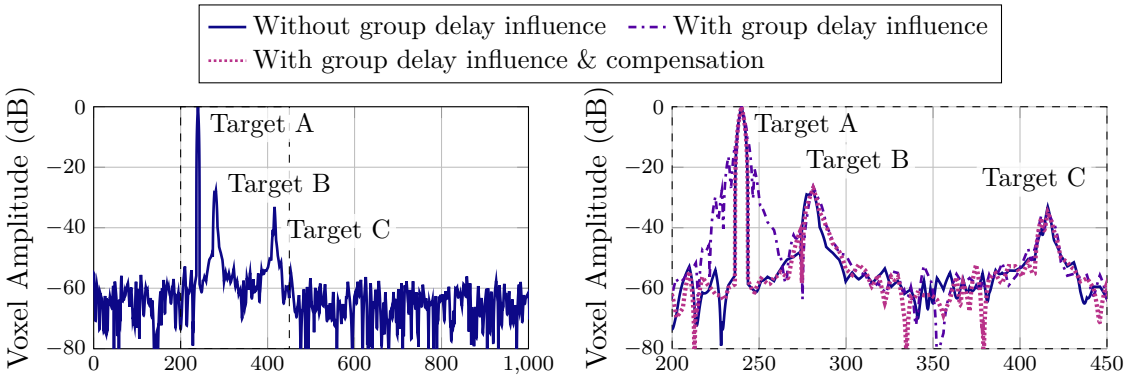

(a) Distance z (mm)

(b) Distance z (mm)

Figure 6.33.: Radar images (a) along the z-axis calculated with a radar simulator (cf. [A133]) considering the antenna group delay and (b), with a magnification for the dashed region in (a), for different cases indicating the compensation ability.

be applied straightforward.

To conclude this section, the group delay dispersion of the antenna prototypes presented here is relevant for radar systems, and it needs to be adequately compensated, e.g., by radar calibration methods.

6.3. Frequency-dependent Polarized Antenna

Based on the results and limitations of the previous candidates, an improved antenna prototype operating between 350 GHz and 450 GHz will be presented in this section. Compared to the earlier approaches, this antenna features a variable polarization, i.e., the polarization vector rotates counter-clockwise with increasing frequency. Here, the capacitive discontinuity is implemented using an interdigital capacitor to reduce the dependence on an accurate layer-stack model (cf. Section 6.4.2) and enable laser-trimming of the antenna. The overall covered relative and absolute bandwidth is increased by utilizing 4 dipole arms of different operating frequencies. However, the large size of this antenna rules out a standard $\lambda/2$ array configuration. As for the previous prototypes, the following sections explain the core antenna concept, provide an EC model for the single radiators, and compare EC, full-wave FDTD, and measurement results.

6.3.1. Design Concept

Four dipoles with the resonance frequencies $f_A = 367\,\text{GHz}$, $f_B = 389\,\text{GHz}$, $f_C = 411\,\text{GHz}$, and $f_D = 433\,\text{GHz}$ are combined using the $\lambda/4$ transformer approach from

above to enhance the operating bandwidth. As shown in Fig. 6.34, the antennas are geometrically arranged in a circle, where the antenna feeding points are separated in azimuth by 45°. Each radiator is rotated to geometrically conform to its azimuth feeding position, which, in combination with the frequency selective feeding network, yields a rotation of the radiated polarisation over the operating bandwidth. Two opposing radiators are geometrically equivalent to form a dipole, and a differential feeding topology or balun in the Tx path or the Rx path is required for a symmetric radiation pattern. The isolated mono- or dipoles will be termed A, B, C, and D with increasing operating frequency. Compared to the RHCP antenna in Section 6.2, the geometrical offset is not used to obtain a CP but to increase the operating bandwidth. Due to the geometrical rotation, the coupling between the single radiators is reduced, thus easing the general design process. As before, the monopoles are designed to occupy the available chip area in this circular arrangement.

6.3.2. Geometry and EC

The single radiators used for this antenna are geometrically equivalent except for the interdigital capacitance used to obtain the capacitive discontinuity. Fig. 6.35 (a) depicts antenna A exemplarily. The antenna consists of two tapered sections which terminate into a circular open circuit. Both sections are separated using an interdigital

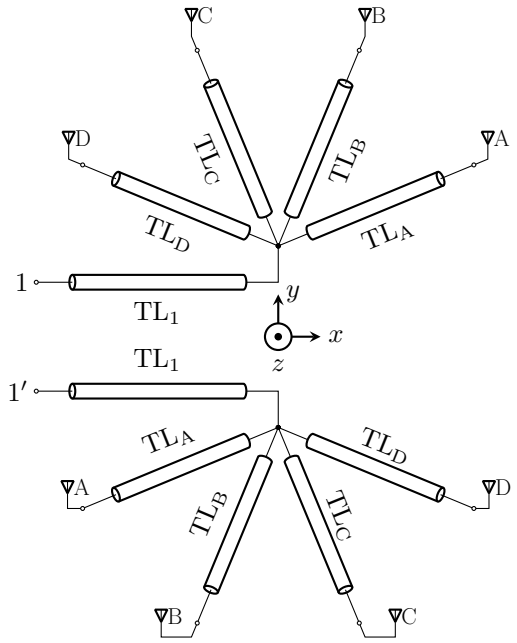

$\mathrm{TL}_1 : \ell \approx 400\,\mu\mathrm{m}$, $Z_\mathrm{C} = 50\,\Omega$
$\mathrm{TL}_\mathrm{A} : 90°@367\,\mathrm{GHz}$, $Z_\mathrm{C} = 92\,\Omega$
$\mathrm{TL}_\mathrm{B} : 90°@389\,\mathrm{GHz}$, $Z_\mathrm{C} = 82\,\Omega$
$\mathrm{TL}_\mathrm{C} : 90°@411\,\mathrm{GHz}$, $Z_\mathrm{C} = 77\,\Omega$
$\mathrm{TL}_\mathrm{D} : 90°@433\,\mathrm{GHz}$, $Z_\mathrm{C} = 76\,\Omega$

Figure 6.34.: Exemplary antenna feeding network for frequency selectivity between the antennas A, B, C, and D. Each antenna is rotated by 45° to the neighboring antennas. The characteristic impedances of the TLs and their corresponding electrical lengths are also given.

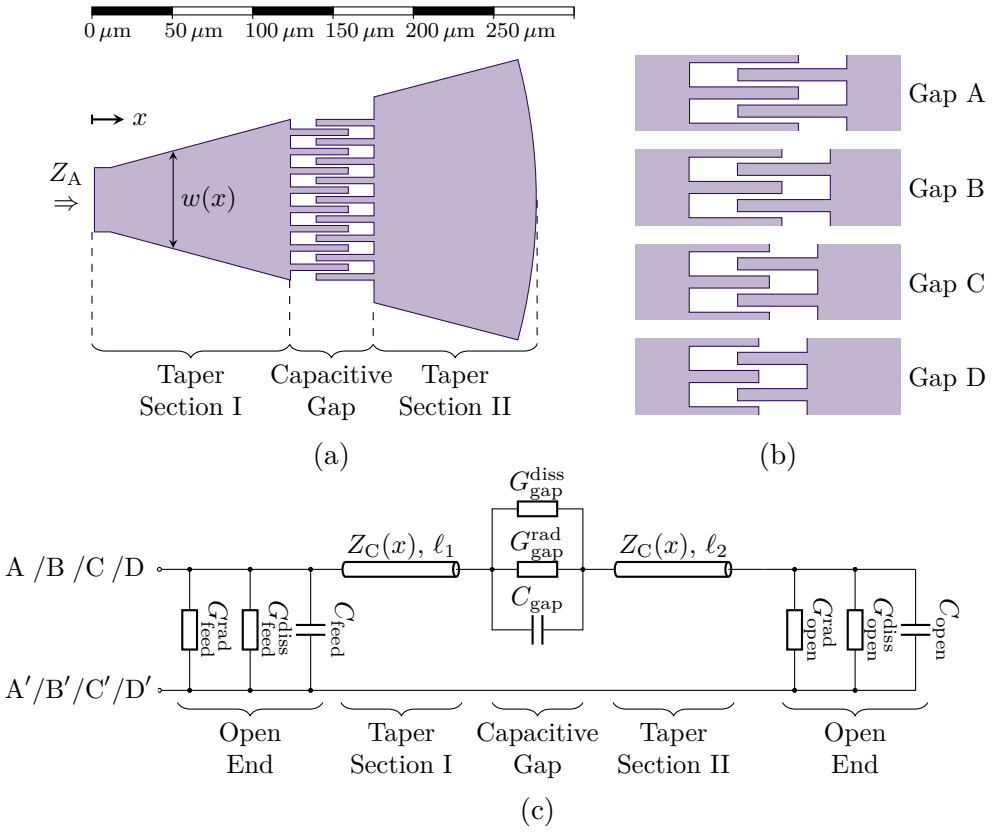

Figure 6.35.: Geometry in top view for (a) the exemplary antenna arm A, (b) the different geometrical realizations of the interdigital gap, and (c) corresponding EC representation. Selected antenna parts are highlighted in geometry and circuit representation.

capacitor, which is used to tune the operating frequencies of the different antennas. All four capacitance implementations are depicted in Fig. 6.35 (b), where the overlapping longitudinal edges of the capacitive fingers decrease to obtain an increasing operating frequency. The corresponding simplified EC model with the open circuit at the feed point, the tapered TL sections, the capacitive gap, and the terminating open end is given in Fig. 6.35 (c). As discussed for the CP antenna, the tapered section will be modeled in the EC as a discontinuity in the MSL width and, although not shown in the EC for clarity, yield further radiation contributions.

A detailed drawing of the interdigital capacitance with essential lengths and the corresponding dimensions for each antenna are given in Fig. 6.36 and Table 6.3. The geometry of the interdigital structure is chosen for compatibility with the DRC. Compared to the previous compact implementations utilizing the floating layers, the typically used capacitance values require relatively long fingers with large overlap resulting in overall longer capacitances. In combination with the thin finger width w_{finger}, the interdigital cap is expected to show increased ohmic losses to floating layer capacitances of similar values. The upside of this implementation is the reduced dependence on the

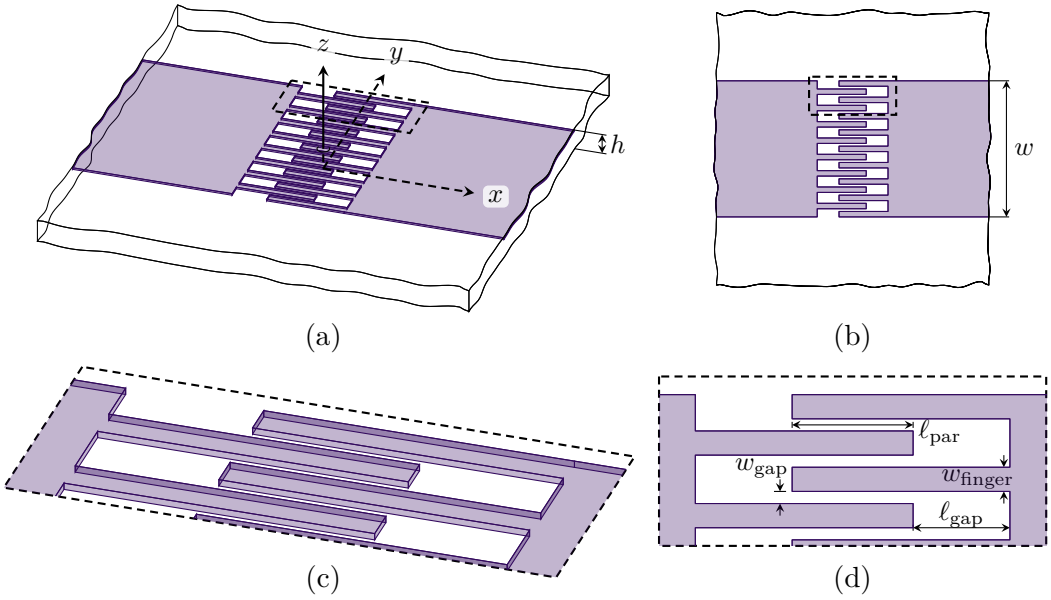

Figure 6.36.: Interdigital gap geometry of the exemplary antenna arm A (a) in perspective and (b) in top view. A close-up in (c) perspective and (d) top view in the outlined area is also given.

	Antenna Type				
Label	A	B	C	D	Description
$\min(w(x))$	40 μm	40 μm	40 μm	40 μm	Narrowest antenna width
$\max(w(x))$	176 μm	176 μm	176 μm	176 μm	Widest antenna width
ℓ_1	150 μm	146.5 μm	143.5 μm	142 μm	Length of taper section I
ℓ_2	125 μm	128.5 μm	131.5 μm	133 μm	Length of taper section II
w_{gap}	2 μm	2 μm	2 μm	2 μm	Cap. gap width
w_{finger}	8 μm	8 μm	8 μm	8 μm	Cap. finger width
ℓ_{gap}	16 μm	16 μm	16 μm	16 μm	Finger gap length
ℓ_{par}	19.9 μm	14.8 μm	10.5 μm	7.1 μm	Parallel finger length

Table 6.3.: Dimensions of the antenna arms A, B, C, and D for the frequency-dependent polarized antenna.

thickness and relative permittivity of the dielectric between the metal layers since this dependence resulted in a severe frequency shift for the linear polarized antenna from Section 6.1. Furthermore, single fingers of the interdigital structure could be isolated using a laser-trimming process to enable a discrete tuning of the capacitance after fabrication.

Whereas the previous gap implementations could be approximated well using the electrostatic capacitance C_{gap} and a conductance dominated by the radiation losses, the interdigital capacitance results in a more complex frequency dependence and, furthermore, non-negligible ohmic losses. For convenience and compatibility with the

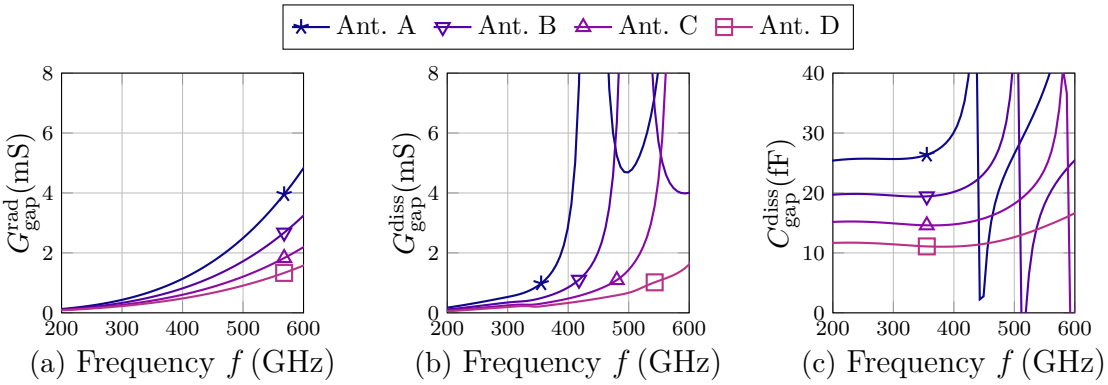

Figure 6.37.: Circuit elements of the interdigital capacitance for the shunt EC. The radiation conductance (a) is calculated using the analytical result in (5.83), and the dissipation conductance in (b) and gap capacitance in (c) are extracted from a full-wave FDTD simulation similar to [A23].

previously used EC model, the shunt circuit represents the gap using a dissipation conductance $G_{\mathrm{gap}}^{\mathrm{diss}}$, a radiation conductance $G_{\mathrm{gap}}^{\mathrm{rad}}$, and a capacitance C_{gap}. A model including the metal losses as a series resistance and the inductance of the interdigital structure is conceivably possible. This model would highlight the self-resonant behavior of the interdigital capacitor; however, it is optional for an accurate EC description of the antenna and thus left out for simplicity and consistency with the previous EC model of the capacitive gap. The frequency-dependent parameters of the shunt circuit model are extracted from a full-wave simulation similar to the approach from [A23], and the radiation conductance is calculated according to (5.83). All parameters are depicted for the different antennas as a function of frequency in Fig. 6.37. Within the calculated frequency range, the resonance frequency of the interdigital gap can be recognized for the antennas A, B, and C at 440 GHz, 510 GHz, and 600 GHz, respectively. This resonance is characterized by a rapidly changing capacitance and a peaking dissipation conductance. Since the capacitive gap is implemented to increase the radiation efficiency, the antenna's operating frequency must be below the resonance frequency of their respective interdigital capacitances. In contrast to the previous implementations of the capacitive discontinuity, the dissipation conductance is of a similar order of magnitude as the radiation conductance, which ultimately limits the radiation efficiency achievable with this approach.

As in the previous chapters, a thorough EC model, including the radiation contributions of the open circuit, the capacitive discontinuity, and the tapered MSL section, is constructed for each antenna and calculated using the *ABCD* matrix approach for the port parameters and the radiation postprocessing to consider the coupled radiation sources and the corresponding radiated fields. For comparison, the single antennas are investigated using a full-wave FDTD solver. A comparison of the simulated input-impedances is given in Fig. 6.38, indicating a good agreement between EC

and FDTD solution for the fundamental operation mode. The higher-order resonance, which corresponds to a λ-current distribution along the antenna, is predicted to be slightly too high, indicating an imperfect capacitance extraction. At $\approx 450\,\mathrm{GHz}$, the input impedance of antenna A (cf. Fig. 6.38 (a)) exhibits a minor resonance in the impedance, which is undoubtedly caused by the resonance of the interdigital gap (cf. Fig. 6.37 (c)). This resonance is not recognizable in the input impedance for the other antennas. The loss mechanism in the interdigital capacitance is also recognizable when observing the current density at the antenna's operating frequency. Figs. 6.39 (c) and (d) show the projection of the current density simulated using the FDTD method for the antennas A and D. The dominant peaking current in the fingers of the capacitive discontinuity is, besides the skin-effect in the tapered MSL section, clearly visible. For comparison, the current distribution calculated using the EC is given with the integrated longitudinal current density from the FDTD method in Figs. 6.39 (a) and (b). Except for the discontinuity, where the distributed design of the interdigital gap can be recognized in the FDTD simulation compared to the concentrated capacitance utilized in the EC model, the current is in good agreement. Finally, the radiation postprocessing (cf. 5.4.3) is used to calculate the radiation efficiency of the single antennas. To consider the dipole arrangement planned for the overall antenna assembly, two identical monopoles are considered in opposing directions and with inverse feed currents, as for the CP antenna above (cf. Fig. 6.23). The resulting radiation efficiency

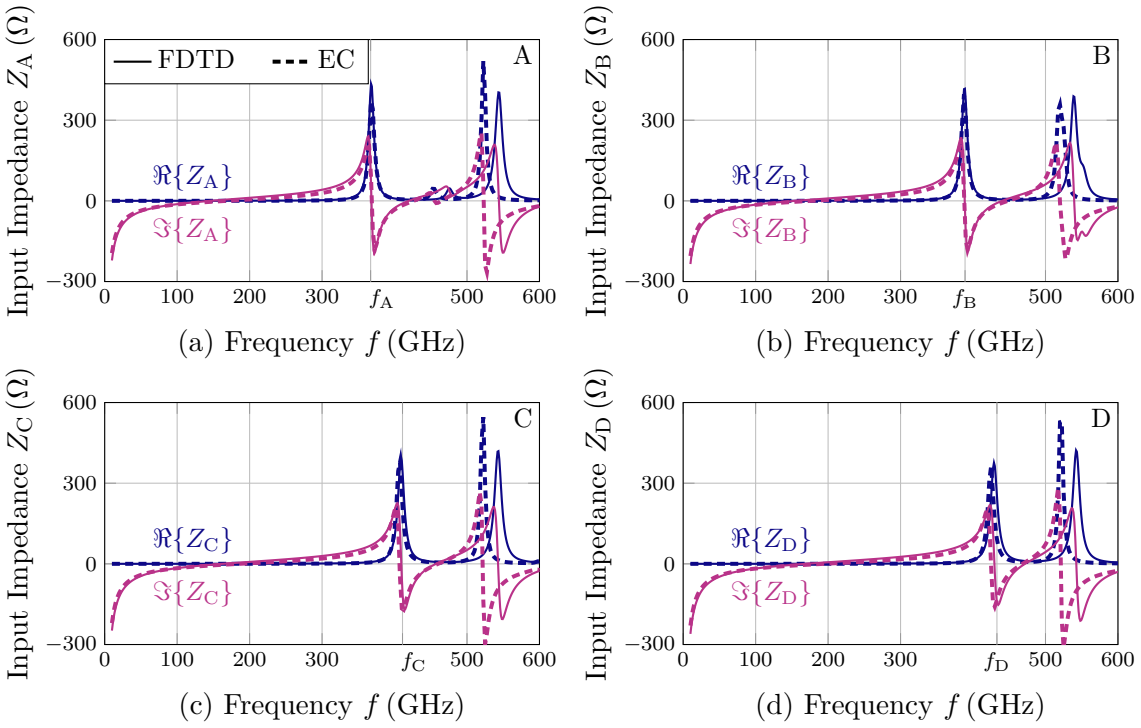

Figure 6.38.: Comparison of the input impedance for the antennas A, B, C, and D calculated by the EC and an FDTD solver.

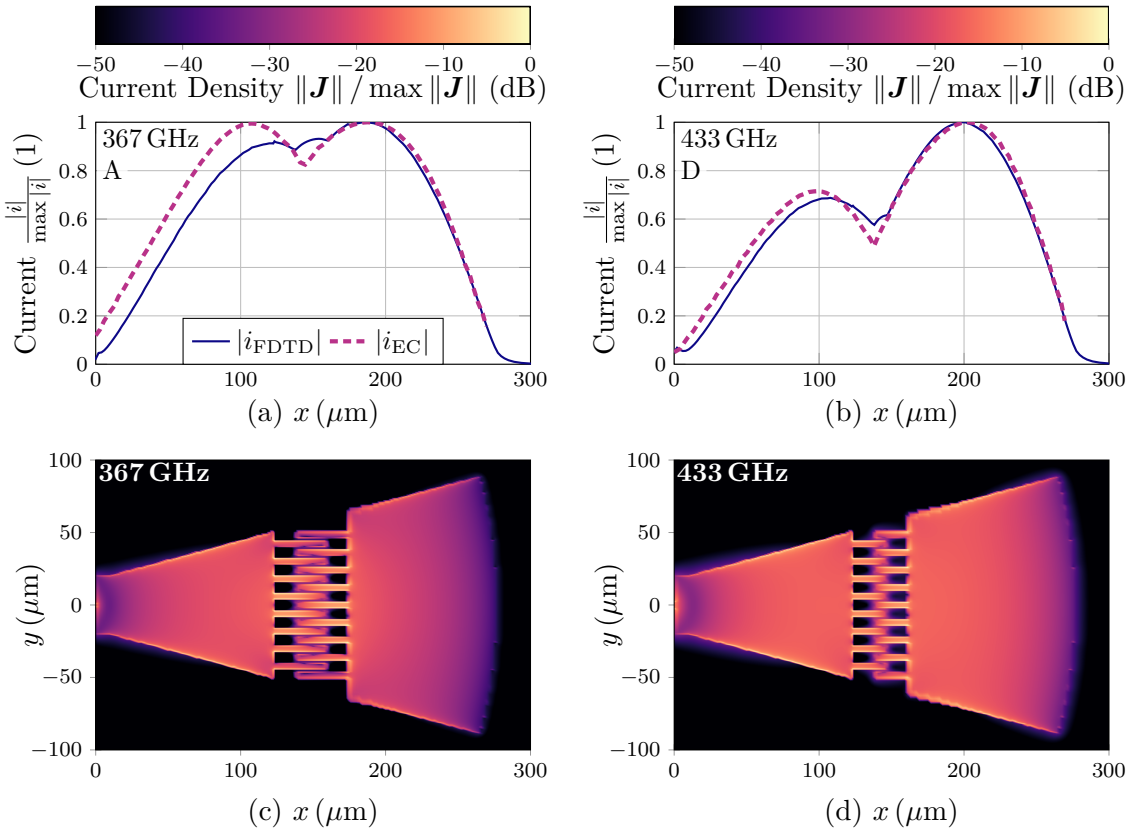

Figure 6.39.: Current distribution along the antenna length (a, b) and the projection of the current density into the x-y-plane calculated using an FDTD method (c, d) for the antennas A and D.

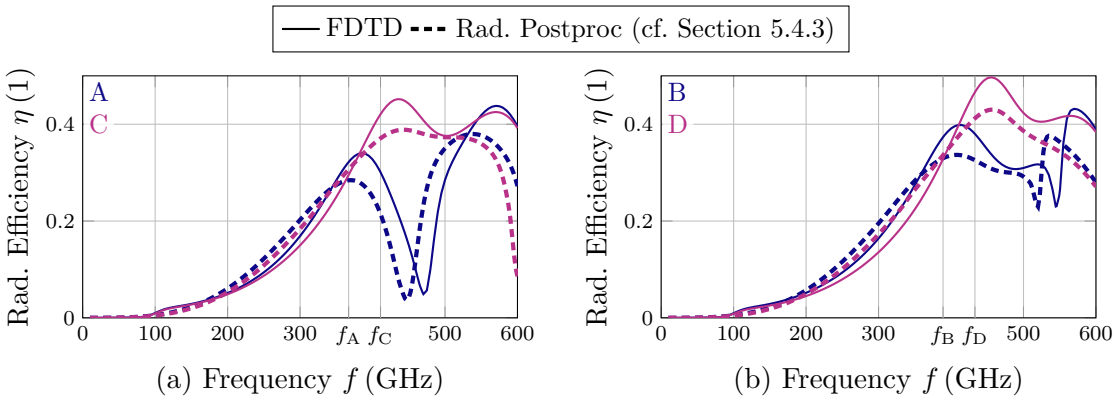

Figure 6.40.: Comparison of the radiation efficiency for (a) the antenna elements A and C calculated by the different circuit-based approaches and an FDTD solver, and (b) for the antenna elements B and D.

is depicted in Fig. 6.40 and compares, except for a small frequency shift probably caused by the extracted data of the capacitance (cf. Fig. 6.37), well with the FDTD results. Furthermore, antennas A and B show a significant efficiency minimum above the operating frequency caused by the capacitive discontinuity's resonance resulting from the high ohmic losses within the gap. Since this minimum is sufficiently separated from the antenna operating frequency and does not affect the input impedance significantly of the single antenna, a degradation of the antenna assembly performance is not expected.

6.3.3. Antenna Assembly

A schematic drawing of the antenna assembly is given in Fig. 6.41. All radiators and the $\lambda/4$ feeding MSLs are implemented using the uppermost aluminum layer, and their width varies slightly between the antennas to optimize the matching bandwidth. More precisely, the $\lambda/4$ MSLs are designed to transform the input impedance of the single radiators A, B, C, and D (cf. Fig. 6.38) to $\approx 35\,\Omega$ for antenna A and to $\approx 25\,\Omega$ for all other radiators. The higher impedance for antenna A results from the limitations of the aluminum layer TL width, which otherwise would result in severe losses. As seen from the drawing, the circular arrangement of the antennas utilizes most of the available chip area; the blank spaces in between are filled with metal grids on different layers to satisfy the metal density rules of the DRC. The antenna is fed from the negative x-direction utilizing two $50\,\Omega$ feed lines with a differential signal.

The input impedance at the $\approx 400\,\mu$m long feed line calculated by the EC and the FDTD simulation are compared in Fig. 6.42 (a) and show a good agreement. A reference impedance of $100\,\Omega$ should be considered for this differential antenna design resulting in a good matching over a wide bandwidth. Even further proof of the correct antenna operation can be obtained with the EC. Whereas the distributed current density within the radiators needed to be observed to gain insight into the operation, the EC allows direct accessing the input power at different poles within the circuit. Although these powers could be obtained from the field data or by recording voltages and currents within a full-wave simulation, they are directly accessible from the circuit simulation. Fig. 6.42 (b) shows the total power incident into each dipole pair, the overall accepted power, and the accumulated power fed into all dipoles normalized to the incident power. This comparison allows accessing mismatch losses by relating P_{acc} to P_{inc} or feed line losses by comparing P_{sum} to P_{acc} and proves the correct operation of the frequency selective $\lambda/4$ network.

A projection of the simulated current density into the x-y-plane is depicted for different frequencies over the operating bandwidth of the antenna assembly in Fig. 6.43. A rotation of the active antenna dipole with increasing frequency, which results in the rotating polarization of the antenna, can be recognized. At the highest depicted frequency, 460 GHz, the beginning operation of antenna A in the higher-order mode can be recognized by an increased current in the capacitive discontinuity.

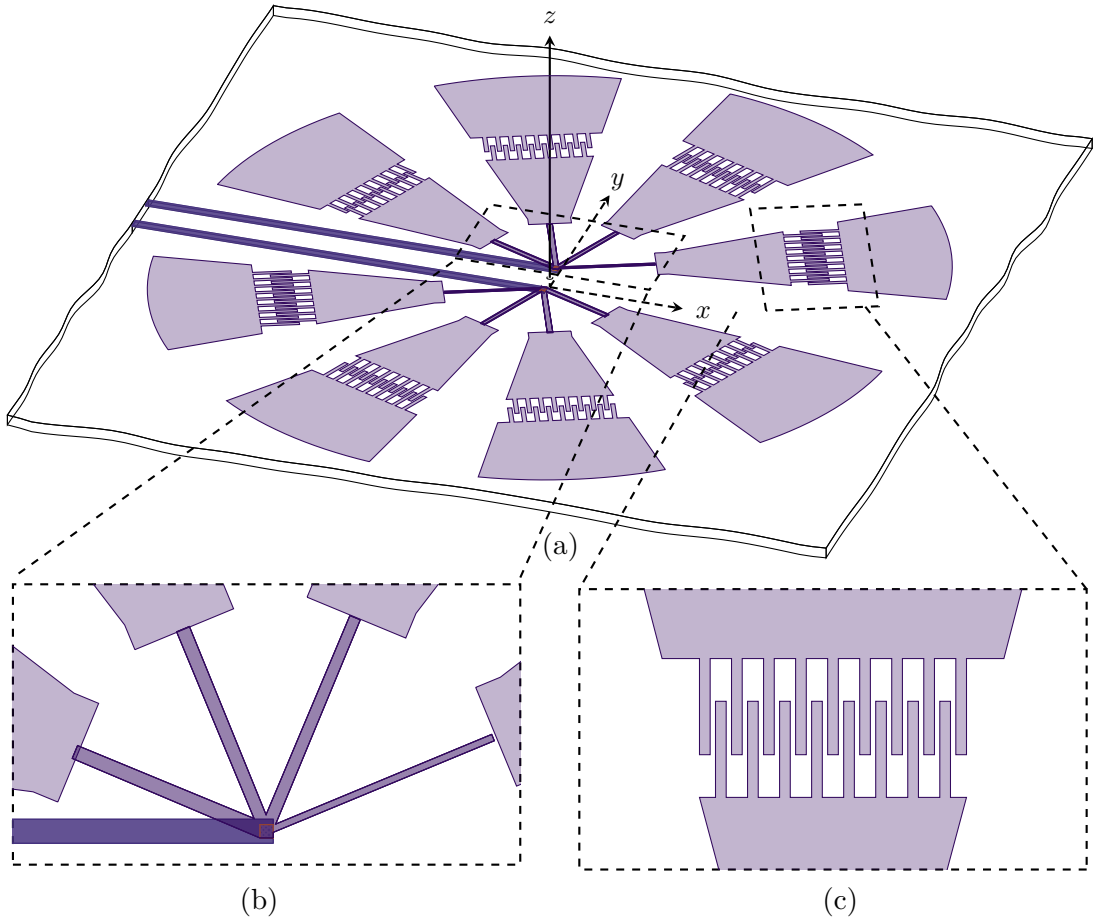

Figure 6.41.: Geometry (a) perspective view and detailed top view on (b) the feeding network and (c) the interdigital capacitor of antenna A.

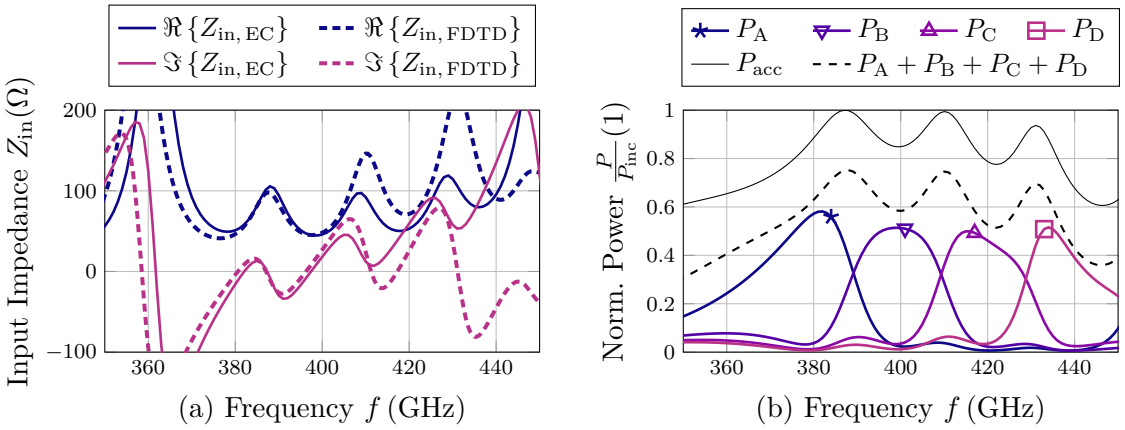

Figure 6.42.: Input impedance (a) of the antenna assembly calculated with the FDTD method and the EC evaluation and (b) accepted power at distinct positions within the feeding network calculated by the EC.

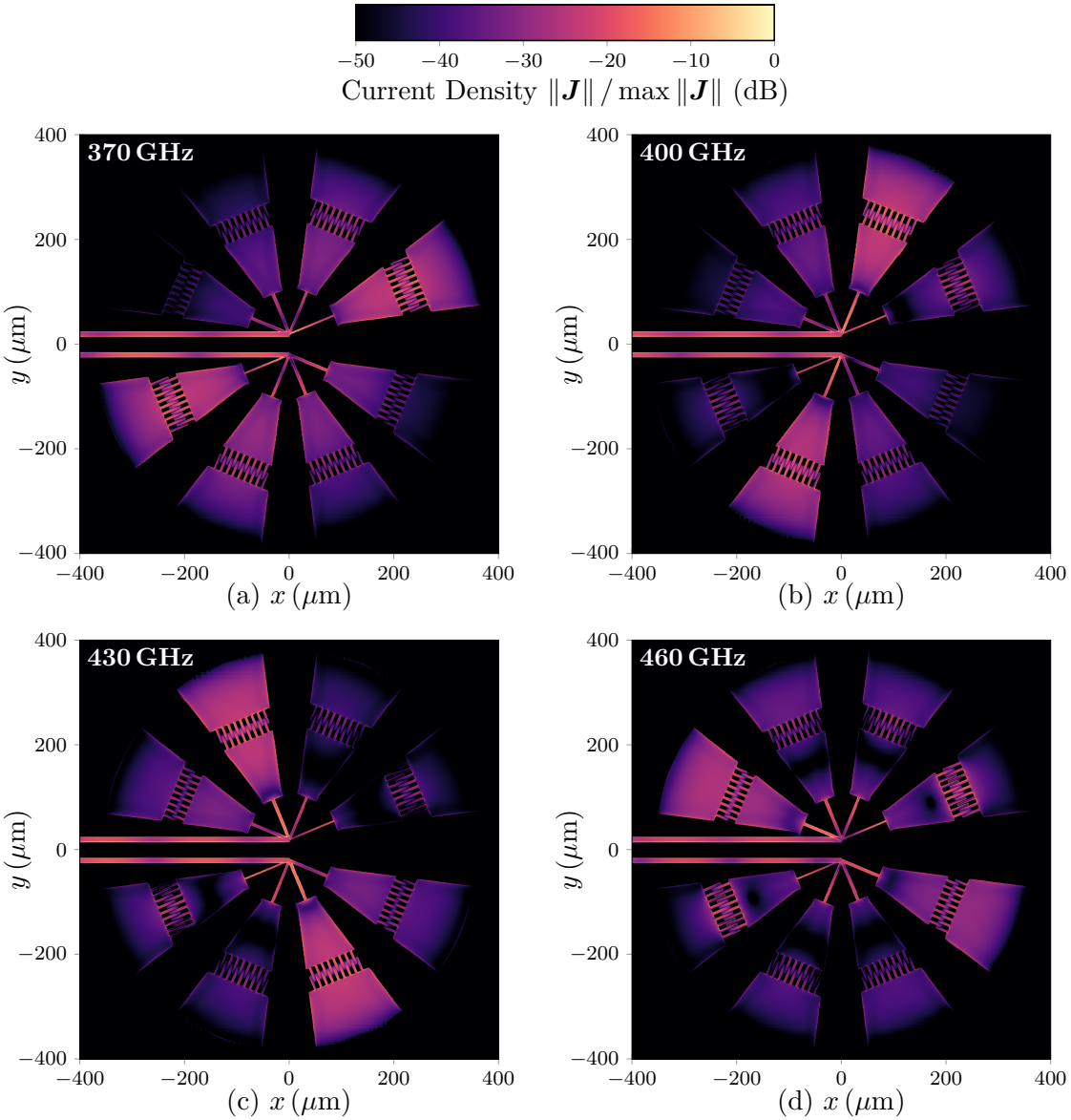

Figure 6.43.: Simulated current density projected from all metal layers into the x-y-plane at (a) 370 GHz, (b) 400 GHz, (c) 430 GHz, and (d) 460 GHz.

6.3.4. Antenna Measurement

The antenna is fabricated in Infineon's B12HFC process and characterized in the far field to prove the broadband operation. A photograph of the absorber-covered on-wafer probe contacting the on-chip antenna and a schematic drawing including the utilized coordinate system are depicted in Fig. 6.44. Although most of the probe tip is covered using a curtain of absorbers, the small uncovered metal housing for the GSG tips can still be seen in the photograph and drawing, which supposedly influences the measured radiation pattern close to $\varphi = 0°$. Since this antenna is the first on-chip

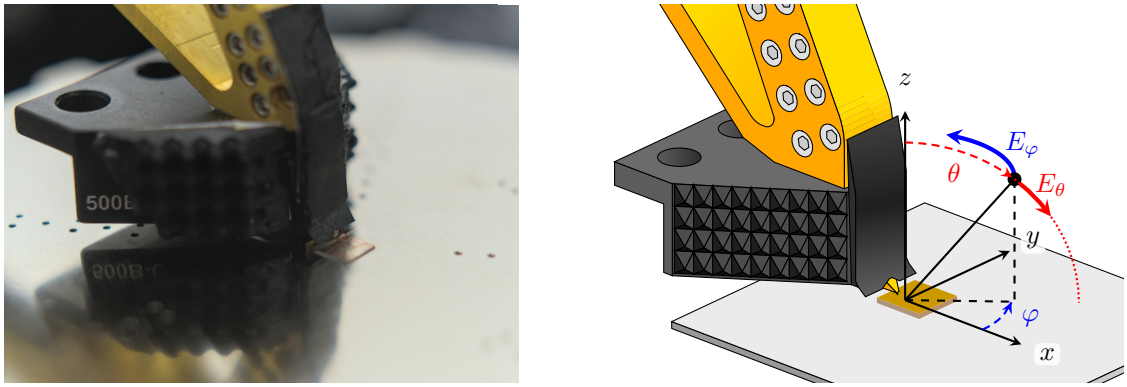

(a) (b)

Figure 6.44.: On-wafer probe contacting the chip antenna as (a) photograph and (b) schematic drawing with measurement coordinate system.

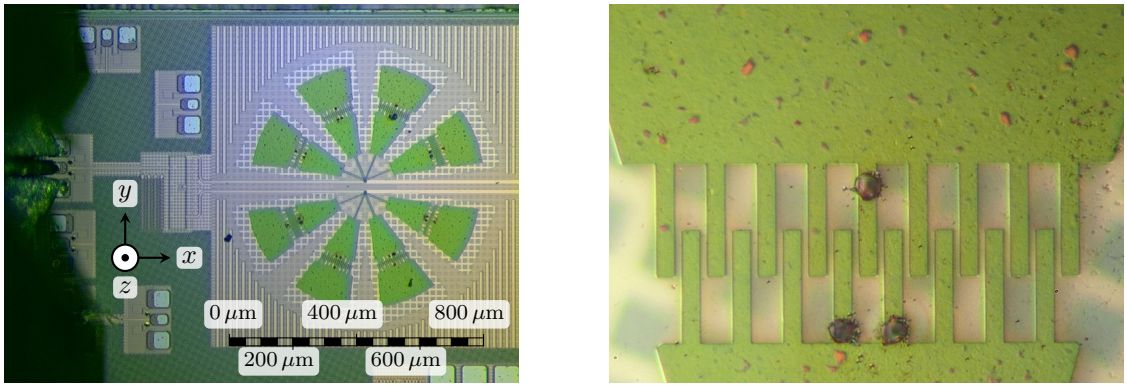

(a) (b)

Figure 6.45.: Micrograph of (a) the broadband on-chip antenna with rat-race coupler balun and (b) detail view on the laser-trimmed capacitive discontinuity, leaving only 14 of the 17 fingers for the capacitive discontinuity.

implementation utilizing the interdigital capacitor, a frequency shift of the prototype was not expected but considered a possibility. By laser-trimming single fingers of the capacitance, the gap discontinuity can be increased to increase the operating frequency. An initial measurement of the broadside gain has shown a severe frequency shift by $\approx -40\,\mathrm{GHz}$. Consequently, three interdigital fingers have been separated using an ultra-violet laser to obtain the desired operating frequency range. A micrograph of the antenna prototype contacted by the on-wafer probe and of the capacitive gap with the three separated fingers are given in Fig. 6.45. An in-depth discussion of the benefits and drawbacks of the different on-chip capacitor implementations, including the difference between simulated and fabricated prototypes, is given in Section 6.4.2.

The realized gain of the antenna is accessed in a far-field measurement utilizing a 25 dBi horn antenna as a reference. To eliminate losses caused by the measurement

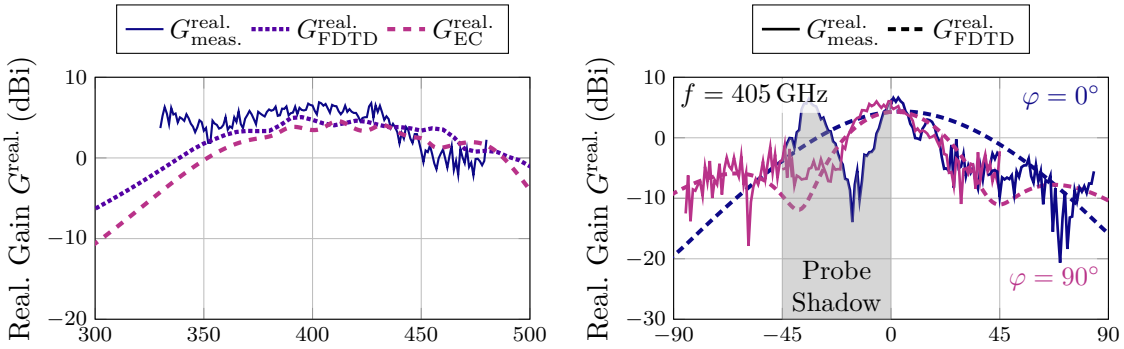

(a) Frequency f (GHz)

(b) Elevation θ (deg)

Figure 6.46.: Realized gain for the antenna assembly (a) over frequency, as well as (b) in $\varphi = 0°$ plane and $\varphi = 90°$ plane comparing measurement, EC, and FDTD results.

system, the losses of the on-wafer probe, the GSG pads on the chip, and the E-plane waveguide bend used to connect the horn antenna have been accessed separately. The characterization of the bend is straightforward using a commercial waveguide calibration kit, and the losses of the on-wafer probe have been accessed by combining two calibration kits. As the probe resembles an interface between a rectangular waveguide and the on-chip environment, the calibration kit for the waveguide is utilized to define the reference plane at the waveguide port of the probe, and an on-wafer Open-Short-Match (OSM) calibration is used to determine the error two-port of the probe, essentially containing the transmission loss S_{21}^{probe}. Finally, the pad losses are accessed by characterizing a back-to-back realization of the pad with a $\approx 100\,\mu$m MSL. The realized gain in the broadside direction is given in Fig. 6.46 (a) and compared to the FDTD and EC solutions. Although the measurement result shows standing waves and a remaining slight down-shift of the operating frequency, the general agreement is reasonable. As before, the measured antenna gain even exceeds the estimation from the EC and the FDTD. Fig. 6.46 (b) compares the $\varphi = 0°$ and $\varphi = 90°$-cuts obtained with the FDTD and the on-chip measurement at 405 GHz. Whereas the agreement is excellent in the $\varphi = 90°$ plane, the $\varphi = 0°$ plane shows severe undulations, which are usually caused by the reflections with the uncovered part of the on-wafer probe. This effect occurs dominantly at $\varphi = 0°$ since this plane is geometrically orthogonal to the uncovered on-wafer probe tip. Furthermore, this plane suffers from shadowing of the probe in the negative θ direction.

However, the investigation of E- and H-planes is more complicated for this antenna type. Due to the geometrical rotation of the antenna arms, the measurement plane needs to be rotated with increasing frequency to track the polarization. Fig. 6.47 (a) shows the cut planes acquired using the spherical antenna measurement system. Here, most of the $\pm 112.5°$-cuts and all measurements of the $\pm 157.5°$ cuts are expected to be shadowed by the on-wafer probe. Contrary, strong interferences due to the uncovered part of the probe tip are expected close to $\varphi = 0°$, e.g., for $\varphi = \pm 22.5°$. The

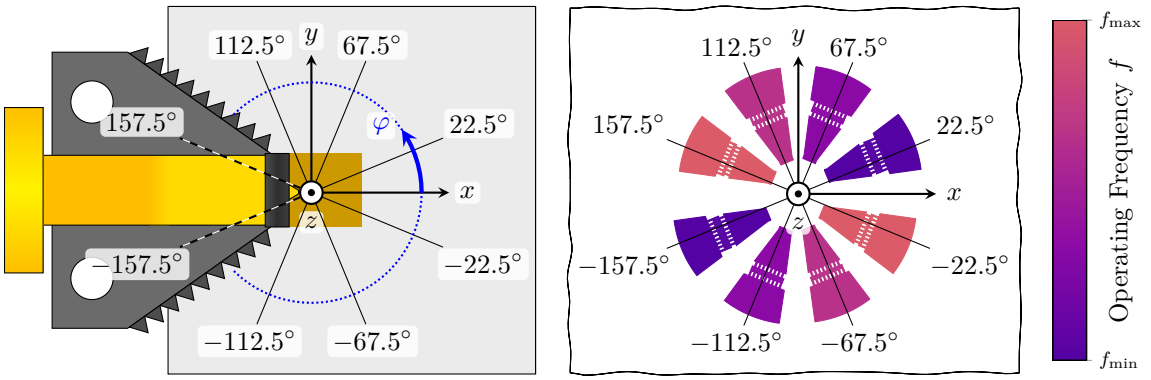

(a) (b)

Figure 6.47.: Schematic drawing of (a) the top view on the on-wafer probe contacting the chip antenna highlighting the possibly shadowed cut planes and (b) the expected frequency-dependent rotation of the E-plane caused by the on-chip antenna.

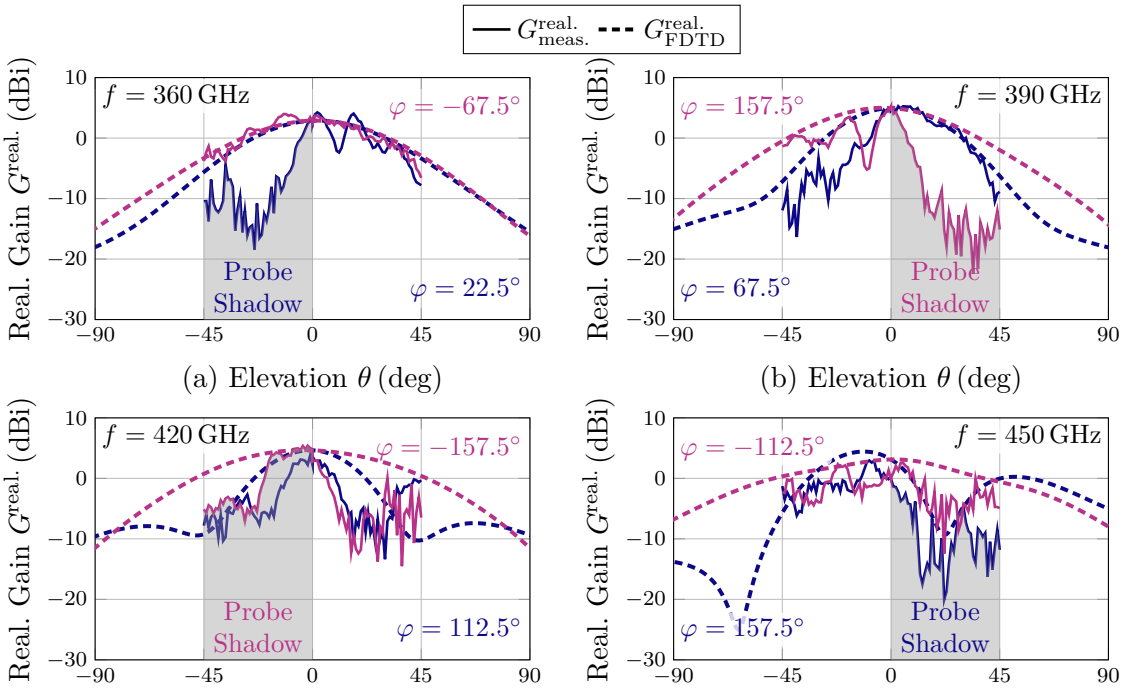

(a) Elevation θ (deg) (b) Elevation θ (deg)

(c) Elevation θ (deg) (d) Elevation θ (deg)

Figure 6.48.: Realized gain for the antenna assembly in E- and H-plane comparing measurements and FDTD results in the cut planes defined according to Fig. 6.47 (b).

corresponding expected rotation associated with the antenna's operating frequency is visualized in Fig. 6.47 (b). The so-acquired cut planes are depicted in Fig. 6.48. Considering the slight frequency downshift observed in Fig. 6.46, the far-field cut planes

are investigated in the frequency range between 360 GHz and 450 GHz. For each frequency, a correspondingly rotated cut plane is measured and compared to results from the FDTD method. The regions strongly affected by the probe shadowing, namely the $\varphi = \pm 157.5°$ cuts, are highlighted separately. Except for slight undulations caused by the on-wafer probe, the measured radiation patterns are exceptionally frequency independent; besides its inherent rotation, the antenna radiation and polarization are remarkably unchanged over the operating bandwidth. Only at the upper frequency limit of $\approx$ 450 GHz, increased undulations can be seen in the FDTD result. Furthermore, the disagreement between the FDTD result and measurement is increased at 420 GHz, possibly indicating stronger interference with the on-wafer probe and the beginning performance degradation for higher frequencies (cf. Fig 6.46 (a)). The overall performance proves both the feasibility of the antenna concept and the desired wideband operation of on-chip antennas despite the utilization of an on-chip ground plane. Last, it should be mentioned that this antenna, as the previous prototypes, should be considered closer to a multi-resonant than to a broadband approach, as, for example, the group delay of this antenna is expected to inherit the multi-resonant behavior. As shown for the RHCP antenna, this behavior can be compensated for utilization in a broadband radar system [A133].

6.4. Discussion of the Antenna Concepts and Implementations

The prototypes presented in this thesis indicate a learning process and performance progress for the antenna implementation. Each fabrication run yields new challenges and limitations within the step-wise improvement and exploration of innovative antenna structures on-chip. The two main objectives of this thesis and, thus, of the antenna progression were increasing the limited radiation efficiency and enabling a wider operating bandwidth. These objectives are approached with two measures, namely implementing multi-resonant antennas to increase the bandwidth and introducing capacitive discontinuities into the antennas to enhance the radiation efficiency. The benefits, limitations, and improvements of the different antenna concepts and capacitance implementations will be discussed separately in the following sections.

6.4.1. Multiresonant Antenna Concepts

The suggested frequency-selective feeding networks utilize $\lambda/4$-transformers to deliver the power to the most suitable antenna element. Since the initial design considers only the input impedance of the single antenna element, this input impedance must be comparable to the antenna element implemented in the overall antenna assembly, i.e., the coupling between the different antenna elements in the assembly must be negligible. This limitation, however, collides with the interest in closely chosen operating

frequencies for the individual elements, which arises from a wideband operation. For example, the linear polarized antenna was initially planned with four different antenna elements to enhance the overall operating bandwidth. However, the coupling between those elements ultimately reduces the usable bandwidth. Consequently, the antenna was implemented using only two different antenna elements and resembled a valuable proof-of-concept for both the capacitively enhanced antennas and the feeding concept. The RHCP antenna developed subsequently featured rotated antenna elements to reduce the coupling. Here, the frequency selectivity of the feeding network is excellent, as the dominant polarization is radiated over a significant bandwidth. However, the simplicity of phase-shifting MSLs utilized to obtain the CP results in suboptimal operation for frequencies other than the design frequency, ultimately reducing the axial ratio and, thus, the purity of the CP. It should be noted that even this elliptical polarization can, especially in the radar context, enable better visibility of dipole-like objects, which could be missed by an unluckily rotated linear polarized radar approach. The finally presented frequency-dependent polarized antenna combines the findings of the previous concepts, as it rotates the antenna elements to reduce the coupling and aims for a large operating bandwidth utilizing four different antenna elements. With the reduced coupling, the frequency selective feeding network can provide the power to the most suitable antenna over a large bandwidth. Even with the electrically very long, and thus lossy, feed line, an antenna gain $> 0\,\mathrm{dBi}$ is achieved over a substantial bandwidth exceeding 100 GHz. This gain is also achieved due to the significant directivity of the antenna resulting from the large occupied aperture. Last, the achievable overall bandwidth is inherently limited by possible higher-order operations of the utilized antennas (cf. Fig. 6.43 (d)) in combination with the feeding network. Since the introduced capacitive discontinuities decrease the antenna bandwidth, they also lower the separation in the frequency domain to higher-order operation modes. Thus, combining the capacitively enhanced antennas with the frequency selective feeding network must be carefully designed, using, e.g., the presented EC model.

6.4.2. Capacitive Discontinuity Implementations

The capacitive discontinuities have been primarily introduced in this thesis to increase the antenna's radiation efficiency. It has been shown in Section 5.3.5 that the radiation of the single capacitive discontinuity cannot be improved; more specifically, it is independent of the geometry of the capacitor and only depends on the utilized MSL and the value of the capacitance. Thus a low-loss implementation of this capacitance can be considered the optimal approach to maximize the antenna's radiation efficiency. The initially designed capacitive discontinuity utilizing the overlapping metal layers is already dominated by the dielectric losses resulting from the capacitance within a lossy dielectric. It is, thus, concerning the antenna efficiency well suited. However, the top metal layers within the on-chip environment are not intended to build distributed capacitances. Consequently, the dielectric thickness and permittivity between the uppermost metal layers are usually not crucial for on-chip systems and, thus, less

important for chip designers and manufacturers. Given the high sensitivity of the antenna to the capacitance (cf. Section 5.2.1), an improper estimation of the capacitance can yield severe frequency offsets in the antenna operating frequency. For example, the linear polarized antenna operates at a higher frequency than initially planned [A23]. This deviation was considered for the design of the RHCP antenna, such that this prototype operates as intended. Since the frequency-dependent polarized antenna has been fabricated on a different technology, the risk of over- or underestimating the distributed capacitance was preconceived by changing the implementation of the on-chip capacitance. The chosen interdigital capacitance is located on one metal layer only and depends thus dominantly on its thickness, whereas the dependence on the lower and higher SiO_2/Si_3N_4 layers is reduced. Furthermore, the possibility to laser-trim single fingers of the capacitors to perform antenna tuning after fabrication relaxes the accuracy required to estimate the capacitance. It has been shown that this approach suffers from severe ohmic losses inherent to the interdigital structure compared to the (concerning losses optimized) overlapping metal capacitors; however, the flexibility of adjusting the antenna performance after fabrication is, given the preparation and processing time of an on-chip fabrication, of great value. Even with uncertainties in the design, the number of fabrication runs necessary to obtain an operating prototype can be significantly reduced.

7. Conclusion

This thesis has presented two prototypes of on-chip antennas operating at 250 GHz and 300 GHz fabricated in Infineon's SiGe BiCMOS B11HFC process and one using the B12HFC process operating at 400 GHz for use in mm-wave radar systems. The prototypes are efficiency-enhanced on-chip antennas utilizing an on-chip ground plane to minimize the effect of substrate waves. They have been shown to operate over an increased bandwidth compared to standard resonant antennas. Here, the bandwidth has been achieved by a frequency-selective matching network which distributes the signal to be radiated to the best-suited radiator element. An adaption of this network has been used for both the linear and the circularly polarized antenna candidates, and the desired antenna operation has been proven using EC calculations, full-wave FDTD simulations, and measurement results. The presented frequency-dependent polarized antenna eliminates the design problems of the previous candidates and proves the concept by obtaining a wide operating bandwidth. Each antenna features capacitive discontinuities to increase the radiation efficiency and the degrees of freedom in the design process. In order to gain physical insight, an EC-based description of the antennas is developed and tested versus full-wave simulation and measurement results. This EC model enables calculating dissipation and radiation losses, current distribution, input impedance, and even radiated far fields through a source superposition. It is based on a thorough description of the radiation mechanism of MSL discontinuities presented in this thesis. The discontinuities are modeled using a combination of the fundamental solutions for open- and short circuits, which enables the calculation of radiation and the coupling between the discontinuities. Additionally, the resulting EC model with different coupling mechanisms is investigated, and different solution strategies for the circuit simulation are discussed based on the application. An astonishing agreement is achieved between the comparably simple EC model and the challenging on-wafer antenna measurement of the complex prototypes. Besides measurements of the antenna radiation pattern, the linear polarized antenna is investigated using a coaxial near-field probe to prove the correct operation. Furthermore, the group delay of the CP antenna has been measured and compensated numerically to prove its applicability for high-resolution radar systems. Last, the frequency-dependent polarized antenna features a capacitance that can be laser-trimmed to optimize the operating frequency after the chip fabrication.

For future applications, it should be noted that the reasonable applicability of these antennas is limited in the frequency range. At very high frequencies, the on-chip environment becomes electrically larger, so even antennas without capacitive disconti-

nuities will achieve acceptable radiation efficiencies. Nevertheless, the discontinuities still offer extra freedom in the antenna design, as they allow for an arbitrary choice of antenna length and, thus, increased antenna aperture. Furthermore, combining antennas with different resonance frequencies remains promising since the achievable bandwidths with on-chip VCOs typically outperform the bandwidth of standard resonant antenna approaches, such as microstrip patch antennas. It has been shown that inherent decoupling achieved by rotating the single antennas eases the design and enables remarkably wide operating bandwidth. This feeding technique is also applicable for other resonant antennas, easing the design process while increasing the bandwidth and, thus, the achievable radar resolution. Investigations to feed a rectangular patch antenna with two polarizations at two corresponding frequencies using this approach have been started.

Last, an overall antenna optimization based on fast circuit simulations is conceivably possible with the presented EC model. Compared to extensive full-wave simulations with simulation times in the order of tens of minutes or even hours, the circuit simulations require only seconds for a wideband analysis. Thus, a fast co-simulation with the circuitry on the MMIC is enabled without generating broadband touchstone files. Here, the simplified EC model enables a broadband antenna description suitable for harmonic balance or transient simulations; and the interaction with the frequency doubler, receive mixer, or variable capacitors can be investigated efficiently. Combined with the thorough antenna description, including radiation efficiency and directivity, this computational efficiency enables a fast parametric optimization toward a high-performing antenna. Initial tests have, however, shown that a large variety of capacitances and antenna lengths achieve comparable radiation efficiencies, such that the single antennas presented in this thesis are already very close to optimal solutions. Thus only a moderate efficiency improvement is expected from this method. Nevertheless, the physical insight gained from the fundamental understanding of the antennas is key for the presented designs and contributes to the presented successful implementations. Since the EC has been shown to determine the radiation properties of the full antenna assembly, more advanced frequency-selective feeding techniques could be investigated considering the antenna-to-antenna coupling. Finally, the radar systems with the CP and the frequency-dependent polarized on-chip antennas need to be tested such that the principal operation and the applicability in a real mm-wave wideband radar system are proven.

Bibliography*

[1] D. Maas, A. Frank, and J. L. M. Van Mechelen, "A breakthrough industrial THz application: Robust in-situ THz-based paint layer monitoring", in *2019 Conf. Lasers Electro-Opt. CLEO*, May 2019, pp. 1–2.

[2] A. Venon, Y. Dupuis, P. Vasseur, and P. Merriaux, "Millimeter wave FMCW radars for perception, recognition and localization in automotive applications: A survey", *IEEE Trans. Intell. Veh.*, vol. 7, no. 3, pp. 533–555, Sep. 2022.

[3] D. M. Mittleman, "Perspective: Terahertz science and technology", *J. Appl. Phys.*, vol. 122, no. 23, p. 230 901, Dec. 2017.

[A4] P. Hillger, M. van Delden, U. S. M. Thanthrige, *et al.*, "Toward mobile integrated electronic systems at THz frequencies", *J. Infrared Milli. THz Waves*, vol. 41, no. 7, pp. 846–869, Jul. 2020.

[5] G. P. Kniffin and L. M. Zurk, "Model-based material parameter estimation for terahertz reflection spectroscopy", *IEEE Trans. THz Sci. Technol.*, vol. 2, no. 2, pp. 231–241, Mar. 2012.

[6] K. K. Tokgoz, S. Maki, J. Pang, *et al.*, "A 120Gb/s 16QAM CMOS millimeter-wave wireless transceiver", in *2018 IEEE Int. Solid - State Circuits Conf. - ISSCC*, San Francisco, CA, USA, Feb. 2018, pp. 168–170.

[7] J. Grzyb, K. Statnikov, N. Sarmah, and U. Pfeiffer, "A wideband 240 GHz lens-integrated circularly polarized on-chip annular slot antenna for a FMCW radar transceiver module in SiGe technology", in *2015 SBMO/IEEE MTT-S Int. Microw. Optoelectron. Conf. IMOC*, Porto de Galinhas, Brazil, Nov. 2015, pp. 1–4.

[8] A. Haderer, P. Scherz, J. Schrattenecker, and A. Stelzer, "Real-time implementation of an FMCW backprojection algorithm for 1D and 2D apertures", in *2011 8th Eur. Radar Conf.*, Manchester, UK, Oct. 2011, pp. 53–56.

[9] B. B. Adela, "Antennas for silicon-based mm-wave FMCW radars: Antenna integration and MIMO system design", Ph.D. dissertation, Electrical Engineering, Technische Universiteit Eindhoven, Eindhoven, Netherlands, Nov. 4, 2019.

*All authored or co-authored publications are highlighted with the prefix *A*.

[10] A. Kaineder, C. Mangiavillano, F. Ahmed, M. Furqan, and A. Stelzer, "240-GHz system on chip FMCW radar for short range applications", in *2020 IEEE MTT-S Int. Conf. Microw. Intell. Mobil. ICMIM*, Linz, Austria, Nov. 2020, pp. 1–4.

[11] S. Kueppers, H. Cetinkaya, R. Herschel, and N. Pohl, "A compact 24 × 24 channel MIMO FMCW radar system using a substrate integrated waveguide-based reference distribution backplane", *IEEE Trans. Microw. Theory Tech.*, vol. 68, no. 6, pp. 2124–2133, Jun. 2020.

[12] S. Hansen, C. Bredendiek, G. Briese, A. Froehly, R. Herschel, and N. Pohl, "A SiGe-chip-based D-band FMCW-radar sensor with 53-GHz tuning range for high resolution measurements in industrial applications", *IEEE Trans. Microw. Theory Tech.*, vol. 70, no. 1, pp. 719–731, Jan. 2022.

[A13] D. Starke, J. Wittemeier, F. Vogelsang, *et al.*, "A fully integrated 0.48 THz FMCW radar transceiver MMIC in a SiGe-technology", in *2022 17th Eur. Microw. Integr. Circuits Conf. EuMIC*, Milan, Italy, Sep. 2022, pp. 56–59.

[14] M. de Kok, A. B. Smolders, and U. Johannsen, "A review of design and integration technologies for D-band antennas", *IEEE Open J. Antennas Propag.*, vol. 2, pp. 746–758, 2021.

[15] A. Babakhani, X. Guan, A. Komijani, A. Natarajan, and A. Hajimiri, "A 77-GHz phased-array transceiver with on-chip antennas in silicon: Receiver and antennas", *IEEE J. Solid-State Circuits*, vol. 41, no. 12, pp. 2795–2806, Dec. 2006.

[16] M. Seyyed-Esfahlan, M. Kaynak, B. Göttel, and I. Tekin, "SiGe process integrated on-chip dipole antenna on finite-size ground plane", *IEEE Antennas Wirel. Propag. Lett.*, vol. 12, pp. 1260–1263, 2013.

[17] C. Bredendiek, N. Pohl, T. Jaeschke, K. Aufinger, and A. Bilgic, "A 240 GHz single-chip radar transceiver in a SiGe bipolar technology with on-chip antennas and ultra-wide tuning range", in *2013 IEEE Radio Freq. Integr. Circuits Symp. RFIC*, Seattle, WA, USA, Jun. 2013, pp. 309–312.

[18] S. Thomas, C. Bredendiek, and N. Pohl, "A SiGe-based 240-GHz FMCW radar system for high-resolution measurements", *IEEE Trans. Microw. Theory Tech.*, vol. 67, no. 11, pp. 4599–4609, Nov. 2019.

[19] T. V. Dinh, D. Lesénéchal, B. Domengès, *et al.*, "Modeling and characterization of bond-wire arrays for distributed chip-package-PCB co-design", in *2015 Eur. Microw. Conf. EuMC*, Paris, France, Sep. 2015, pp. 1022–1025.

[20] S. Sinha, R. Doerner, F.-J. Schmückle, *et al.*, "Flip-chip approach for 500 GHz broadband interconnects", *IEEE Trans. Microw. Theory Tech.*, vol. 65, no. 4, pp. 1215–1225, Apr. 2017.

[21] R. Munson, "Conformal microstrip antennas and microstrip phased arrays", *IEEE Trans. Antennas Propag.*, vol. 22, no. 1, pp. 74–78, Jan. 1974.

[A22] F. Sheikh, A. Prokscha, J. M. Eckhardt, *et al.*, "THz measurements, antennas, and simulations: From the past to the future", *IEEE J. Microw.*, vol. 3, no. 1, pp. 289–304, Jan. 2023.

[A23] B. Sievert, J. T. Svejda, J. Wittemeier, N. Pohl, D. Erni, and A. Rennings, "Equivalent circuit model separating dissipative and radiative losses for the systematic design of efficient microstrip-based on-chip antennas", *IEEE Trans. Microw. Theory Techn.*, vol. 69, no. 2, pp. 1282–1294, Feb. 2021.

[24] A. Ruehli, "Equivalent circuit models for three-dimensional multiconductor systems", *IEEE Trans. Microw. Theory Tech.*, vol. 22, no. 3, pp. 216–221, Mar. 1974.

[25] Y. S. Cao, L. J. Jiang, and A. E. Ruehli, "An equivalent circuit model for graphene-based terahertz antenna using the PEEC method", *IEEE Trans. Antennas Propag.*, vol. 64, no. 4, pp. 1385–1393, Apr. 2016.

[26] N. Uzunoglu, N. Alexopoulos, and J. Fikioris, "Radiation properties of microstrip dipoles", *IEEE Trans. Antennas Propag.*, vol. 27, no. 6, pp. 853–858, Nov. 1979.

[27] D. Pozar, "Input impedance and mutual coupling of rectangular microstrip antennas", *IEEE Trans. Antennas Propag.*, vol. 30, no. 6, pp. 1191–1196, Nov. 1982.

[28] C. Caloz and T. Itoh, *Electromagnetic Metamaterials: Transmission Line Theory and Microwave Applications: The Engineering Approach*. Hoboken, NJ, USA: John Wiley & Sons, Inc., Nov. 11, 2005.

[29] M. Asada and S. Suzuki, "Terahertz emitter using resonant-tunneling diode and applications", *Sensors*, vol. 21, no. 4, p. 1384, Jan. 2021.

[30] K. Okada, K. Kasagi, N. Oshima, S. Suzuki, and M. Asada, "Resonant-tunneling-diode Terahertz oscillator using patch antenna integrated on slot resonator for power radiation", *IEEE Trans. Terahertz Sci. Technol.*, vol. 5, no. 4, pp. 613–618, Jul. 2015.

[31] S. Thomas, C. Bredendiek, T. Jaeschke, F. Vogelsang, and N. Pohl, "A compact, energy-efficient 240 GHz FMCW radar sensor with high modulation bandwidth", in *2016 Ger. Microw. Conf. GeMiC*, Bochum, Germany, Mar. 2016, pp. 397–400.

[32] J. Grzyb, K. Statnikov, N. Sarmah, B. Heinemann, and U. R. Pfeiffer, "A 210–270-GHz circularly polarized FMCW radar with a single-lens-coupled SiGe HBT chip", *IEEE Trans. Terahertz Sci. Technol.*, vol. 6, no. 6, pp. 771–783, Nov. 2016.

[33] S. Thomas, "System- und Antennenkonzepte für ein FMCW-Radarsystem auf Basis eines 240-GHz-SiGe-Transceiver-MMIC", Ph.D. dissertation, Fakultät für Elektrotechnik und Informationstechnik, Ruhr-Universität Bochum, Bochum, Germany, 2021.

[34] J. Gamba, *Radar Signal Processing for Autonomous Driving* (Signals and Communication Technology). Singapore: Springer Singapore, 2020.

[35] C. J. Baker and S. O. Piper, "Continuous wave radar", in *Principles of Modern Radar. 3: Radar Applications*, W. L. Melvin and J. A. Scheer, Eds., Raleigh, NC, USA: SciTech Publishing, 2010.

[36] B. M. Keel, "Fundamentals of pulse compression waveforms", in *Principles of Modern Radar. 1: Basic Principles*, M. A. Richards, J. Scheer, and W. A. Holm, Eds., Raleigh, NC, USA: SciTech Publishing, 2010.

[37] V. Winkler, "Range doppler detection for automotive FMCW radars", in *2007 Eur. Microw. Conf.*, Munich, Germany, Oct. 2007, pp. 1445–1448.

[38] M. I. Skolnik, Ed., *Radar Handbook*, 2nd ed. New York, NY, USA: McGraw-Hill, 1990.

[39] W. Wiesbeck and L. Sit, "Radar 2020: The future of radar systems", in *2014 Int. Radar Conf.*, Lille, France, Oct. 2014, pp. 1–6.

[40] J. A. Scheer and W. A. Holm, "Introduction and radar overview", in *Principles of Modern Radar. 1: Basic Principles*, M. A. Richards, J. A. Scheer, and W. A. Holm, Eds., Raleigh, NC, USA: SciTech Publishing, 2010.

[41] S. Scherr, "FMCW-Radarsignalverarbeitung zur Entfernungsmessung mit hoher Genauigkeit", Ph.D. dissertation, Fakultät für Elektrotechnik und Informationstechnik, Karlsruher Institut für Technologie (KIT), Karlsruhe, Germany, 2017.

[42] D. Aalfs, "Adaptive digital beamforming", in *Principles of Modern Radar. 2: Advanced Techniques*, W. L. Melvin and J. A. Scheer, Eds., Edison, NJ, USA: SciTech Publishing, 2013.

[43] R. E. Collin, *Antennas and Radiowave Propagation* (McGraw-Hill Series in Electrical Engineering), 1st ed. New York, NY, USA: McGraw-Hill Book Company, 1985.

[44] D. Brandwood, *Fourier transforms in radar and signal processing* (Artech House radar library). Boston, MA, USA: Artech House, 2003.

[45] C. Vasanelli, F. Roos, A. Durr, *et al.*, "Calibration and direction-of-arrival estimation of millimeter-wave radars: A practical introduction", *IEEE Antennas Propag. Mag.*, vol. 62, no. 6, pp. 34–45, Dec. 2020.

[46] K. W. Forsythe and D. W. Bliss, "MIMO radar: Concepts, performance enhancements, and applications", in *MIMO Radar Signal Processing*, J. Li and P. Stoica, Eds., Hoboken, NJ, USA: J. Wiley & Sons, 2009.

[47] H. Krim and M. Viberg, "Two decades of array signal processing research: The parametric approach", *IEEE Signal Process. Mag.*, vol. 13, no. 4, pp. 67–94, Jul. 1996.

[48] F. Roos, P. Hügler, L. L. T. Torres, *et al.*, "Compressed sensing based single snapshot DoA estimation for sparse MIMO radar arrays", in *2019 12th Ger. Microw. Conf. GeMiC*, Stuttgart, Germany, Mar. 2019, pp. 75–78.

[49] H. M. Cheema, F. Khalid, and A. Shamim, "Codesign of circuits and antennas", in *Antenna-on-Chip: Design, Challenges, and Opportunities*, Boston, MA, USA: Artech House, Jun. 30, 2021.

[50] T. Maekawa, H. Kanaya, S. Suzuki, and M. Asada, "Oscillation up to 1.92 THz in resonant tunneling diode by reduced conduction loss", *Appl. Phys. Express*, vol. 9, no. 2, p. 024 101, Jan. 22, 2016.

[51] M. Andree, J. Grzyb, R. Jain, B. Heinemann, and U. R. Pfeiffer, "Broadband modeling, analysis, and characterization of SiGe HBT terahertz direct detectors", *IEEE Trans. Microwave Theory Techn.*, vol. 70, no. 2, pp. 1314–1333, Feb. 2022.

[52] K. Statnikov, J. Grzyb, N. Sarmah, B. Heinemann, and U. R. Pfeiffer, "A lens-coupled 210–270 GHz circularly polarized FMCW radar transceiver module in SiGe technology", in *2015 Eur. Microw. Conf. EuMC*, Paris, France, Sep. 2015, pp. 550–553.

[53] H. M. Cheema, F. Khalid, and A. Shamim, *Antenna-on-Chip: Design, Challenges, and Opportunities*. Boston, MA, USA: Artech House, Jun. 30, 2021, 275 pp.

[54] A. Altaf and M. Seo, "A review of the D-band antennas", in *2022 14th Glob. Symp. Millim.-Waves Terahertz GSMM*, Seoul, Republic of Korea, May 2022, pp. 16–18.

[55] Y. He, Y. Chen, L. Zhang, S.-W. Wong, and Z. N. Chen, "An overview of terahertz antennas", *China Commun.*, vol. 17, no. 7, pp. 124–165, Jul. 2020.

[56] C. A. Balanis, *Antenna Theory: Analysis and Design*, 3rd ed. Hoboken, NJ, USA: John Wiley & Sons, Inc., 2005.

[57] W. A. Ahmad, M. Kucharski, A. Di Serio, H. J. Ng, C. Waldschmidt, and D. Kissinger, "Planar highly efficient high-gain 165 GHz on-chip antennas for integrated radar sensors", *IEEE Antennas Wirel. Propag. Lett.*, vol. 18, no. 11, pp. 2429–2433, Nov. 2019.

[58] H. J. Ng, R. Wang, and D. Kissinger, "On-chip antennas in SiGe BiCMOS technology: Challenges, state of the art and future directions", in *2018 Asia-Pac. Microw. Conf. APMC*, Kyoto, Japan, Nov. 2018, pp. 621–623.

[59] J. Böck, K. Aufinger, S. Boguth, *et al.*, "SiGe HBT and BiCMOS process integration optimization within the DOTSEVEN project", in *2015 IEEE Bipolar/BiCMOS Circuits Technol. Meet. - BCTM*, Oct. 2015, pp. 121–124.

[60] T. Zimmer, J. Böck, F. Buchali, *et al.*, "SiGe HBTs and BiCMOS technology for present and future millimeter-wave systems", *IEEE J. Microw.*, vol. 1, no. 1, pp. 288–298, Jan. 2021.

[61] M. Hitzler, "Breitbandige hochintegrierte FMCW-Radare bei 160 GHz für industrielle Anwendungen", Ph.D. dissertation, Fakultät für Ingenieurwissenschaften, Informatik und Psychologie, Universität Ulm, Ulm, Germany, Feb. 27, 2019.

[62] M. K. Hedayati, A. Abdipour, R. Sarraf Shirazi, *et al.*, "Challenges in on-chip antenna design and integration with RF receiver front-end circuitry in nanoscale CMOS for 5G communication systems", *IEEE Access*, vol. 7, pp. 43 190–43 204, 2019.

[63] H. M. Cheema and A. Shamim, "The last barrier: On-chip antennas", *IEEE Microw. Mag.*, vol. 14, no. 1, pp. 79–91, Jan. 2013.

[64] N. Alexopoulos and D. Jackson, "Fundamental superstrate (cover) effects on printed circuit antennas", *IEEE Trans. Antennas Propagat.*, vol. 32, no. 8, pp. 807–816, Aug. 1984.

[65] H.-Y. Yang, N. Alexopoulos, and D. Jackson, "Analysis of microstrip open-end and gap discontinuities in a substrate-superstrate configuration", in *1988 IEEE MTT-S Int. Microw. Symp. Dig.*, New York, NY, USA, May 1988, 705–708 vol.2.

[66] H.-Y. Yang, N. Alexopoulos, and D. Jackson, "Microstrip open-end and gap discontinuities in a substrate-superstrate structure", *IEEE Trans. Microw. Theory Techn.*, vol. 37, no. 10, pp. 1542–1546, Oct. 1989.

[67] H. Zhang and A. Shamim, "Gain enhancement of millimeter-wave on-chip antenna through an additively manufactured functional package", *IEEE Trans. Antennas Propag.*, vol. 68, no. 6, pp. 4344–4353, Jun. 2020.

[68] H. Saeidi, S. Venkatesh, X. Lu, and K. Sengupta, "THz prism: One-shot simultaneous localization of multiple wireless nodes with leaky-wave THz antennas and transceivers in CMOS", *IEEE J. Solid-State Circuits*, vol. 56, no. 12, pp. 3840–3854, Dec. 2021.

[A69] P. Lu, T. Haddad, J. Tebart, *et al.*, "Mobile THz communications using photonic assisted beam steering leaky-wave antennas", *Opt. Express*, vol. 29, no. 14, pp. 21 629–21 638, Jul. 5, 2021.

[A70] P. Lu, T. Haddad, J. Tebart, B. Sievert, A. Rennings, and A. Stöhr, "THz beam steering with InP-based leaky-wave antenna", in *2020 45th Int. Conf. Infrared Millim. THz Waves IRMMW-THz*, Buffalo, NY, USA, Nov. 2020, pp. 1–2.

[A71] P. Lu, V. Rymanov, S. Dülme, B. Sievert, A. Rennings, and A. Stöhr, "THz beam forming and beam switching using lens-assisted quasi-optical THz transmitter", in *2017 Int. Top. Meet. Microw. Photonics MWP*, Beijing, China, Oct. 2017, pp. 1–4.

[A72] A. Rennings, B. Sievert, W. Liu, K. Arzi, W. Prost, and D. Erni, "Broadband millimeter-wave detector based on triple-barrier resonant tunneling diode and tailored archimedean spiral antenna", in *2017 IEEE Asia Pac. Microw. Conf. APMC*, Kuala Lumpur, Malaysia, Nov. 2017, pp. 775–778.

[73] W. Ahmad, M. Kucharski, H. Ng, and D. Kissinger, "A compact efficient D-band micromachined on-chip differential patch antenna for radar applications", in *2019 IEEE Int. Symp. Antennas Propag. USNC-URSI Radio Sci. Meet.*, Atlanta, GA, USA, Jul. 2019, pp. 2201–2202.

[74] W. A. Ahmad, H. J. Ng, C. Waldschmidt, and D. Kissinger, "Micromachined 160 GHz endfire antenna in 130-nm BiCMOS technology for radar applications", in *2020 IEEE Int. Symp. Antennas Propag. North Am. Radio Sci. Meet.*, Montreal, Canada, Jul. 2020, pp. 1859–1860.

[A75] B. Sievert, D. Erni, and A. Rennings, "Circular high impedance surface for radially polarized fields", in *2017 IEEE Asia Pac. Microw. Conf. APMC*, Kuala Lumpur, Malaysia, Nov. 2017, pp. 1337–1340.

[A76] B. Sievert, D. Erni, and A. Rennings, "Spatially modulated high impedance surface based on a multilayer approach", in *2018 11th Ger. Microw. Conf. GeMiC*, Freiburg, Germany, Mar. 2018, pp. 259–262.

[77] B. Gashi, D. Meier, L. John, *et al.*, "Broadband 400 GHz on-chip antenna with a metastructured ground plane and dielectric resonator", *IEEE Trans. Antennas Propag.*, pp. 1–1, 2022.

[A78] K. Arzi, S. Clochiatti, E. Mutlu, *et al.*, "Broadband detection capability of a triple barrier resonant tunneling diode", in *2019 2nd Int. Workshop Mob. THz Syst. IWMTS*, Bad Neuenahr, Germany, Jul. 2019.

[79] Y. Koyama, Y. Kitazawa, K. Yukimasa, *et al.*, "A high-power terahertz source over 10 mW at 0.45 THz using an active antenna array with integrated patch antennas and resonant-tunneling diodes", *IEEE Trans. Terahertz Sci. Technol.*, vol. 12, no. 5, pp. 510–519, Sep. 2022.

[A80] B. Sievert, J. T. Svejda, D. Erni, and A. Rennings, "Mutually coupled dielectric resonators for on-chip antenna efficiency enhancement", in *2019 2nd Int. Workshop Mob. THz Syst. IWMTS*, Bad Neuenahr, Germany, Jul. 2019, pp. 1–4.

[81] D. L. Cuenca and J. Hesselbarth, "Self-aligned microstrip-fed spherical dielectric resonator antenna", in *2015 9th Eur. Conf. Antennas Propag. EUCAP*, Lisbon, Portugal, Apr. 2015, pp. 1–5.

[82] J. Grzyb, M. Andree, R. Jain, B. Heinemann, and U. R. Pfeiffer, "A lens-coupled on-chip antenna for dual-polarization SiGe HBT THz direct detector", *IEEE Antennas Wirel. Propag. Lett.*, vol. 18, no. 11, pp. 2404–2408, Nov. 2019.

[83] Z. Tong, A. Fischer, X. Wang, A. Stelzer, and L. Maurer, "Wideband differential antenna in package with superstrate structure at 77GHz", in *2012 IEEE Asia-Pac. Conf. Antennas Propag.*, Singapore, Aug. 2012, pp. 203–206.

[84] S. Beer, H. Gulan, C. Rusch, and T. Zwick, "Integrated 122-GHz antenna on a flexible polyimide substrate with flip chip interconnect", *IEEE Trans. Antennas Propag.*, vol. 61, no. 4, pp. 1564–1572, Apr. 2013.

[85] A. Bhutani, H. Gulan, B. Goettel, *et al.*, "122 GHz aperture-coupled stacked patch microstrip antenna in LTCC technology", in *2016 10th Eur. Conf. Antennas Propag. EuCAP*, Davos, Switzerland, Apr. 2016, pp. 1–5.

[86] Y. Wu, T. Yu, M. Zhang, D. Yu, J. Hirokawa, and Q. H. Liu, "A W-band corporate-fed hollow-waveguide slot array antenna by glass micromachining", in *2020 Int. Symp. Antennas Propag. ISAP*, Osaka, Japan, Jan. 2021, pp. 435–436.

[87] A. Karimi and J. Oberhammer, "Design of an amplitude-tapered corporate-feed slot array antenna with reduced side-lobe level for silicon micromachining", in *2022 16th Eur. Conf. Antennas Propag. EuCAP*, Madrid, Spain, Mar. 2022, pp. 1–5.

[88] S. Biber, J. Schur, A. Hofmann, and L.-P. Schmidt, "Design of new passive THz devices based on micromachining techniques", in *5th Int. Kharkov Symp. Phys. Eng. Microw. Millim. Submillimeter Waves*, vol. 1, Kharkov, Ukraine, Jun. 2004, 26–31 Vol.1.

[89] J. Hebeler, L. Steinweg, and T. Zwick, "Differential bondwire interface for chip-to-chip and chip-to-antenna interconnect above 200 GHz", in *2022 52nd Eur. Microw. Conf. EuMC*, Milan, Italy, Sep. 2022, pp. 306–309.

[90] T. Galler, T. Chaloun, W. Mayer, *et al.*, "Glass package for radar MMICs above 150 GHz", *IEEE J. Microw.*, vol. 2, no. 1, pp. 97–107, Jan. 2022.

[A91] P.-Y. Wang, B. Sievert, J. T. Svejda, *et al.*, "A liquid crystal tunable metamaterial unit cell for dynamic metasurface antennas", *IEEE Trans. Antennas Propag.*, vol. 71, no. 1, pp. 1135–1140, Jan. 2023.

[92] L. Schmitt, J. Barowski, and M. Hoffmann, "THz phase shifter based on MEMS-actuated slot waveguides", in *2022 5th Int. Workshop Mob. Thz Syst. IWMTS*, Duisburg, Germany, Jul. 2022, pp. 1–4.

[93] M. R. Karim, X. Yang, and M. F. Shafique, "On chip antenna measurement: A survey of challenges and recent trends", *IEEE Access*, vol. 6, pp. 20 320–20 333, 2018.

[94] H. Gulan, C. Luxey, and D. Titz, "Mm-wave sub-mm-wave antenna measurement", in *Handbook of Antenna Technologies*, Z. N. Chen, D. Liu, H. Nakano, X. Qing, and T. Zwick, Eds., Singapore: Springer, 2016, pp. 2191–2238.

[95] Q. Liu, A. C. F. Reniers, U. Johannsen, M. C. van Beurden, and A. B. Smolders, "Improved probing reliability in antenna-on-chip measurements", *IEEE Antennas Wirel. Propag. Lett.*, vol. 17, no. 9, pp. 1745–1749, Sep. 2018.

[96] H. Zhang and A. Shamim, "Tackling the issues of millimeter-wave on-chip antenna measurements", in *2019 13th Eur. Conf. Antennas Propag. EuCAP*, Krakow, Poland, Mar. 2019, pp. 1–5.

[97] K. Daffé, G. Dambrine, F. von Kleist-Retzow, and K. Haddadi, "RF wafer probing with improved contact repeatability using nanometer positioning", in *2016 87th ARFTG Microw. Meas. Conf. ARFTG*, San Francisco, CA, USA, May 2016, pp. 1–4.

[98] R. Sakamaki, R. Kishikawa, Y. Tojima, *et al.*, "Demonstration of non-invasive probing of CMOS devices with aluminum pads at frequencies up to 500 GHz", in *2022 99th ARFTG Microw. Meas. Conf. ARFTG*, Denver, CO, USA, Jun. 2022, pp. 1–4.

[99] S. Fregonese, M. Deng, M. De Matos, *et al.*, "Comparison of on-wafer TRL calibration to ISS SOLT calibration with open-short de-embedding up to 500 GHz", *IEEE Trans. THz Sci. Technol.*, vol. 9, no. 1, pp. 89–97, Jan. 2019.

[A100] C. Biurrun-Quel, T. Haddad, B. Sievert, *et al.*, "Design and characterization of terahertz CORPS beam forming networks", *J. Infrared Millim. Terahertz Waves*, to be published.

[A101] T. Haddad, C. Biurrun-Quel, P. Lu, *et al.*, "Photonic-assisted 2-D terahertz beam steering enabled by a LWA array monolithically integrated with a BFN", *Opt. Express*, vol. 30, no. 21, pp. 38 596–38 612, Oct. 10, 2022.

[102] J. Schoepfel, T. T. Braun, S. Kueppers, K. Aufinger, and N. Pohl, "A fully differential hybrid coupler for automotive radar applications", in *2022 17th Eur. Microw. Integr. Circuits Conf. EuMIC*, Milan, Italy, Sep. 2022, pp. 107–110.

[103] H. Chu, Y.-X. Guo, T.-G. Lim, Y. M. Khoo, and X. Shi, "135-GHz micromachined on-chip antenna and antenna array", *IEEE Trans. Antennas Propag.*, vol. 60, no. 10, pp. 4582–4588, Oct. 2012.

[104] D. Novotny, M. Francis, R. Wittmann, J. Gordon, J. Guerrieri, and A. Curtin, "Multi-purpose configurable range for antenna testing up to 220 GHz", in *10th Eur. Conf. Antennas Propag. EUCAP*, Davos, Switzerland, Apr. 2016, pp. 1–3.

[A105] B. Sievert, J. T. Svejda, D. Erni, and A. Rennings, "Spherical mm-Wave/THz antenna measurement system", *IEEE Access*, vol. 8, pp. 89 680–89 691, 2020.

[106] J. A. Gordon, D. R. Novotny, M. H. Francis, *et al.*, "Millimeter-wave near-field measurements using coordinated robotics", *IEEE Trans. Antennas Propag.*, vol. 63, no. 12, pp. 5351–5362, Dec. 2015.

[107] D. R. Novotny, "Reducing effects of LO cable movement in antenna and long distance VNA measurements", in *2019 Jt. Int. Symp. Electromagn. Compat. Sapporo Asia-Pac. Int. Symp. Electromagn. Compat.*, Sapporo, Japan, Jun. 2019, pp. 585–588.

[108] L. Boehm, M. Hitzler, F. Roos, and C. Waldschmidt, "Probe influence on integrated antenna measurements at frequencies above 100 GHz", in *46th Eur. Microw. Conf.*, London, UK, Oct. 2016, pp. 552–555.

[109] D. Titz, F. Ferrero, and C. Luxey, "Development of a millimeter-wave measurement setup and dedicated techniques to characterize the matching and radiation performance of probe-fed antennas", *IEEE Antennas Wirel. Propag Lett*, vol. 54, no. 4, pp. 188–203, Aug. 2012.

[110] D. Titz, F. Ferrero, P. Brachat, G. Jacquemod, and C. Luxey, "Efficiency measurement of probe-fed antennas operating at millimeter-wave frequencies", *IEEE Antennas Wireless Propag. Lett.*, vol. 11, pp. 1194–1197, 2012.

[111] D. J. van Rensburg and S. F. Gregson, "Parametric study of probe positioning errors in articulated spherical near-field test systems for mm-wave applications", in *2014 IEEE Conf. Antenna Meas. Appl.*, Antibes Juan-les-Pins, France, Nov. 2014, pp. 1–4.

[112] A. Jam and K. Sarabandi, "A submillimeter-wave near-field measurement setup for on-wafer pattern and gain characterization of antennas and arrays", *IEEE Trans. Instrum. Meas.*, vol. 66, no. 4, pp. 802–811, Apr. 2017.

[113] Y. Tanaka, G. Ducournau, C. Belem-Goncalves, *et al.*, "Photonics-based near-field measurement and far-field characterization for 300-GHz band antenna testing", *IEEE Open J. Antennas Propag.*, vol. 3, pp. 24–31, 2022.

[114] S. Sahin, N. K. Nahar, and K. Sertel, "Noncontact characterization of antenna parameters in mmW and THz bands", *IEEE Trans. Terahertz Sci. Technol.*, vol. 12, no. 1, pp. 42–52, Jan. 2022.

[115] L. Piotrowsky, V. Bernhardt, J. Barowski, I. Rolfes, and N. Pohl, "Antenna pattern characterization with an industrial robot assisted FMCW radar system", in *2019 IEEE Asia-Pac. Microw. Conf. APMC*, Singapore, Dec. 2019, pp. 153–155.

[116] A. C. Granich, R. Moch, A. Al-Bassam, and D. Heberling, "Radiation pattern measurements using an active radar module", in *2022 Antenna Meas. Tech. Assoc. Symp. AMTA*, Oct. 2022, pp. 1–5.

[117] C. Vasanelli, R. Batra, A. D. Serio, F. Boegelsack, and C. Waldschmidt, "Assessment of a millimeter-wave antenna system for MIMO radar applications", *IEEE Antennas Wirel. Propag. Lett.*, vol. 16, pp. 1261–1264, 2017.

[118] C. Schulz, B. Will, I. Rolfes, N. Pohl, C. Baer, and T. Musch, "Characterization of a beam steering lens antenna for industrial radar measurements in harsh environments", in *2013 Eur. Radar Conf.*, Nuremberg, Germany, Oct. 2013, pp. 117–120.

[119] W. A. Ahmad, J. Wessel, H. J. Ng, and D. Kissinger, "IoT-ready millimeter-wave radar sensors", in *2020 IEEE Glob. Conf. Artif. Intell. Internet Things GCAIoT*, Dubai, United Arab Emirates, Dec. 2020, pp. 1–5.

[120] A. Antonucci, M. Corrà, A. Ferrari, *et al.*, "Performance analysis of a 60-GHz radar for indoor positioning and tracking", in *2019 Int. Conf. Indoor Position. Indoor Navig. IPIN*, Pisa, Italy, Sep. 2019, pp. 1–7.

[121] E. Öztürk, H. J. Ng, W. Winkler, and D. Kissinger, "0.1mm² SiGe BiCMOS RX / TX channel front-ends for 120 GHz phased array radar systems", in *2017 IEEE 17th Top. Meet. Silicon Monolith. Integr. Circuits RF Syst. SiRF*, Phoenix, AZ, USA, Jan. 2017, pp. 50–53.

[122] C. Waldschmidt, J. Hasch, and W. Menzel, "Automotive radar — from first efforts to future systems", *IEEE J. Microw.*, vol. 1, no. 1, pp. 135–148, Jan. 2021.

[123] J. Hasch, U. Wostradowski, R. Hellinger, and D. Mittelstrass, "77 GHz automotive radar sensor in low-cost PCB technology", in *2011 8th Eur. Radar Conf. EuRAD*, Manchester, UK, Oct. 2011, pp. 101–104.

[124] S. Chen, W. Shangguan, J. Taghia, U. Kühnau, and R. Martin, "Automotive radar interference mitigation based on a generative adversarial network", in *2020 IEEE Asia-Pac. Microw. Conf. APMC*, Hong Kong, Hong Kong, Dec. 2020, pp. 728–730.

[125] M. E. Asghar, S. Buddappagari, F. Baumgärtner, *et al.*, "Radar target simulator and antenna positioner for real-time over-the-air stimulation of automotive radar systems", in *2020 17th Eur. Radar Conf. EuRAD*, Utrecht, Netherlands, Jan. 2021, pp. 95–98.

[126] S. Wald, T. Mathy, S. Nair, C. M. Leon, and T. Dallmann, "ATRIUM: Test environment for automotive radars", in *2020 IEEE MTT-S Int. Conf. Microw. Intell. Mobil. ICMIM*, Linz, Austria, Nov. 2020, pp. 1–4.

[127] H. J. Ng, R. Feger, and D. Kissinger, "Scalable mm-wave 4-Channel radar SoC with vector modulators and demodulators for MIMO and phased array applications", in *2018 IEEE/MTT-S Int. Microw. Symp. - IMS*, Philadelphia, PA, USA, Jun. 2018, pp. 1472–1475.

[128] A. Dürr, D. Schwarz, S. Häfner, *et al.*, "High-resolution 160-GHz imaging MIMO radar using MMICs with on-chip frequency synthesizers", *IEEE Trans. Microw. Theory Tech.*, vol. 67, no. 9, pp. 3897–3907, Sep. 2019.

[129] S. Beer, B. Göttel, C. Rusch, H. Gulan, and T. Zwick, "Off-chip antenna designs for fully integrated, low-cost millimeter-wave transceivers", in *2013 Int. Workshop Antenna Technol. IWAT*, Karlsruhe, Germany, Mar. 2013, pp. 199–202.

[130] B. B. Adela, P. T. M. van Zeijl, U. Johannsen, and A. B. Smolders, "On-chip antenna integration for millimeter-wave single-chip FMCW radar, providing high efficiency and isolation", *IEEE Trans. Antennas Propag.*, vol. 64, no. 8, pp. 3281–3291, Aug. 2016.

[131] J. Hasch, E. Topak, R. Schnabel, T. Zwick, R. Weigel, and C. Waldschmidt, "Millimeter-wave technology for automotive radar sensors in the 77 GHz frequency band", *IEEE Trans. Microw. Theory Tech.*, vol. 60, no. 3, pp. 845–860, Mar. 2012.

[132] J. Li and P. Stoica, "MIMO radar — Diversity means superiority", in *MIMO Radar Signal Processing*, J. Li and P. Stoica, Eds., Hoboken, NJ, USA: J. Wiley & Sons, 2009.

[A133] J. Wittemeier, B. Sievert, M. Dedic, D. Erni, A. Rennings, and N. Pohl, "The impact of group delay dispersion on radar imaging with multiresonant antennas", *IEEE Microw. Wirel. Compon. Lett.*, pp. 1–4, 2021.

[134] M. Harter, J. Hildebrandt, A. Ziroff, and T. Zwick, "Self-calibration of a 3-D-digital beamforming radar system for automotive applications with installation behind automotive covers", *IEEE Trans. Microw. Theory Tech.*, vol. 64, no. 9, pp. 2994–3000, Sep. 2016.

[135] L. Piotrowsky, T. Jaeschke, S. Kueppers, J. Siska, and N. Pohl, "Enabling high accuracy distance measurements with FMCW radar sensors", *IEEE Trans. Microw. Theory Tech.*, vol. 67, no. 12, pp. 5360–5371, Dec. 2019.

[136] T. T. Braun, M. van Delden, C. Bredendiek, J. Schoepfel, and N. Pohl, "A low phase noise phase-locked loop with short settling times for automotive radar", in *2021 16th Eur. Microw. Integr. Circuits Conf. EuMIC*, London, UK, Apr. 2022, pp. 205–208.

[137] M. van Delden, N. Pohl, K. Aufinger, C. Baer, and T. Musch, "A low-noise transmission-type yttrium iron garnet tuned oscillator based on a SiGe MMIC and bond-coupling operating up to 48 GHz", *IEEE Trans. Microw. Theory Tech.*, vol. 67, no. 10, pp. 3973–3982, Oct. 2019.

[138] K. Gupta, R. Garg, and R. Chadha, "Characterization of discontinuities II - Striplines and microstrip lines", in *Computer-aided Design of Microwave Circuits*, ser. Artech microwave library, Derham, MA, USA: Artech, 1981.

[139] H. Wheeler, "Transmission-line properties of a strip on a dielectric sheet on a plane", *IEEE Trans. Microw. Theory Techn.*, vol. 25, no. 8, pp. 631–647, Aug. 1977.

[140] H. Wheeler, "Formulas for the skin effect", *Proc. IRE*, vol. 30, no. 9, pp. 412–424, Sep. 1942.

[141] D. M. Pozar, *Microwave Engineering*, 4th ed. Hoboken, NJ, USA: John Wiley & Sons, Inc., 2012.

[142] R. Jackson and D. Pozar, "Full-wave analysis of microstrip open-end and gap discontinuities", *IEEE Trans. Microwave Theory Techn.*, vol. 33, no. 10, pp. 1036–1042, Oct. 1985.

[143] D. Pozar, "Considerations for millimeter wave printed antennas", *IEEE Trans. Antennas Propag.*, vol. 31, no. 5, pp. 740–747, Sep. 1983.

[144] A. Ishimaru, *Electromagnetic Wave Propagation, Radiation, and Scattering* (IEEE Press Series on Electromagnetic Wave Theory), 1st ed. Hoboken, NJ, USA: John Wiley & Sons, Inc., 2017.

[145] S. A. Schelkunoff, "The impedance concept and its application to problems of reflection, refraction, shielding and power absorption", *Bell Syst. Tech. J.*, vol. 17, no. 1, pp. 17–48, Jan. 1938.

[146] H. Wheeler, "Transmission-line properties of parallel strips separated by a dielectric sheet", *IEEE Trans. Microw. Theory Techn.*, vol. 13, no. 2, pp. 172–185, Mar. 1965.

[147] M. V. Schneider, "Microstrip lines for microwave integrated circuits", *Bell Syst. Techn. J.*, vol. 48, no. 5, pp. 1421–1444, May 1969.

[148] E. O. Hammerstad, "Equations for microstrip circuit design", in *1975 5th Eur. Microw. Conf.*, Hamburg, Germany, Sep. 1975, pp. 268–272.

[149] R. Owens, "Accurate analytical determination of quasi-static microstrip line parameters", *Radio Electron. Eng.*, vol. 46, no. 7, pp. 360–364, Jul. 1976.

[150] E. Hammerstad and O. Jensen, "Accurate models for microstrip computer-aided design", in *1980 IEEE MTT-S Int. Microw. Symp. Dig.*, vol. 80, Washington, DC, USA, 1980, pp. 407–409.

[151] R. E. Collin and F. J. Zucker, *Antenna Theory Part 1.* (Inter University Electronic Series, vol. 7), 1st ed. New York, NY, USA: McGraw-Hill, 1969.

[152] P. H. Smith, *Electronic Applications of the Smith Chart: In Waveguide, Circuit, and Component Analysis*. New York, NY, USA: McGraw-Hill Book Company, 1969.

[153] S. R. Best, "Small and fractal antennas", in *Modern Antenna Handbook*, C. A. Balanis, Ed., Hoboken, NJ, USA: Wiley, 2008.

[154] C. Balanis, "Antenna theory: A review", *Proc. IEEE*, vol. 80, no. 1, pp. 7–23, Jan. 1992.

[155] C. A. Balanis, *Advanced Engineering Electromagnetics*, 2nd ed. Hoboken, NJ, USA: John Wiley & Sons, Inc., 2012.

[156] H. Sobal, "Radiation conductance of open-circuit microstrip (Correspondence)", *IEEE Trans. Microw. Theory Techn.*, vol. 19, no. 11, pp. 885–887, Nov. 1971.

[157] D. B. Davidson, *Computational Electromagnetics for RF and Microwave Engineering*, 2nd ed. Cambridge, UK: Cambridge University Press, 2010.

[158] A. Sommerfeld and E. G. Straus, *Partial Differential Equations in Physics* (Pure and Applied Mathematics 6), P. A. Smith and S. Eilenberg, Eds. New York, NY, USA: Academic Press, 1949.

[159] D. B. Brick, "The radiation of a hertzian dipole over a coated conductor", Cruft Lab., Harvard Univ., Cambridge, MA, USA, Rep. 172, May 1953.

[160] J. A. Stratton, *Electromagnetic Theory* (IEEE Press Series on Electromagnetic Wave Theory), D. G. Dudley, Ed. Hoboken, NJ, USA: John Wiley & Sons, Ltd, 2007.

[161] G. Tsandoulas, "Excitation of a grounded dielectric slab by a horizontal dipole", *IEEE Trans. Antennas Propag.*, vol. 17, no. 2, pp. 156–161, Mar. 1969.

[162] S. Shastry and A. Kumar, "Dipole over a dielectric-coated conducting plane", *IETE Journal of Research*, vol. 31, no. 1, pp. 12–19, Jan. 1985.

[163] G. Goubau, "On the excitation of surface waves", *Proc. IRE*, vol. 40, no. 7, pp. 865–868, Jul. 1952.

[164] S. Richter, "Comment on "Excitation of a grounded dielectric slab by a horizontal dipole"", *IEEE Trans. Antennas Propag.*, vol. 18, no. 2, pp. 290–290, Mar. 1970.

[165] G. Dubost, M. Nicolas, and H. Havot, "Theory and applications of broadband microstrip antennas", in *6th Eur. Microw. Conf.*, Rome, Italy, Oct. 1976, pp. 275–279.

[166] A. Derneryd, "Linearly polarized microstrip antennas", *IEEE Trans. Antennas Propag.*, vol. 24, no. 6, pp. 846–851, Nov. 1976.

[167] A. Derneryd, "A theoretical investigation of the rectangular microstrip antenna element", *IEEE Trans. Antennas Propag.*, vol. 26, no. 4, pp. 532–535, Jul. 1978.

[168] P. Silvester and P. Benedek, "Equivalent capacitances of microstrip open circuits", *IEEE Trans. Microw. Theory Techn.*, vol. 20, no. 8, pp. 511–516, Aug. 1972.

[169] M. Maeda, "An analysis of gap in microstrip transmission lines", *IEEE Trans. Microw. Theory Techn.*, vol. 20, no. 6, pp. 390–396, Jun. 1972.

[170] E. Hammerstad, "Computer-aided design of microstrip couplers with accurate discontinuity models", in *1981 IEEE MTT-S Int. Microw. Symp. Dig.*, Los Angeles, CA, USA, Jun. 1981, pp. 54–56.

[171] M. Kirschning, R. H. Jansen, and N. H. L. Koster, "Accurate model for open end effect of microstrip lines", *Electron. Lett.*, vol. 17, no. 3, pp. 123–125, Feb. 5, 1981.

[A172] B. Sievert, D. Erni, and A. Rennings, "Resonant antenna periodically loaded with series capacitances for enhanced radiation efficiency", in *2019 12th Ger. Microw. Conf. GeMiC*, Stuttgart, Germany, Mar. 2019, pp. 20–23.

[173] L. Lewin, "Radiation from discontinuities in strip-line", *Proc. IEE C Monogr. UK*, vol. 107, no. 12, p. 163, 1960.

[174] L. Lewin, "Spurious radiation from microstrip", *Proc. Inst. Electr. Eng. UK*, vol. 125, no. 7, p. 633, 1978.

[175] E. Denlinger, "Radiation from microstrip resonators (Correspondence)", *IEEE Trans. Microw. Theory Tech.*, vol. 17, no. 4, pp. 235–236, Apr. 1969.

[176] F. Djahli, A. Mayouf, and M. Dekik, "Modelling of microstrip open-end and gap discontinuities using an ameliorated moments method", *Int. J. Electron.*, vol. 86, no. 2, pp. 245–254, Feb. 1999.

[177] N. Das and D. Pozar, "A generalized spectral-domain Green's function for multilayer dielectric substrates with application to multilayer transmission lines", *IEEE Trans. Microwave Theory Techn.*, vol. 35, no. 3, pp. 326–335, Mar. 1987.

[178] T.-S. Horng, S.-C. Wu, H.-Y. Yang, and N. Alexopoulos, "A generalized method for distinguishing between radiation and surface-wave losses in microstrip discontinuities", *IEEE Trans. Microw. Theory Techn.*, vol. 38, no. 12, pp. 1800–1807, 12 Dec. 1990.

[179] N. Alexopoulos and S.-C. Wu, "Frequency-independent equivalent circuit model for microstrip open-end and gap discontinuities", *IEEE Trans. Microw. Theory Techn.*, vol. 42, no. 7, pp. 1268–1272, Jul. 1994.

[180] P. Benedek and P. Silvester, "Equivalent capacitances for microstrip gaps and steps", *IEEE Trans. Microw. Theory Techn.*, vol. 20, no. 11, pp. 729–733, Nov. 1972.

[181] M. Kirschning, R. Jansen, and N. Koster, "Measurement and computer-aided modeling of microstrip discontinuities by an improved resonator method", in *1983 IEEE MTT-S Int. Microw. Symp. Dig.*, Boston, MA, USA, May 1983, pp. 495–497.

[A182] B. Sievert, M. Degen, J. T. Svejda, D. Erni, and A. Rennings, "An analytical model to approximate the radiation conductance of microstrip gaps", in *2022 52nd Eur. Microw. Conf. EuMC*, Milan, Italy, Sep. 2022, pp. 238–241.

[183] A. Vladirmirescu, "Shaping the history of SPICE", *IEEE Solid-State Circuits Mag.*, vol. 3, no. 2, pp. 36–39, 2011.

[184] R. E. Collin, *Field Theory of Guided Waves*, 2nd ed. New York, NY, USA: IEEE Press, 1991.

[185] J. Murdock, E. Ben-Dor, F. Gutierrez, and T. S. Rappaport, "Challenges and approaches to on-chip millimeter wave antenna pattern measurements", in *2011 IEEE MTT-S Int. Microw. Symp.*, Baltimore, MD, USA, Jun. 2011, pp. 1–4.

[186] K. Mohammadpour-Aghdam, S. Brebels, A. Enayati, R. Faraji-Dana, G. A. E. Vandenbosch, and W. DeRaedt, "RF probe influence study in millimeter-wave antenna pattern measurements", *Int. J. RF Microw. Comput.-Aided Eng.*, vol. 21, no. 4, pp. 413–420, 2011.

[187] Z.-M. Tsai, Y.-C. Wu, S.-Y. Chen, T. Lee, and H. Wang, "A V-band on-wafer near-field antenna measurement system using an IC probe station", *IEEE Trans. Antennas Propag.*, vol. 61, no. 4, pp. 2058–2067, Apr. 2013.

[A188] B. Sievert, J. Wittemeier, J. T. Svejda, N. Pohl, D. Erni, and A. Rennings, "Coaxial cable-based magnetic and electric near-field probes to measure on-chip components up to 330 GHz", *IEEE Antennas Wirel. Propag. Lett.*, vol. 22, no. 10, pp. 2472–2476, Oct. 2023.

[A189] B. Sievert, J. Wittemeier, J. T. Svejda, N. Pohl, D. Erni, and A. Rennings, "Bandwidth-enhanced circularly polarized mm-wave antenna with on-chip ground plane", *IEEE Trans. Antennas Propag.*, vol. 70, no. 10, pp. 9139–9148, Oct. 2022.

[190] R. Waterhouse, "Small microstrip patch antenna", *Electron. Lett.*, vol. 31, no. 8, p. 604, 1995.

[191] S. Bhardwaj and J. L. Volakis, "Hexagonal waveguide based circularly polarized horn antennas for sub-mm-wave/Terahertz band", *IEEE Trans. Antennas Propag.*, vol. 66, no. 7, pp. 3366–3374, Jul. 2018.

[192] S. Bhardwaj, N. K. Nahar, and J. L. Volakis, "Novel phaseless gain characterization for circularly polarized antennas at mm-Wave and THz Frequencies", *IEEE Trans. Antennas Propag.*, vol. 63, no. 10, pp. 4263–4270, Oct. 2015.

[193] B. Goettel, J. Schaefer, H. Gulan, W. Winkler, and T. Zwick, "Double circularly polarized on-chip antenna for a 120 – 130 GHz amplitude monopulse radar", in *Eur Radar Conf EURAD*, London, UK, Oct. 2016, pp. 409–412.

[194] J. G. Marin and J. Hesselbarth, "Circularly-polarized on-chip dielectric resonator antenna", in *12th Eur. Conf. Antennas Propag. EUCAP*, London, UK, Apr. 2018, pp. 1–4.

[195] M. Marschner, F. Baum, and W. Keusgen, "Design of a WR10 rotary joint with two 3D-printed TE01 mode transducers", in *94th Microw. Meas. Symp. ARFTG*, San Antonio, TX, Jan. 2020, pp. 1–4.

[196] M. D. Blech, S. Koch, and S. Saito, "Rectangular waveguide based polarizer for mm-wave antenna measurements", in *6th Eur. Conf. Antennas Propag. EUCAP*, Prague, Czech Republic, Mar. 2012, pp. 3487–3490.

[197] M. Hitzler, S. Bader, and C. Waldschmidt, “Key aspects of robot based antenna measurements at millimeter wave frequencies”, in *8th Eur. Conf. Antennas Propag. EUCAP*, The Hague, Netherlands, Apr. 2014, pp. 392–396.

[198] J. A. G. Malherbe, *Microwave Transmission Line Filters*. Norwood, MA, USA: Artech House, 1979.

[199] C. Roblin, “Representation, characterization and modeling of ultra wide band antennas”, in *Ultra Wide Band Antennas*, X. Begaud, Ed., Hoboken, NJ, USA: John Wiley & Sons, Inc., Mar. 2013.

[200] S. Thomas, A. Froehly, C. Bredendiek, R. Herschel, and N. Pohl, “High resolution SAR imaging using a 240 GHz FMCW radar system with integrated on-chip antennas”, in *2021 15th Eur. Conf. Antennas Propag. EuCAP*, Düsseldorf, Germany, Mar. 2021, pp. 1–5.

[201] P. Miller, “The measurement of antenna group delay”, in *8th Eur. Conf. Antennas Propag. EUCAP*, The Hague, Netherlands, Apr. 2014, pp. 1488–1492.

Publications by the Author

Journal papers (Author)

1. B. Sievert, J. T. Svejda, D. Erni, and A. Rennings, "Spherical mm-Wave/THz antenna measurement system", *IEEE Access*, vol. 8, pp. 89 680–89 691, 2020.
2. B. Sievert, J. T. Svejda, J. Wittemeier, N. Pohl, D. Erni, and A. Rennings, "Equivalent circuit model separating dissipative and radiative losses for the systematic design of efficient microstrip-based on-chip antennas", *IEEE Trans. Microw. Theory Techn.*, vol. 69, no. 2, pp. 1282–1294, Feb. 2021.
3. B. Sievert, J. Wittemeier, J. T. Svejda, N. Pohl, D. Erni, and A. Rennings, "Bandwidth-enhanced circularly polarized mm-wave antenna with on-chip ground plane", *IEEE Trans. Antennas Propag.*, vol. 70, no. 10, pp. 9139–9148, Oct. 2022.
4. B. Sievert, J. Wittemeier, J. T. Svejda, N. Pohl, D. Erni, and A. Rennings, "Coaxial cable-based magnetic and electric near-field probes to measure on-chip components up to 330 GHz", *IEEE Antennas Wirel. Propag. Lett.*, vol. 22, no. 10, pp. 2472–2476, Oct. 2023.

Journal papers (Co-Author)

1. D. Erni, A. Rennings, J. T. Svejda, *et al.*, "Multi-functional RF coils for ultra-high field MRI based on 1D/2D electromagnetic metamaterials", *J. Phys.: Conf. Ser.*, vol. 1092, no. 1, p. 012 031, Sep. 1, 2018.
2. P. Hillger, M. van Delden, U. S. M. Thanthrige, *et al.*, "Toward mobile integrated electronic systems at THz frequencies", *J. Infrared Milli. THz Waves*, vol. 41, no. 7, pp. 846–869, Jul. 2020.
3. M. H. Hassan, B. Sievert, J. T. Svejda, *et al.*, "OAM mode order conversion and clutter rejection with OAM-coded RFID tags", *IEEE Access*, vol. 8, pp. 218 729–218 738, 2020.
4. K. Jerbic, K. Neumann, J. T. Svejda, B. Sievert, A. Rennings, and D. Erni, "Limits of effective material properties in the context of an electromagnetic tissue model", *IEEE Access*, vol. 8, pp. 223 806–223 826, 2020.

5. M. H. Hassan, B. Sievert, J. T. Svejda, *et al.*, "Beam divergence reduction of vortex waves with a tailored lens and a tailored reflector", *IEEE Access*, vol. 9, pp. 9800–9811, 2021.

6. P. Lu, T. Haddad, B. Sievert, *et al.*, "InP-based THz beam steering leaky-wave antenna", *IEEE Trans. THz Sci. Technol.*, vol. 11, no. 2, pp. 218–230, Mar. 2021.

7. P. Lu, T. Haddad, J. Tebart, *et al.*, "Mobile THz communications using photonic assisted beam steering leaky-wave antennas", *Opt. Express*, vol. 29, no. 14, pp. 21 629–21 638, Jul. 5, 2021.

8. J. Wittemeier, B. Sievert, M. Dedic, D. Erni, A. Rennings, and N. Pohl, "The impact of group delay dispersion on radar imaging with multiresonant antennas", *IEEE Microw. Wirel. Compon. Lett.*, pp. 1–4, 2021.

9. X. Liu, L. Schmitt, B. Sievert, *et al.*, "Terahertz beam steering using a MEMS-based reflectarray configured by a genetic algorithm", *IEEE Access*, vol. 10, pp. 84 458–84 472, 2022.

10. E. Farokhipour, B. Sievert, J. T. Svejda, A. Rennings, N. Komjani, and D. Erni, "Wide-angle spoof surface plasmon polariton leaky-wave antenna exploiting prefractal structures with backfire to nearly endfire scanning", *IEEE Antennas Wirel. Propag. Lett.*, vol. 21, no. 12, pp. 2507–2511, Dec. 2022.

11. T. Haddad, C. Biurrun-Quel, P. Lu, *et al.*, "Photonic-assisted 2-D terahertz beam steering enabled by a LWA array monolithically integrated with a BFN", *Opt. Express*, vol. 30, no. 21, pp. 38 596–38 612, Oct. 10, 2022.

12. P.-Y. Wang, B. Sievert, J. T. Svejda, *et al.*, "A liquid crystal tunable metamaterial unit cell for dynamic metasurface antennas", *IEEE Trans. Antennas Propag.*, vol. 71, no. 1, pp. 1135–1140, Jan. 2023.

13. F. Sheikh, A. Prokscha, J. M. Eckhardt, *et al.*, "THz measurements, antennas, and simulations: From the past to the future", *IEEE J. Microw.*, vol. 3, no. 1, pp. 289–304, Jan. 2023.

14. K. Jerbic, J. T. Svejda, B. Sievert, A. Rennings, J. Fröhlich, and D. Erni, "The importance of subcellular structures to the modeling of biological cells in the context of computational bioelectromagnetics simulations", *Bioelectromagnetics*, vol. 44, no. 1-2, pp. 26–46, Feb. 2023.

15. C. Biurrun-Quel, T. Haddad, B. Sievert, *et al.*, "Design and characterization of terahertz CORPS beam forming networks", *J. Infrared Millim. Terahertz Waves*, to be published.

16. K.-D. Jenkel, B. Sievert, A. Rennings, M. Sakaki, D. Erni, and N. Benson, "Radar cross-section of ceramic corner reflectors in the W-band fabricated with the LCM-method", submitted for publication.

Conference Papers (Author)

1. B. Sievert, D. Erni, and A. Rennings, "Circular high impedance surface for radially polarized fields", in *2017 IEEE Asia Pac. Microw. Conf. APMC*, Kuala Lumpur, Malaysia, Nov. 2017, pp. 1337–1340.
2. B. Sievert, D. Erni, and A. Rennings, "Spatially modulated high impedance surface based on a multilayer approach", in *2018 11th Ger. Microw. Conf. GeMiC*, Freiburg, Germany, Mar. 2018, pp. 259–262.
3. B. Sievert, D. Erni, and A. Rennings, "Resonant antenna periodically loaded with series capacitances for enhanced radiation efficiency", in *2019 12th Ger. Microw. Conf. GeMiC*, Stuttgart, Germany, Mar. 2019, pp. 20–23.
4. B. Sievert, J. T. Svejda, D. Erni, and A. Rennings, "Mutually coupled dielectric resonators for on-chip antenna efficiency enhancement", in *2019 2nd Int. Workshop Mob. THz Syst. IWMTS*, Bad Neuenahr, Germany, Jul. 2019, pp. 1–4.
5. B. Sievert, M. Degen, J. T. Svejda, D. Erni, and A. Rennings, "An analytical model to approximate the radiation conductance of microstrip gaps", in *2022 52nd Eur. Microw. Conf. EuMC*, Milan, Italy, Sep. 2022, pp. 238–241.

Conference Papers (Co-Author)

1. P. Lu, V. Rymanov, S. Dülme, B. Sievert, A. Rennings, and A. Stöhr, "THz beam forming and beam switching using lens-assisted quasi-optical THz transmitter", in *2017 Int. Top. Meet. Microw. Photonics MWP*, Beijing, China, Oct. 2017, pp. 1–4.
2. A. Rennings, B. Sievert, W. Liu, K. Arzi, W. Prost, and D. Erni, "Broadband millimeter-wave detector based on triple-barrier resonant tunneling diode and tailored archimedean spiral antenna", in *2017 IEEE Asia Pac. Microw. Conf. APMC*, Kuala Lumpur, Malaysia, Nov. 2017, pp. 775–778.
3. K. Jerbic, B. Sievert, J. Svejda, A. Rennings, and D. Erni, "On the applicability of homogenization in composite material models for tissue analysis in the mm-wave range", in *Photonics Electromagn. Res. Symp. Electromagn. Res. Symp. PIERS 2019*, Rome, Italy, Jun. 17, 2019.
4. M. H. Hassan, B. Sievert, A. Rennings, and D. Erni, "Reducing the divergence of vortex waves with a lens tailored to the utilized circular antenna array", in *2019 2nd Int. Workshop Mob. THz Syst. IWMTS*, Bad Neuenahr, Germany, Jul. 2019, pp. 1–4.
5. K. Arzi, S. Clochiatti, E. Mutlu, *et al.*, "Broadband detection capability of a triple barrier resonant tunneling diode", in *2019 2nd Int. Workshop Mob. THz Syst. IWMTS*, Bad Neuenahr, Germany, Jul. 2019.

6. P.-Y. Wang, F.-Y. Meng, Y.-L. Lyu, B. Sievert, A. Rennings, and D. Erni, "Holographic metasurface reflectarray for Terahertz radiation", in *Photonics Electromagn. Res. Symp. Electromagn. Res. Symp. PIERS 2019*, Xiamen, China, Dec. 17, 2019.

7. A. Stöhr, P. Lu, T. Haddad, *et al.*, "Microwave photonic mm-wave & THz beam steering for imaging, radar and communications", in *Asia Comm Photon Conf ACPC*, Chengdu, China: Optical Society of America, Nov. 2, 2019.

8. M. H. Hassan, M. Al-Mulla, B. Sievert, A. Rennings, and D. Erni, "Evaluation of different phased array approaches for orbital angular momentum beam steering", in *2020 Ger. Microw. Conf. GeMiC*, Cottbus, Germany, Mar. 2020, pp. 44–47.

9. M. H. Hassan, A. A. Abbas, A. Jiménez-Sáez, *et al.*, "Passive orbital angular momentum RFID tag based on dielectric resonator arrays", in *2020 3rd Int. Workshop Mob. THz Syst. IWMTS*, Essen, Germany, Jul. 2020, pp. 1–4.

10. M. H. Hassan, B. Sievert, A. Rennings, and D. Erni, "Generation of vortex waves using crossed 2λ-dipole antennas", in *2021 15th Eur. Conf. Antennas Propag. EUCAP*, Düsseldorf, Germany, Mar. 2021, pp. 1–3.

11. K. Jerbic, J. T. Svejda, B. Sievert, *et al.*, "The identification of spectral signatures in randomized (sub-)surface material systems", in *2022 5th Int. Workshop Mob. Thz Syst. IWMTS*, Duisburg, Germany, Jul. 2022, pp. 1–5.

12. Z. Tian, B. Sievert, M. Eube, P. Hildenhagen, D. Erni, and A. Rennings, "Rotationally symmetric lens antenna with biconical feed for broadband measurement applications", in *2022 52nd Eur. Microw. Conf. EuMC*, Milan, Italy, Sep. 2022, pp. 612–615.

13. K.-D. Jenkel, B. Sievert, A. Rennings, S. Masoud, D. Erni, and N. Benson, "Enhanced radar cross-section for W-band corner reflectors using ceramic additive manufacturing", in *2022 IEEE 12th Int. Conf. RFID Technol. Appl. RFID-TA*, Cagliari, Italy, Sep. 2022, pp. 37–39.

14. D. Starke, J. Wittemeier, F. Vogelsang, *et al.*, "A fully integrated 0.48 THz FMCW radar transceiver MMIC in a SiGe-technology", in *2022 17th Eur. Microw. Integr. Circuits Conf. EuMIC*, Milan, Italy, Sep. 2022, pp. 56–59.

List of Figures

List of Tables

Abbreviations

BEOL	Back End of Line
BiCMOS	Bipolar – Complementary Metal Oxide Semiconductor
CAD	Computer Aided Design
CP	Circular Polarization
CPW	Coplanar Waveguide
CW	Continuous Wave
DRC	Design Rule Check
EC	Equivalent Circuit
EM	Electro Magnetic
FEM	Finite Element Method
FEOL	Front End of Line
FFT	Fast Fourier Transform
FDTD	Finite Difference Time Domain
FMCW	Frequency Modulated Continuous Wave
GSG	Ground Signal Ground
IF	Intermediate Frequency
InP	Indium Phosphide
LHCP	Left Hand Circular Polarized
MIM	Metal Insulator Metal
MIMO	Multiple Input Multiple Output
MMIC	Monolithic Microwave Integrated Circuit
MoM	Method of Moments
MSL	Microstrip Line
NF2FF	Near Field to Far Field
OSM	Open-Short-Match
PCB	Printed Circuit Boards
PEC	Perfect Electric Conductor
PEEC	Partial Element Equivalent Circuit
PLL	Phase Locked Loop
PMC	Perfect Magnetic Conductor
RCS	Radar Cross Section
Radar	RAdio Detection And Ranging
RF	Radio Frequency
RHCP	Right Hand Circular Polarized
Rx	Receiver
Si	Silicon

SiGe	Silicon Germanium
Si_3N_4	Silicon Nitride
SiO_2	Silicon Dioxide
SIW	Substrate Integrated Waveguide
SIMO	Single Input Multiple Output
SNR	Signal to Noise Ratio
SPICE	Simulation Program with Integrated Circuit Emphasis
TE	Transverse Electric
TEM	Transverse Electro Magnetic
TM	Transverse Magnetic
TL	Transmission Line
TRL	Through-Reflect-Line
Tx	Transmitter
UC	Unit Cell
VCO	Voltage Controlled Oscillator
VNA	Vector Network Analyser

Appendix

A. Open-Circuited MSL Radiation Power Integration

An altered coordinate system is used to ease the far-field integration of the open-circuited MSL, where the MSL extends along the z-direction, as depicted in Fig. A.1. With the changed coordinate system, the current is referred to as $i_{\text{open}}(z)$, and its image is below the ground plane. Both include the propagation constant of the MSL β_{TL}, and a reflection coefficient of $\Gamma = 1$ is assumed.

$$i_{\text{open}}(z) = i^{+}_{\text{open}} \left(\exp[-\mathrm{j}\beta_{\text{TL}} z] - \Gamma \exp[+\mathrm{j}\beta_{\text{TL}} z]\right) \tag{A.1}$$

Based on the vector potential of a line current (cf. (4.9)), the dot-product of $\mathbf{e}_r$ and $z'\mathbf{e}_z$ gives $z' \cos\theta$, such that the current above the ground plane yields the vector potential

$$A_{z,\,\text{top,\,open}} = A_0(r) \int_{-L}^{0} \left(\exp[\mathrm{j}z'(-\beta_{\text{TL}} - k_0\,\cos\theta)] - \exp[\mathrm{j}z'(\beta_{\text{TL}} - k_0\,\cos\theta)]\right) \mathrm{d}z', \tag{A.2}$$

$$A_{z,\,\text{top,\,open}} = A_0(r) \left[\frac{\exp[\mathrm{j}z'(-\beta_{\text{TL}} - k_0\,\cos\theta)]}{\mathrm{j}(-\beta_{\text{TL}} - k_0\,\cos\theta)} - \frac{\exp[\mathrm{j}z'(\beta_{\text{TL}} - k_0\,\cos\theta)]}{\mathrm{j}(\beta_{\text{TL}} - k_0\,\cos\theta)} \right]_{-L}^{0}, \tag{A.3}$$

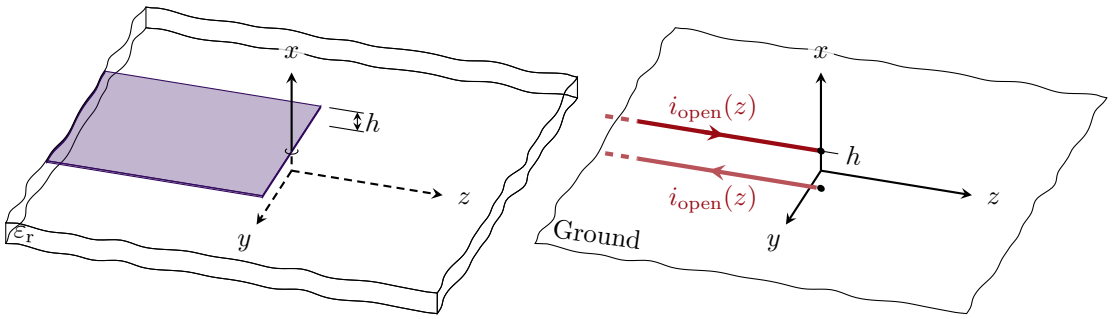

Figure A.1.: Geometry of (a) the MSL open circuit and (b) its representation by a grounded line current $i_{\text{open}}(z)$.

with

$$A_0(r) = \frac{\mu_0\, i^+_{\text{open}}}{4\pi}\,\frac{\exp[-\mathrm{j}k_0 r]}{r}. \tag{A.4}$$

As described in Section 5.3.1, only the upper integration bound is evaluated, yielding

$$A_{z,\,\text{top},\,\text{open}} = A_0(r)\left(\frac{1}{\mathrm{j}(-\beta_{\text{TL}} - k_0\,\cos\theta)} - \frac{1}{\mathrm{j}(\beta_{\text{TL}} - k_0\,\cos\theta)}\right). \tag{A.5}$$

The ground plane at distance h is considered by an image current, which results in an additional factor $2\mathrm{j}\,\sin\left(k_0 h\cos\varphi\,\sin\theta\right)$. For electrically small heights $k_0 h \ll \pi/4$, the first-order Taylor-series representation yields $\sin(x) \approx x$ resulting in

$$A_{z,\,\text{open}} = 2\,k_0 h A_0(r)\left(\frac{1}{(-\beta_{\text{TL}} - k_0\,\cos\theta)} - \frac{1}{(\beta_{\text{TL}} - k_0\,\cos\theta)}\right)\cos\varphi\,\sin\theta. \tag{A.6}$$

The electric field in spherical coordinates can be accessed from the vector potential using (4.10), where the choice of the coordinate system results in only an E_θ component

$$E_{\theta,\,\text{open}} = \mathrm{j}\omega 2\,k_0 h\frac{\mu_0\, i^+_{\text{open}}}{4\pi}\,\frac{\exp[-\mathrm{j}k_0 r]}{r}\,\frac{2\beta_{\text{TL}}}{k_0^2}\left(\frac{1}{(\beta_{\text{TL}}/k_0)^2 - \cos^2\theta}\right)\cos\varphi\,\sin^2\theta, \tag{A.7}$$

which can be simplified using Pythagorean identity to

$$E_{\theta,\,\text{open}} = \mathrm{j}\omega\,\frac{\mu_0\, i^+_{\text{open}} h k_z}{\pi k_0}\,\frac{\exp[-\mathrm{j}k_0 r]}{r}\left(\frac{1-\cos^2\theta}{(\beta_{\text{TL}}/k_0)^2 - \cos^2\theta}\right)\cos\varphi. \tag{A.8}$$

The integration in spherical coordinates yields the radiated power

$$\begin{aligned} P &= \frac{1}{2\eta_0} \int_0^{\pi}\int_{-\pi/2}^{\pi/2} |E_{\theta,\,\text{open}}|^2 |\boldsymbol{r}|^2 \sin\theta\,\mathrm{d}\varphi\,\mathrm{d}\theta \\ &= \frac{1}{2\eta_0} P_0 \int_0^{\pi}\int_{-\pi/2}^{\pi/2} \frac{\left(1-\cos^2\theta\right)^2\,\cos^2\varphi}{\left((\beta_{\text{TL}}/k_0)^2 - \cos^2\theta\right)^2}\sin\theta\,\mathrm{d}\varphi\,\mathrm{d}\theta \\ &= \frac{1}{2\eta_0} P_0 \int_0^{\pi}\cos^2\varphi\,\mathrm{d}\varphi \int_{-\pi/2}^{\pi/2} \frac{\left(1-\cos^2\theta\right)^2}{\left((\beta_{\text{TL}}/k_0)^2 - \cos^2\theta\right)^2}\sin\theta\,\mathrm{d}\theta \end{aligned} \tag{A.9}$$

with

$$P_0 = \frac{\omega^2\mu_0^2 |i^+_{\text{open}}|^2 h^2 \beta_{\text{TL}}^2}{\pi^2 k_0^2}. \tag{A.10}$$

The θ-integral is carried out by substituting $u = \cos\theta$ according to [173]

$$
\begin{aligned}
I &= \int_{-\pi/2}^{\pi/2} \frac{\left(1-\cos^2\theta\right)^2}{\left((\beta_{\mathrm{TL}}/k_0)^2-\cos^2\theta\right)^2}\sin\theta\,\mathrm{d}\theta \\
&= \int_{1}^{-1} \frac{-\left(1-u^2\right)^2}{\left((\beta_{\mathrm{TL}}/k_0)^2-u^2\right)^2}\mathrm{d}u = \int_{-1}^{1} \frac{\left(1-2u^2+u^4\right)}{\left((\beta_{\mathrm{TL}}/k_0)^2-u^2\right)^2}\mathrm{d}u \\
&= \int_{-1}^{1} \frac{1\,\mathrm{d}u}{\left((\beta_{\mathrm{TL}}/k_0)^2-u^2\right)^2} + (-2)\int_{-1}^{1} \frac{u^2\,\mathrm{d}u}{\left((\beta_{\mathrm{TL}}/k_0)^2-u^2\right)^2} + \int_{-1}^{1} \frac{u^4\,\mathrm{d}u}{\left((\beta_{\mathrm{TL}}/k_0)^2-u^2\right)^2}.
\end{aligned}
$$

Substituting $a = \beta_{\mathrm{TL}}/k_0$ and solving the integrals gives

$$
\begin{aligned}
I &= \left[\frac{u}{2a^2\left(a^2-u^2\right)} + \frac{1}{4a^3}\ln\left|\frac{a+u}{a-u}\right|\right]_{-1}^{1} + (-2)\left[\frac{u}{2(a^2-u^2)} - \frac{1}{4a}\ln\left|\frac{a+u}{a-u}\right|\right]_{-1}^{1} \\
&\quad + \left[\frac{a^2\,u}{2(a^2-u^2)} + u - \frac{3a}{4}\ln\left|\frac{a+u}{a-u}\right|\right]_{-1}^{1} \\
&= \frac{1}{a^2}\frac{1}{a^2-1} + \frac{1}{2a^3}\ln\left|\frac{a+1}{a-1}\right| + (-2)\left[\frac{1}{a^2-1} - \frac{1}{2a}\ln\left|\frac{a+1}{a-1}\right|\right] \\
&\quad + \frac{a^2}{a^2-1} + 2 - \frac{3a}{2}\ln\left|\frac{a+1}{a-1}\right| \\
&= 3 - \left(\frac{k_0}{\beta_{\mathrm{TL}}}\right)^2 + \frac{k_0^4 + 2\beta_{\mathrm{TL}}^2\,k_0^2 - 3\beta_{\mathrm{TL}}^4}{2\beta_{\mathrm{TL}}^3 k_0}\ln\left|\frac{\beta_{\mathrm{TL}}+k_0}{\beta_{\mathrm{TL}}-k_0}\right|.
\end{aligned}
$$

Which finally gives the radiated power $P_{\mathrm{rad}}^{\mathrm{open}}$ of the open circuit, as given in (5.36):

$$
P_{\mathrm{rad}}^{\mathrm{open}} = \frac{P_0}{2\eta_0}\frac{\pi}{2}\left[3 - \left(\frac{k_0}{\beta_{\mathrm{TL}}}\right)^2 + \frac{k_0^4 + 2\beta_{\mathrm{TL}}^2\,k_0^2 - 3\beta_{\mathrm{TL}}^4}{2\beta_{\mathrm{TL}}^3 k_0}\ln\left|\frac{\beta_{\mathrm{TL}}+k_0}{\beta_{\mathrm{TL}}-k_0}\right|\right]. \tag{A.11}
$$

DOI: 10.17185/duepublico/81323
URN: urn:nbn:de:hbz:465-20240206-081840-9